Non-intrusive reduced order models and their applications

Dunhui Xiao
Supervised by:
Dr. Fangxin Fang
Prof. Christopher C. Pain
Dr. Andrew Buchan

Submitted for the degree of Doctor of Philosophy
and the Diploma of Imperial College

Applied Modelling and Computation Group
Department of Earth Science and Engineering
Imperial College London

January, 2016

Abstract

Reduced order models (ROMs) have become prevalent in many fields of physics as they offer the potential to simulate dynamical systems with substantially increased computation efficiency in comparison to standard techniques. Among the model reduction techniques, the proper orthogonal decomposition (POD) method has proven to be an efficient means of deriving a reduced basis for high-dimensional flow systems. The intrusive ROM (IROM) is normally derived by the POD and Galerkin projection methods. The IROM is appealing for non-linear and linear model reductions and has been successfully applied to numerous research fields.

However, IROMs suffer from instability and non-linearity efficiency issues. In addition, they can be complex to code because they are intrusive. In most cases the source code describing the physical system has to be modified in order to generate the reduced order model. These modifications can be complex, especially in legacy codes, or may not be possible if the source code is not available (*e.g.* in some commercial software). To circumvent these shortcomings, non-intrusive approaches have been introduced into ROMs. The Non-Intrusive ROM (NIROM) is independent of the original physical system.

The key contribution of this thesis are: Firstly, three novel NIROMs have been presented in this thesis: POD/Taylor series, POD-Smolyak and POD-RBF (radial basis function). Secondly, two NIROMs with varying material properties have been presented. Thirdly, these newly developed NIROMs were implemented and tested under the framework of an unstructured mesh finite element model (FLUIDITY) and a combined finite-discrete element method based solid model (Y2D). Fourthly, these NIROMs have been used to construct ROMs for multi-scale 3-D free surface flows, multi-phase porous media flows, fluid-structure interaction and blasting problems.

Copyright Declaration

The copyright of this thesis rests with the author and is made available under a Creative Commons Attribution Non-Commercial No Derivatives licence. Researchers are free to copy, distribute or transmit the thesis on the condition that they attribute it, that they do not use it for commercial purposes and that they do not alter, transform or build upon it. For any reuse or redistribution, researchers must make clear to others the licence terms of this work.

Declaration

I hereby certify that the work presented in this dissertation is the result of my own investigations during the PhD project. Text and results obtained from other sources are referenced and properly acknowledged.

Dunhui Xiao

Acknowledgements

First of all, I would like to express my appreciation to my supervisors: Dr. Fangxin Fang, Prof. Christopher Pain and Dr. Andrew Buchan. The work described in this thesis would not have been completed without their help, patient guidance and encouragement throughout this research. In particular, Dr. Fangxin's help is tremendous. She devoted much time to my work. My gratitude to her can not be expressed in a few words here. I also would like to express my gratitude to Prof. Michael Navon's. He is a pioneer in the reduced order modelling field. His profound experience lead this work to right direction and his insightful ideas have contributed this work. Prof. Ann Muggeridge's help also contributed greatly to this work. They have both been a huge support, being happy to discuss progress and direction of the work throughout.

I would like to thank the department of Earth Science and Engineering for the Janet Watson scholarship which funded my research. Without the funding, I would not have completed this research.

I appreciate the help from all the members of the AMCG group. They created a great research environment, for example, Dr Gerard Gorman, Dr Matthew D Piggott, Dr John-Paul Latham, Professor Peter A Allison and so on. Their passion for scientific research made me work hard. I was also lucky to have been able learn a great deal from constant discussion with colleagues involved in related work − in particular Dr. Frank Milthaler, Dr. Simon Leo Mouradian, Dr. Jiansheng Xiang, Pan Yang, Dr James R Percival, Dr Claire E Heaney, Dr Dimitrios Pavlidis, Dr Christian T Jacobs, Dr Zhihua Xie, Dr Pablo Salinas, Dr Alexandros Avdis, Stephan Kramer Dr Timothy M B Greaves and other AMCG members. I would like to express my appreciation to Dr. Richard Heddle, Dr. Brian Davies and Dr. Malcolm Woodman

from BP Exploration. I would like to thank my parents and my uncle - who I cannot thank enough - and the rest of my family for the unlimited support and patience over the years.

Table of Contents

1 Introduction **30**

1.1 Motivation of the thesis 30

1.2 Contributions of the thesis 33

1.3 Literature review of reduced order modelling of fluid dynamics problems 34

1.3.1 Intrusive reduced order modelling 35

1.3.1.1 Stability 35

1.3.1.2 Non-linearity 37

1.3.2 Non-intrusive reduced order modelling 39

1.3.3 ROM for free surface, porous media multiphase and fluid-solid interaction problems 40

1.3.3.1 ROM for free surface problems 40

1.3.3.2 ROM for porous media multiphase problems 41

1.3.3.3 ROM for fluid-solid interaction problems 42

1.3.4 Outline of the thesis 43

2 Non-intrusive reduced order modelling of the Navier-Stokes equations **47**

2.1 Abstract 47

2.2 Introduction 48
2.3 Reduced Order Modelling of the Navier-Stokes Equations 50
2.3.1 Governing Equations 50
2.3.2 Reduction via Proper Orthogonal Decomposition 50
2.3.2.1 Proper Orthogonal Decomposition 50
2.3.2.2 Implementation of a standard (Galerkin projection) POD reduced order model 52
2.4 The Taylor series method for the calculation of the POD coefficients . 54
2.4.1 Taylor expression of the POD Coefficients 54
2.4.2 Offline calculation of the first and second derivative matrices in the Taylor series 55
2.5 The Smolyak sparse grid method for calculating the POD coefficients 57
2.6 Numerical examples of Smolyak sparse grid and Taylor series expansion methods 59
2.6.1 Flow past a cylinder 60
2.6.2 The Gyre Problem 68
2.7 POD/RBF formulation of reduced order Navier-Stokes equations . . . 75
2.7.1 Radial basis functions interpolation 75
2.7.1.1 Calculation of the weights 76
2.7.1.2 Choice of radial basis functions 76
2.7.2 RBF POD reduced order modelling 77
2.7.3 Numerical Examples of POD-RBF NIROM 78
2.7.3.1 2-D Lock exchange 78
2.7.3.2 Flow past a cylinder 83
2.8 Conclusions 85

3 Non-intrusive Reduced Order Modeling for multi-scale free surface

flows **89**

3.1 Abstract . . . 89

3.2 Introduction . . . 90

3.3 Three Dimensional Governing Equations . . . 91

3.3.1 Continuous governing equations and free surface boundary conditions . . . 91

3.3.2 Discretisation of free surface equations . . . 92

3.4 Construction NIROM for free surface flows using Smolyak sparse grid 93

3.5 Numerical Examples . . . 96

3.5.1 Balzano test cases . . . 96

3.5.2 Okushiri tsunami test case . . . 101

3.6 Conclusions . . . 110

4 Non-intrusive Reduced Order Modeling for multi-phase porous media flows **111**

4.1 Abstract . . . 111

4.2 Introduction . . . 112

4.3 Governing equations . . . 113

4.4 Construction of the NIROM for multi-phase porous media problems . 114

4.5 Numerical Examples . . . 117

4.5.1 Introduction of an unstructured mesh multiphase fluid model . 117

4.5.2 General description of test cases . . . 117

4.5.3 Two material layer test case . . . 118

4.5.4 Low permeability domain embedded in a high permeability domain . . . 124

4.5.5 3D fluvial channel case . . . 129

4.5.6 Computational efficiency of the POD-RBF model . . . 131

4.6 Conclusion 131

5 Non-intrusive reduced order modeling of fluid-structure interactions 133

5.1 Abstract 133

5.2 Introduction 134

5.3 Governing equations 134

5.3.1 Governing equations for fluid dynamics 134

5.3.2 Governing equations for solid dynamics 135

5.3.3 Fluid-solid coupling equations 135

5.3.3.1 One way coupling 136

5.3.3.2 Two way coupling 137

5.4 Construction of FSI NIROM using POD-RBF 138

5.5 Illustrative numerical examples 143

5.5.1 One way coupling test case - flow past a cylinder 143

5.5.2 Two-way coupling case - a 2D free-falling square in water . . . 147

5.5.3 Vortex-induced vibrations of an elastic beam 150

5.5.4 Computational efficiency of the FSI NIROM 156

5.6 Conclusion 156

6 Model reduction for compressible fluid-solid coupling and its application to blasting 159

6.1 Abstract 159

6.2 Introduction 160

6.3 Description of compressible fluid and solid coupling problem 160

6.3.1 Governing equations for compressible fluids under the framework of FLUIDITY 161

6.3.2 Fracture modelling 161
6.4 Model reduction schema 164
6.5 Application to compressible fluid and solid problems 169
6.5.1 Case 1: an immersed wall in a fluid 169
6.5.1.1 Case 1a: fluid and fracture solid coupling NIROM results with mean subtraction before constructing the POD basis 169
6.5.1.2 Case 1b: the fluid and fracture solid coupling NIROM results without mean subtraction before constructing the POD basis 173
6.5.2 Case 2: blasting test case 179
6.5.2.1 Case 2a: fluid and fracture solid coupling NIROM results with mean subtraction before constructing the POD basis 180
6.5.2.2 Case 2b: fluid and fracture solid coupling NIROM solutions without mean subtraction before constructing the POD basis 183
6.5.3 Efficiency of the POD-RBF model 191
6.6 Conclusions 192

7 Variable parametric non-intrusive reduced order modelling of Navier-Stokes equations 193

7.1 Abstract 193
7.2 Introduction 194
7.3 Variable parametric non-intrusive model reduction methodology . . . 195
7.3.1 Construction of basis functions 195
7.3.2 Smolyak sparse grid representing the parameter space 196
7.3.3 Constructing the second level RBF interpolation 201
7.3.4 Calculating the undetermined POD coefficients 202

7.4 Numerical Examples . . . 203
7.4.1 Flow past a cylinder . . . 203
7.4.2 Lock exchange . . . 210
7.4.3 Efficiency of the NIROM model . . . 215
7.5 Conclusion . . . 215

8 Variable-material non-intrusive reduced order modelling of multi-phase porous media flows 217

8.1 Abstract . . . 217
8.2 Introduction . . . 218
8.3 Methodology of constructing the NIROM for variable-material multi-phase porous media flows . . . 218
8.3.1 Material property surfaces based on Smolyak sparse grid . . . 219
8.3.2 Permeability distribution surfaces based on radial basis functions 219
8.4 Numerical Examples . . . 223
8.4.1 Four material layers test case . . . 223
8.4.2 Reservoir with four baffles . . . 228
8.4.3 Reservoir with eight baffles . . . 237
8.4.4 3D fluvial channel case . . . 244
8.4.5 Efficiency of the NIROM . . . 250
8.5 Conclusion . . . 250

9 Conclusions and future work 253

9.1 Conclusions . . . 253
9.2 Future work . . . 256
9.2.1 Possible extensions and applications . . . 256
9.2.2 Subdomain based reduced order model . . . 257

9.2.3 Non-intrusive ROM for problems with adaptive meshes 258

Bibliography **259**

List of Figures

2.1 Flow past a cylinder at $Re = 400$ 61

2.2 Flow past a cylinder: The graphs shows the solution velocities predicted by the full model, POD model, Taylor expansion method and the Smolyak sparse grid ROM at positions: 0.19397,0.28101, Re=400. 62

2.3 Flow past a cylinder at $Re = 400$: The graphs shows the singular eigenvalues in order of decreasing magnitude. 64

2.4 Flow past a cylinder at $Re = 3600$: The figures displayed above show the solutions of the flow past a cylinder problem at time instances 3.0 and 10.0. The solutions compare the predictions from Smolyak sparse grid ROM and Taylor/POD non-intrusive models with the full model and the standard POD model using 12 POD basis functions. . 65

2.5 Flow past a cylinder at $Re = 3600$: The figures displayed above show the solution difference between the full model and the standard POD and the Smolyak sparse grid ROM of the flow past a cylinder problem at time instances 3.0 and 10.0 using 12 POD basis and 24 POD bases. 66

2.6 Flow past a cylinder at $Re = 3600$: The figures displayed above show the solutions of the flow past a cylinder problem at time instances 3.0 and 10.0. The solutions compare the predictions from Smolyak sparse grid non-intrusive ROM using 24 POD basis functions. 67

2.7 Flow past a cylinder at $Re = 3600$: The figures displayed above show the solutions of the flow past a cylinder problem at time instances 3.0 and 10.0. The solutions compare the predictions from Smolyak sparse grid non-intrusive ROM using 35 POD basis functions. 67

2.8 Flow past a cylinder at $Re = 3600$: The graphs show the velocity speed predicted by the full model, and the Smolyak sparse grid ROM at positions a (0.195, 0.267) and b (0.619, 0.298). These results were obtained using a reduced order model with 24 and 35 POD functions. 69

2.9 Flow past a cylinder at $Re = 3600$: The graphs show the RMSE of results obtained from Smolyak ROM. 70

2.10 Flow past a cylinder at $Re = 3600$: The graphs show the comparison between full model with different levels of Smolyak grid using 12 POD bases at $t = 6$. 70

2.11 Flow past a cylinder at $Re = 3600$: Computational times to compute each time step as a function of mesh size (number of nodes) in the full model. Comparisons are made between the full model and the non-intrusive ROM. 71

2.12 Gyre: the figures displayed above show the solutions of the gyre problem at time instance 41 (left) and 93 days (right). The solutions compare the predictions from the full model (top), the Smolyak sparse grid ROM (middle) **using 6 POD functions** (middle). The Figures at the bottom are the difference between full and Smolyak sparse grid ROM. 72

2.13 Gyre: The figures displayed above show the solutions of the gyre problem at time instance 41 (left) and 93 days (right). The solutions compare the predictions from the full model (top), the Smolyak sparse grid ROM (middle) **using 12 POD functions** (middle). The figures at the bottom are the errors between full and Smolyak sparse grid ROM 73

2.14 Gyre: The graph shows the RMSE errors calculated for the Smolyak sparse grid ROM. 74

2.15 Gyre: The graph shows the correlation coefficient calculated for the Smolyak sparse grid ROM. 74

2.16 Lock exchange: the figures displayed above show the velocity solutions of the lock exchange problem at time instances 20 and 30 seconds. The solutions compare the predictions from RBF/POD model with full and POD model using 12 POD basis functions. 79

2.17 Lock exchange: the figures displayed above show the velocity solutions of the lock exchange problem at time instances 20 and 30 seconds. The solutions compare the predictions from RBF/POD model with full and POD model using 24 POD basis functions. 80

2.18 Lock exchange: the figures displayed above show the velocity solutions of the lock exchange problem at time instances 20 and 30 seconds. The solutions compare the predictions from RBF/POD model with full and POD model using 32 POD basis functions. 80

2.19 Lock exchange: the figures displayed above show the velocity difference between full model and POD and RBF/POD of the lock exchange problem at time instances 20.0 and 30.0 seconds using 24 POD basis 81

2.20 Lock exchange: the figures displayed above show the pressure solutions of the lock exchange problem at time instances 20 and 30 seconds. The solutions compare the predictions from RBF/POD model with full and POD model using 32 POD basis functions. 81

2.21 Lock exchange: the graphs shows the solution velocities of the lock exchange case predicted by the full model, POD model and the RBF/-POD model at a position (0.39801, 0.095). These results were obtained using a reduced order model with 12 and 32 POD functions respectively. 82

2.22 Flow past a cylinder: the figures displayed above show the solutions of the flow past a cylinder problem at time instances 5.25 and 12.0 seconds. The solutions compare the predictions from RBF/POD model with full and POD model using 24 POD basis functions. 84

2.23 Flow past a cylinder: the figures displayed above show the solutions of the flow past a cylinder problem at time instances 5.25 and 12.0 seconds. The solutions compare the predictions from RBF/POD model with full and POD model using 35 POD basis functions. 85

2.24 Flow past a cylinder: the graphs shows the solution velocities of the flow past a cylinder case predicted by the full model, and the RBF/-POD model at a position(0.2029, 0.26535). These results were obtained using a reduced order model with 24 POD functions 86

2.25 Flow past a cylinder: the graph shows the RMSE errors calculated for the RBF/POD model for the flow past a cylinder. 87

2.26 Flow past a cylinder: the graph shows the correlation coefficient calculated for the RBF/POD model for the flow past a cylinder. 87

2.27 Flow past a cylinder: The graphs shows the solution velocities predicted by the full model, POD model, Taylor expansion method, Smolyak sparse grid NIROM and the RBF NIROM at positions: 0.19397,0.28101, Re=400. 12 POD basis functions were used in NIROMs. 88

3.1 Balzano case: The computational domain and mesh used in Balzano case. 97

3.2 Balzano case: the graphs shows the singular eigenvalues in order of decreasing magnitude 97

3.3 Balzano case: the figures show the first 6 POD bases functions for pressure. 98

3.4 Balzano case: The solutions of pressure from the full model and NIROM at time instances 10.2 (left panel) and 25 (right panel). Top panel: the full model; middle panel: NIROM using 2 POD bases; and bottom panel: NIROM using 6 POD bases. 98

3.5 Balzano case: The pressure solutions from the full model and NIROM at location: $(x = 296.8, y = 686.25, z = 0)$. 99

3.6 Balzano case: the error of pressure solutions between the full model and NIROM, using 2 and 6 POD bases at time instances 10.2 (left panel) and 25 (right panel). 99

3.7 Balzano case: The RMSE errors of pressure solutions between the full high fidelity and non-intrusive reduced order models. 99

3.8 Balzano case: The correlation coefficient of pressure solutions between the full and non-intrusive reduced order models. 100

3.9 Okushiri tsunami case: The computational domain and unstructured meshes used. . . . 102

3.10 Schematic of typical free-surface flow problem in ocean modelling context. . . . 103

3.11 Okushiri tsunami case: wetting and drying front (dark line) at time instances 15.60 (left panel) and 18.75 (right panel) seconds. . . . 103

3.12 Okushiri tsunami case: The solutions of pressure from the full model and NIROM at time instances 10.2 (left panel) and 25 (right panel). Top panel: the full model; upper-middle panel: NIROM using 6 POD bases; down-middle panel: NIROM using 12 POD bases; bottom panel: NIROM using 18 POD bases. . . . 104

3.13 Okushiri tsunami case: The graphs shows the singular eigenvalues in order of decreasing magnitude. . . . 105

3.14 Okushiri tsunami case: The figures show the first 18 POD bases functions for pressure. . . . 106

3.15 Okushiri tsunami case: The error of pressure solutions between the full model and NIROM, using 6, 12 and 18 POD basis at time instances 10.2 (left panel) and 25 (right panel) seconds. . . . 107

3.16 Okushiri tsunami case: The RMSE errors of pressure solutions between the full and non-intrusive reduced order models. . . . 108

3.17 Okushiri tsunami case: The correlation coefficient of pressure solutions between the full and non-intrusive reduced order models. . . . 108

3.18 Okushiri tsunami case: The comparison of pressure solutions between the full model and NIROM model at location ($x = 0.6595, y = 1.63, z = -0.1995$). . . . 109

4.1 Waterflooding technique for oil production. . . . 119

4.2 Two material layers case: the figures displayed the first 18 the POD bases functions of the 2D two material layer problem. . . . 120

4.3 Two material layers case: the figure shows the singular eigenvalues in order of decreasing magnitude. . . . 121

4.4 Two material layers case: the figures displayed above show the saturation solutions of the two material layer problem at time instances 0.01 and 0.02 (where 6, 12 and 18 POD bases are chosen with 50 snapshots). The permeability on the top half part is 4, and the bottom half part is 1. 121

4.5 Two material layers case: the graph shows the solution saturations predicted by the full model and the POD-RBF ROM at a position (0.026937, 0.16246) (where 6, 12 and 18 POD bases are chosen with 50 snapshots) 122

4.6 Two material layers case: Saturation along lines parallel to the x axies. 123

4.7 Two material layers case: The graph shows the RMSE and correlation coefficient of solutions between the full and POD-RBF models. 123

4.8 Low permeability domain embedded in a high permeability domain: the figures displayed above shows the leading POD bases functions of saturation. They are the 1^{st}, 2^{nd}, 3^{rd}, 4^{th}, 6^{th}, 10^{th}, 12^{th} and 18^{th} POD bases functions respectively. 125

4.9 Low permeability domain embedded in a high permeability domain: the figures displayed above show the saturation solutions of the low permeability domain embedded in a higher permeability domain problem at time instances 0.05 and 0.1. The solutions compare the predictions from the non-intrusive POD-RBF model with full model using 6, 12 and 18 POD bases functions. The low permeability is 0.001 and the high permeability is 1. 126

4.10 Low permeability domain embedded in a high permeability domain: the graph shows the solution saturations predicted by the full model and the POD-RBF ROM at a position: $x = 0.58515, y = 0.43611$ using 6, 12 and 18 POD bases. 127

4.11 Low permeability domain embedded in a high permeability domain: Saturation along lines parallel to the x axies. 128

4.12 Low permeability domain embedded in a high permeability domain: the figures displayed above show the saturation error between full model and POD-RBF model of the low permeability domain embedded in a higher permeability domain problem at time instances 0.05 and 0.1 seconds using 6, 12 and 18 POD basis. 128

4.13 3D fluvial channel: the figures displayed above show the water channel profile. 129

4.14 3D fluvial channel: the figures displayed above show the saturation of full model and NIROM of the 3D fluvial channel problem at time instances 43200000 and 69120000 seconds using 36 POD basis. 130

4.15 3D fluvial channel: the figures displayed above show the values of saturation at a particular point in the mesh-see figure(a). 130

5.1 Flow past a cylinder: the figure shows the singular eigenvalues in order of decreasing magnitude. 144

5.2 Flow past a cylinder: the figures displayed above show the velocity solutions at time instances 2.0 (left panel) and 3.2 (right panel). In NIROM, 3, 6 and 20 POD bases are chosen with 100 snapshots). . . . 145

5.3 Flow past a cylinder: the figures displayed above show the solution difference between the full model and the FSI NIROM using 3, 6 and 20 POD bases at time instances 2.0 (left panel) and 3.2 (right panel). 146

5.4 A 2D free-falling square in water: Velocity solution from high fidelity model and FSI NIROM using 3, 6 and 20 POD bases at point (x=0.27543, y=0.29336) 146

5.5 A 2D free-falling square in water: the figure shows the singular eigenvalues in order of decreasing magnitude. 147

5.6 A 2D free-falling square in water: the figures displayed above show the first, second, third, $12^{th}, 36^{th}, 38^{th}, 71^{th}$ and 72^{th} POD bases. . . . 148

5.7 A 2D free-falling square in water: the figures displayed above show the solutions from full model and NIROM using 12, 36 and 72 POD bases at $t = 1.0$ (top left panel), $t = 1.5$ (top right panel), $t = 2.0$ (bottom left panel) and $t = 2.5$ (bottom right panel). In each panel, from left to right, full model, NIROM with 12, 36 and 72 POD basis functions, respectively. 149

5.8 Vortex-induced vibrations: A comparison of pressure solutions between the high fidelity model and FSI NIROM at a particular point(x=2, y=1.05). 151

5.9 Vortex-induced vibrations: A comparison of velocity solutions between the high fidelity model and FSI NIROM with 6, 12 and 50 POD bases at time instances $t = 0.15$ (left panel) and $t = 0.5$ (right panel). 152

5.10 Vortex-induced vibrations: Error in velocity solutions obtained from FSI NIROM with 6, 12 and 50 POD bases at time instances $t = 0.15$ (left panel) and $t = 0.5$ (right panel). 153

5.11 Vortex-induced vibrations: A comparison of Pressure solutions between the high fidelity model and FSI NIROM with 6, 12 and 50 POD bases at time instances $t = 0.15$ (left panel) and $t = 0.5$ (right panel). 154

5.12 Vortex-induced vibrations: A comparison of pressure solutions between the high fidelity model and FSI NIROM at a particular point(x=2, y=1.05). 155

5.13 Vortex-induced vibrations: RMSE and correlation coefficient of pressure solutions between the high fidelity and FSI NIROM with 6, 12 and 50 POD bases. 155

6.1 A 2-D solid discontinuous element with a 4-node joint element. 163

6.2 A Mohr-Coulomb failure criterion with a tension cut-off. 163

6.3 Case 1a: the figure shows the logarithm of the singular eigenvalues of velocity, pressure, density and solid concentration in order of decreasing magnitude with mean subtraction before constructing the POD basis. 170

6.4 Case 1a: a comparison of pressure solutions between the full model and fluid and fracture solid coupling NIROM using 30 POD bases at time instances $t = 0.3$ and $t = 0.8$. The mean is not used to construct the POD basis functions. 171

6.5 Case 1a: a comparison of velocity solutions between the full model and fluid and fracture solid coupling NIROM using 30 POD bases at time instances $t = 0.3$ and $t = 0.8$. The mean is not used to construct the POD basis functions. 172

6.6 Case 1a: the correlation coefficient and RMSE of pressure solutions between the high fidelity and fluid and fracture solid coupling NIROM using 30 POD bases, where the mean is not used to construct the POD basis functions. 172

6.7 Case 1b : the figure shows the logarithm of the singular eigenvalues of velocity, pressure, density and solid concentration in order of decreasing magnitude without mean subtraction before constructing the POD basis. 174

6.8 Case 1b: a comparison of pressure solutions between the full model and fluid and fracture solid coupling NIROM with 12, 18 and 30 POD bases at time instances $t = 0.3$ and $t = 0.8$, where the mean is used to construct the POD basis functions. 175

6.9 Case 1b: a comparison of velocity solutions between the full model and fluid and fracture solid coupling NIROM with 30 POD bases at time instances $t = 0.3$ and $t = 0.8$, where the mean is used to construct the POD basis functions. 176

6.10 Case 1b: error between the high fidelity model and fluid and fracture solid coupling NIROM with 12, 18 and 30 POD bases at time instances $t = 0.3$ and $t = 0.8$, where the mean is used to construct the POD basis functions. 177

6.11 Case 1b: RMSE and correlation coefficient of pressure solutions between the high fidelity and fluid and fracture solid coupling NIROM with 12, 18 and 30 POD bases, where the mean is used to construct the POD basis functions. 178

6.12 Case 2a: temperature solutions obtained from the full model at time levels $t = 0.04\,s$ and $t = 0.16\,s$. 179

6.13 Case 2a: The logarithm of the singular eigenvalues of velocity, pressure, density and solid concentration in order of decreasing magnitude with mean subtraction before constructing the POD basis. 180

6.14 Case 2a: a comparison of velocity solutions between the full model and fluid and fracture solid coupling NIROM using 100 POD bases at time instances $t = 0.04\,s$ and $t = 0.16\,s$, where the mean is not used to construct the POD basis functions. 181

6.15 Case 2a: a comparison of pressure solutions between the full model and NIROM with 100 POD bases at time instances $t = 0.04\,s$ and $t = 0.16\,s$, where the mean is not used to construct the POD basis functions. 182

6.16 Case 2b: The logarithm of the singular eigenvalues of velocity, pressure, density and solid concentration in order of decreasing magnitude without mean subtraction before constructing the POD basis. 184

6.17 Case 2b: A comparison of velocity solutions between the full model and fluid and fracture solid coupling NIROM with 6, 12 and 50 POD bases at time instances $t = 0.04\,s$ and $t = 0.16\,s$, where the is used to construct the POD basis functions. 185

6.18 Case 2b: the difference of velocity solutions between the high fidelity model and fluid and fracture solid coupling NIROM using 6, 12 and 50 POD bases at time instances $t = 0.04\,s$ and $t = 0.16\,s$, where the mean is used to construct the POD basis functions. 186

6.19 Case 2b: a comparison of pressure solutions between the full model and fluid and fracture solid coupling NIROM with 6, 12 and 50 POD bases at time instances $t = 0.04\,s$ and $t = 0.16\,s$, where the mean is used to construct the POD basis functions. 187

6.20 Case 2b: the difference of pressure solutions between the high fidelity model and fluid and fracture solid coupling NIROM with 6, 12 and 50 POD bases at time instances $t = 0.04\,s$ and $t = 0.16\,s$, where the mean is not used to construct the POD basis functions. 188

6.21 Case 2b: velocity comparison at a point ($x = 1.5\,m, y = 1.6333\,m$), where the mean is used to construct the POD basis functions. 189

6.22 Case 2b: the correlation coefficient and RMSE of pressure solutions between the high fidelity and fluid and fracture solid coupling NIROM with 6, 12 and 50 POD bases, where the mean is used to construct the POD basis functions. 190

7.1 Example of 1-D grid: the graph shows the 1-D smolyak grid with level 0, level 1 and full tensor product grid (top to bottom) respectively. 197

7.2 Examples of grids: the figures displayed above shows the full tensor product grid and 2-D smolyak sparse grid with level 0, 1 and 2. . . . 198

7.3 Flow past a cylinder: the graph shows the first 36 eigenvalues in a decreasing order. 205

7.4 Flow past a cylinder: the figures show the some of the first 36 POD bases functions of flow past a cylinder test case. 205

7.5 Flow past a cylinder: the figures displayed above shows the velocity from full model and the NIROM with 6, 12 and 36 POD bases at time instances 3 and 6. 206

7.6 Flow past a cylinder: the figures show the velocity error between high fidelity model and NIROM with 6, 12 and 36 POD basis at time instances 3 and 6. 207

7.7 Flow past a cylinder: the graph shows the velocity solutions from high fidelity model, NIROM with 6, 12 and 36 basis functions at location (x=0.89514, y=0.32519). 208

7.8 Flow past a cylinder: the graph shows the root mean squared error(RMSE) and correlation coefficient between full model and NIROM with 6, 12 and 36 POD bases. 209

7.9 Lock exchange: the graph shows the computational domain of the 2-D lock exchange problem. 211

7.10 Lock exchange: the graph shows the singular values of the 2-D lock exchange problem. 211

7.11 Lock exchange: the figure shows some of the first 36 basis functions of the problem. 212

7.12 Lock exchange: the figures displayed above shows the temperature from full model and the NIROM of 6, 12 and 36 POD bases at time instances 15 and 30. 213

7.13 Lock exchange: the figures show the temperature error between high fidelity model and NIROM with 6, 12 and 36 POD basis at time instances 15 and 30. 213

7.14 Lock exchange: the graph shows the root mean squared error(RMSE) and correlation coefficient between full model and NIROM with 6, 12 and 36 POD bases. 214

8.1 Four material layers test case: the figures displayed above shows the saturation from the high fidelity model and NIROM with 6, 12 and 18 POD bases at time instances 0.01 and 0.025. 225

8.2 Four material layers test case: the figures show the some of the first 18 POD bases functions of the four material layers test case. 226

8.3 Four material layers test case: the graph shows the saturation solutions predicted by the full model and the NIROM using 6, 12 and 18 POD bases at a position (x= 0.0625 y=0.075). 227

8.4 Four baffles case: distribution of permeabilities in the domain, the permeability of the four barriers(barrier 1: top; barrier 2: bottom; barrier 3: right; barrier 4: left) are between 0.1 and 0.5, and the permeability of the background is 10. 231

8.5 Four baffles case: the figures displayed above shows the solutions of saturation from full model and the NIROM of 6, 12 and 24 POD bases at time instances 1.5 and 4.0 using smolyak *level one*. 232

8.6 Four baffles case: some of the first 24 POD basis functions of the reservoir with four baffles. 233

8.7 Four baffles case: the figures displayed above shows the solutions of saturation from full model and the NIROM of 6, 12 and 24 POD bases at time instances 1.5 and 4.0 using smolyak *level two*. 234

8.8 Four baffles case: the graphs show the solution velocities predicted by the full model, and the NIROM with level one (middle) and level two (bottom) at location (6.1905, 6.1905). 235

8.9 Four baffles case: the graph shows the RMSE errors and correlation coefficient calculated for the NIROMs of the four barriers case. 236

8.10 Eight baffles case: distribution of permeability in the domain, the permeability of the eight barriers are between 0.1 and 0.5, and the permeability of the background is 10. 238

8.11 Eight baffles case: the figures displayed above shows the solutions of saturation from full model and the NIROM of 6, 12 and 24 POD bases at time instances 1.5 and 4.0 using smolyak *level one*. 239

8.12 Eight baffles case: the graphs show the solution velocities predicted by the full model, and the NIROM at position (6.1905 6.1905). 241

8.13 Eight baffles case: the graph shows the RMSE errors and correlation coefficient calculated for the NIROM model for the 8 layers case. . . . 242

8.14 8 baffles case: saturation comparison between the high fidelity full model, NIROM with Smolyak sparse grid and NIROM with RBF at time level $t = 5$ s. 242

8.15 8 baffles case: saturation values comparison between the full model, NIROM with Smolyak grid and RBF using 24 POD basis functions at a particular point (x=1.9048, y=2.381) on the domain. 243

8.16 (a) the different channel types (wide channels: blue), (medium width channels: yellow) and (small channels: red) ; (b) the distribution of permeabilities used for the red and blue channels 245

8.17 Channel case: the saturation distribution obtained from the full physical model and NIROM with 12 POD basis functions at time level $t = 15$ days for the permeabilities shown at point A (460, 360) in Figure 8.16 (b). Figure (c) shows a comparison of the saturation value at $x = 184.25, y = 110$ in the computational domain, see figure 8.16 (a). 246

8.18 Channel case: the saturation distribution obtained from the full physical model and NIROM with 12 POD basis functions at time level $t = 25$ days at location B in figure 8.16 (b). 246

8.19 Channel case: the saturation distribution obtained from the full physical model and NIROM with 12 POD basis functions at time level $t = 30$ days at location C in figure 8.16 (a). 247

8.20 two examples of 22 different channel types. 248

8.21 Channel case: Saturation solutions at an untrained point from full model and NIROM with 22 varying input permeabilities. 249

8.22 Reservoir with 22 types of channels: the graph shows the saturation comparison between the full model and NIROM at an unseen point based on 49 training simulations particular point (x=-18.378, y=184.25, z=110). 250

9.1 Framework for hyper-reduction and sub-grid-scale reservoir modelling. 257

List of Tables

2.1 Flow past a cylinder at $Re = 3600$: Comparison of the online CPU time (second) required for running the full model and ROM for each time step 64

2.2 Some well-known radial basis functions 77

2.3 Comparison of CPU (unit: s) required for running the full model and ROM for each time step 86

3.1 Comparison of the online CPU time (dimensionless) required for running the full model and NIROM during one time step. 103

4.1 Comparison of the online CPU time (dimensionless) required for running the full model and POD-RBF NIROM during one time step. . . 131

5.1 Variables and definitions. 139

5.2 Online CPU time (seconds) required for running the full model and FSI NIROM one time step for three test cases. 156

6.1 Case 1: comparison of $|| \varphi_0 - \Phi\Phi^T\varphi_0 ||_2$ (where φ_0 being the initial solutions of full model) for four variables between NIROM with mean subtraction and NIROM without mean subtraction. 174

6.2 Comparison of the online CPU cost (unit second) required for running the high fidelity model and NIROM during one snapshot. 191

6.3 Offline computational cost (seconds) required for constructing POD basis functions using different numbers of POD bases 192

6.4 Offline computational cost (seconds) required for constructing POD basis functions using different numbers of snapshots 192

7.1 Online CPU cost required for simulating the two test cases using the full model and NIROM during one time step. 215

8.1 Permeability specifications for four-layer case 224

8.2 Permeability combinations for four-barrier case with level one 228

8.3 Permeability sets for the 4 barrier case with level two excluding level one–part I 230

8.4 Permeability sets for the 4 barrier case with level two excluding level one–part II 230

8.5 Permeability combinations for eight-barrier case with level one 237

8.6 Comparison of the online CPU time (dimensionless) required for running the full model and Smolyak-RBF-POD ROMs during one time step. 251

Chapter

ONE

Introduction

1.1 Motivation of the thesis

Numerical simulations have become an important part of the analysis of many natural systems in physics, climatology, astrophysics, biology, chemistry, economics, psychology and engineering. These simulations often involve solving partial differential equations (PDEs) with suitable boundary and initial conditions using discretisation methods (for example, finite element methods). The discretised system for complex problems often has a huge number of degrees of freedom (*e.g.* $10^6 - 10^9$). Even with moderate complexity problems, the computation cost can still be prohibitive. This has motivated the development of reduced order modelling (ROM) techniques.

In addition to the complexity of the systems, in the context of uncertainty studies, sensitivity analysis or optimal design, many simulations (*e.g.* hundreds or thousands) are needed in order to analyse the system parameters (see for instance, Saltelli (2002); Saltelli *et al.* (2008); Iman & Helton (1988); Sacks *et al.* (1989)). This also results in an intensive additional computational cost. In this case, reduced order modelling has shown to be a viable way of mitigating the expensive computational cost issue since it offers the potential to simulate physical and dynamic systems with substantially increased computation efficiency while maintaining accuracy (Schilders *et al.* (2008)). Reduced order modelling is a rapidly growing discipline, with signif-

icant potential advantages in: interactive use, emergency response, ensemble calculations, and data assimilation. ROM is expected to play a major role in facilitating real-time turn-around of computational results.

Among model reduction techniques, the proper orthogonal decomposition (POD) method has proven to be an efficient means of deriving a reduced basis for high-dimensional nonlinear flow systems. Lumley (1967) firstly introduced POD method into fluid dynamics for investigating turbulent flows. The POD method has a number of variants, such as the principal component analysis (PCA) method (see Pearson (1901)) in statistics; Karhunen-Loeve method (see Fukunaga (1990)) in signal analysis and pattern recognition; and empirical orthogonal functions (EOF) (see Crommelin. & Majda (2004); Jolliffe (2002)) in geophysical fluid dynamics and meteorology. The POD technique and its variants have been applied successfully to a numerous research fields such as:

- **ocean modelling** (Xiao *et al.* (2013); Cao *et al.* (2007); Xiao *et al.* (2015d,e); Cao *et al.* (2006); Luo *et al.* (2007a,b); R.Stefanescu & Navon (2013); Stefanescu *et al.* (2014a); Daescu & Navon (2008); Bistrian & Navon (2015); Chen *et al.* (2011, 2012b); Du *et al.* (2013a); F.Fang *et al.* (2013); Fang *et al.* (2009b)),
- **air pollution modelling** (Fang *et al.* (2014)),
- **a coupled ocean – atmosphere model** (Ballabrera-Poy *et al.* (2001)),
- **fluids control** (Ahuja & Rowley (2010); Akhtar (2008); Akhtar *et al.* (2009); Bagheri *et al.* (2009); Barbagallo *et al.* (2009); Bergmann *et al.* (2005); Borggaard *et al.* (2010); Cohen *et al.* (2003); Graham *et al.* (1999b,a); Hoepffner *et al.* (2006); Ito & Ravindran (1998b); Ma *et al.* (2011); Ito & Schroeter (2001); Kunisch *et al.* (2004); Lehmann *et al.* (2005); Ravindran (2000)),
- **data assimilation** (Hoteit & Köhl (2006); Hoteit & Pham (2004); Altaf *et al.* (2013); Ştefănescu *et al.* (2015); Daescu & Navon (2007); Qiu & Chou (2006); Dimitriu *et al.* (2010); Du *et al.* (2013c)),
- **neutron and photon transport problems** (Buchan *et al.* (2015)),
- **convective Boussinesq flows** (San & Borggaard (2015)),
- **fluid – structure interaction** (Chang & Modarres-Sadeghi (2015)),

- **shape optimisation** (Xiao *et al.* (2012); Ghoman *et al.* (2012); Goss & Subbarao (2008); Coelho *et al.* (2008); Raghavan *et al.* (2013)),
- **mesh optimisation model** (Fang *et al.* (2010)),
- **borehole induction modelling** (Ardjmandpour *et al.* (2014))

POD in combination with the Galerkin projection method is an effective method for deriving a reduced order model (ROM). However, the main issues of this method are stability and non-linear inefficiency (see Schlegel & Noack (2015); Osth *et al.* (2014); Franca & Frey (1992a); Chaturantabut & Sorensen (2010)). Various methods have been proposed to overcome the stability and non-linear inefficiency issues, see section 1.3.1.1 and 1.3.1.2. However, these methods are still dependent on the governing equations of the full physical system. In most cases the source code describing the physical model has to be modified in order to generate the reduced order model. These modifications can be complex, especially in legacy codes, or may not be possible if the source code is not available (*e.g.* in some commercial software) (see Han (2012)). To circumvent these shortcomings, more recently, non-intrusive methods that require no knowledge of the governing equations and the original code have been introduced into ROMs. The non-intrusive reduced order modelling is the primary focus of this thesis.

Engineering applications of a newly developed methods are also very important. This thesis focuses on three important engineering areas: multiphase porous media, free surface and fluid-solid interaction problems. Large-scale complex multiphase modelling involves solving highly-coupled, strongly nonlinear, three-dimensional partial differential equations, which constitutes a formidable computing-intensive task (see Wörner (2012)). This is often complicated by the need to resolve vastly disparate length and time-scales: from micrometer to kilometre, and from microsecond to hour-scale. It is therefore infeasible to use such large-scale simulations for real-time operations such as the control of a particular multiphase flow or industrial device. Reduced-order modelling is an approach that can address this challenge directly, and has been applied successfully to multiphase flow problems. Another example requiring ROM is reservoir modelling. Enhanced Oil Recovery (EOR) is a key current and future technology for the UK, especially in the North Sea (see Awan *et al.* (2008)). EOR projects are designed using detailed reservoir simulations of the behaviour of injected and resident fluids in the underground rocks. The high cost of collecting geological and well information, especially in deep water, combined

with geological complexity of the underground rock formations means that such models have to be calibrated against production data (also called history matching). The computational cost of running one simulation is intensive and during history matching such models have to be run repeatedly until a suitably history match is obtained. In this case a reduced order model can provide a convenient way of performing computationally intensive tasks such as: sensitivity analysis, history matching and uncertainty quantification.

1.2 Contributions of the thesis

The novel contributions are:

1. Three new non-intrusive reduced order models (NIROMs) have been developed: a NIROM based on POD and Taylor series expansion, a NIROM based on POD and a Smolyak sparse grid and a NIROM based on POD and radial basis functions.

2. A novel NIROM for three-dimensional (3D) free surface flows has been developed. What distinguishes this NIROM (1) the inclusion of 3D dynamics with a free surface (the 3D computational domain and meshes are changed with the movement of the free surface) and (2) the incorporation of wetting-drying. Most importantly, the change of the computational domain with free surface movement is taken into account in reduced order modelling. Its capabilities have been validated using a Balzano test case and a Okushiri tsunami test case.

3. A novel NIROM for multiphase flows in porous media has been developed. The capability has been numerically illustrated in two multiphase flows in porous media: a two material layer case and a low permeability domain embedded in a high permeability domain case.

4. A novel non-intrusive reduced order model (NIROM) for fluid-structure interaction (FSI) has been developed. The NIROM is the first implementation of the FSI NIROM under the framework of an unstructured mesh finite element multiphase model (FLUIDITY) and a combined finite-discrete element method based

solid model (Y2D). The capability of this new NIROM for FSI is numerically illustrated in three coupling simulations: a one-way coupling case (flow past a cylinder), a two-way coupling case (a free-falling cylinder in water) and a vortex-induced vibrations of an elastic beam test case.

5. A NIROM for compressible fluid and solid fracture coupling models has been developed. This is the first time to apply such NIROM reduced to compressible fluids and fractured solids problems, especially the highly nonlinear problem - the blasting test case.

6. A novel variable parametric NIROM for Navier-Stokes equations has been presented. It is based on a two-level interpolation. The first level interpolation representing the variable parameters, such as initial conditions, is constructed through a RBF interpolation or Smolyak sparse grid interpolation method. The data points used to construct the first level approximation function are chosen by Smolyak sparse grid. The second level interpolation represents the time-dependent fluid dynamics, and it is constructed by RBF interpolation. This approach has been numerically illustrated in varying initial and boundary conditions of the flow past a cylinder case and lock exchange case. The capability has also been numerically illustrated in three multiphase flows in porous media: a four different material layer case, a reservoir with four different permeabilities baffles and a reservoir with eight different permeabilities baffles case.

1.3 Literature review of reduced order modelling of fluid dynamics problems

Reduced order modelling methods are ubiquitous and are of interest in various contexts, *e.g.* electro-mechanical systems, integrated circuit design, chemical engineering, fluid dynamics and aerodynamics. A wide range of theoretical and application studies have been undertaken. Among the theoretical studies, the projection based model reduction method can be considered as the hottest topic. It includes the proper orthogonal decomposition (POD) method (see Berkooz *et al.* (1993)), reduced basis method (see for instance, Peterson (1989); Haasdonk & Ohlberger

(2008); Ito & Ravindran (1998a, 2001)), (empirical) cross Gramian method (see for instance, Baur & Benner (2008); Himpe & Ohlberger (2014)), piecewise tangential interpolation method (see Baur *et al.* (2011)), matrix interpolation method (see for instance, Panzer *et al.* (2010); Degroote *et al.* (2010)), approximate balancing method (see Chiu (1996)) and balanced truncation method (see for instance, Gugercin & Antoulas (2004); Lall *et al.* (2002); Mehrmann & Stykel (2005)). The applications include various areas from ocean modelling to neutron and photon transport problems, see section 1.1. In this review, we focus on reduced modelling methods based on POD in the field of fluid dynamics problems: free surface flows, porous media multiphase flows and fluid-solid interaction problems. The reduced order models can be divided into two categories in terms of the dependency on the govern- ing equations: intrusive ROM and non-intrusive ROM (see Frangos *et al.* (2010)). Non-intrusive ROM is the focus of this thesis.

The literature related to the POD based ROM in the field of fluid dynamics is extensive. This review is from author's experiences and perspective, therefore, it is not exhaustive.

1.3.1 Intrusive reduced order modelling

Intrusive ROM is dependent of governing equations and source code and it is commonly derived by POD and Galerkin projection. It retains much of the physical characteristics from the original system due to its intrusiveness. Two key issues in intrusive ROM are stability (see Schlegel & Noack (2015); Osth *et al.* (2014)) and non-linearity efficiency (see Nguyen & Peraire (2008)).

This section 1.3.1 is derived from and expands upon two journal papers: (Xiao *et al.* (2013)) and (Xiao *et al.* (2014)).

1.3.1.1 Stability

The POD/Galerkin lacks stability and spurious oscillations can degrade the reduced order solution for flows with high Reynolds numbers (see Franca & Frey (1992b)). The instabilities commonly observed in the POD method are due to oscillations forming in the solutions as a result of applying a standard Bubnov-Galerkin projection of equations onto the reduced order space. This is very similar to the Gibbs oscillations that form in FEM solutions when the standard Bubnov-Galerkin method

is applied. These oscillations feed into the non-linear terms resulting in unstable simulations.

Various approaches have been presented to overcome the stability of the POD/Galerkin method. Xiao *et al.* (2013) presented a Petrov−Galerkin method for reduced order modelling of the Navier−Stokes equations. This Petrov−Galerkin method is based on the use of the cosine rule between the advection direction in Cartesian space-time and the direction of the gradient of the solution, and improved the stability of ROM results without tuning parameters. F.Fang *et al.* (2013) presented a Petrov−Galerkin method for nonlinear hyperbolic problems and discontinuous Galerkin (DG) ROMs.

Feriedoun Sabetghadam (2012) found a type of regularisation to solve the instability of the POD/Galerkin modelling of strongly-stiff systems. Carlberg *et al.* (2011a); Chu *et al.* (2011) introduced a diffusion term into ROMs without requiring tuning or optimising and stabilised the solutions of the POD model. Aubry *et al.* (1988) succeeded in stabilising the POD/Galerkin approximation of the Navier-Stokes equations by employing numerical dissipation. Later, Sirisup & Karniadakis (2004) presented a spectral viscosity diffusion convolution operator based dissipative model to control the stability of long-term behavior of the POD solutions. Sirisup & Karniadakis (2005) proposed a POD-penalty approach to stablise the reduced order model for unsteady fluid flows. Noack *et al.* (2003) introduced a shift-mode correction approach.

The numerical stability is also related to the choice of the inner product used to define the Galerkin projection. A stable symmetrical inner product that guarantees certain stability bounds for the linearized compressible Euler equations was proposed by (Kalashnikova & Barone (2009)). Iollo *et al.* (2000a) and Iollo *et al.* (2000b) proposed two stabilization methods for POD/ROM: one that relies on the explicit addition of an artificial dissipation term whose construction is similar to that of the Lax-Wendroff scheme; another one that consists in constructing the POD for both function and gradient values (POD in H_1). Feriedoun Sabetghadam (2012) found another type of regularisation method is to improve the stability of the POD/Galerkin models of strongly-stiff systems. The method replaces the POD eigenmodes of the non-linear terms by their Helmholtz filtered counterparts. Bond & Daniel (2008) used a set of linear constraints for projection matrix to guarantee a stable ROM.

1.3.1.2 Non-linearity

Another issue arises in intrusive reduced order modelling is the non-linearity reduction inefficiency. The ROM is commonly derived by POD and Galerkin method. The Galerkin method is limited to the linear terms. After projecting onto the reduced space, the nonlinear term still depends on the original full system. The full physical system governed by partial differential equations (PDEs) has a high dimensional size, in this case, the computational complexity of the reduced model still depends on the high dimensional size of the full physical systems (see Nguyen & Peraire (2008); Nguyen *et al.* (2008)). A number of non-linear reduction methods have been proposed to mitigate this problem.

One approach is to apply the discrete empirical interpolation method (DEIM) to address the reduction of the nonlinear components and reduce the computational complexity of the POD method. DEIM is a discrete variant of the empirical interpolation method (EIM) proposed by Barrault *et al.* (2004) in the context of reduced-basis model order reduction discretization of nonlinear partial differential equations. DEIM methods have been demonstrated to be able to obtain factors of 10-100 speed up in CPU time over the original non-reduced model. The economy in CPU time is proportional to the dimension of the reduced order model (see for instance Ştefănescu & Navon (2013a)) and therefore to the number of DEIM points.

The applications were suggested and analysed by the work (see for instance, Chaturantabut (2008); Chaturantabut & Sorensen (2010, 2012, 2011a); Ştefănescu & Navon (2013b); Hinze & Kunkel (2012); Baumann (2013); Gildin *et al.* (2013); Buffoni & Willcox (2010); Lass & Volkwein (2013); Dimitriu *et al.* (2014); Ghasemi *et al.* (2015); Schmidt *et al.* (2012); Fosas de Pando *et al.* (2013); Ghommem *et al.* (2015); Stefanescu *et al.* (2014b); Ghasemi (2015); Chaturantabut & Sorensen (2011b); Fink & Ehlers (2015)). Other important contributions to the Empirical Interpolation Method (EIM) include the work done by Barrault *et al.* (2004) and Anthony Patera related to another model reduction approach namely the reduced basis approach (see for instance, Rozza *et al.* (2008); Nguyen *et al.* (2009); Boyaval *et al.* (2010); Eftang *et al.* (2011)).

Regarding the use of DEIM like approaches, Barrault *et al.* presented a strategy for choosing the optimal set of sampling points at the discrete levelBarrault *et al.* (2004). The algorithm consists of selecting the sampling components that minimize the distance between the recovered reduced basis coefficients and the optimal coefficients

(which are obtained by projecting the snapshots onto the reduced order subspace). The main advantage of the DEIM algorithm is that only values at the nodes of the finite element mesh are required. This results in a strategy very convenient for the reconstruction of non-smooth functions, like the right-hand-side of the system of equations arising from the reduced order strategy for the incompressible Navier-Stokes equations with the formulation used herein.

Xiao *et al.* (2014) presented the residual DEIM method, which is a combination of the quadratic expansion method and the DEIM. It is based on initially applying the quadratic expansion method to the non-linear terms and then applying the DEIM approach to resolve the residual between the reduced order model and the full model. That is, the DEIM is used to absorb the remaining errors left over from the quadratic expansion approach. This approach means that the method can still exactly represent discrete quadratic non-linearities - unlike DEIM - but can also be used for highly non-linear discrete systems - unlike the quadratic expansion approach. The residual DEIM method is well suited to dealing with potentially highly non-linearities that arise from a ROM with a non-linear Petrov-Galerkin discretization proposed by Xiao *et al.* (2013) and F.Fang *et al.* (2013).

Du *et al.* (2013a) proposed a quadratic expansion treatment of non-linear terms of PDEs. This method is suitable for the treatment of the discretised quadratic non-linear operators as the method represents the non-linear term through expansions of precomputed matrices. Critically, as these matrices are precomputed they can easily be transformed into reduced equation sets.

Trajectory piecewise-linear (TPWL) approximation is also a non-linear reduction method, which is based on approximating a nonlinear function by a weighted sum of linearized models at selected points along a state trajectory (see Rewienski (2003); He & Durlofsky (2015)). The application of TPWL can be found in the work of (see for instance, Bechtold *et al.* (2008); Rewieński & White (2006); Voβ *et al.* (2007); Voß (2007); Qu & Chapman (2004); Rewienski & White (2002); Mohaghegh *et al.* (2010); Ansari (2014)). Other non-linear reduction methods include Gauss−Newton with approximated tensors method (see Carlberg *et al.* (2013)), masked projection of discrete equations methods (see Galbally *et al.* (2010)), Karhunen-Loeve expansion and dual weighted residual methods (see Meyer & Matthies (2003)), balanced empirical Gramians (see Hahn & Edgar (2002)), a sparsity pattern method for non-linear parts (see Goyal & Barooah (2012)), piecewise polynomial method (see Dong & Roychowdhury (2003)), space vectors clustering POD (see Sahyoun & Djouadi

(2014)), local reduced order bases (see Amsallem *et al.* (2012)) and tangent space alignment method (see Zhang & Zha (2004)).

1.3.2 Non-intrusive reduced order modelling

The NIROMs require no knowledge of the physical systems. In this section, the methods of constructing NIROMs and their applications are reviewed.

One reason for developing the non-intrusive reduced order modelling methods is that, in most cases, the source code describing the physical model has to be modified in order to generate the reduced order model and these modifications can be complex, especially in legacy codes, or may not be possible if the source code is not available (*e.g.* in some commercial software) (see Han (2012)). To this end, a number of non-intrusive ROMs have been proposed by researchers from various fields.

Noack *et al.* (2011) and Noori *et al.* (2013) introduced the neural network into ROMs. Vasile *et al.* (2013) and Winter & Breitsamter (2014) proposed a non-intrusive method based on POD and RBF artificial neural network. Neural network is one type of machine learning method, and it is capable of approximating an arbitrary function using observed data. It has a wide applications in fluid dynamics (see for instance, Peña *et al.* (2012); Gholami *et al.* (2015); Baghalian *et al.* (2012); Elsayed & Lacor (2013); De Giorgi *et al.* (2014)). The disadvantage of the machine learning method is the intensive training time.

Han (2012) proposed a Black Box Stencil interpolation non-intrusive method, which is based on parametric regression methods, and applied it to a one dimensional chemical reaction problem and two dimensional porous media flow problems. C.Audouze *et al.* (2013) and Audouze *et al.* (2009) proposed a non-intrusive Radial Basis Function (RBF) reduced-order modeling method for approximating the solutions of nonlinear time-dependent parameterized partial differential equations (Burgers equation and a parameterized convection-reaction-diffusion problem). Walton *et al.* (2013) and Xiao *et al.* (2015e) also proposed a non-intrusive ROM based on POD-RBF.

E.Iuliano & D.Quagliarella (2013) developed an non-intrusive POD ROM for aerodynamic shape optimization. Guénot *et al.* (2013), F.Casenave *et al.* (2014) and H.Klie (2013) proposed a non-intrusive POD ROM based on RBF and the EIM/DEIM algorithm. Wirtz *et al.* (2013) and Wirtz & Haasdonk (2012) proposed the kernel methods where the learning methods are based on both support vector machines

and a vectorial kernel greedy algorithm. Xiao *et al.* (2010) proposed a non-intrusive ROM based on constrained POD and Kriging interpolation method. In their work, the Kriging interpolation was used to calculate the POD coefficients (solutions of ROM). Raisee *et al.* (2015) presented a non-intrusive method for the polynomial chaos representation. The idea of that work is to extract a set of optimal basis functions from a coarser mesh, then use them to perform finer mesh analysis. Bui *et al.* (2013) proposed a method based on a combination of POD and In Situ Adaptive Tabulation (ISAT) and applied it into aircraft air control systems.

1.3.3 ROM for free surface, porous media multiphase and fluid-solid interaction problems

In this section, ROM for free surface problem is firstly reviewed, then the porous media multiphase flows and then the fluid-solid interaction problem.

1.3.3.1 ROM for free surface problems

The numerical simulation of ocean modelling is important to a wide range of applications such as atmosphere, sea ice, climate prediction, biospheric management and especially natural disasters (for example, flooding and tsunami). The natural disasters often have tragic consequences with loss of life. In order to reduce the consequences, a real-time, early-warning and rapid assessment model is required. In comparison with 2D modelling, 3D ocean modelling provides better understanding and much more information about local flow structure, including; vertical inertia, water level changes, unsteady dynamic load on structure interacting with fluids and dikes etc. However, the majority of existing 3D ocean models suffer from a large computational cost and thus may not be able to respond rapidly for tsunami forecasting. In this case, model reduction technology has been developed to mitigate the expensive CPU computational cost since the model reduction technology offers the potential to simulate complex systems with substantially increased computation efficiency.

POD ROM approaches have been applied to ocean problems Fang *et al.* (2009a,b); My Ha *et al.* (2008); Zokagoa & Soulaïmani (2012). My Ha *et al.* (2008) introduced ROM into tsunami forecasting, and Zokagoa & Soulaïmani (2012) used POD/ROM

for Monte-Carlo-type applications. In their work, the POD-based reduced-order models were constructed from shallow water equations. However shallow water models can perform poorly in problems with abrupt topography changes, short waves and local flow around buildings. The work of Fang *et al.* (2009a,b), Du *et al.* (2013b), and Xiao *et al.* (2013) introduced POD ROM for 2D/3D Navier-Stokes unstructured mesh finite element fluid modelling. However 3D free surface flow examples were not included in their work due to the difficulty in implementation of intrusive POD-ROMs. The implementation difficulty was caused by the change of both the computational domain and unstructured meshes with free surface movement. However, non-intrusive ROM is capable of handling this issue easily. In this thesis, I will construct a non-intrusive ROM for free surface problems using POD and Smolyak sparse grid methods. This is the first work of non-intrusive reduced order method in 3D free surface modelling.

1.3.3.2 ROM for porous media multiphase problems

The numerical simulation of porous media multiphase flows is very important, especially in petroleum reservoir engineering. However, in the context of uncertainty studies, sensitivity analyses or optimal design, hundreds or thousands of runs of the reservoir model are needed in order to analyse the parameters statistically. This high computational cost renders the analysis almost impractical. In these cases, model reduction technology is a viable way to mitigate the computational cost as it offers the potential to simulate systems with substantially increased computation efficiency while maintaining accuracy.

A variety of model reduction methods have been proposed to ease the intensive computational cost in porous media multiphase flow problems. For example, reduced physics models that simplify the physics (see Batycky *et al.* (1997); Wilson & Durlofsky (2013)), upscaling methods that solve the system using a coarser grid (see Durlofsky & Chen (2012)), multi-scale methods that solve the equations on coarse grids using basis functions captured on the fine grids (see Jenny *et al.* (2005, 2006)) and snapshot-based methods that record results from solutions at each time step. The snapshot based model reduction method are based on proper orthogonal decomposition (POD) and its variants (see He (2013)).

Streamline methods are one type of reduced physics model. The idea of the stream-

line method is that it decouples the flow and transport equations into a set of one dimensional problems and then solves it sequentially. It is used in reservoir simulations (see Ginevra Di Donato *et al.* (2003); Siavashi *et al.* (2014)) and history matching (see Milliken *et al.* (2001)). These reduced physics models result in a considerable speedup for some problems (see He (2013)). Upscaling methods allow the problem to be simulated on a much coarser mesh (see Barker *et al.* (1997)). This can result in a considerable improvement in CPU time but the methods themselves tend to be empirical and the resulting coarse grid model may not always reproduce the results obtained from a fine grid simulation (see Barker & Dupouy (1999); Renard & De Marsily (1997)). Multi-scale models use different scale grids (fine and coarse) to discretise the underlying governing equations. This method has been reported to provide a factor of 10-20 speedup in the finite volume framework for reservoir simulation (see Tchelepi *et al.* (2007)).

1.3.3.3 ROM for fluid-solid interaction problems

Fluid-structure interaction is an interaction phenomena between deformable or movable solid structures with a surrounding or internal fluid flow (see Bungartz & Schäfer (2006)). The FSI problem plays an important role in many scientific and engineering areas such as aerospace wing design (see Kamakoti & Shyy (2004)), biology (see Bodnár *et al.* (2014)), turbomachinery (see Carstens *et al.* (2003)) and blood flow in veins and arteries (see Yang *et al.* (2003)). However, the computational cost for simulating FSI problems is intensive.

Recently, the reduced order modelling method has been applied to fluid-structure interaction problems. Barone *et al.* (2009) constructed a ROM for coupled fluid and structure problems using POD and Galerkin projection. The ROM is validated by applying it to problems of supersonic and inviscid flow past a square, elastic and thin rectangular plate problems. Tchieu (2011) derived a ROM for three fluid and structure interaction problems: a thin airfoil undertaking small scale unsteady motions with a freestream flow, vortex-induced vibrations of an arbitrary bluff body with vortices and two bodies in an inviscid fluid. Papadrakakis *et al.* (2014) constructed computationally efficient ROMs for aeroelastic computations using POD and Polynomial Chaos Expansion. Kalashnikova *et al.* (2013) developed a stable ROM for a linear fluid and structure interaction problems, which involves linearized inviscid compressible flow over a flat linear von-Krmn plate. Lieu *et al.* (2006, 2005) applied POD based ROM to aeroelastic modeling of a complete F-16 jet fighter air-

craft configuration. Liberge *et al.* (2010) constructed a ROM for fluid interacting with rigid body problems. Forti & Rozza (2014) used POD and radial basis function method to analysis the shape parametrisation for the ROM. However, those methods are intrusive. Xiao *et al.* (2016a) presented a non-intrusive method to construct a ROM for fluid and solid interaction problems using POD and radial basis function interpolation methods. This method is validated using three fluid-solid coupling test cases: a one-way coupling case (flow past a cylinder), a two-way coupling case (a free-falling cylinder in water) and a vortex-induced vibrations of a elastic beam test case.

1.3.4 Outline of the thesis

This thesis is structured as follows. In chapter 1, an introduction is given, along with the aim and contribution of this thesis and then the literature review. Some contents in the literature review is derived from:
Xiao, D., Fang, F., Du, J., Pain, C.C., Navon, I.M., Buchan, A. G., ElSheikh, A.H., Hu, G. 2013. Non-Linear Petrov-Galerkin Methods for Reduced Order Modelling of the Navier-Stokes Equations using a Mixed Finite Element Pair. Computer Methods In Applied Mechanics and Engineering, 255, 147-157
Xiao, D., Fang, F., Buchan, A. G., Pain, C.C., Navon, I.M., Du, J., Hu, G. 2014. Non-linear model reduction for the Navier-Stokes equations using Residual DEIM method. Journal of Computational Physics, 263, 1-18.

In chapter 2, three new non-intrusive model reduction methods are presented. This chapter is derived and expands upon:
Xiao, D., Fang, F., Buchan, A.G., Pain, C.C., Navon, I.M., Muggeridge, A. 2015. Non-intrusive reduced order modelling of the Navier-Stokes equations. Computer Methods in Applied Mechanics and Engineering, 293, 552-541.
Xiao, D., Fang, F., Pain, C., Hu, G. 2015. Non-intrusive reduced order modelling of the Navier-Stokes equations based on RBF interpolation. International Journal for Numerical Methods in Fluids, 79(11), 580-595.

In chapter 3, a NIROM for three-dimensional (3D) free surface flows using POD-Smolyak is formed. This chapter is derived and expands upon:
Xiao, D., Fang, F., Pain, C.C., Navon, I.M. 2015. Non-intrusive reduced order 3D

free surface modelling. submitted to Ocean Engineering.

In chapter 4, a NIROM for multi-phase porous media flows using POD-RBF is built. This chapter is derived and expands upon:
Xiao, D., Fang, F., Pain, C.C., Navon, I.M., Salinas, P., Muggeridge, A. 2015. Non-intrusive reduced order modeling of multi-phase flow in porous media using the POD-RBF method. submitted to Computer and Geosciences.
Xiao, D., Lin, Z., Fang, F., Pain, C., Navon, I.M., Salinas, P., Muggeridge, A. 2016. Non-intrusive reduced order modelling for multiphase porous media flows using Smolyak sparse grids. International Journal for Numerical Methods in Fluids, DOI: 10.1002/fld.4263

In chapter 5, a NIROM for incompressible fluid-structure problem is constructed. This chapter is derived and expands upon:
Xiao, D., Yang, P, Fang, F., Xiang, J, Pain, C.C., Navon, I.M. 2016. Non-intrusive reduced order modeling of fluid-structure interactions. Computer Methods in Applied Mechanics and Engineering, 303, 35-54

In chapter 6, a compressible fluid-solid coupling problem is constructed and applied it into a complex test case: blasting. This chapter is derived and expands upon:
Xiao, D., Yang, P, Fang, F., Xiang, J, Pain, C.C., Navon, I.M., Chen, M. 2015. A non-intrusive reduced-order model for compressible fluid and fractured solid coupling and its application to blasting. Submitted to Journal of computational physics.

In chapter 7, a variable parameters NIROM for the Navier-Stokes equations using two-level RBF interpolation method is presented. This chapter is derived and expands upon:
Xiao, D., Fang, F., Pain, C.C., Navon, I.M. 2016. Variable parameters non- intrusive reduced order modelling of Navier-Stoke equations. Will be submitted to computer methods in applied mechanics and engineering.

In chapter 8, a variable material NIROM using the Smolyak and RBF interpolation for multi-phase porous media flows is presented. This chapter is derived and expands upon:

Xiao, D., Fang, F., Pain, C.C., Navon, I.M., Muggeridge, A. 2016. Variable-material non-intrusive reduced order modelling of multi-phase porous media flows. Will be submitted to computer methods in applied mechanics and engineering.

Chapter

TWO

Non-intrusive reduced order modelling of the Navier-Stokes equations

2.1 Abstract

This chapter presents three new non-intrusive reduced order models based upon proper orthogonal decomposition (POD) for solving the Navier-Stokes equations. The novelty of these methods resides in how the reduced order models are formed, that is, how the coefficients of the POD expansions are calculated. Rather than taking a standard approach of projecting the underlying equations onto the reduced space through a Galerkin projection, here three different techniques are developed. The first method applies a second order Taylor series to calculate the POD coefficients at each time step from the POD coefficients at earlier time steps. The second method uses a Smolyak sparse grid collocation method to calculate the POD coefficients, where again the coefficients at earlier time steps are used as the inputs. The third method employs radial basis function interpolation methods to predict the POD coefficients. The advantage of those approaches are that they are non-intrusive and so do not require modifications to a source code of the system; they

are therefore very easy to implement. They also provide accurate solutions for modelling flow problems, and this has been demonstrated by the simulation of flows past a cylinder, lock exchange and within a gyre. It is demonstrated that accuracy relative to the high fidelity model is maintained whilst CPU times are reduced by several orders of magnitude in comparison to high fidelity models.

This chapter is derived from and expands upon two journal papers: Xiao *et al.* (2015d) and Xiao *et al.* (2015e).

2.2 Introduction

The interpolation based non-intrusive ROM involves high-dimensional interpolation. The dimension size may increase exponentially with the dimension size of problems. In ROM, the dimension size $d = P \times N_v$, where P is the number of POD bases and N_v is the number of variables to be solved.

The Smolyak sparse grid method (see Smolyak (1963)) is an efficient method of integrating/interpolating multidimensional functions based on a univariate quadrature rule. This sparse grid method has been widely applied in various applications (see for instance, Garcke & Griebel (2013); Pflüger *et al.* (2010); John Burkardt (2012)), including numerical integration (see Gerstner & Griebel (1998)), partial differential equations (see Nobile *et al.* (2008)), economics (see Judd *et al.* (2014); Heiss & Winschel (2008)), stochastic natural convection problems (see Ganapathysubramanian & Zabaras (2007)), sensitivity analysis (see Buzzard & Xiu (2011)), portfolio problems (see Gavilan Gonzalez & Rojas (2009)) and high dimensional interpolation (see Barthelmann *et al.* (2000)). Recently, the sparse grid method has been applied to ROMs. Peherstorfer (2013) presented a reduced-order model of parametrised systems by employing a sparse grid machine learning method and applied this new ROM to thermal conduction and chemical reaction simulations. Sumant *et al.* (2010) used a Smolyak algorithm to compute orthogonal polynomial expansions coefficients in the reduction of random input variables for an electromagnetic problems. Cheng (2013) presented a method for numerical simulation of the stochastic Berger equation, and investigated the sparsity property in terms of Karhunen-Loeve expansions. Ullmann & Lang (2014) assessed the applicability of POD/Galerkin to stochastic

collocation on the sparse grid.

The thesis uses a Smolyak sparse grid collocation approach and POD to construct the non-intrusive reduced order model. Another non-intrusive model reduction method presented in this thesis is based on POD and Taylor series expansion, which is also the first time to use Taylor series expansion to derive solutions of the ROM (POD coefficients). The third non-intrusive model reduction method presented in this thesis is based radial basis function interpolation and POD.

The reduced order models are constructed using a finite element Bubnov-Galerkin discretisation of the FLUIDITY fluid dynamics modelling software (see Pain *et al.* (2005)) taking snapshots of the solution variables at regular time intervals. In the Smolyak sparse grid ROM and radial basis function approach, solutions of the full model are recorded (as a sequence of snapshots), and from this data appropriate basis functions are formed that optimally represent the problem. Then, the Smolyak sparse grid method and radial basis function method are used to construct interpolation functions for a set of hyper-surfaces representing the system. In the Taylor/POD approach, the model based on snapshots is expanded through a Taylor expansion to second order so as to capture the quadratic non-linearities in the high fidelity system.

The structure of this chapter is as follows. Section 2.3 presents the governing equations, followed by the derivation of the standard POD model reduction. Section 2.4 presents the non-intrusive method based on the second order Taylor series theory. Section 2.5 presents the Smolyak sparse grid method in reduced order modelling. Section 2.6 demonstrates the capabilities of Smolyak sparse grid and Taylor series by solving the two flow problems: flow past a cylinder and gyre. Section 2.7.3 presents the non-intrusive method based on radial basis function, and also demonstrates the capabilities of the method by solving the two flow problems: flow past a cylinder and lock exchange. Finally in section 2.8, the summary and conclusions are presented.

2.3 Reduced Order Modelling of the Navier-Stokes Equations

2.3.1 Governing Equations

This chapter considers the three dimensional non-hydrostatic Navier-Stokes equations describing the conservation of mass and momentum of a fluid,

$$\nabla \cdot \mathbf{u} = 0, \tag{2.1a}$$

$$\frac{\partial \mathbf{u}}{\partial t} + \mathbf{u} \cdot \nabla \mathbf{u} + f\mathbf{k} \times \mathbf{u} = -\nabla p + \nabla \cdot \tau. \tag{2.1b}$$

In these equations the term $\mathbf{u} \equiv (u_x, u_y, u_z)^T$ denotes the velocity vector, p the perturbation pressure ($p = p'/\rho_0$, ρ_0 is the constant reference density and p' is non-hydrostatic pressure) and f the Coriolis inertial force. The stress tensor τ included in the diffusion term represents the viscous forces, and this is defined in terms of a deformation rate tensor $\mathbf{S}$ which is given by,

$$\tau_{ij} = 2\mu_{ij}S_{ij}, \quad S_{ij} = \frac{1}{2}\left(\frac{\partial u_i}{\partial x_j} + \frac{\partial u_j}{\partial x_i}\right) - \frac{1}{3}\sum_{k=1}^{3}\frac{\partial u_k}{\partial x_k}, \quad i,j = \{x,y,z\}. \tag{2.2}$$

In this expression μ denotes the kinematic viscosity and it is assumed that there is no summation over repeated indices. The horizontal (μ_{xx}, μ_{yy}) and vertical (μ_{zz}) kinematic viscosities are assumed to take constant values and define the off diagonal components of τ in equation (2.2) by $\mu_{ij} = (\mu_{ii}\mu_{jj})^{1/2}$. For barotropic flow, the pressure p consists of hydrostatic $p_h(z)$ and non-hydrostatic $p_{nh}(x,y,z,t)$ components.

2.3.2 Reduction via Proper Orthogonal Decomposition

2.3.2.1 Proper Orthogonal Decomposition

In the POD formulation a new set of basis functions is constructed from a collection of snapshots that are taken at a number of time instances of the full model solution. The model described in equations (2.1a) and (2.1b) are solved and snapshots of the solution are taken as it evolves through time. In the formulation presented here snap-

shots of each component of the velocity vector $\mathbf{u} = (u_x, u_y, u_z)$ and pressure p are recorded individually. Each snapshot is a size of $\mathcal{N}$ and holds the values of the respective solution component at the nodes of the finite element mesh. For each velocity or pressure component, the sampled values at the snapshot s are stored in the vectors $\mathcal{U}_s^x, \mathcal{U}_s^y, \mathcal{U}_s^z$ and $\mathcal{U}_s^p$ (where the superscripts denote space direction or pressure) with $\mathcal{N}$ entries ($\mathcal{N}$ being the number of nodes). A collection of all $\mathcal{U}_s^x, \mathcal{U}_s^y, \mathcal{U}_s^z$ and $\mathcal{U}_s^p$ constructs four separate matrices $\mathcal{U}^x = (\mathcal{U}_1^x, \ldots, \mathcal{U}_s^x, \ldots, \mathcal{U}_S^x)$, $\mathcal{U}^y = (\mathcal{U}_1^y, \ldots, \mathcal{U}_s^y, \ldots, \mathcal{U}_S^y)$, $\mathcal{U}^z = (\mathcal{U}_1^z, \ldots, \mathcal{U}_s^z, \ldots, \mathcal{U}_S^z)$ and $\mathcal{U}^p = (\mathcal{U}_1^p, \ldots, \mathcal{U}_s^p, \ldots, \mathcal{U}_S^p)$ respectively (where S is the number of snapshots). From here on each snapshot matrix will be treated separately, but in an identical manner, and so the superscripts are omitted for the sake of simplicity of notation and the details are provided for a general snapshot matrix $\mathcal{U}$.

Taking the deviation from the mean forms a modified snapshot matrix $\tilde{\mathcal{U}}$ by,

$$\tilde{\mathcal{U}}_s = \mathcal{U}_s - \overline{\mathcal{U}}, \quad s \in \{1, 2, \ldots, S\}, \tag{2.3}$$

where

$$\overline{\mathcal{U}} = \frac{1}{S} \sum_{s=1}^{S} \mathcal{U}_s. \tag{2.4}$$

The goal of POD is to find a set of orthogonal basis functions $\{\Phi_s\}$, $s \in \{1, 2, \ldots, S\}$, such that it maximises

$$\frac{1}{S} \sum_{s=1}^{S} \left| < \tilde{\mathcal{U}}_s, \Phi_s >_{L^2} \right|^2, \tag{2.5}$$

subject to

$$\sum_{s=1}^{S} | < \Phi_s, \Phi_s >_{L^2} |^2 = 1, \tag{2.6}$$

where $< \cdot, \cdot >_{L^2}$ is the canonical inner product in L^2 norm.

The approach introduced by Sirovich (see Sirovich (1987)) is used to find an optimal set of basis functions Φ of the optimisation problem (2.5). This involves performing a Singular Value Decomposition (SVD) of the snapshot matrix $\tilde{\mathcal{U}}$ given in the form,

$$\tilde{\mathcal{U}} = U \Sigma V^T. \tag{2.7}$$

The terms $U \in R^{\mathcal{N} \times \mathcal{N}}$ and $V \in R^{S \times S}$ are the matrices that consist of the orthogonal vectors for $\tilde{\mathcal{U}}\tilde{\mathcal{U}}^T$ and $\tilde{\mathcal{U}}^T\tilde{\mathcal{U}}$, respectively and Σ is a diagonal matrix of size $\mathcal{N} \times S$.

The non zero values of Σ are the singular values of $\tilde{\mathcal{U}}$, and these are assumed to be listed in order of their decreasing magnitude. It can be shown in the work of (Chaturantabut (2008)) that the POD vectors are defined to be the column vectors of the matrix V,

$$\Phi_s = \tilde{\mathcal{U}} V_{:,s}/\sqrt{\lambda_s}, \qquad \text{for } s \in \{1, 2 \dots S\}, \tag{2.8}$$

and the optimal basis set of size P consists of the functions corresponding to the largest P singular values (*i.e.* the first P columns of U). In equation 2.8, λ denotes singular values and $V_{:,s}$ is the first s column of matrix V. These vectors are optimal in the sense that no other rank P set of basis vectors can be closer to the snapshot matrix $\tilde{\mathcal{U}}$ in the Frobenius norm.

In POD, any variable ψ (for example, the velocity and pressure components) can be expressed by the expansion,

$$\psi = \overline{\psi} + \sum_{j=1}^{P} \alpha_j \Phi_j, \tag{2.9}$$

where α_j denote the coefficients of the POD expansion need to be solved in ROM and $\overline{\psi}$ is the mean of the ensemble of snapshots for the variable ψ.

As a final note, the loss of information due to the truncation of the POD expansion set to P vectors can be quantified by the following ratio,

$$I = \frac{\sum_{j=1}^{P} \lambda_j^2}{\sum_{j=1}^{S} \lambda_j^2}, \tag{2.10}$$

The value of I will tend to 1 as P is increased to the value S, which would imply no loss of information.

2.3.2.2 Implementation of a standard (Galerkin projection) POD reduced order model

For simplicity equations (2.1a) and (2.1b) can be re-written in the general form:

$$\frac{\partial \psi}{\partial t} = F(\psi). \tag{2.11}$$

Taking the POD basis function as the test function, then integrating (2.11) over the computational domain Ω, yields:

$$\left\langle \frac{\partial \psi}{\partial t}, \Phi_j \right\rangle_{\Omega} = \langle F(\psi), \Phi_j \rangle_{\Omega}. \tag{2.12}$$

Substituting (2.9) into (2.12), the POD reduced order equations are then obtained:

$$\frac{\partial \alpha_k}{\partial t} = \left\langle F\left(\bar{\psi} + \sum_{j=1}^{P} \alpha_j \Phi_j\right), \Phi_k \right\rangle_{\Omega}, \qquad \text{for } k \in \{1, 2 \dots P\}, \tag{2.13}$$

subject to the initial condition

$$\alpha_k(t) = ((\psi(t) - \bar{\psi}), \Phi_k), \quad at\ t = 0. \tag{2.14}$$

Equation (2.13) at time level n can be written:

$$\frac{\alpha_k^n - \alpha_k^{n-1}}{\Delta t} = \left\langle F\left(\bar{\psi} + \sum_{j=1}^{P} \alpha_j^{n-1} \Phi_j\right), \Phi_k \right\rangle_{\Omega}, \qquad \text{for } k \in \{1, 2 \dots P\}, \tag{2.15}$$

where, Δt is the time step size to be used. Equation (2.15) can be rewritten in the general form below:

$$\alpha_k^{n+1} = f_k(\alpha^n), \quad k \in \{1, 2, \dots P\}, \tag{2.16}$$

In this work, alternative approaches are sought for quickly estimating the multidimensional functions f_k in (2.16). This enables us to then estimate the POD coefficients of the reduced order model at arbitrary times. The first of these methods is implemented through a Taylor series expansion, the second is through a Smolyak sparse grid method and the third one is carried out via radial basis function interpolation method. These are detailed in the following sections.

2.4 The Taylor series method for the calculation of the POD coefficients

2.4.1 Taylor expression of the POD Coefficients

For a new time step, say $n+2$, a first order Taylor expansion of the POD coefficients $\alpha^{n+2} = (\alpha_1^{n+2}, \ldots, \alpha_P^{n+2})^T$ (where α denotes the complete set of coefficients for velocity and pressure) can be written as,

$$\alpha^{n+2} = \alpha^{n+1} + \frac{\partial \alpha^{n+1}}{\partial \alpha^n}(\alpha^{n+1} - \alpha^n), \tag{2.17}$$

in terms of the POD coefficients on the previous two time steps. The term $(\alpha^{n+1} - \alpha^n)$ denotes the change in coefficient values over time steps $n+1$ and n, where $n \in \{1, 2, \ldots, N\}$ (N is the total number of time levels). Due to the Navier-Stokes equations having quadratic non-linearities, it is more appropriate to extend this Taylor expansion to second order accuracy,

$$\alpha^{n+2} = \alpha^{n+1} + \left(M_0 + \sum_{k=1}^{P} (\alpha_k^{n+1} - \alpha_k^n) M_k \right) (\alpha^{n+1} - \alpha^n), \tag{2.18}$$

which is expressed in terms of matrices M_0 and M_k, for $k \in \{1, 2, \ldots P\}$, that have dimensions $P \times P$. These denote the derivatives of the POD coefficients at one time step with respect to a change in the POD coefficients at the previous time step. The matrix M_0 holds the first order derivatives and is given by,

$$(M_0)_{i,j} = \frac{\partial \alpha_i^{n+1}}{\partial \alpha_j^n} \approx \frac{\partial \alpha_i^1}{\partial \alpha_j^0}, \quad i, j \in \{1, 2, \ldots P\}, \tag{2.19}$$

whereas the matrices M_k contain the second order derivatives which are given by,

$$(M_k)_{i,j} = \frac{\partial^2 \alpha_i^{n+1}}{\partial \alpha_j^n \partial \alpha_k^n} \approx \frac{\partial^2 \alpha_i^1}{\partial \alpha_j^0 \partial \alpha_k^0}, \quad i, j, k \in \{1, 2, \ldots P\}. \tag{2.20}$$

Note that the matrices M_0 and M_k, for $k \in \{1, 2, \ldots P\}$ are assumed to be constant in time and so can be pre-calculated. Once the solutions α^0 and α^1 at the first two time instances $t = 0, 1$ are determined, the POD coefficients at time level n can be estimated from equation (2.17).

2.4.2 Offline calculation of the first and second derivative matrices in the Taylor series

An efficient way to calculate the derivative matrices M_0 and M_k, for $k \in \{1, 2, \dots P\}$ is through a perturbation of the POD coefficients at one time instance. Suppose the perturbation vector is $\mathbf{\Delta}\alpha_j^0 = (0, ..., \delta\alpha_j^0, ..., 0)^T$ for a perturbation $\delta\alpha_j^0$ of the j^{th} entry in α^0, then the i^{th} element of the computed POD vector $\hat{\alpha}^1$ at time instance 1 will provide the variation of the i^{th} POD coefficient with respect to the change in α^0. This can be used to compute the first derivative matrix, M_0 through the relationship:

$$(M_0)_{i,j} = \frac{\hat{\alpha}_i^1 - \alpha_i^1}{\delta\alpha_j^0}, \quad i, j \in \{1, 2, \dots P\}. \tag{2.21}$$

The perturbed solutions $\hat{\alpha}^1$ at time step 1 can be thus calculated using the following process:

(a) Map the vectors $\alpha^0 + \mathbf{\Delta}\alpha_j^0$ to the full space, then obtain the perturbed initial solution $\hat{\psi}^0 = \overline{\psi} + \sum_{j=1}^{P}(\alpha^0 + \mathbf{\Delta}\alpha_j^0)\Phi_j$;

(b) Calculate the solution at the next time step, $\hat{\psi}^1$, through running the full model one time instance;

(c) Obtain the perturbed POD vector $\hat{\alpha}_i^1$ by projecting $\hat{\psi}^1$ onto the reduced space, $\hat{\alpha}^1 = \Phi^T\hat{\psi}^1$.

The whole matrix M_0 can be computed by repeating the process P times and perturbing each POD coefficient α_j^0 $(j \in \{1, 2, \dots P\})$ in turn.

The calculation of the second derivative matrix M_k in (2.20) follows an extended route similar to that used in the generation of the matrix M_0. For each k, two perturbed vectors are created, $\hat{\alpha}_k^{0,+}$ and $\hat{\alpha}_k^{0,-}$, which have small positive and negative perturbations in the k^{th} entry of the original vector α^0, *i.e.* $\hat{\alpha}_k^{0,\pm} = \alpha^0 \pm \mathbf{\Delta}\alpha_k^0$, where, $\mathbf{\Delta}\alpha_k^0 = (0, ..., \delta\alpha_k^0, ..., 0)^T$. Using these two vectors, two first order derivative matrices are generated using the process described above, these are denoted M_k^+ and M_k^- and have elements defined as,

$$(M_0)_{i,j}^{\pm} = \frac{\partial\alpha_i^{\pm,1}}{\partial\alpha_j^{\pm,0}} \quad i, j \in \{1, 2, \dots P\}. \tag{2.22}$$

The second order derivatives are formed from the two Taylor expansions,

$$(M_k)^{\pm}_{i,j} = (M_0)_{i,j} \pm \frac{\partial}{\partial \alpha^0_k}(M_0)_{i,j}\|\delta\alpha^0_k\|, \tag{2.23}$$

which, by subtracting one from the other, can be re-arranged to form,

$$(M_k) = \frac{1}{2\|\delta\alpha_k\|}(M^+_k - M^-_k). \tag{2.24}$$

2.5 The Smolyak sparse grid method for calculating the POD coefficients

The Smolyak sparse grid algorithm is an efficient method that is used to solve high dimensional linear tensor product problems. Using the Smolyak method, the interpolation function values need to be determined only at the sparse grid mesh points rather than on the full tensor product grid, thus resulting in an impressive computational savings in comparison to tensor product evaluations, as the number of points no longer increases exponentially with the dimensional size d. In this work, the Smolyak sparse grid interpolation method (see Smolyak (1963)) is used to construct a set of interpolating multidimensional functions $\hat{f}_k$, $(k \in \{1, 2, \dots P\})$ for representing the functions f_k in equation (2.16). An issue regarding this tensor product approximation is that it requires $O_{l_1} \times ... \times O_{l_d}$ values of the function f on a grid, which increases exponentially with dimensions d.

Let $\hat{f}_k^{d,l}$ denote a Smolyak interpolant of dimension d with an approximation level l, which is a linear combination of tensor product operators:

$$\hat{f}_k^{d,l}(\alpha^n) = \sum_{max(d,l+1)\leq|\mathbf{i}|\leq d+l} (-1)^{d+l-|\mathbf{i}|} \cdot \begin{pmatrix} d-1 \\ d+l-|\mathbf{i}| \end{pmatrix} (U^{i_1} \otimes \cdots \otimes U^{i_d}) f(\alpha^n), \quad (2.25)$$

where $|\mathbf{i}| = i_1 + \cdots + i_d$ (here $i_1, \dots, i_d$ are indices in each dimension respectively), $(-1)^{d+l-|\mathbf{i}|} \cdot \begin{pmatrix} d-1 \\ d+l-|\mathbf{i}| \end{pmatrix}$ is a counting coefficient. The tensor product operator of a d-dimensional function f_k is defined as:

$$(U_k^{i_1} \otimes \cdots \otimes U^{i_d})(f_k) = \sum_{j_1=1}^{O_{l_1}} \cdots \sum_{j_d=1}^{O_{i_d}} f_k(x_{j_1}^{i_1}, ..., x_{j_d}^{i_d}).(P_{j_1}^{i_1} \otimes \cdots \otimes P_{j_d}^{i_d}), \quad (2.26)$$

where $P_{j_1}^{i_1}, P_{j_2}^{i_2}, ..., P_{j_d}^{i_d}$ are the basis functions and $O_{l_1}, O_{l_2} ... O_{l_d}$ are the number of basis functions used in each dimension with $O_{i_d} = 2^{i_d - 1} + 1$ respectively, $f(x_{j_1}^{i_1}, ..., x_{j_d}^{i_d})$ represents the function value at $(x_{j_1}^{i_1}, ..., x_{j_d}^{i_d})$, and $i_d = 1, 2, ..., O_{l_d}$.

A set of Smolyak interpolation functions $\hat{f}_k^{d,l}(\alpha^n)$ in the form of (2.25) is now used to estimate the POD coefficient α_k^n at time level $n+1$,

$$\alpha_k^{n+1} = \hat{f}_k(\alpha^n), \quad k \in \{1, 2, \dots P\}, \quad (2.27)$$

where the spatial dimensional size d equals to the size of the reduced order space (*i.e.* the number of POD bases P). The input for each interpolation function $\hat{f}_k(\alpha^n)$ is the complete set of POD coefficients $\alpha^n = (\alpha_1^n, \alpha_2^n, \ldots, \alpha_P^n)$ at the previous times step n. The output of $\hat{f}_k^{d,l}(\alpha^n)$ is the k^{th} POD coefficient α^{n+1} at time step $n+1$, *i.e.*,

$$\hat{f}_k^{d,l}(\alpha^n) : \alpha^n \rightarrow \alpha_j^{n+1}, \quad k \in \{1, 2, \ldots P\}. \tag{2.28}$$

The Smolyak interpolation functions $\hat{f}_k^{d,l}(\alpha^n)$ are calculated offline using the functional values at the Smolyak grids. Each interpolation function denotes a supercube surface or a P-dimensional hyper-surface. Once the interpolation functions are constructed, the POD coefficients at the current time level $n+1$ are obtained by entering the POD coefficients at the previous time level n into the interpolation functions.

The offline calculation of the Smolyak interpolation functions $\hat{f}_k^{d,l}(\alpha^n)$ can be described as follows:

(a) Choose a set of sparse interpolation grids $\alpha^{r,0} = (\alpha_1^{r,0}, \alpha_2^{r,0}, \ldots, \alpha_P^{r,0})$ (where $r \in \{1, 2, \ldots, R\}$, R is the number of sparse grids to be chosen), which lie in some product interval

$$[A_{min}, A_{max}] = [\alpha_{1,min}, \alpha_{1,max}] \cdots \otimes [\alpha_{j,min}, \alpha_{j,max}] \cdots \otimes [\alpha_{P,min}, \alpha_{P,max}]$$

(where $\alpha_{k,min}$ and $\alpha_{k,max}$ are the minimum and maximum values of the k^{th} POD coefficient, $k \in \{1, 2, \ldots, P\}$);

(b) Calculate a corresponding set of the function value $\alpha_k^{r,1} = f_k(\alpha^{r,0})$ located at the sparse grids through running the full model one time step from time level 0 to 1:

  (i) Determine the initial condition $\psi^{r,0}$ for the full model by projecting $\alpha^{r,0}$ onto the full space, where ψ denotes any variable in the full model, for example, the velocity components u_x, u_y and u_z, and the pressure p;

  (ii) Determine the full solution $\psi^{r,1}$ by running the full model one time level;

  (iii) Calculate the function value $\alpha_j^{r,1}$ at sparse grid r by projecting $\psi^{r,1}$ onto the reduced order space;

  (iv) Repeat the above procedures (i)-(iii) and obtain all the function values at the sparse grids $r \in \{1, 2, \ldots, R\}$;

(c) Given a set of $\alpha_j^{r,1}$, construct the interpolation function $\hat{f}_k^{d,l}(\alpha^n)$, $k \in \{1, 2, \ldots, P\}$.

2.6 Numerical examples of Smolyak sparse grid and Taylor series expansion methods

A demonstration of the use of the non-intrusive POD reduced order modelling schemes is presented in this section. This numerical illustration consists in solving two problems. In one we model flow past a cylinder and in the other we model flow within a gyre. We used the Arpack package to perform the singular Value Decomposition and, in particular, to obtain the leading singular value. The Smolyak grid was determined using the "SPARSE_INTERP_ND Multidimensional Sparse Interpolant" authored by Burkardt (see John Burkardt (2012); J.Burkardt (2014)) whilst the original fine grid simulations were calculated using FLUIDITY (see Pain *et al.* (2005)). These provided the exact solutions for model comparison, as well as the snapshots for the POD function generation.

In this demonstration a comparison between the full model and the non-intrusive model reduction approach has been made. In addition to comparing solution profiles the analysis compares the solution root mean square errors, as well as correlation coefficients. The measured error is given by the root mean square error (RMSE) which is calculated for each time step n by,

$$RMSE^n = \sqrt{\frac{\sum_{i=1}^{\mathcal{N}}(\psi_i^n - \psi_{o,i}^n)^2}{\mathcal{N}}}. \tag{2.29}$$

In this expression ψ_i^n and $\psi_{o,i}^n$ denote the POD (mapped onto the full mesh) and the full model solution at the node i, respectively, and F represents the number of nodes on the full mesh. The correlation coefficient is computed for each time step, and is defined for given expected values μ_{ψ^n} and $\mu_{\psi_o^n}$ and standard deviations σ_{ψ^n} and $\sigma_{\psi_o^n}$,

$$corr(\psi^n, \psi_o^n)^n = \frac{cov(\psi^n, \psi_o^n)}{\sigma_{\psi^n}\sigma_{\psi_o^n}} = \frac{E(\psi^n - \sigma_{\psi^n})(\psi_o^n - \sigma_{\psi_o^n})}{\sigma_{\psi^n}\sigma_{\psi_o^n}}, \tag{2.30}$$

where E denotes mathematical expectation, cov denotes covariance, σ denotes standard deviation.

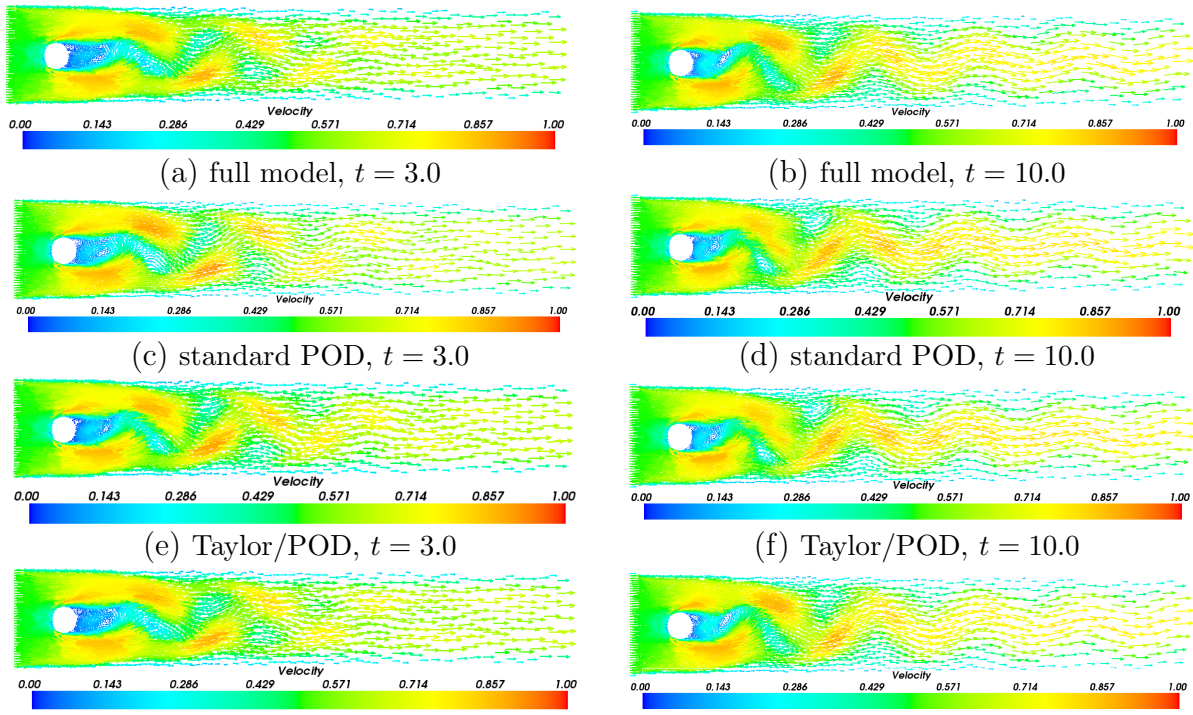
2.6.1 Flow past a cylinder

We illustrate the novel non-intrusive methods via two numerical examples. Both cases typify non-laminar flows. In the first numerical example a two dimensional flow past a cylinder is simulated. In fluid dynamics, vortex shedding is an oscillating flow that takes place when a fluid such as air or water flows past a cylindrical body at certain velocities, depending on the size and shape of the body. These are called Von Karman vortices.

The problem domain is 2 units in length and 0.4 units in width, and it contains a cylinder of radius 0.12 units at location(0.2, 0.2). The dynamics of the fluid flow are caused by a slightly compressible fluid flowing through the domain with a velocity 1. This enters the domain through the left boundary. The fluid is allowed to flow past the cylinder and out of the domain through the right boundary. No slip and zero outward flow conditions are applied to the upper and lower edges of the problem, whilst Dirichlet boundary conditions are applied to the cylinder's wall. From the full model simulation, with a mesh of 3213 nodes, 400 snapshots were obtained at regularly spaced time intervals $\Delta t = 0.02$ for each of the u, v and p solution variables.

In order to evaluate the capabilities and the difference between the Smolyak sparse grid ROM and the Taylor expansion POD model, two cases one with a Reynolds number of 400 and the other with a Reynolds number of 3600 were investigated. The simulation period is $[2 - 10]$, and a time step of $\Delta t = 0.01$ was used for all models.

Figure 2.1 shows the solutions for the flow past the cylinder at time instances 3.0 and 10.0, as calculated using the two non-intrusive models (Smolyak sparse grid ROM and Taylor/POD model respectively), the full high fidelity model and the standard (Galerkin projection) POD model using 12 POD basis functions. The Reynolds number was 400 in this case. These solutions show that both non-intrusive models and the standard POD model have performed particularly well at resolving the flow at both time instances. This is highlighted further in figure 2.2 which presents the solution velocities predicted by all methods at the position (0.19397, 0.28101) on the domain. It can be seen from this figure that the Smolyak sparse grid ROM is in closer agreement with the full model, whilst both the standard and Taylor POD models are able to capture the wave pattern, but have a large error near the peak of waves during the spin-up period of modelling *i.e.* $[200, 550]$. It is shown



(a) full model, $t = 3.0$ (b) full model, $t = 10.0$

(c) standard POD, $t = 3.0$ (d) standard POD, $t = 10.0$

(e) Taylor/POD, $t = 3.0$ (f) Taylor/POD, $t = 10.0$

(g) Smolyak sparse grid ROM, $t = 3.0$ (h) Smolyak sparse grid ROM, $t = 10.0$

Figure 2.1: Flow past a cylinder at $Re = 400$: The figures displayed above show the solutions of the flow past a cylinder problem at time instances 3.0 and 10.0. The solutions compare the predictions from non-intrusive models (Smolyak sparse grid ROM and Taylor/POD) with full model and standard (Galerkin projection) POD model using 12 POD bases functions.

the Smolyak sparse grid ROM can perform better than other POD models since it is highly customizable through the choice of admissible multi-index sets and well converges to the tensor product of exact operators (see Conrard & Marzouk (2013)).

To further demonstrate the capability of the non-intrusive models, the Reynolds number was then increased to $Re = 3600$. Visual inspection of figure 2.3 shows that decrease of eigenvalues satisfies exponential Kolmogorov n-width. This helps us to choose the number of POD bases. The more number of POD bases are chosen, the more energy is captured. In this case, 12, 24 and 35 POD bases are used to demonstrate the performance of ROM.

The comparison of results between the full and POD models (the standard, Taylor and Smolyak sparse grid non-intrusive POD models) was carried out. Figure 2.4 shows the simulated flow patterns at time instances 3.0 and 10.0 (where 12 POD bases are used). As shown in the figures the Smolyak sparse grid non-intrusive

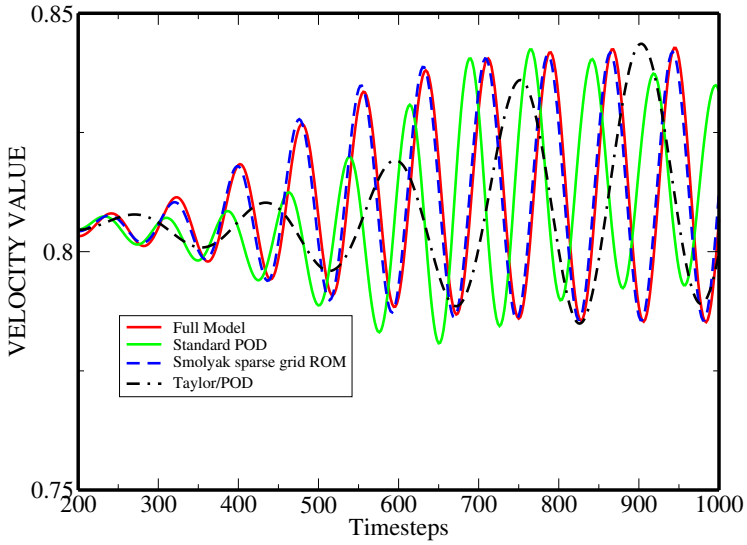


Figure 2.2: Flow past a cylinder: The graphs shows the solution velocities predicted by the full model, POD model, Taylor expansion method and the Smolyak sparse grid ROM at positions: 0.19397,0.28101, Re=400.

model performs well for this Reynolds number. However, it can be seen that the Taylor/POD non-intrusive model does not capture well the complex flow patterns and eddies for this high Reynolds number while the standard POD model has a large error near the cylinder. Figures 2.5 shows the difference between the full model and Smolyak sparse grid and standard POD of the flow past a cylinder problem at time instances 3.0 and 10.0 using 12 and 24 POD basis functions, respectively. The figures illustrate the fact that the error between the full model and the Smolyak sparse grid ROM is smaller than that between full model and the standard POD model.

In this study case, it is demonstrated that the Smolyak sparse grid ROM can reproduce better solutions in comparison with the other POD models for $Re = 400, 3500$. The standard POD model is formed by projecting the full model onto the reduced order space through a Galerkin projection, thus introducing errors into the POD model which may even grow exponentially and have contributed to the poorer performance of the standard POD approach compared with the sparse grid ROM. A new Petrov-Galerkin method was introduced to stabilize the resulting equations and produce more accurate results (see Xiao *et al.* (2013)). Here, we use the standard POD approach. In the Smolyak ROM, the POD coefficients are computed using sparse grid interpolation (see equation (2.28)) where the functional values are calculated accurately from the full model. It has been argued by others (see Conrard & Marzouk (2013)) that 'Smolyak algorithms constitute the ideal blending of different

full tensor approximations from the perspective of exact sets; that is, the exact set of the Smolyak algorithm contains the union of the exact sets of the component full tensor approximations'. See also (Eldred & Burkardt (2009)). Also the Smolyak sparse grid ROM with an increase of approximation levels is able to represent not only quadratic (*e.g.* the Taylor POD ROM proposed here), but also high order non-linearities. These arguments explain why the Smolyak ROM can perform better than other POD ROMs (both intrusive and non-intrusive).

The accuracy of the POD ROM results can be further improved by increasing the number of POD bases. Figures 2.6 and 2.7 compare the full solution and the Smolyak sparse grid non-intrusive reduced order model when using 24 and 35 POD basis functions respectively. In both cases there is a visual improvement in the Smolyak ROM's predictions in comparison to the solutions provided by the standard POD ROM when the same number of basis functions is used. Figure 2.8 shows the velocity speed at two points in the domain using 12 POD bases and 35 POD bases. It is again shown that the accuracy of velocity solution is improved by increasing the number of POD bases to 35. In this case, the Smolyak sparse grid ROM can perform well only using 12 POD bases when there are no abrupt change in solutions, however, this abrupt change in time can be captured by increasing the number of POD bases, as shown in figure 2.8. It is also seen in figure 2.9 that the RMSE of velocity results obtained from the Smolyak sparse grid ROM decreases as the number of POD bases increases.

Figure 2.10 compares the full model and Smolyak sparse grid ROM using different sparse grid levels l with $l \in \{0, 1, 2\}$ using 12 POD bases. Each dimension has the number of nodes $n^l = 2^l + 1$ in which l denotes the number of levels. As we can see from figure 2.10, even level one (3 points at each dimension) performs well, while level zero (one point at each dimension, mean value of each dimension) failed to capture the energy of the flows.

Figure 2.11 shows the online CPU time required to compute a single time step with varying mesh size. The offline CPU time for calculating the Smolyak interpolation functions and the first/second order derivative matrices for the Taylor/POD method are not taken into account. It shows the cost of the ROM models remain static with increased resolution of mesh, and that significant CPU speed-ups are obtained using mesh with the largest number of nodes. For the largest mesh the CPU costs were reduced by a factor of 100 compared to the cost of the high fidelity model. Table 2.1 shows comparison of the online CPU time required for running the full model and

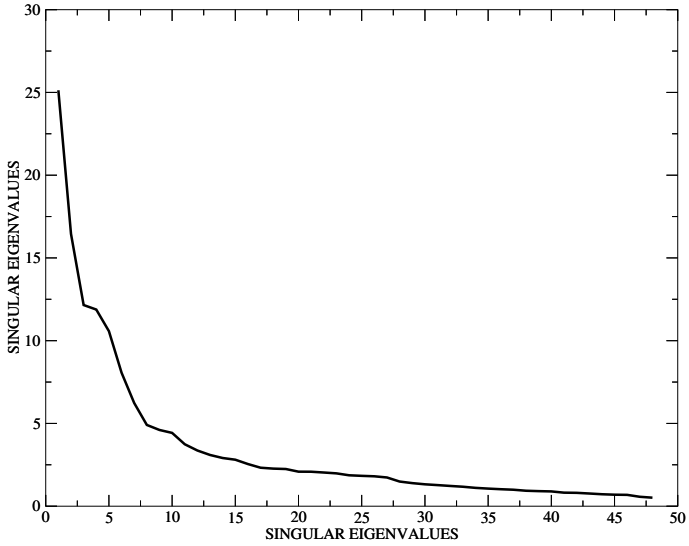
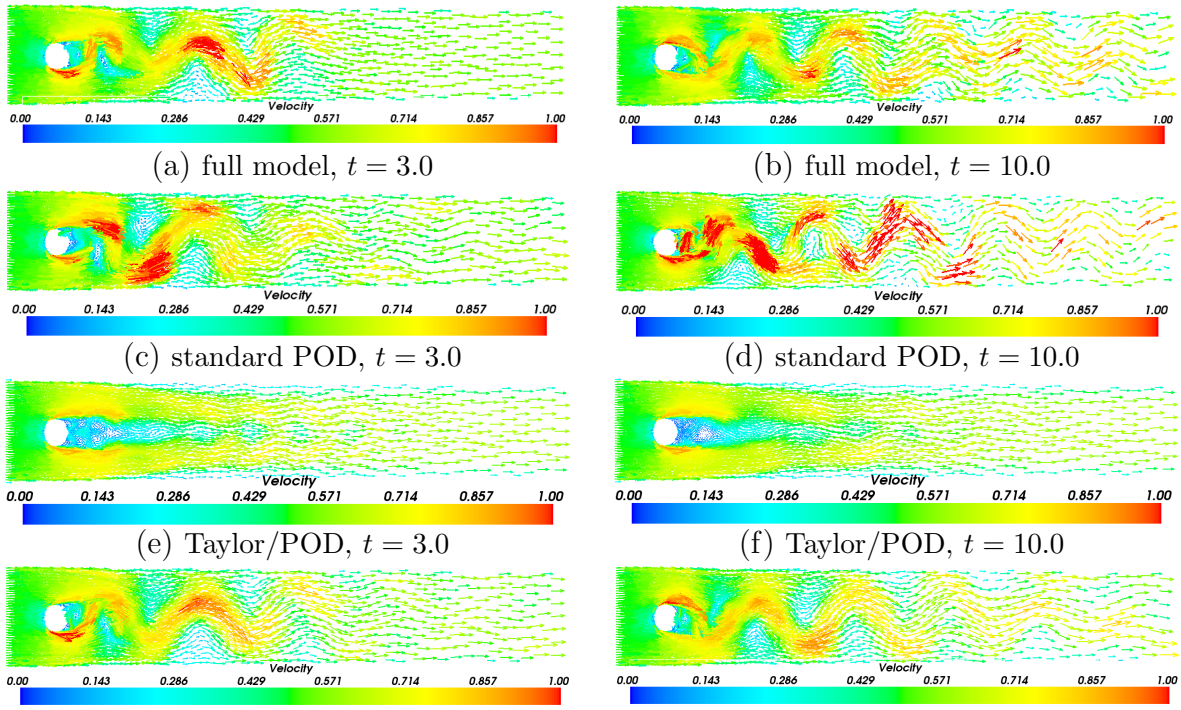


Figure 2.3: Flow past a cylinder at $Re = 400$: The graphs shows the singular eigenvalues in order of decreasing magnitude.

non-intrusive ROMs for each time step. The online CPU time listed here includes the time for assembling and solving the matrix for the full model while interpolating (Smolyak), Matrix multiplication (Taylor) and projecting the POD solution onto the full space for the non-intrusive ROM. In this study case, the CPU time required for matrix multiplication can be ignored since the dimensional size (36×36) of matrices is very small. It can be seen that the non-intrusive ROM is CPU time efficient, since it does not involve assembling and solving the matrices process, thus resulting in a speed-up of CPU time of two orders of magnitude.

Table 2.1: Flow past a cylinder at $Re = 3600$: Comparison of the online CPU time (second) required for running the full model and ROM for each time step

Model	Assembling	Solving	Projection	Interpolation (Smolyak) matrix multiplication (Taylor)	Total
Full model	3.004	0.113	0.000	0.000	3.117
POD ROM	0.303	0.000	0.008	0.000	0.311
Smolyak ROM	0.000	0.000	0.008	0.004	0.012
Taylor/POD	0.000	0.000	0.008	0.000	0.008



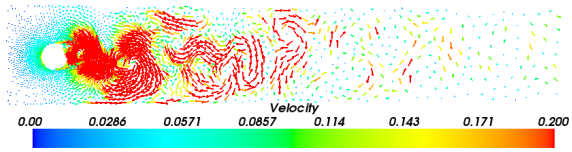
(a) full model, $t = 3.0$ (b) full model, $t = 10.0$

(c) standard POD, $t = 3.0$ (d) standard POD, $t = 10.0$

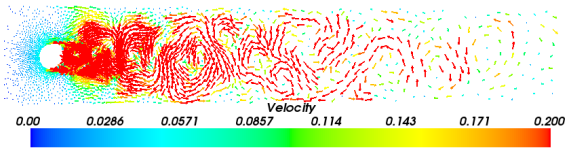
(e) Taylor/POD, $t = 3.0$ (f) Taylor/POD, $t = 10.0$

(g) Smolyak sparse grid ROM, $t = 3.0$ (h) Smolyak sparse grid ROM, $t = 10.0$

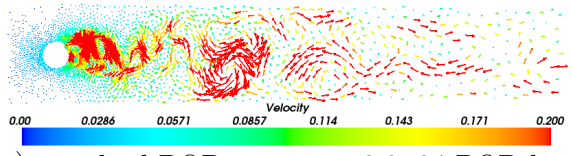
Figure 2.4: Flow past a cylinder at $Re = 3600$: The figures displayed above show the solutions of the flow past a cylinder problem at time instances 3.0 and 10.0. The solutions compare the predictions from Smolyak sparse grid ROM and Taylor/POD non-intrusive models with the full model and the standard POD model using 12 POD basis functions.



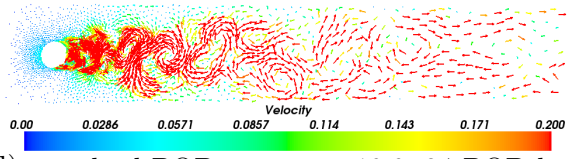
(a) standard POD error, $t = 3.0$, 12 POD bases



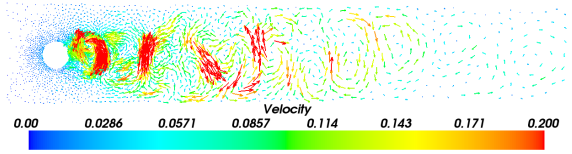
(b) standard POD error, $t = 10.0$, 12 POD bases



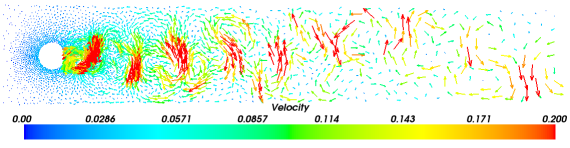
(c) standard POD error, $t = 3.0$, 24 POD bases



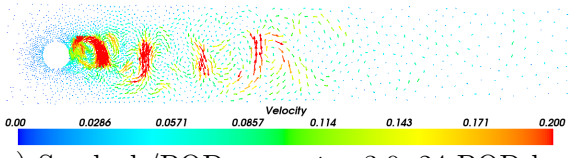
(d) standard POD error, $t = 10.0$, 24 POD bases



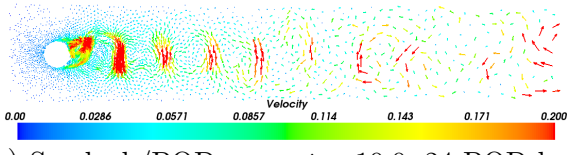
(e) Smolyak/POD error, $t = 3.0$, 12 POD bases



(f) Smolyak/POD error, $t = 10.0$, 12 POD bases

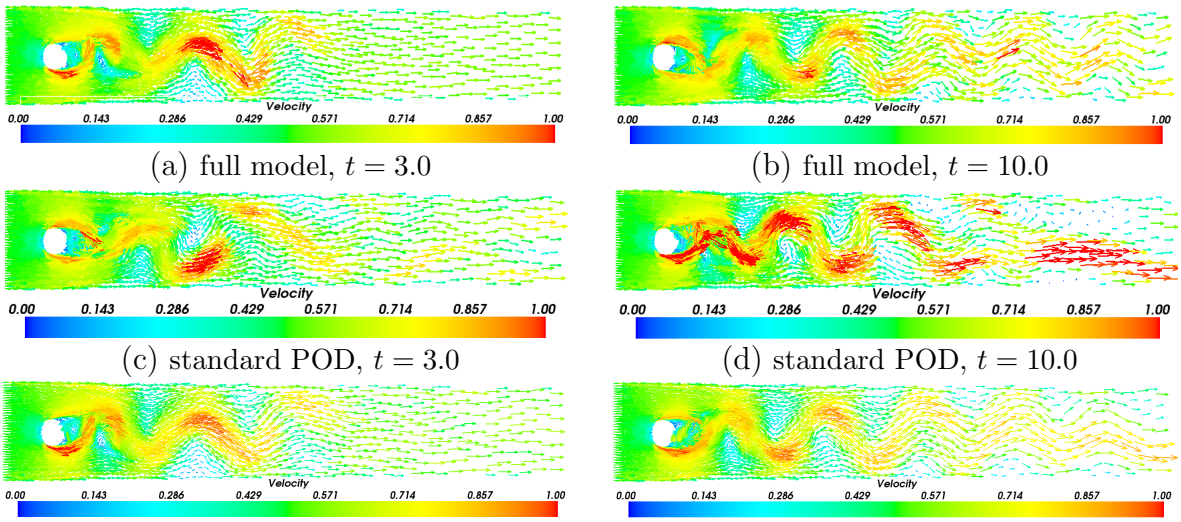


(g) Smolyak/POD error, $t = 3.0$, 24 POD bases



(h) Smolyak/POD error, $t = 10.0$, 24 POD bases

Figure 2.5: Flow past a cylinder at $Re = 3600$: The figures displayed above show the solution difference between the full model and the standard POD and the Smolyak sparse grid ROM of the flow past a cylinder problem at time instances 3.0 and 10.0 using 12 POD basis and 24 POD bases.

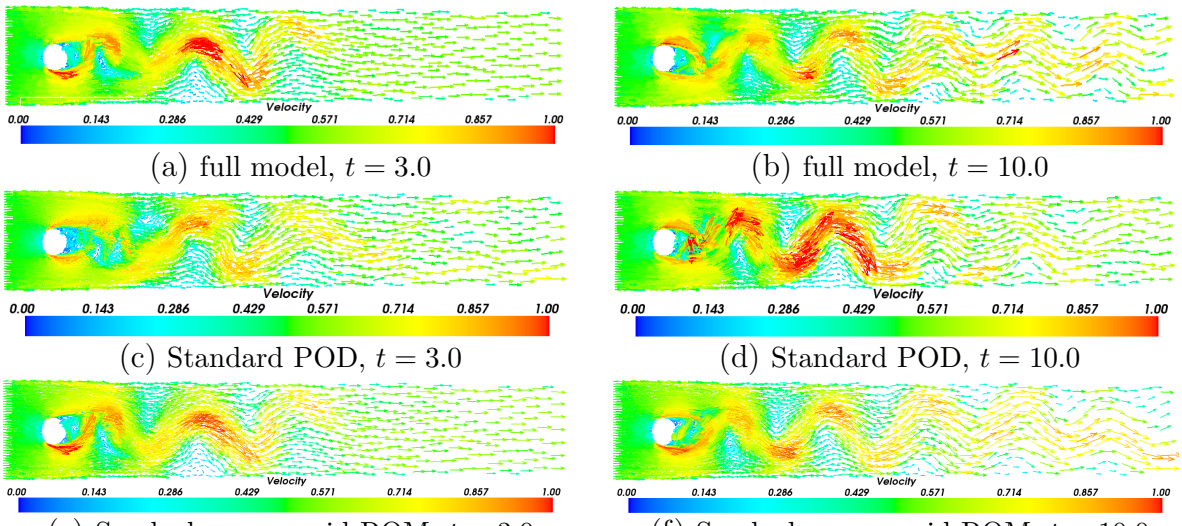


(a) full model, $t = 3.0$ (b) full model, $t = 10.0$

(c) standard POD, $t = 3.0$ (d) standard POD, $t = 10.0$

(e) Smolyak sparse grid ROM, $t = 3.0$ (f) Smolyak sparse grid ROM, $t = 10.0$

Figure 2.6: Flow past a cylinder at $Re = 3600$: The figures displayed above show the solutions of the flow past a cylinder problem at time instances 3.0 and 10.0. The solutions compare the predictions from Smolyak sparse grid non-intrusive ROM using 24 POD basis functions.



(a) full model, $t = 3.0$ (b) full model, $t = 10.0$

(c) Standard POD, $t = 3.0$ (d) Standard POD, $t = 10.0$

(e) Smolyak sparse grid ROM, $t = 3.0$ (f) Smolyak sparse grid ROM, $t = 10.0$

Figure 2.7: Flow past a cylinder at $Re = 3600$: The figures displayed above show the solutions of the flow past a cylinder problem at time instances 3.0 and 10.0. The solutions compare the predictions from Smolyak sparse grid non-intrusive ROM using 35 POD basis functions.

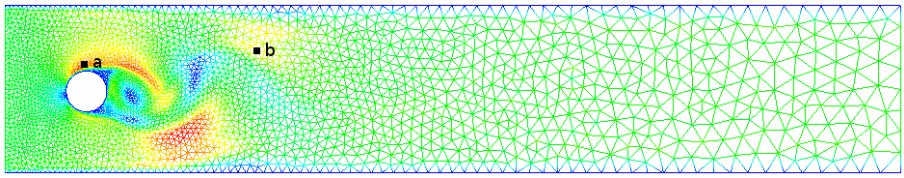
2.6.2 The Gyre Problem

The second numerical example involves the simulation of a gyre for which a circulating fluid moves across a domain that is 1000×1000 km across and 500m in depth. The solution's free surface is driven by a wind with a force strength given by the expression,

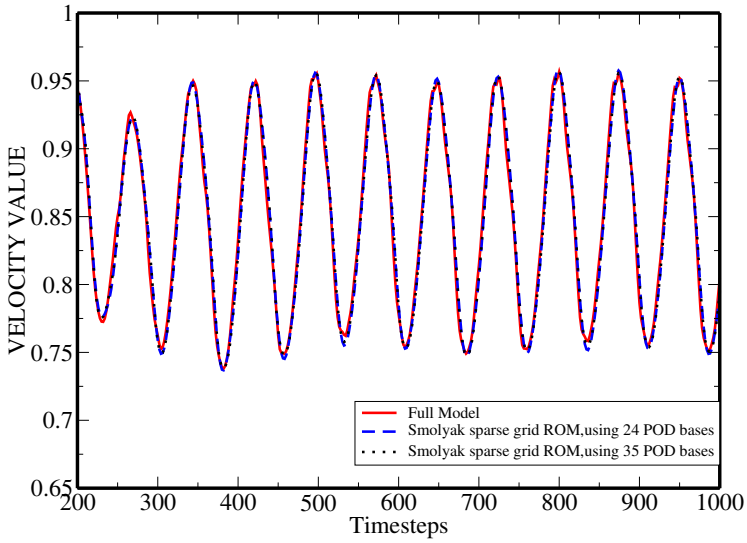
$$\tau_y = \tau_0 cos(\pi y/L) \quad \text{and} \quad \tau_x = 0.0, \tag{2.31}$$

where L is the system length ($L = 1000\ km$). The terms τ_x and τ_y are the wind stresses on the free surface that act along the x and y directions, respectively. In this example the maximum zonal wind stress was set to $\tau_0 = 0.1\ Nm^{-1}$ in the latitude(y) direction. The Coriolis terms are taken into account with the beta-plane approximation($f = \beta y$) where $\beta = 1.8 \times 10^{-11}$ and the reference density of the fluid is set to $\rho_0 = 1000\ kgm^{-3}$. The velocity is $3.510^2 m/s^{-1}$. With this setup the Reynolds number of the problem was calculated to be $Re = 300$.

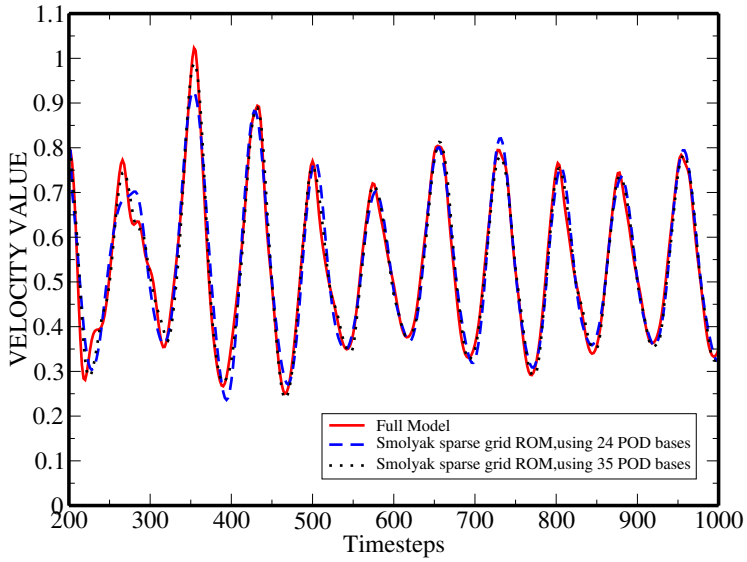
The gyre was simulated using a finite element model for a period of 161 days using a time step of $\Delta t = 0.322$ days. From this simulation 500 snapshots of the solution were recorded and from this data 12 POD basis functions were generated. It was found that this POD basis set captured over 99% of the energy of the u, v and p snapshot data. The problem was then re-simulated using the newly developed non-intrusive reduced order model. Figure 2.12 shows the velocity profiles obtained from the full model at 41 and 93 days using 6 POD bases. The errors between the full model and the non-intrusive order model are shown at the bottom of figure 2.12. Figure 2.13 shows the velocity profiles obtained from the full model at 41 and 93 days using 12 POD bases. The numerical results obtained show that the main gyre is accurately resolved using non-intrusive reduced order model. Figure 2.14 shows the RMSE between the full model and the non-intrusive model, which means the solutions of the non-intrusive model are in close agreement with the high-fidelity full model solutions. Figure 2.15 displays the correlation coefficient between the full model and the non-intrusive model, this indicates that the RMSE of velocity results obtained from the Smolyak sparse grid model is smaller than that from the standard POD model. The non-intrusive Smolyak sparse grid model exhibits an overall good agreement with the full model. It can be also seen that an increase in the number of POD bases leads an improvement in the accuracy of the POD model - the RMSE of velocity results is decreased.



(a) Locations a(0.195, 0.267) and b(0.619, 0.298)



(b) Fluid speed at a(0.195, 0.267)



(c) Fluid speed at b(0.619, 0.298)

Figure 2.8: Flow past a cylinder at $Re = 3600$: The graphs show the velocity speed predicted by the full model, and the Smolyak sparse grid ROM at positions a (0.195, 0.267) and b (0.619, 0.298). These results were obtained using a reduced order model with 24 and 35 POD functions.

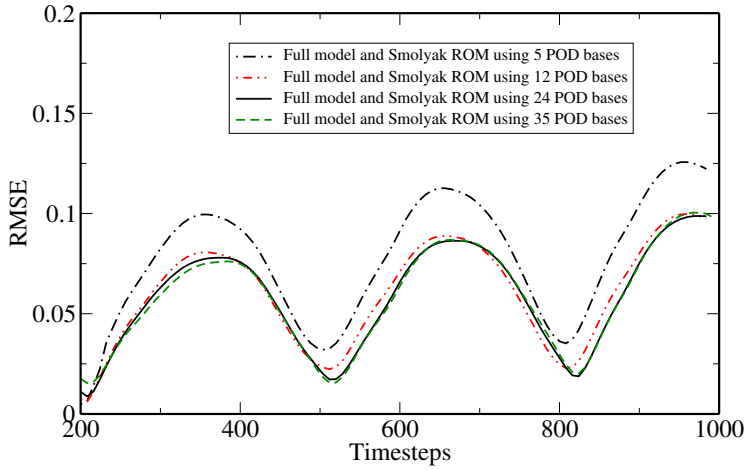
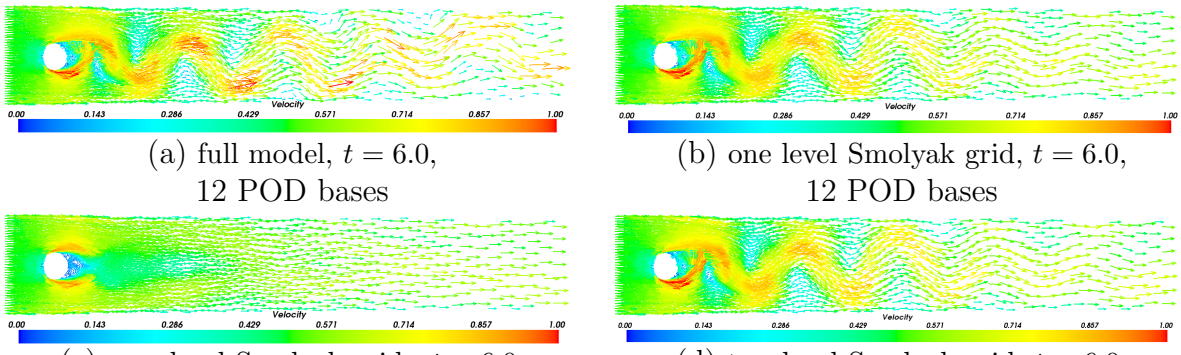


Figure 2.9: Flow past a cylinder at $Re = 3600$: The graphs show the RMSE of results obtained from Smolyak ROM.



(a) full model, $t = 6.0$, 12 POD bases

(b) one level Smolyak grid, $t = 6.0$, 12 POD bases

(c) zero level Smolyak grid , $t = 6.0$, 12 POD bases

(d) two level Smolyak grid, $t = 6.0$, 12 POD bases

Figure 2.10: Flow past a cylinder at $Re = 3600$: The graphs show the comparison between full model with different levels of Smolyak grid using 12 POD bases at $t = 6$.

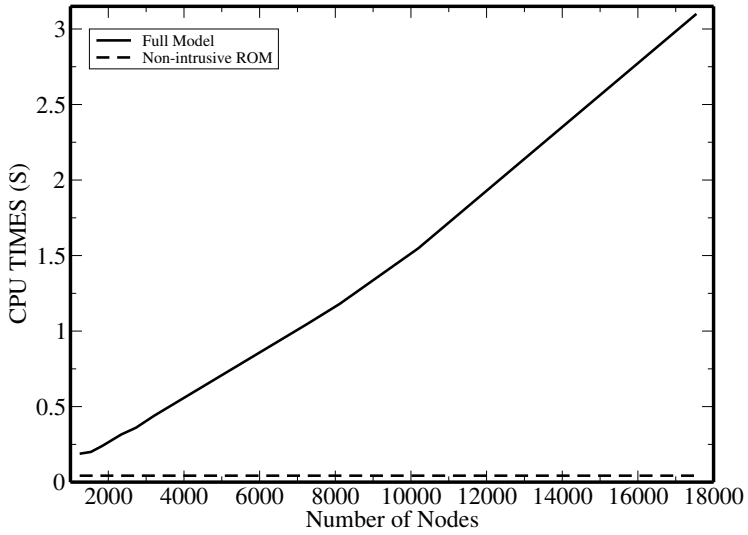
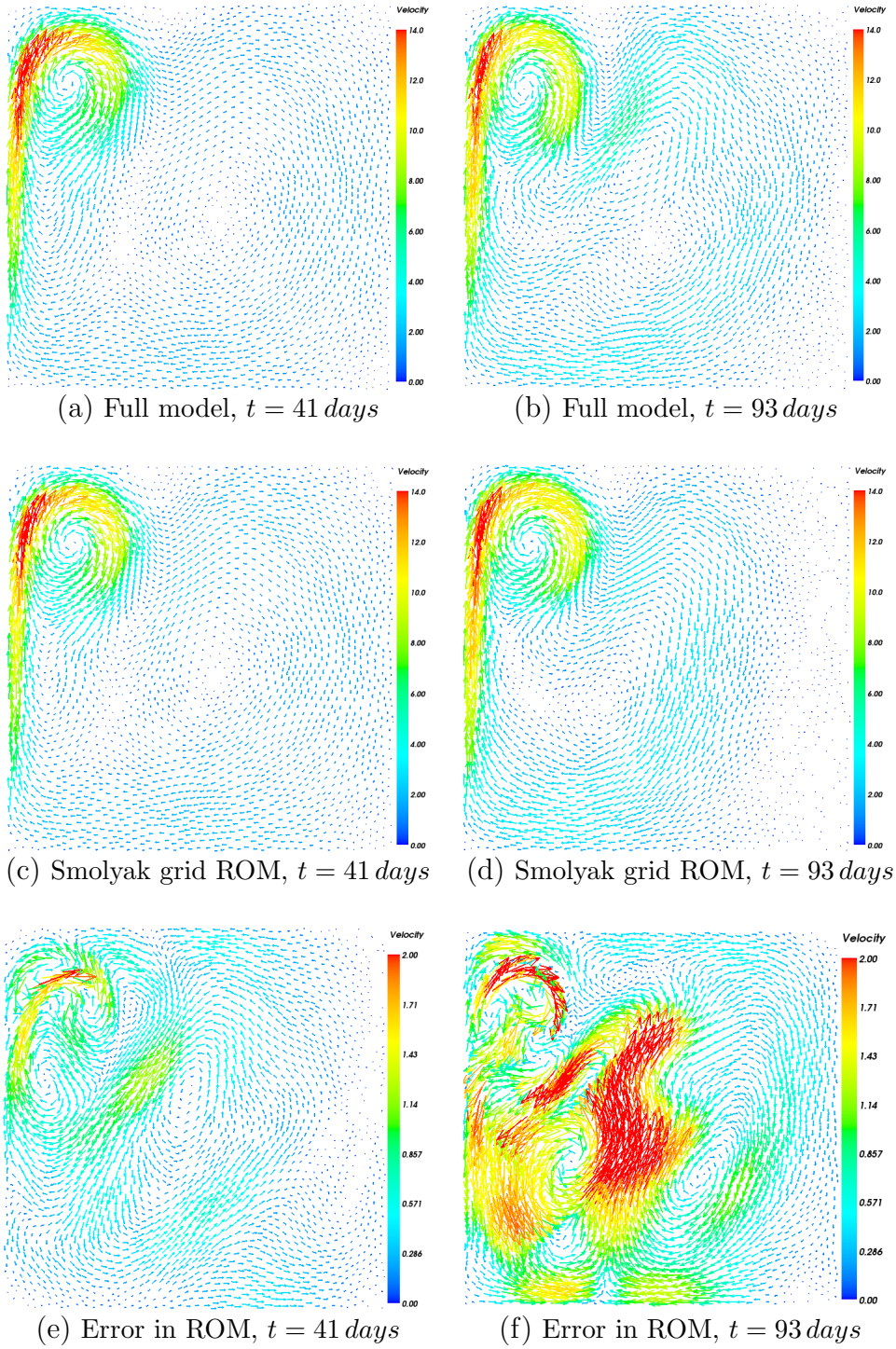


Figure 2.11: Flow past a cylinder at $Re = 3600$: Computational times to compute each time step as a function of mesh size (number of nodes) in the full model. Comparisons are made between the full model and the non-intrusive ROM.



(a) Full model, $t = 41\,days$

(b) Full model, $t = 93\,days$

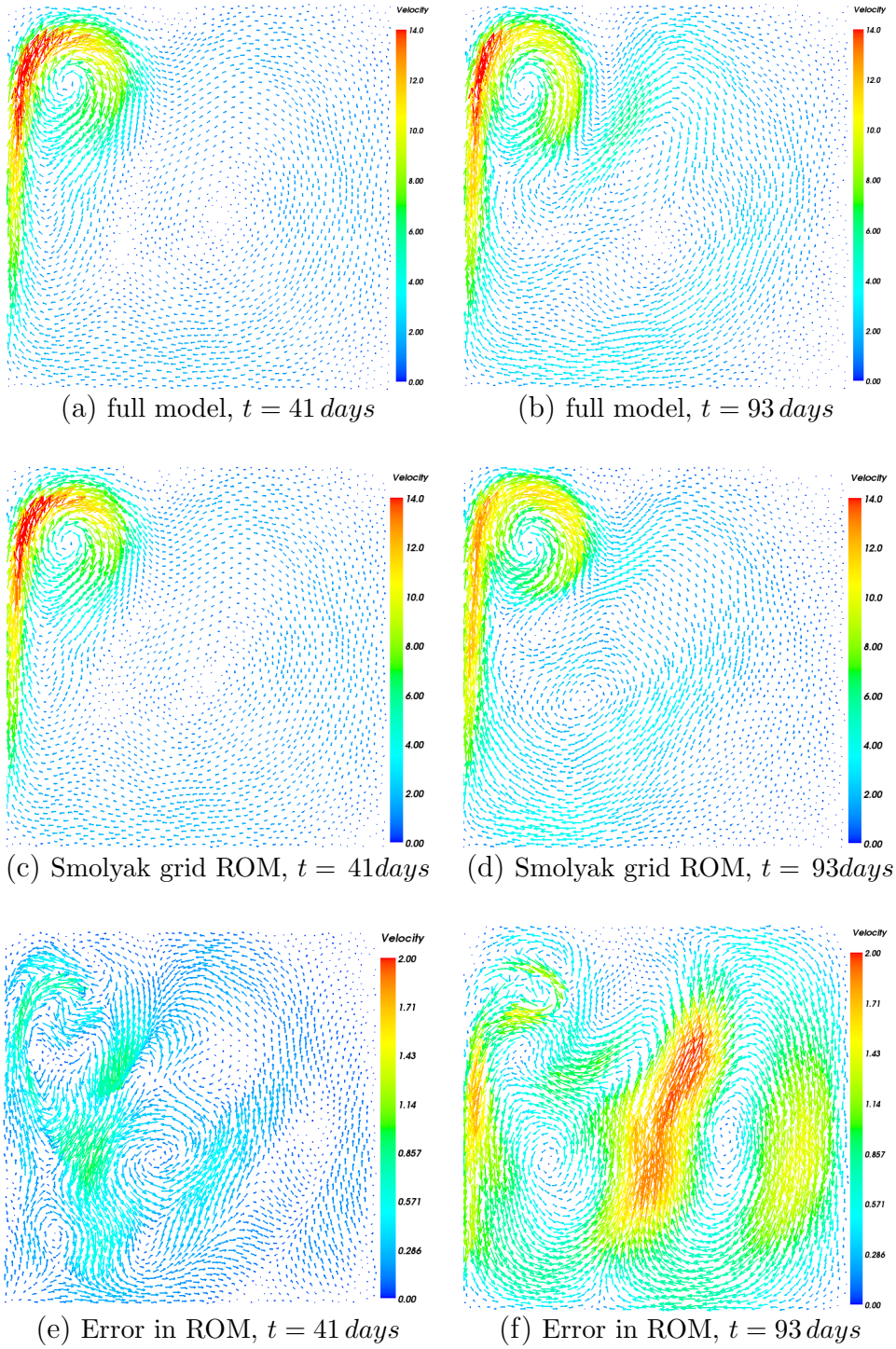
(c) Smolyak grid ROM, $t = 41\,days$

(d) Smolyak grid ROM, $t = 93\,days$

(e) Error in ROM, $t = 41\,days$

(f) Error in ROM, $t = 93\,days$

Figure 2.12: Gyre: the figures displayed above show the solutions of the gyre problem at time instance 41 (left) and 93 days (right). The solutions compare the predictions from the full model (top), the Smolyak sparse grid ROM (middle) **using 6 POD functions** (middle). The Figures at the bottom are the difference between full and Smolyak sparse grid ROM.



(a) full model, $t = 41\,days$ (b) full model, $t = 93\,days$

(c) Smolyak grid ROM, $t = 41 days$ (d) Smolyak grid ROM, $t = 93 days$

(e) Error in ROM, $t = 41\,days$ (f) Error in ROM, $t = 93\,days$

Figure 2.13: Gyre: The figures displayed above show the solutions of the gyre problem at time instance 41 (left) and 93 days (right). The solutions compare the predictions from the full model (top), the Smolyak sparse grid ROM (middle) **using 12 POD functions** (middle). The figures at the bottom are the errors between full and Smolyak sparse grid ROM

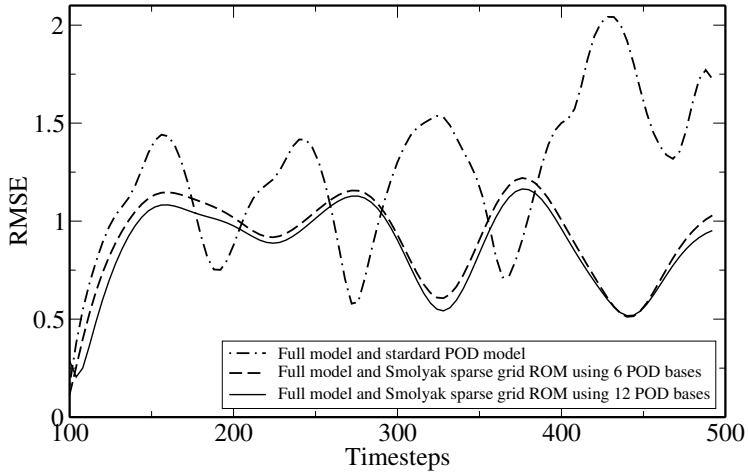


Figure 2.14: Gyre: The graph shows the RMSE errors calculated for the Smolyak sparse grid ROM.

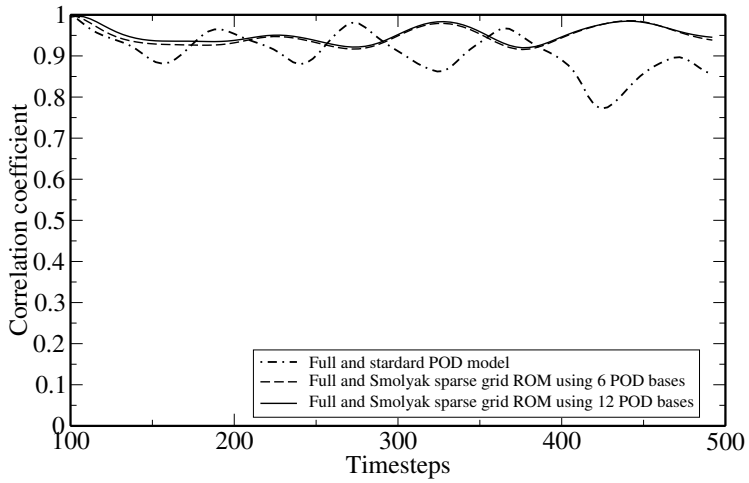


Figure 2.15: Gyre: The graph shows the correlation coefficient calculated for the Smolyak sparse grid ROM.

2.7 POD/RBF formulation of reduced order Navier-Stokes equations

In this section, a new non-intrusive reduced order modelling formulation is introduced. It is based on a combination of POD and RBF. The comparison between NIROM using Smolyak sparse grid and NIROM using RBF is carried out in section 2.7.3.2. And also, a more complicated multi-phase porous media case test is used to compare the accuracy of NIROMs based on Smolyak sparse grid and RBF, this can be found in the section 8.4.3 of chapter 8. RBF interpolation is a method that represents a function through scattered data and it has been applied to various research areas such as partial differential equations (PDEs) (see Sharan *et al.* (1997)), coupled problem (see Shankar *et al.* (2014)), mesh generation (see Costin & Allen (2013)), facial recognition (see Er *et al.* (2002)), and feedback control (see Seshagiri & Khalil (2000)). The method can be effective for any dimensional scattered data and has been demonstrated to be flexible, convenient and accurate (see Fornberg & Flyer (2005)).

2.7.1 Radial basis functions interpolation

Let $\hat{f}_i(\boldsymbol{\alpha}^{n-1})$ denotes a RBF interpolation function for a single POD coefficient α_i from the complete set of POD coefficient $\boldsymbol{\alpha}$ ($\boldsymbol{\alpha} = \alpha_1, \alpha_2, \ldots, \alpha_P$). The RBF interpolation function is a linear combination of N radial basis functions ϕ_k in the form of:

$$\hat{f}_i(\boldsymbol{\alpha}^{n-1}) = \sum_{j=1}^{N} w_i^{n-1}(j) * \phi(\left\|\boldsymbol{\alpha}^{n-1} - \hat{\boldsymbol{\alpha}}(j)\right\|), \quad i \in \{1, 2, \ldots, P) \tag{2.32}$$

where

- the vectors $\boldsymbol{\alpha}^{n-1}$ denote a complete set of POD coefficients for solution fields (for example velocity and pressure fields) at time step $n-1$, *i.e.* $\boldsymbol{\alpha}^{n-1} = (\alpha_1^{n-1}, \alpha_2^{n-1}, \ldots, \alpha_P^{n-1})^T$ with a dimensional size P;
- $w_i^{n-1}(j)$ is a weighting vector of size N (number of data points) to calculate for each POD coefficients α_i. Each data point has a dimension size of P;
- the vector $\hat{\boldsymbol{\alpha}}(j)$ (where $j \in 1, 2, \ldots, N$) are a set of N center points of the radial

basis functions. Where $\hat{\boldsymbol{\alpha}}(j) = (\hat{\alpha}_1(j), \hat{\alpha}_2(j), \ldots, \hat{\alpha}_P(j))^T$ with a dimensional size P. The center points are data points. In particular, those center points do not necessarily correspond to any of the data points (see Lowe (1988));

- $\|\boldsymbol{\alpha}^{n-1} - \hat{\boldsymbol{\alpha}}_j\|$ is a scalar distance defined by the L_2 norm. The norm is Euclidean distance;

- ϕ is a set of radial basis functions associated with different centers $\hat{\boldsymbol{\alpha}}$, and weighted by a coefficient w_i^{n-1}.

2.7.1.1 Calculation of the weights

In a scatter data interpolation problem, the weight coefficients w_i are determined so as to ensure that the interpolation function values $\hat{f}_i$ at the data points $\boldsymbol{\alpha}^{n-1}, k \in \{1, 2, \ldots, N_t\}$ match the given data $y(k)$ exactly, *i.e.*, $y(k) = \sum_{j=1}^{N} w_i^{n-1}(j) * \phi(\|\boldsymbol{\alpha}^{n-1} - \hat{\boldsymbol{\alpha}}(j)\|)$. This can be expressed by,

$$Aw_i = y, \tag{2.33}$$

where

$$A = \begin{bmatrix} \phi\left(\left\|\boldsymbol{\alpha}_1^{n-1} - \hat{\boldsymbol{\alpha}}_1\right\|_2\right) & \phi\left(\left\|\boldsymbol{\alpha}_1^{n-1} - \hat{\boldsymbol{\alpha}}_2\right\|_2\right) & \cdots \phi\left(\left\|\boldsymbol{\alpha}_1^{n-1} - \hat{\boldsymbol{\alpha}}_N\right\|_2\right) \\ \phi\left(\left\|\boldsymbol{\alpha}_2^{n-1} - \hat{\boldsymbol{\alpha}}_1\right\|_2\right) & \phi\left(\left\|\boldsymbol{\alpha}_2^{n-1} - \hat{\boldsymbol{\alpha}}_2\right\|_2\right) & \cdots \phi\left(\left\|\boldsymbol{\alpha}_2^{n-1} - \hat{\boldsymbol{\alpha}}_N\right\|_2\right) \\ \vdots & \vdots & \vdots \\ \phi\left(\left\|\boldsymbol{\alpha}_N^{n-1} - \hat{\boldsymbol{\alpha}}_1\right\|_2\right) & \phi\left(\left\|\boldsymbol{\alpha}_N^{n-1} - \hat{\boldsymbol{\alpha}}_2\right\|_2\right) & \cdots \phi\left(\left\|\boldsymbol{\alpha}_N^{n-1} - \hat{\boldsymbol{\alpha}}_N\right\|_2\right) \end{bmatrix}, \tag{2.34}$$

$$w_i^{n-1} = [w_i^{n-1}(1), w_i^{n-1}(2), \ldots, w_i^{n-1}(N)]^T, \tag{2.35}$$

$$y = [y(1), y(2), \ldots, y(N)]^T = [\alpha_1^n, \alpha_2^n, \ldots, \alpha_N^n]^T \tag{2.36}$$

The coefficients w_i^{n-1} are then determined by solving the linear system (2.33). N is the number of data points. It equals to time levels in the computational simulation N_t. The ϕ in equation (2.34) denotes the radial basis function.

2.7.1.2 Choice of radial basis functions

A radial basis function is a real-valued function whose value depends on the distance from the origin or other center point $\hat{\boldsymbol{\alpha}}$, so that $\phi(\boldsymbol{\alpha}) = \phi(\|\boldsymbol{\alpha}\|)$ or $\phi(\boldsymbol{\alpha}, \hat{\boldsymbol{\alpha}}) = \phi(\|\boldsymbol{\alpha} - \hat{\boldsymbol{\alpha}}\|)$. Any function ϕ that satisfies the property $\phi(\boldsymbol{\alpha}) = \phi(\|\boldsymbol{\alpha}\|)$ is a radial

function.

In this work any function ϕ that satisfies $\phi(\boldsymbol{\alpha}^{n-1}) = \phi\left(\|\boldsymbol{\alpha}^{n-1} - \hat{\boldsymbol{\alpha}}_j\|\right)$ can be chosen to be a radial function. The values of interpolation function $\hat{f}_i(\boldsymbol{\alpha}^{n-1})$ in (2.32) depend on the distance $r = \|\boldsymbol{\alpha}^{n-1} - \hat{\boldsymbol{\alpha}}(j)\|$ from the center $\hat{\boldsymbol{\alpha}}(j)$. A list of well-known RBFs ϕ is provided in table (2.2) (where r is a radius or the distance(here, $\sigma > 0$ is a shape parameter). In this work, the multi-quadratic function is chosen since it ensures the matrice A in Eq. (2.33) is non-singular and symmetric (see Powell (1992); Khattak *et al.* (2009); Dehghan & Shokri (2009)).

Table 2.2: Some well-known radial basis functions

Functions	definition
Gaussian (GA)	$\phi(r) = e^{-(r/\sigma)^2}$
Linear Spline	$\phi(r) = r$
Multi-Quadratic	$\phi(r) = \sqrt{r^2 + \sigma^2}$
Inverse Multistory	$\phi(r) = \frac{1}{\sqrt{r^2+\sigma^2}}$
Inverse Caddric	$\phi(r) = \frac{1}{r^2+\sigma^2}$
Cubic Spline	$\phi(r) = r^3$
Thin Plate Spline	$\phi(r) = r^2 log\, r$

2.7.2 RBF POD reduced order modelling

The RBF interpolation function in (2.32) denotes an n-dimensional hyper surface. Once a set of interpolation functions $\hat{f}_i$ is constructed, it is then used to estimate the POD coefficient α_i^n at time level n,

$$\alpha_i^n = \hat{f}_i(\boldsymbol{\alpha}^{n-1}), \quad i \in \{1, 2, \ldots P\}. \tag{2.37}$$

The input for each interpolation function $\hat{f}_i(\boldsymbol{\alpha}^{n-1})$ is the complete set of POD coefficients $\boldsymbol{\alpha}^{n-1} = (\alpha_1^{n-1}, \alpha_2^{n-1}, \ldots, \alpha_P^{n-1})$ at the previous times step $n-1$. The output of $\hat{f}_i(\boldsymbol{\alpha}^n)$ is the i^{th} POD coefficient $\boldsymbol{\alpha}^n$ at time step n. The whole procedure of RBF POD reduced order modelling can be algorithmically described as follows:

(a) Calculate the functional values $y = (y(1), y(2), \ldots, y(N))^T$ at a set of data points $\boldsymbol{\alpha}^{n-1}(k) = (\boldsymbol{\alpha}^{n-1}(1), \boldsymbol{\alpha}^{n-1}(2), \ldots, \boldsymbol{\alpha}^{n-1}(N))^T$ through the solution from the full models, where $k \in \{1, 2, \ldots N\}$;

(b) Find the weights $w_i(j)$ such that the interpolation function $\hat{f}_i(\boldsymbol{\alpha}^{n-1})$ in (2.37) goes through the data points $\boldsymbol{\alpha}^{n-1}(k)$, (here, $\boldsymbol{\alpha}^{n-1}(k) = (\boldsymbol{\alpha}^{n-1}(1), \boldsymbol{\alpha}^{n-1}(2), \ldots, \boldsymbol{\alpha}^{n-1}(N))^T, k \in \{1, 2, \ldots N\}$), *i.e.*, $y(k) = \hat{f}_i(\boldsymbol{\alpha}^{n-1}) = \sum_{j=1}^{N} w_i^{n-1}(j) * \phi(\|\boldsymbol{\alpha}^{n-1}(k) - \hat{\boldsymbol{\alpha}}(j)\|)$. The norm is Euclidean distance;

(c) Estimate the POD coefficient $\boldsymbol{\alpha}^c = (\alpha_1^c, \ldots, \alpha_P^c))$ of current time step using the RBF interpolation (2.37), where c denotes current time step, and P denotes the dimension of the problem;

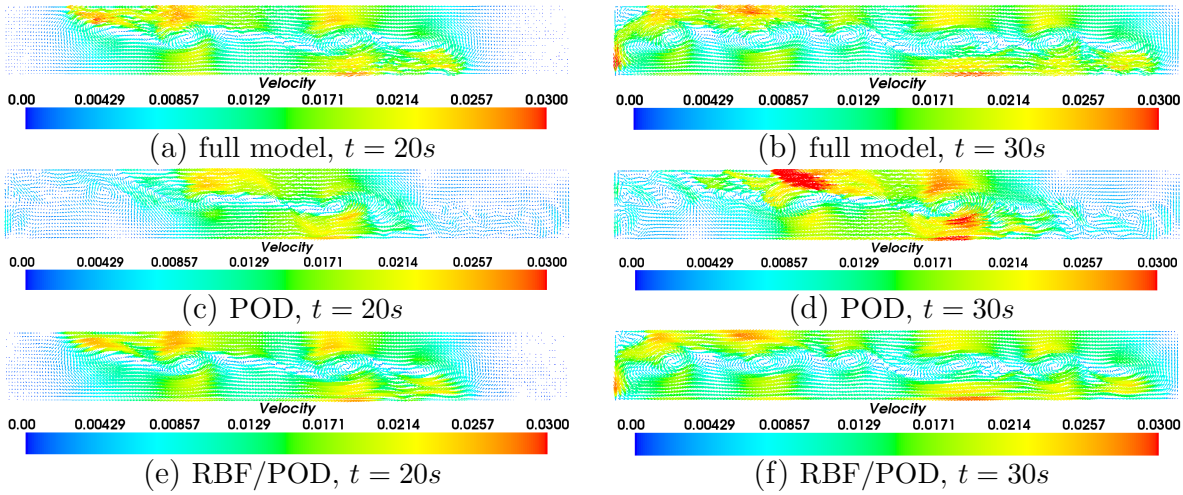
(d) Obtain the solution of variables $\mathbf{u}^{n+1}$ and $\mathbf{p}^{n+1}$ by projecting $\boldsymbol{\alpha}^c$ onto the full space (see (2.9)).

2.7.3 Numerical Examples of POD-RBF NIROM

An illustration of the use of the non-intrusive reduced order modelling scheme based on RBF is presented in this section. It consists of two test problems where the flow past a cylinder and lock exchange are resolved respectively. Both problems were initially solved in order to obtain a full solution, and the high fidelity solution was obtained using fluidity model that is formulated within a finite element framework (see Pain *et al.* (2005)). From these full model simulations the snapshots of the solution variables were taken. Using this snapshot data the reduced order models were then formed and used to re-solve the problems.

2.7.3.1 2-D Lock exchange

The first numerical example involves the simulation of 2-D lock-exchange, which consists of two fluids of different density, namely hot and cold fluids that are separated by a lock. Two gravity currents propagate horizontally along the tank when the lock is removed. This laboratory-scale set up incorporates dynamics observed in gravity currents over a range of scales (see Benjamin (1968)). The problem domain consists of a non-dimensional rectangle of the size 0.8×0.1. The initial condition for the non-dimensional temperature is T = 0.5 for the cold fluid at the left side of the lock and T = 0.5 for the hot fluid at the right side of the lock. The initial conditions for the velocity and pressure are $u = 0$ and $p = 0$ respectively. The isotropic value of viscosity is 1×10^{-10}. The Crank−Nicolson method is applied in the temporal discretisation. In this work the non-intrusive RBF/POD model is only considering the velocity and pressure variables. From the full model simulation, with a mesh of



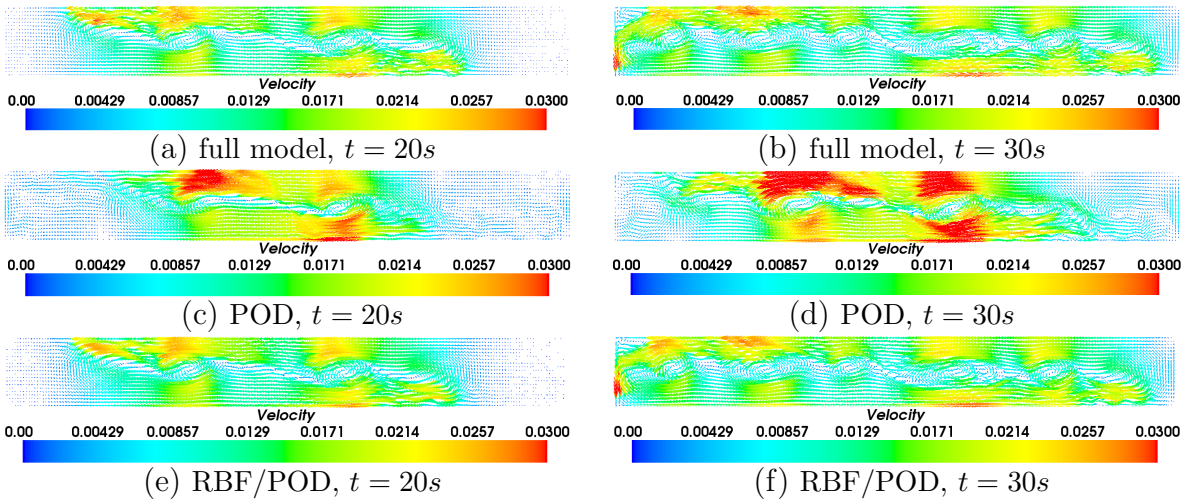
(a) full model, $t = 20s$ (b) full model, $t = 30s$

(c) POD, $t = 20s$ (d) POD, $t = 30s$

(e) RBF/POD, $t = 20s$ (f) RBF/POD, $t = 30s$

Figure 2.16: Lock exchange: the figures displayed above show the velocity solutions of the lock exchange problem at time instances 20 and 30 seconds. The solutions compare the predictions from RBF/POD model with full and POD model using 12 POD basis functions.

14271 nodes, 28000 elements and 1750 snapshots were obtained at regularly spaced time intervals $\Delta t = 0.02$ for each of the u, v and p solution variables, respectively. Figure 2.16, 2.17 and 2.18 show the solutions of the lock exchange problem at $t = 20s$ and $t = 30s$ respectively, as calculated using the full high fidelity model, the non-intrusive RBF/POD model, and the POD model using 12, 24 and 32 POD basis functions, respectively. The isotropic value of viscosity is taken to be 1×10^{-10}.
Figure 2.19 shows the velocity difference between full model and POD and RBF/-POD of the lock exchange problem at time instances 20.0 and 30.0 seconds using 24 POD basis. This indicates that the non-intrusive RBF/POD performs better than POD model.
Figure 2.20 shows the pressure solutions of the lock exchange problem at time instances 20 and 30 seconds. The solutions compare the predictions from RBF/POD model with full and POD models using 32 POD basis functions.
Figure 2.21 shows the solution velocities of the lock exchange case predicted by the full model, POD model and the RBF/POD model at a position (0.39801, 0.095). These results were obtained using a reduced order model with 12 and 32 POD basis functions, respectively.

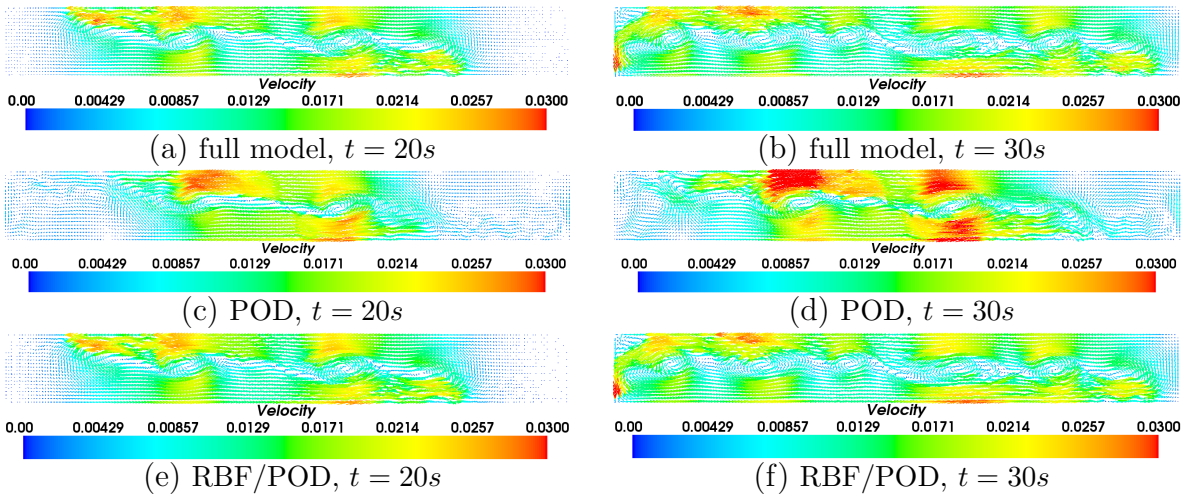


(a) full model, $t = 20s$ (b) full model, $t = 30s$

(c) POD, $t = 20s$ (d) POD, $t = 30s$

(e) RBF/POD, $t = 20s$ (f) RBF/POD, $t = 30s$

Figure 2.17: Lock exchange: the figures displayed above show the velocity solutions of the lock exchange problem at time instances 20 and 30 seconds. The solutions compare the predictions from RBF/POD model with full and POD model using 24 POD basis functions.

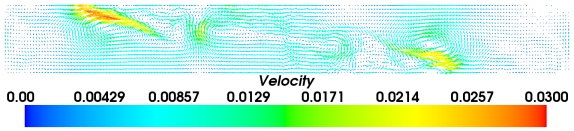


(a) full model, $t = 20s$ (b) full model, $t = 30s$

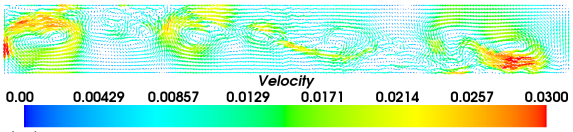
(c) POD, $t = 20s$ (d) POD, $t = 30s$

(e) RBF/POD, $t = 20s$ (f) RBF/POD, $t = 30s$

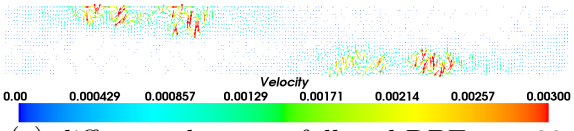
Figure 2.18: Lock exchange: the figures displayed above show the velocity solutions of the lock exchange problem at time instances 20 and 30 seconds. The solutions compare the predictions from RBF/POD model with full and POD model using 32 POD basis functions.



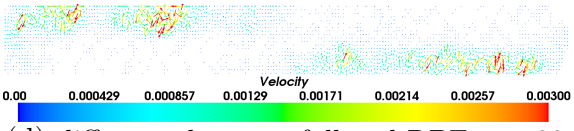
(a) difference between full and POD, $t = 20s$



(b) difference between full and POD, $t = 30s$

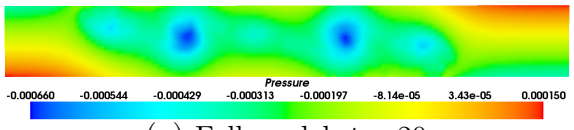


(c) difference between full and RBF, $t = 20s$

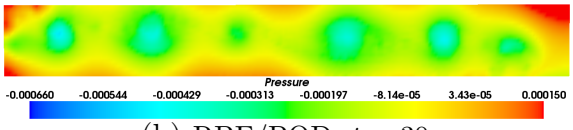


(d) difference between full and RBF, $t = 30s$

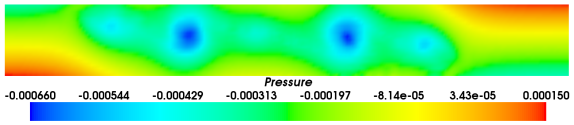
Figure 2.19: Lock exchange: the figures displayed above show the velocity difference between full model and POD and RBF/POD of the lock exchange problem at time instances 20.0 and 30.0 seconds using 24 POD basis



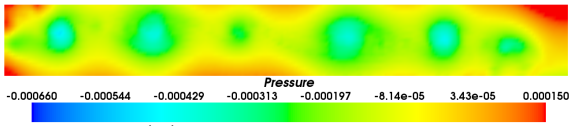
(a) Full model, $t = 20s$



(b) RBF/POD, $t = 30s$



(c) Full model, $t = 20s$



(d) RBF/POD, $t = 30s$

Figure 2.20: Lock exchange: the figures displayed above show the pressure solutions of the lock exchange problem at time instances 20 and 30 seconds. The solutions compare the predictions from RBF/POD model with full and POD model using 32 POD basis functions.

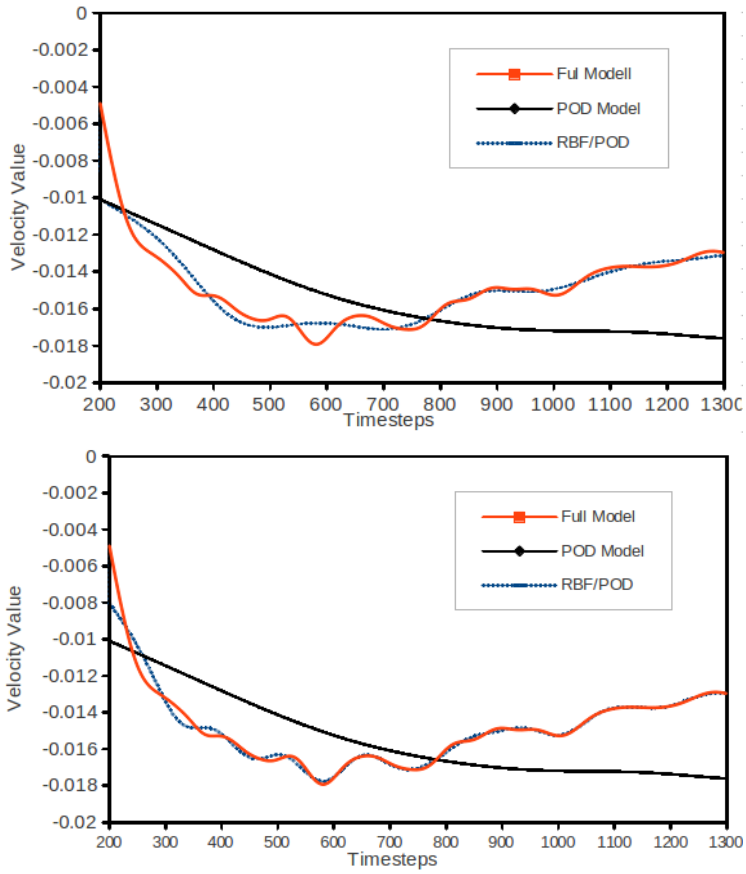


Figure 2.21: Lock exchange: the graphs shows the solution velocities of the lock exchange case predicted by the full model, POD model and the RBF/POD model at a position (0.39801, 0.095). These results were obtained using a reduced order model with 12 and 32 POD functions respectively.

2.7.3.2 Flow past a cylinder

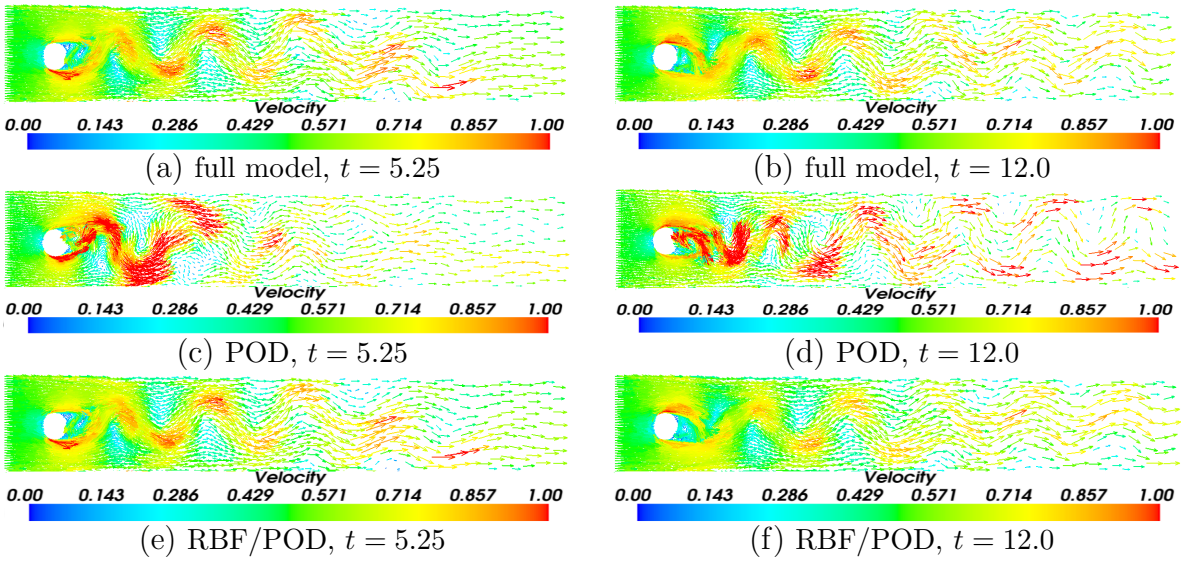
In the second numerical example a two dimensional flow past a cylinder is simulated. The problem domain is 2 non-dimensional units in length and 0.4 non-dimensional units in width, and it contains a cylinder of radius 0.12 units at location (0.2, 0.2). The dynamics of the fluid flow are driven by an in-flowing liquid with velocity 1 unit/sec, and this enters the domain through the left boundary.The fluid is allowed to flow past the cylinder and out of the domain through the right boundary. No slip and zero outward flow conditions are applied to the upper and lower edges of the problem whilst Dirichlet boundary conditions are applied to the cylinder's wall. The properties of the fluid are such that the Reynolds number for this problem is calculated to be $Re = 5000$.

The problem was simulated for a period of 10 seconds$[2s - 12s]$, and for all models a time step size of $\Delta t = 0.001$ was used. From the full model simulation, with a mesh of 3213 nodes, 1000 snapshots were obtained at equal time intervals for each of the u, v and p solution variables between the period 2s to 12s.

Figures 2.22 and 2.23 present the simulated flow patterns at time instances 5.25 and 12.0 seconds. They compare the high fidelity model against reduced order models (POD model and RBF/POD model). In each of the figures the number of POD functions used in the simulation increases from 24 to 35 functions. It is can be seen that the non-intrusive ROM based on RBF interpolation performs well. In addition, the magnitude of the non-intrusive ROM profiles appears to be in close agreement to the high fidelity solutions. This is highlighted in the graphs presented in figure 2.24 which show the solution velocities at a point in the domain.

Figure 2.25 shows the RMSE between the full model and the non-intrusive model, which means the solutions of the non-intrusive model are in close agreement with the high-fidelity full model solutions. Figure 2.26 shows the correlation coefficient between the full model and the non-intrusive model; this indicates that the full model and the non-intrusive model are highly correlated.

Table 2.3 shows a comparison of CPU (unit: s) required for running the full model and non-intrusive RBF/POD ROM for each time step. It can be seen that the non-intrusive ROM is CPU time efficient, since it does not involve assembling and solving the matrices process, thus resulting in a speed-up of CPU time of two to three orders of magnitude in these two cases. The most time consuming process in RBF interpolation lies in obtaining the weights w_i in (2.33). The flow past a cylinder



(a) full model, $t = 5.25$ (b) full model, $t = 12.0$

(c) POD, $t = 5.25$ (d) POD, $t = 12.0$

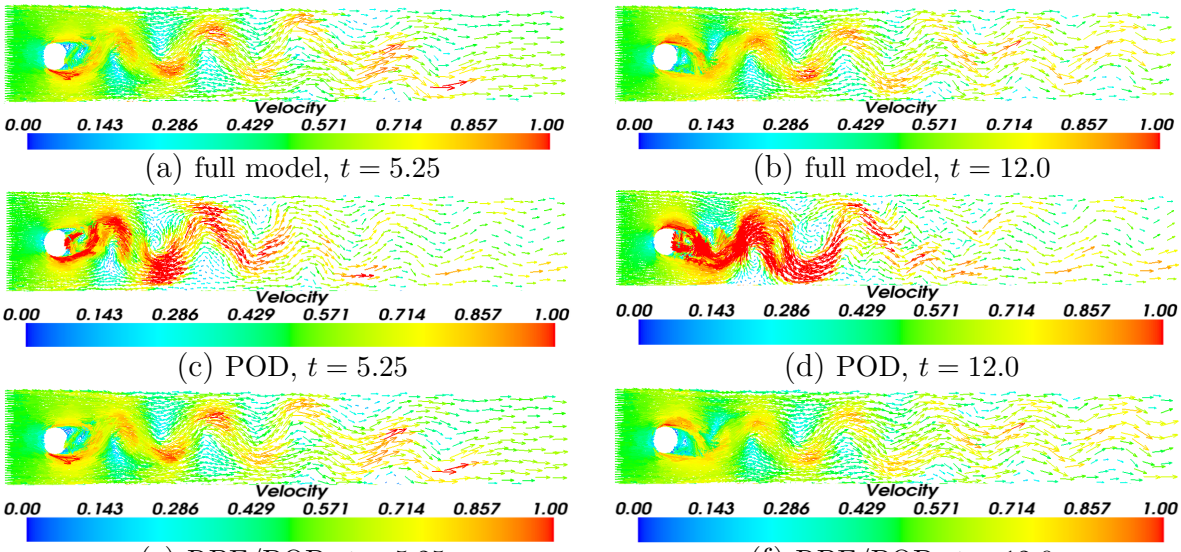
(e) RBF/POD, $t = 5.25$ (f) RBF/POD, $t = 12.0$

Figure 2.22: Flow past a cylinder: the figures displayed above show the solutions of the flow past a cylinder problem at time instances 5.25 and 12.0 seconds. The solutions compare the predictions from RBF/POD model with full and POD model using 24 POD basis functions.

takes 0.201s to obtain the weights. This process is precomputed alongside construction of the interpolation functions $\hat{f}_i(\boldsymbol{\alpha}^{n-1})$ in (2.37), which means the process is not involved when calculating current POD coefficients through the interpolation functions$\hat{f}_i(\boldsymbol{\alpha}^{n-1})$.

From the two cases illustrated above, it is clear that the non-intrusive ROM based on RBF interpolation performs better than traditional POD since RBF interpolation method can provide spectral convergence rates (see Madych (1992); Buhmann & Dyn (1993)) and is capable of capturing the non-linearity in dynamic system (see Mokhasi & Rempfer (2010)).

In order to compare those three NIROMs, the velocity solutions predicted by all reduced order models and the high fidelity full model at the position (0.19397, 0.28101) on the domain are given in figure 2.27. The figure shows that both NIROM with Smolyak sparse grid and NIROM with RBF perform closely to the full model. The NIROM with RBF has slightly more accurate results than the that of the NIROM with Smolyak sparse grid in this case. The advantage of the Smolyak sparse grid lies in its ability to tackle the 'curse of dimensionality'. This advantage can be used to reduce the number of training simulations for varying parameter problems. The varying parameter problem will be discussed in chapters 7 and 8.



(a) full model, $t = 5.25$ (b) full model, $t = 12.0$

(c) POD, $t = 5.25$ (d) POD, $t = 12.0$

(e) RBF/POD, $t = 5.25$ (f) RBF/POD, $t = 12.0$

Figure 2.23: Flow past a cylinder: the figures displayed above show the solutions of the flow past a cylinder problem at time instances 5.25 and 12.0 seconds. The solutions compare the predictions from RBF/POD model with full and POD model using 35 POD basis functions.

2.8 Conclusions

In this chapter three new non-intrusive reduced order methods are presented. Those methods are based on POD methodologies where optimal basis functions are generated through the method of snapshots. However rather than using a standard Galerkin projection ROM approach (code intrusive), the three approaches based on the Smolyak sparse grid interpolation method, radial basis function method and on a second order Taylor series expansion, are employed to calculate the POD coefficients. The smolyak sparse grid method and radial basis function method construct a set of hyper-surfaces that replace the governing equations within the reduced space. The other method uses a second order Taylor expansion to capture the quadratic non-linearities in the Navier-Stokes equations. The benefits of the non-intrusive model reduction approaches presented here is that they do not require any modifications to the source code, due to the fact that they are independent of the equation of the system, and simply work from a number of snapshots of the full solution.

The methods have been numerically compared against a finite element unstructured adaptive mesh fluid model (FLUIDITY) on three flow problems. The three problems were based on the simulation of flow past a cylinder, lock exchange and wind driven

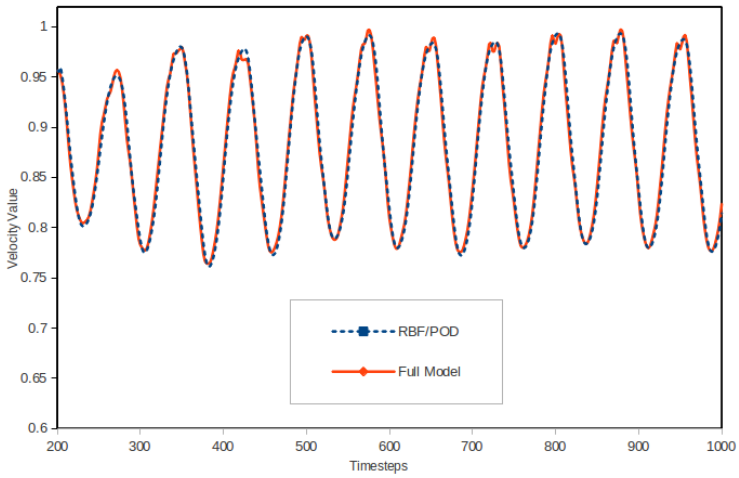


Figure 2.24: Flow past a cylinder: the graphs shows the solution velocities of the flow past a cylinder case predicted by the full model, and the RBF/POD model at a position(0.2029, 0.26535). These results were obtained using a reduced order model with 24 POD functions

Table 2.3: Comparison of CPU (unit: s) required for running the full model and ROM for each time step

Cases	Model	assembling	solving	projection	interpolation	total
Lock exchange	Full model	1.4960	0.488000	0.000	0	1.98400
	POD ROM	0.1600	0.000000	0.008	0	0.16800
	RBF/POD	0.0000	0.000000	0.003	0.001	0.00400
Flow past a cylinder	Full model	3.00373	0.112598	0.000	0	3.116328
	POD ROM	0.30280	0.000000	0.008	0	0.322700
	RBF/POD	0.00000	0.000000	0.003	0.001	0.00400

gyre, respectively. The non-intrusive methods gave accurate solutions for modelling flow problems. It is demonstrated that accuracy of solutions from the non-intrusive models is maintained whilst online CPU times are reduced by several orders of magnitude in comparison to high fidelity models. However, for higher Reynolds numbers the Smolyak method and radial basis function method were shown to be more robust in maintaining accuracy for resolving the more complex flows. In the following chapter, the capability of NIROM with Smolyak sparse grid will be shown using more complicated applications : free surface problems. Then, in the other applications, NIROM with RBF will be used more frequently in terms of its accuracy. An error analysis has also been carried out for the validation and accuracy assessment of the newly non-intrusive models. The non-intrusive Smolyak sparse grid model and ra-

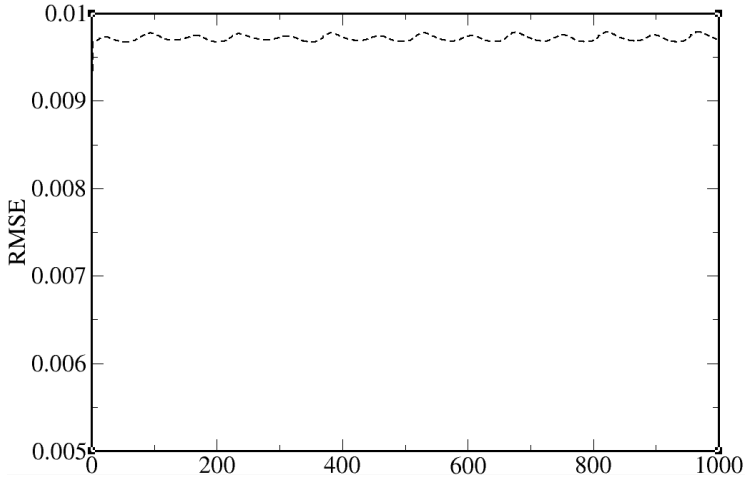


Figure 2.25: Flow past a cylinder: the graph shows the RMSE errors calculated for the RBF/POD model for the flow past a cylinder.

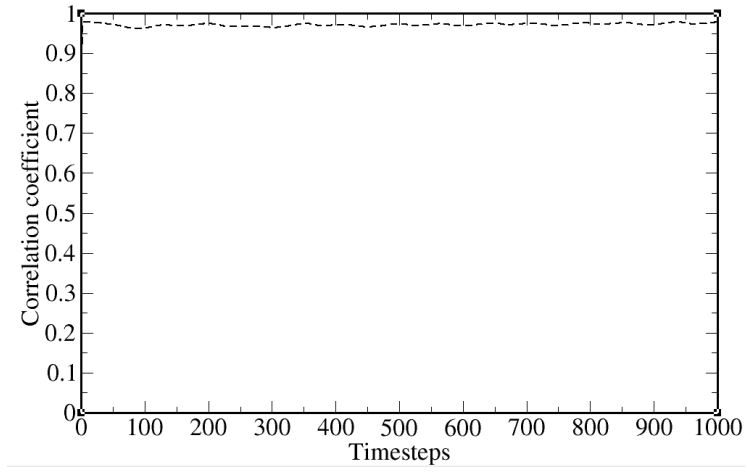


Figure 2.26: Flow past a cylinder: the graph shows the correlation coefficient calculated for the RBF/POD model for the flow past a cylinder.

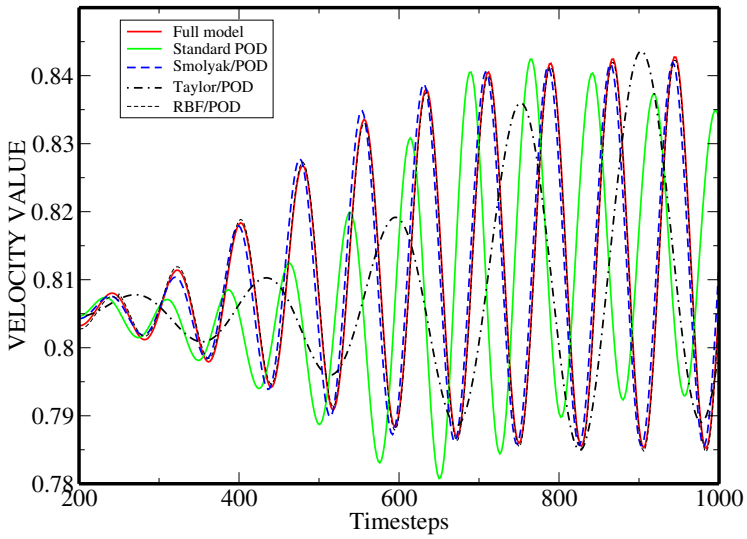


Figure 2.27: Flow past a cylinder: The graphs shows the solution velocities predicted by the full model, POD model, Taylor expansion method, Smolyak sparse grid NIROM and the RBF NIROM at positions: 0.19397,0.28101, Re=400. 12 POD basis functions were used in NIROMs.

dial basis function model exhibit an overall good agreement with the full model. It can be also seen that an increase in the number of POD bases leads an improvement in the accuracy of the POD model.

Chapter

THREE

Non-intrusive Reduced Order Modeling for multi-scale free surface flows

3.1 Abstract

In this chapter, we describe a novel non-intrusive reduction model for three-dimensional (3D) free surface flows. By using the new NIROM based on Smolyak sparse grid method, we have developed a robust and efficient reduced order model for free surface flows. What distinguishes the reduced order model developed here from other existing reduced order ocean models is (1) the inclusion of 3D dynamics with a free surface (moving movement); (2) the incorporation of wetting-drying; and (3) the first implementation of non-intrusive reduced order method in ocean modelling. Most importantly, the change of the computational domain with free surface movement is taken into account in reduced order modelling. The capabilities of the new non-intrusive free surface flow ROM have been demonstrated in Balzano and Okushiri tsunami test cases. Results obtained show that the accuracy of free surface problems relative to the high fidelity model is maintained in NIROM whilst the CPU time is reduced by several orders of magnitude in comparison to the high fidelity models.

This chapter is derived from and expands upon Xiao *et al.* (2015a).

3.2 Introduction

The work in this chapter, for the first time, constructs a non-intrusive ROM for free surface flows in the framework of an unstructured mesh finite element ocean model. This is achieved by using the Smolyak sparse grid interpolation method. As discussed earlier, the Smolyak sparse grid method is a widely used interpolation method and is used to overcome the curse of dimensionality. Apart from that, it is also used for uncertainty quantification for electromagnetic devices. For example, Sumant *et al.* (2012) used the Smolyak sparse grid to calculate statistically varying material and geometric parameters which are the inputs of the ROM. Xiao *et al.* (2015d) also used Smolyak sparse grid to construct a ROM and it has been shown to be a promising non-intrusive method for representing complex physical system using a set of hyper-surface interpolating functions.

In the work described in this chapter, the newly presented NIROM method based on Smolyak sparse grid (see Xiao *et al.* (2015d)) is applied to complex ocean free surface flows. Two free surface test cases: Balzano test case and Okushiri tsunami test case are numerically tested and illustrated. The solutions from the full fidelity ocean model are recorded as a sequence of snapshots, and from these snapshots appropriate basis functions are generated that optimally represent the three-dimensional (3D) free surface problem. The Smolyak sparse grid interpolation method is then used to form a set of hyper-surfaces that represent the ROM. Once a set of hyper-surfaces has been constructed, the POD coefficient at current time level can be obtained by providing the POD coefficients at previous time levels to the hyper-surface. Numerical comparisons between the high fidelity model and this NIROM are made to investigate the accuracy of this novel NIROM for free surface flows.

The structure of the chapter is as follows. Section 3.3 presents the governing equations of free surface flows. Section 3.4 presents the derivation of the POD model reduction and re-formulation of the governing equations using the Smolyak sparse grid method. Section 3.5 illustrates the methodology derived above via two numerical examples. This is based on two test problems where the Balzano test case and Okushiri tsunami test case are numerically simulated. Finally in section 3.6 con-

clusions are presented and the novelty of the manuscript is fully summarized and illuminated.

3.3 Three Dimensional Governing Equations

3.3.1 Continuous governing equations and free surface boundary conditions

The three dimensional incompressible Navier-Stokes equations with Boussinesq approximation and the conservative equation of mass are used in this work, see equations 2.1a and 2.1b.

The no-normal flow boundary condition is applied on the bottom and sides of the computational domain:

$$\mathbf{u} \cdot \vec{n} = 0, \tag{3.1}$$

where $\vec{n}$ denotes the unit normal vector on boundary surface.

The free surface kinematic free surface boundary condition is expressed as follows:

$$\frac{\partial \eta}{\partial t} = -\left.\mathbf{u}_H\right|_{z=\eta} \cdot \nabla_H \eta + \left. u_z \right|_{z=\eta} \quad \text{on} \quad \partial\Omega_s, \tag{3.2}$$

where η is the free surface elevation, $\partial\Omega_s \subset \partial\Omega$ is the free surface boundary, $\nabla_H \equiv (\partial/\partial x, \partial/\partial y)^T$, and $\mathbf{u}_H$ is the horizontal component of $\mathbf{u}$. Using the fact that the normal vector $\vec{n}$ at the free surface is $\frac{(-\frac{\partial \eta}{\partial x}, -\frac{\partial \eta}{\partial y}, 1)^T}{||(-\frac{\partial \eta}{\partial x}, -\frac{\partial \eta}{\partial y}, 1)^T||}$, equation (3.2) can be reformulated to

$$\frac{\partial \eta}{\partial t} = \frac{\mathbf{u} \cdot \vec{n}}{\vec{n} \cdot \vec{k}}, \tag{3.3}$$

where $\vec{k} = (0, 0, 1)$ is the vertical standard basis vector. Note that in spherical geometries $\vec{k}$ is replaced with $\vec{r} = (\sin\theta\cos\phi, \sin\theta\sin\phi, \cos\theta)$ where ϕ and θ are the azimuthal and co-latitudinal angles respectively.

Taking into account $p = \rho_0 g \eta$ on the free surface $\partial\Omega_s$, gives the combining kinematic free surface boundary condition:

$$\vec{n} \cdot \vec{k} \frac{1}{\rho_0 g} \frac{\partial p}{\partial t} = \vec{n} \cdot \mathbf{u}. \tag{3.4}$$

3.3.2 Discretisation of free surface equations

The previous section introduced the continuous governing equations. This section describes the discretisation form of the governing equations. In a finite element expansion, the velocity components and pressure terms of the solution are represented:

$$u_x = \sum_j^{\mathcal{N}} N_j u_{xj}, \;\; u_y = \sum_j^{\mathcal{N}} N_j u_{yj}, \;\; u_z = \sum_j^{\mathcal{N}} N_j u_{zj}, \tag{3.5}$$

and

$$p = \sum_j^{\mathcal{M}} M_j p_j, \tag{3.6}$$

respectively, where N_j and M_j denote the finite element basis functions. By multiplying equations (2.1a) and (2.1b) by M_i and N_i, respectively, and integrating over space, the discretised equations are formed:

$$\int_\Omega M_i \nabla \cdot \mathbf{u} \; d\Omega = 0, \tag{3.7}$$

$$\int_\Omega N_i \left(\frac{\partial \mathbf{u}}{\partial t} + \mathbf{u} \cdot \nabla \mathbf{u} + f\vec{k} \times \mathbf{u} + \nabla p - \nabla \cdot \tau \right) \; d\Omega = 0. \tag{3.8}$$

In the momentum equation the time term is treated using the θ-method. By substituting (3.5) and (3.6) into the above equations, the discrete equations at time level $n+1$ are formed:

$$C^T \mathbf{u}^{n+1} = 0, \tag{3.9}$$

$$N \frac{\mathbf{u}^{n+1} - \mathbf{u}^n}{\Delta t} + A(\mathbf{u}^n)\mathbf{u}^{n+\theta} + K\mathbf{u}^{n+\theta} + C\mathbf{p}^{n+1} = \mathbf{s}^n, \tag{3.10}$$

where the matrix C denotes the pressure gradient matrix, the vectors $\mathbf{u}$ and $\mathbf{p}$ consist of solutions of velocity and pressure components at nodes respectively, N is the mass matrix involving the finite element basis functions N_i, $A(u^n)$ is the solution dependent discretised streaming operator, K is the matrix related to the rest of the linear terms of velocity, and $\mathbf{s}$ is the vector accounting for the forces acting upon the solution, where $\theta \in [0, 1]$ and the terms $\mathbf{u}^{n+\theta}$ is given by,

$$\mathbf{u}^{n+\theta} = \theta \mathbf{u}^{n+1} + (1-\theta)\mathbf{u}^n. \tag{3.11}$$

The discrete form of free surface equation (3.4) is written:

$$M_s \frac{\mathbf{p}^{n+1} - \mathbf{p}^n}{g\Delta t} = G\mathbf{u}^{n+1}, \tag{3.12}$$

where $M_{s,ij} = \int_{\partial\Omega_s} \vec{k} M_i M_j d\Omega$ and $G_{ij} = \int_{\partial\Omega_s} \vec{n} \cdot \mathbf{u} N_i M_j d\Omega$.

Taking into account the free surface kinematic boundary condition (3.12), the discrete continuity equation (3.9) can be re-written:

$$C^T \mathbf{u}^{n+1} + G\mathbf{u}^{n+1} = 0, \tag{3.13}$$

that is

$$C^T \mathbf{u}^{n+1} + M_s \frac{\mathbf{p}^{n+1} - \mathbf{p}^n}{g\Delta t} = 0. \tag{3.14}$$

3.4 Construction NIROM for free surface flows using Smolyak sparse grid

The process of constructing the NIROM for free surface flows using the Smolyak sparse grid interpolation method is derived in this section. The core of this method lies in constructing a set of Smolyak interpolation functions ($\hat{f}_j, j \in \{1, 2, \ldots m\}$), which has the form of

$$\alpha_j^{n+1} = \hat{f}_j(\alpha_1^n, \alpha_2^n, \ldots, \alpha_m^n), \quad j \in \{1, 2, \ldots m\}, \tag{3.15}$$

where m is the number of POD bases. The input variables of the Smolyak interpolation function ($\hat{f}_j$) is complete set of POD coefficients $\alpha^n = (\alpha_1^n, \alpha_2^n, \ldots, \alpha_m^n)$ at the previous times step n. The output of the Smolyak interpolation function ($\hat{f}_j$) is the j^{th} POD coefficient α^{n+1} at time step $n+1$. For more details of constructing non-intrusive ROM using Smolyak sparse grid method, see (Xiao *et al.* (2015d)). Algorithm (1) outlines the steps of constructing the NIROM for free surface flows.

In algorithm (1), the interpolation function values need to be determined only at the Smolyak sparse grid nodes rather than on the full tensor product grid, thus resulting in an impressive computational economy.

Algorithm 1: POD-Smolyak NIROM algorithm for free surface flows

(1) Generate the snapshots over the time period$[1 - N_t]$ by running the full model;

(2) Obtain the POD bases Φ_u and Φ_p using the POD method;

(3) Generate a set of Smolyak sparse nodes $\alpha^{r,0} = (\alpha_1^{r,0}, \alpha_2^{r,0}, \ldots, \alpha_m^{r,0})$ (where $r \in \{1, 2, \ldots, R\}$, R is the number of sparse points to be chosen) at the full tensor product grid:
$[A_{min}, A_{max}] = [\alpha_{1,min}, \alpha_{1,max}] \cdots \otimes [\alpha_{j,min}, \alpha_{j,max}] \cdots \otimes [\alpha_{m,min}, \alpha_{m,max}]$, where $\alpha_{j,min}$ and $\alpha_{j,max}$ are the minimum and maximum values of the j^{th} POD coefficient;

(4) Obtain the function values $\alpha_j^{r,1} = f_j(\alpha^{r,0})$ associated with the Smolyak sparse nodes through running the full model one time step:

for $n = 1$ *to* R **do**

(i) Determine the initial condition $\psi^{r,0}$ for the full model by projecting $\alpha^{r,0}$ onto the full space, where ψ denotes any variable in the full model, for example, the velocity components u_x, u_y and u_z, and the pressure p;

(ii) Determine the full solution $\psi^{r,1}$ by running the full model one time level;

(iii) Calculate the function value $\alpha_j^{r,1}$ at sparse point r by projecting $\psi^{r,1}$ onto the reduced order space;

end for

(5) Give a set of $\alpha_j^{r,1}$, and then construct the interpolation function $\hat{f}_j(q, d)$, $j \in \{1, 2, \ldots, m\}$ using (2.25);

(6) Initialize $\alpha_u^{r,0}$ and $\alpha_p^{r,0}$, and give them to the interpolation function $\hat{f}_j$, $j \in \{1, 2, \ldots, m\}$ to obtain solutions for current time step using online algorithm (2).

Algorithm 2: Online calculation of POD coefficients of NIROM for free surface flows

(1) Initialize ${\alpha_u}^{r,0}$ and ${\alpha_p}^{r,0}$;

(2) Calculate solutions for current time step using following loop: ;

for $n = 1$ *to* N_t **do**
for $j = 1$ *to* m **do**
Calculate the solution (POD coefficients $\alpha^n_{u,r,j}$ and $\alpha^n_{p,r,j}$) at current time step by ${\alpha_j}^n = \hat{f}_j({\alpha_1}^{n-1}, {\alpha_2}^{n-1}, \ldots, {\alpha_m}^{n-1})$
end for

(i) Calculation of velocity components and pressure (u^n_x, u^n_y, u^n_z and p^n_x) by projecting α^n_j onto the full space,
$u^n_x = \overline{u}^x + \Phi^x \alpha^{x,n}$, $u^n_y = \overline{u}^y + \Phi^y \alpha^{y,n}$, $u^n_z = \overline{u}^z + \Phi^z \alpha^{z,n}$, $p^n = \overline{p}^p + \Phi^p \alpha^{p,n}$.

(ii) Updating of the free surface values at all nodes and 3D mesh locations (keeping the coordinates of x and y unchanged, replace the z-direction with the new free surface value at each node).

end for

3.5 Numerical Examples

The capability of the new non-intrusive reduced order model for 3D free surface flows has been evaluated in this section. This is based on two numerical test problems: the Balzano test case and Okushiri tsunami test case (see Funke *et al.* (2011)). Evaluation of accuracy of the POD model was carried out through comparison of POD solutions with those from the full model. The high fidelity full model solutions were obtained through the use of FLUIDITY Pain *et al.* (2005)). From these full model simulations the snapshots of the solution variables were taken. Using this snapshot data the reduced order models were then formed and used to re-solve the problems.

3.5.1 Balzano test cases

The first example used for validation of the new 3D free surface model was the Balzano test case (see Balzano (1998)) for benchmarking different wetting and drying methods. The problem domain consists of slope with size of 13.8 km $\times$ 1 km and a depth of zero meter at one end and five meters at the other end (see figure 3.1). No normal flow boundary conditions are applied at both sides, the bottom and the shallow end of the slope. A Manning−Strickler drag with n= $0.02sm^{\frac{1}{3}}$ is applied at the bottom. The gravity is $9.81ms^{-2}$.

The problem was simulated for a period of 50000 seconds, and a time step size of $\Delta t = 500s$ was used. From the full simulation by running FLUIDITY, with an unstructured finite element mesh of 180 nodes, 100 snapshots were obtained at equally spaced time intervals for each of the u_x, u_y and p solution variables during the simulation period. A $P_1 - P_1$ finite element pair was used.

Figure 3.2 shows the singular eigenvalues in decreasing order. It can be seen that the singular eigenvalue curve decreases drastically between the first two leading POD bases, *i.e.* satisfying Kolmogorov condition. In this case, only three POD bases with 100 snapshots are capable of capturing 98% of 'energy' in the original flow dynamic system. The first six POD bases are shown in figure 3.3. Again, most of flow wave features are captured within the first six leading POD bases. In this work, two and six POD bases were chosen to generate the reduced order model using the Smolyak sparse grid method described above.



Figure 3.1: Balzano case: The computational domain and mesh used in Balzano case.

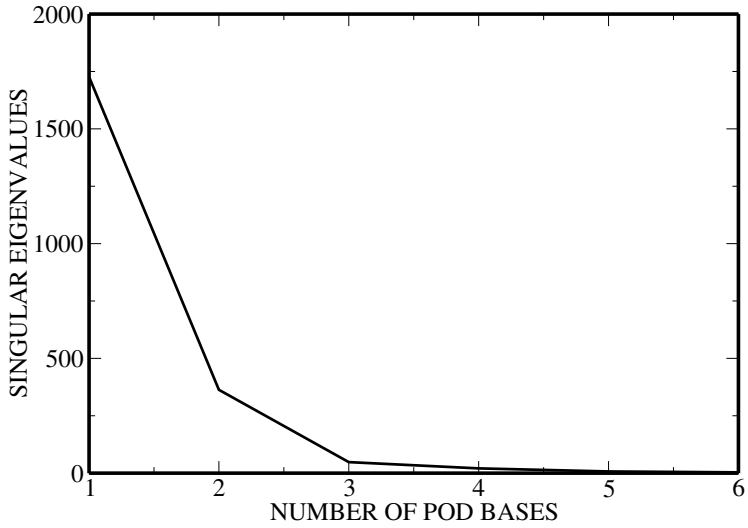
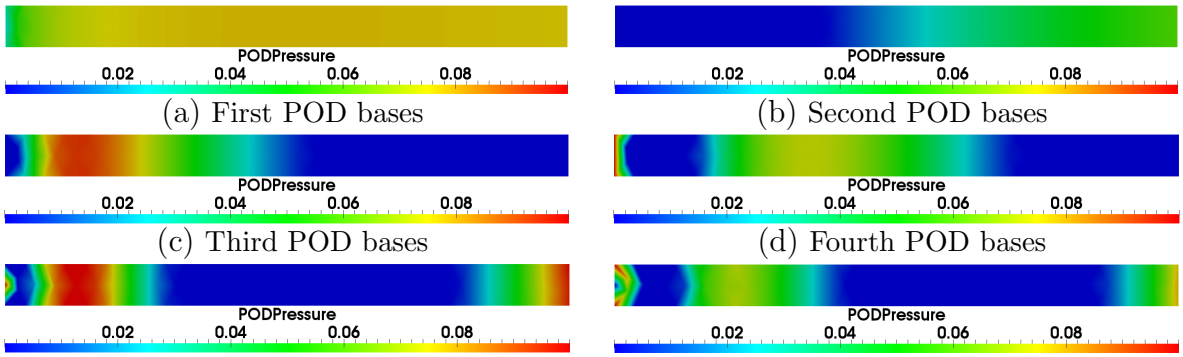


Figure 3.2: Balzano case: the graphs shows the singular eigenvalues in order of decreasing magnitude

Figure 3.4 shows the solutions of pressure from the full model and NIROM using 2 and 6 POD bases at time instances 10.2 and 25. A good agreement is achieved between the high fidelity full solutions and reduced order results. To further estimate the accuracy of NIROM, the pressure solutions at a particular location ($x = 296.8$, $y = 686.25$, $z = 0$) within the domain (black point in figure 3.1) are plotted in figure 3.5. Again, it can be seen that the results of NIROM with both 2 and 6 POD bases are in agreement with those from the full model.

To evaluate the accuracy of NIROM solutions, figure 3.6 shows the error of pressure solutions between the full model and NIROM with 2 and 6 POD bases at time instances 10.2 and 25 seconds. It is shown that the error of pressure solutions from NIROM using 6 POD bases is smaller than that using 2 POD bases. The error of pressure solutions is further analysed by RMSE and correlation coefficient. The RMSE and correlation coefficient of pressure solutions are given in figure 3.7 and 3.8 respectively, which shows the accuracy of NIROM is improved by increasing the number of POD bases.

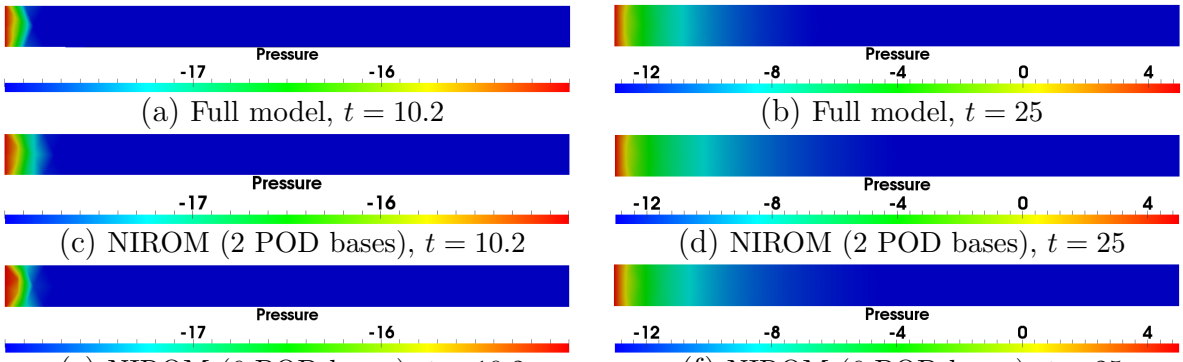


(a) First POD bases (b) Second POD bases

(c) Third POD bases (d) Fourth POD bases

(e) Fifth POD bases (f) Sixth POD bases

Figure 3.3: Balzano case: the figures show the first 6 POD bases functions for pressure.



(a) Full model, $t = 10.2$ (b) Full model, $t = 25$

(c) NIROM (2 POD bases), $t = 10.2$ (d) NIROM (2 POD bases), $t = 25$

(e) NIROM (6 POD bases), $t = 10.2$ (f) NIROM (6 POD bases), $t = 25$

Figure 3.4: Balzano case: The solutions of pressure from the full model and NIROM at time instances 10.2 (left panel) and 25 (right panel). Top panel: the full model; middle panel: NIROM using 2 POD bases; and bottom panel: NIROM using 6 POD bases.

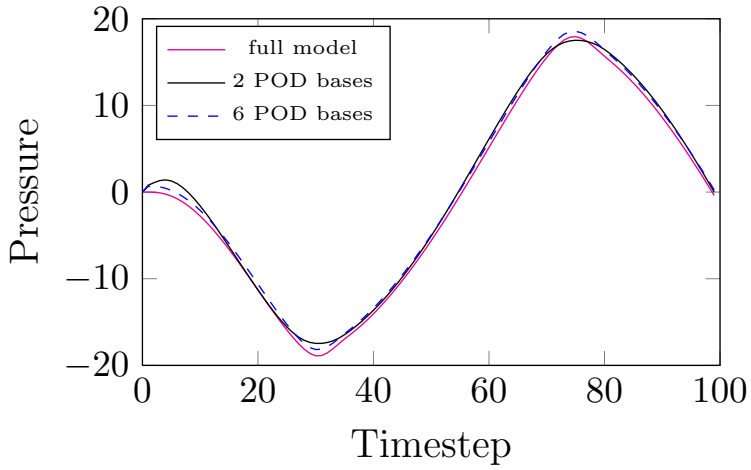
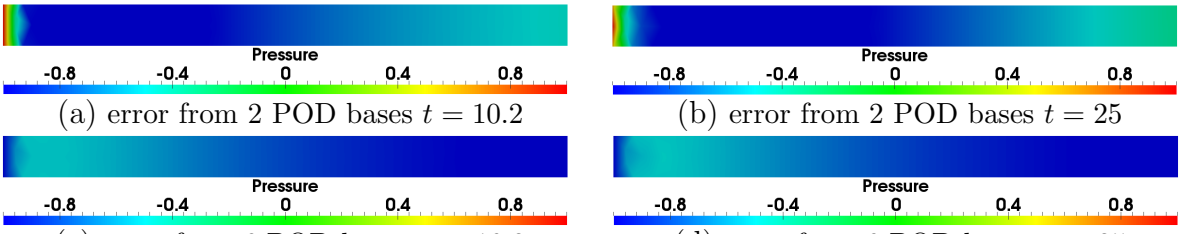


Figure 3.5: Balzano case: The pressure solutions from the full model and NIROM at location: $(x = 296.8, y = 686.25, z = 0)$.



(a) error from 2 POD bases $t = 10.2$

(b) error from 2 POD bases $t = 25$

(c) error from 6 POD bases, $t = 10.2$

(d) error from 6 POD bases, $t = 25$

Figure 3.6: Balzano case: the error of pressure solutions between the full model and NIROM, using 2 and 6 POD bases at time instances 10.2 (left panel) and 25 (right panel).

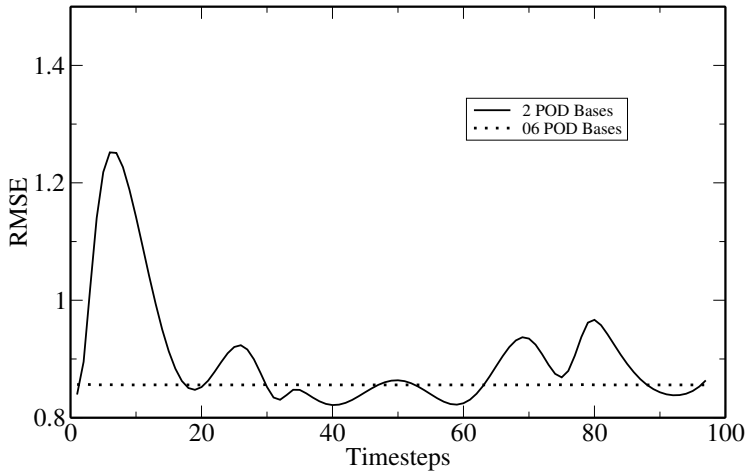


Figure 3.7: Balzano case: The RMSE errors of pressure solutions between the full high fidelity and non-intrusive reduced order models.

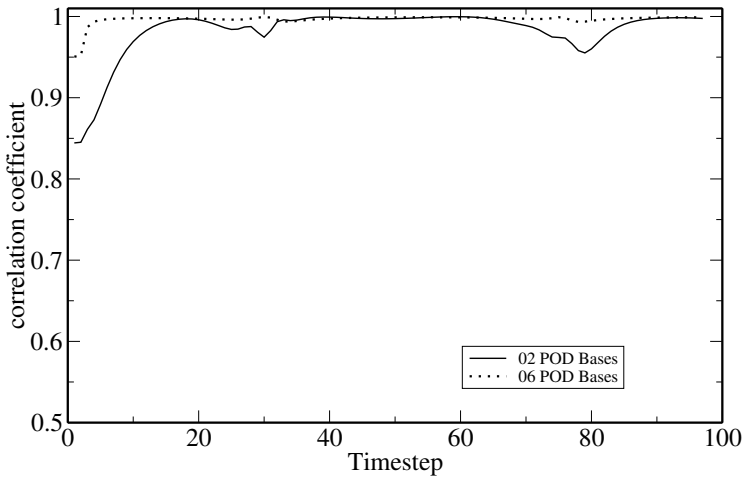


Figure 3.8: Balzano case: The correlation coefficient of pressure solutions between the full and non-intrusive reduced order models.

3.5.2 Okushiri tsunami test case

The second case is a Okushiri tsunami test case. In 1993, the Okushiri tsunami generated huge run-up heights of almost 30 meters in Okushiri, Japan. A $P_1 - P_1$ finite element pair is used to solve the equations. The computational domain is $5.448\,m \times 3.402\,m$ in horizontal and the free surface is extruded to the bathymetry and coastal topography in vertical (see figure 3.9). A water height representing a tsunami wave is imposed to the left boundary and no normal flow boundary conditions are enforced to the bottom and other sides resembling the solid boundaries. The threshold value of wetting and drying (d_0) is set to be $0.5\,mm$ in dry area to prevent non-physical flows in numerical simulation. The isotropic kinematic viscosity is set to be 0.0025 $m^2 s^{-1}$. The acceleration of gravity magnitude is $9.81\,ms^{-2}$.

The tsunami problem was simulated for a period of 25 seconds, and a time step size of $\Delta t = 0.2$ was used. From the full model simulation, with a unstructured finite element mesh of 6830 nodes, 125 snapshots were obtained every time step for each of the u_x, u_y and p solution variables between the simulation period.

Figure 3.10 shows the schematic of a typical free-surface flow problem in ocean modelling context. Figure 3.11 shows the front/interface of wetting and drying. It can be seen that the shape of the computational domain is changing as the free surface keeps moving up and down.

Figure 3.12 shows the solutions of pressure from the high fidelity model and NIROM using 6, 12 and 18 POD bases at time instances $t = 10.2$ and $t = 25$. From this figure it is shown that the NIROM captures the solution's main structural details well even using only 6 POD bases in this case. It is also shown that the solution appears to be closer to high fidelity model as more POD bases are chosen. The more POD bases are chosen, the more energy of the system will be captured. The ratio of energy captured can be quantified by equation (2.10). This can also be evaluated by figure 3.13 which shows the singular eigenvalues of tsunami case in decreasing order of magnitude. The 6 POD bases capture 92.8% of the energy and 12 POD bases capture almost 98% of the energy.

The first 18 leading POD bases are illustrated in figure 3.14. As can be seen from the figure, the first six POD bases capture most of large-scale flow features while the 7^{st} - 18^{th} POD bases capture the details of small-scale flow features.

To further evaluate the performance of NIROM, the absolute error between the high

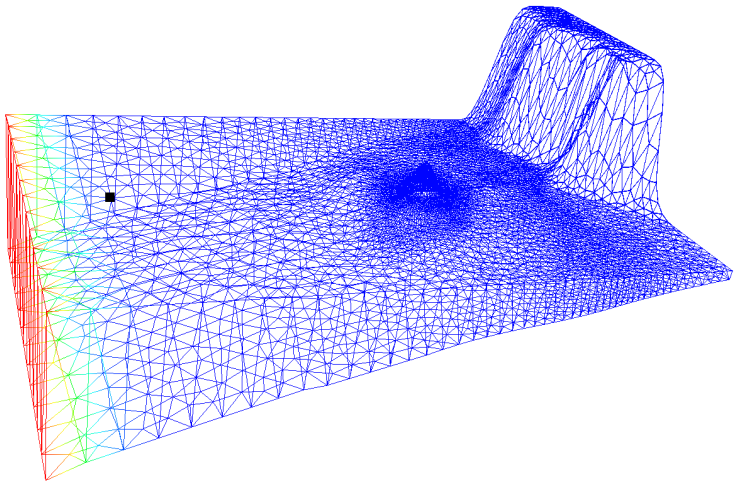


Figure 3.9: Okushiri tsunami case: The computational domain and unstructured meshes used.

fidelity model and NIROM using 6, 12 and 18 POD bases is given in figure 3.15. Again, it is shown that the error of the NIROM decreases as the number of POD bases used increases. Figure 3.18 shows the solutions of full model and the NIROM model using different number of POD bases at the point ($x = 0.6595, y = 1.63, z = -0.1995$) in the domain (black point in figure 3.9). It can be seen that the NIROM using more POD bases gets closer to the solution of the full model.

The RMSE and correlation coefficient of pressure solutions between the high fidelity model and its NIROM counterpart are presented in figure 3.16 and figure 3.17 respectively. The figures indicate that NIROM using 12 and 18 POD bases perform better than NIROM using 6 POD bases. The difference between NIROM using 12 POD bases and 18 POD bases is barely distinguishable since NIROM using 12 POD bases has already captured almost 98% energy.

Table 3.1 shows the online CPU cost required for simulating the high fidelity full model and NIROM for each time step. The simulations were performed on 12 cores workstation of an Intel(R) Xeon(R) X5680 CPU processor with 3.3GHz and 48GB RAM. The two cases were run in serial, which means only one core was used when running the test cases. The time used for the full model roughly equals to the time of assembling and solving the discretised matrices. It can be seen that the NIROM is CPU time efficient, since it does not involve assembling and solving the matrices process. In addition, the CPU cost of the full model is dependent on the resolution of mesh, which means the computation time increases when finer mesh is used.

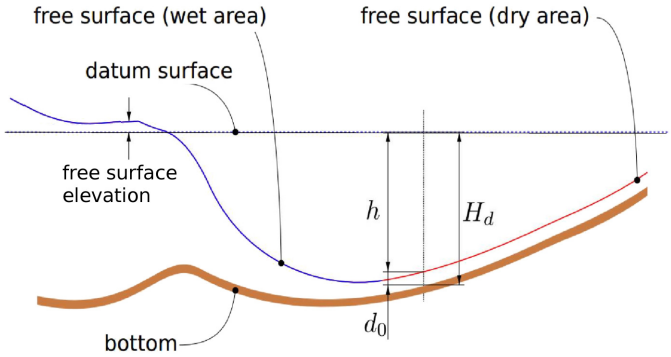
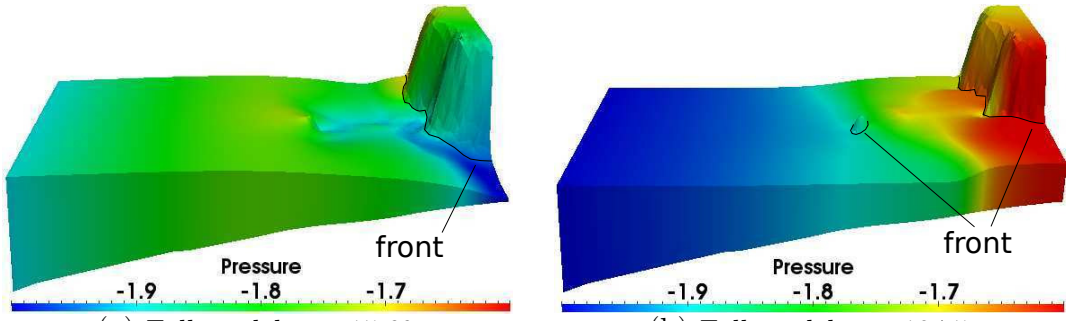


Figure 3.10: Schematic of typical free-surface flow problem in ocean modelling context.

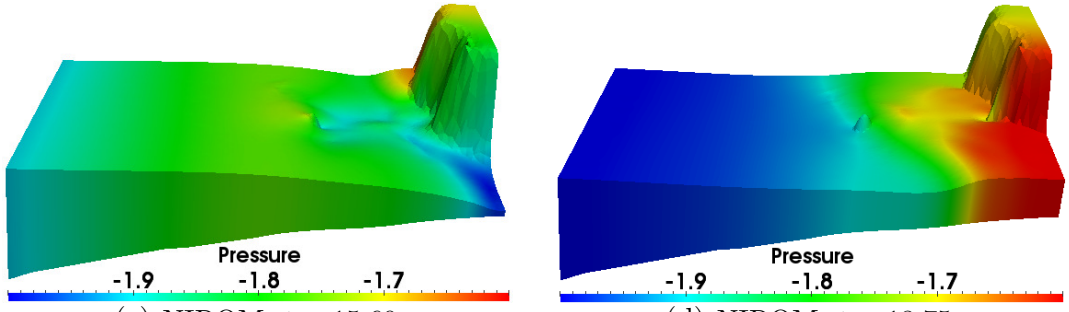
Table 3.1: Comparison of the online CPU time (dimensionless) required for running the full model and NIROM during one time step.

Cases	Model	assembling and solving	projection	interpolation	nonlinear iteration times	total
Okushiri tsunami case	Full model	7.71248	0	0	4	30.84992
	NIROM	0	0.003	0.001	0	0.0040
Balzano case	Full model	0.0520	0	0	15	0.7800
	NIROM	0	0.003	0.001	0	0.0040



(a) Full model, $t = 15.60s$

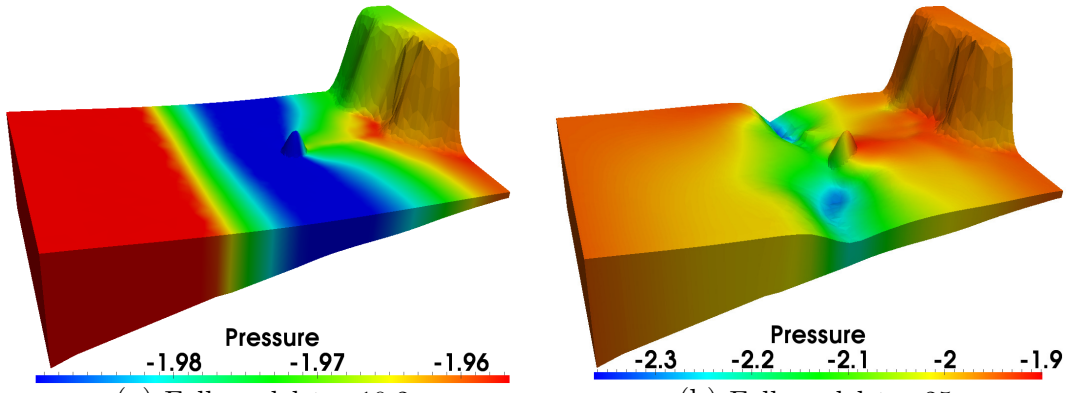
(b) Full model, $t = 18.75s$



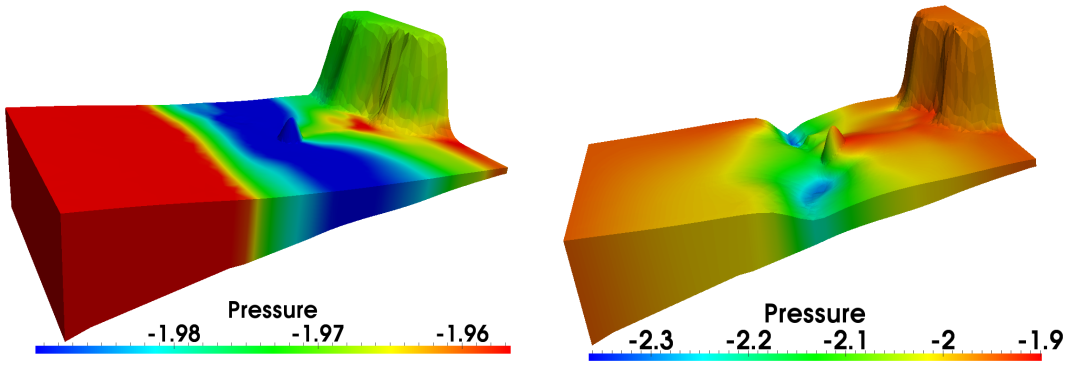
(c) NIROM, $t = 15.60s$

(d) NIROM, $t = 18.75s$

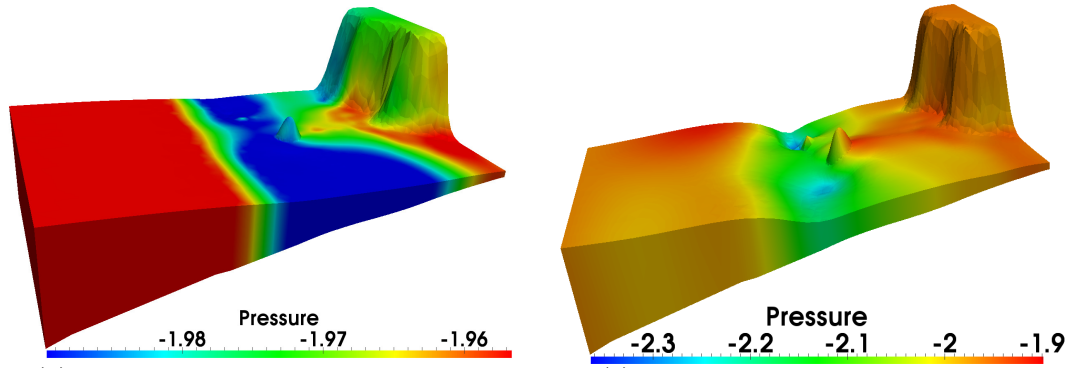
Figure 3.11: Okushiri tsunami case: wetting and drying front (dark line) at time instances 15.60 (left panel) and 18.75 (right panel) seconds.



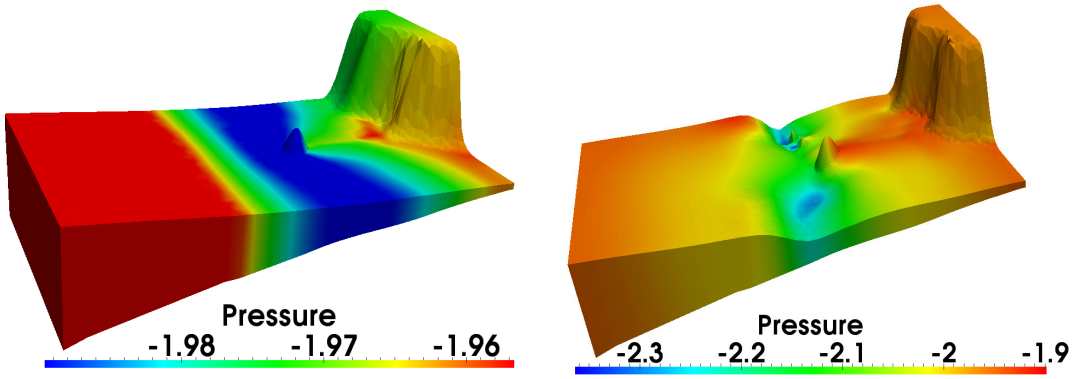
(a) Full model $t = 10.2$ (b) Full model $t = 25$



(c) NIROM 6 POD bases, $t = 10.2$ (d) NIROM 6 POD bases, $t = 25$



(e) NIROM 12 POD bases, $t = 10.2$ (f) NIROM 12 POD bases, $t = 25$



(g) NIROM 18 POD bases, $t = 10.2$ (h) NIROM 18 POD bases, $t = 25$

Figure 3.12: Okushiri tsunami case: The solutions of pressure from the full model and NIROM at time instances 10.2 (left panel) and 25 (right panel). Top panel: the full model; upper-middle panel: NIROM using 6 POD bases; down-middle panel: NIROM using 12 POD bases; bottom panel: NIROM using 18 POD bases.

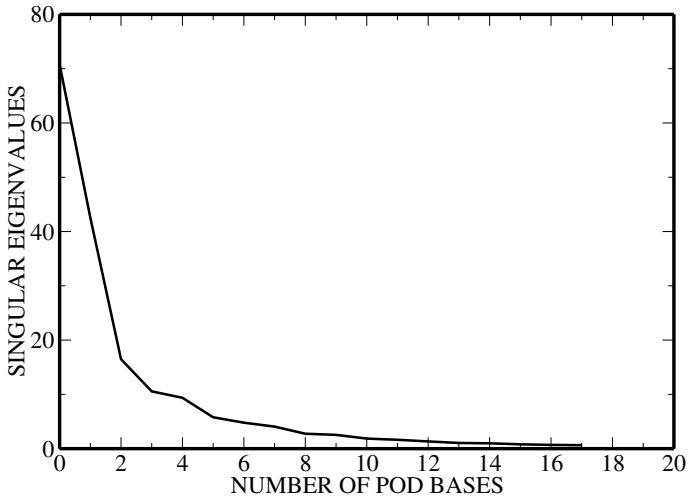
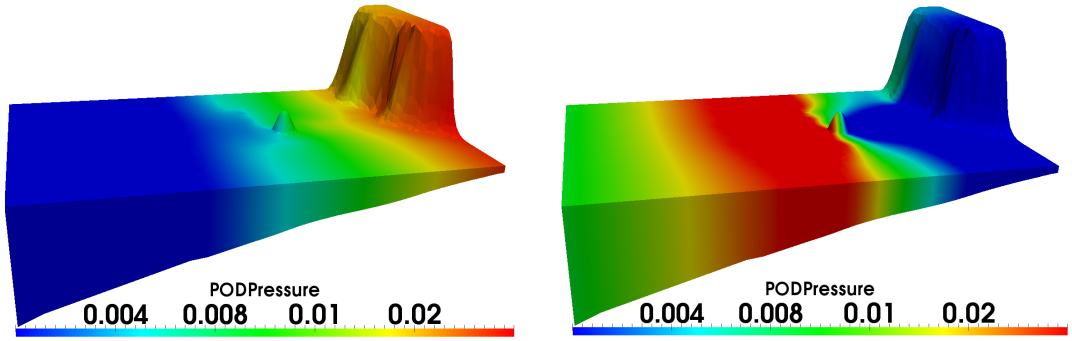
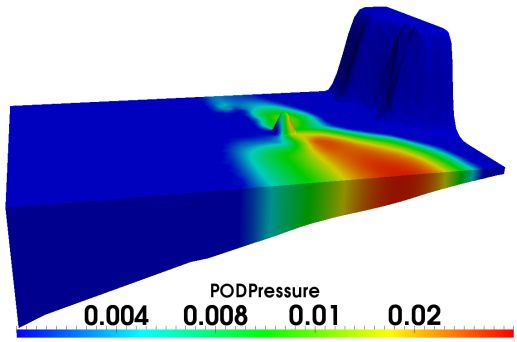


Figure 3.13: Okushiri tsunami case: The graphs shows the singular eigenvalues in order of decreasing magnitude.

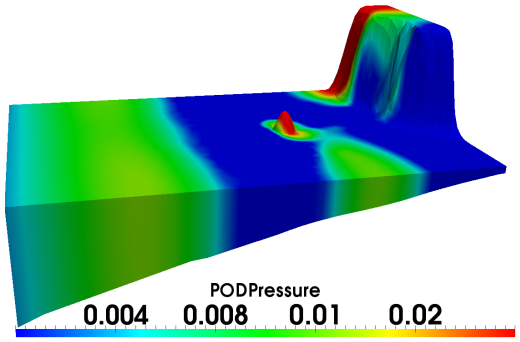


(a) the first POD bases

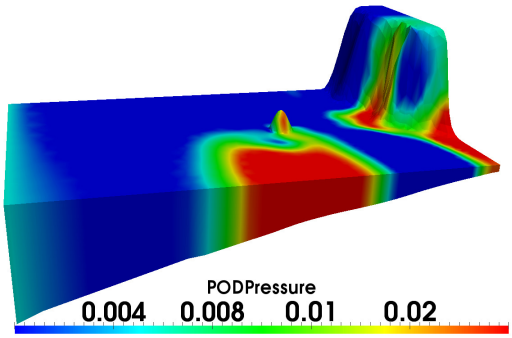
(b) the second POD bases



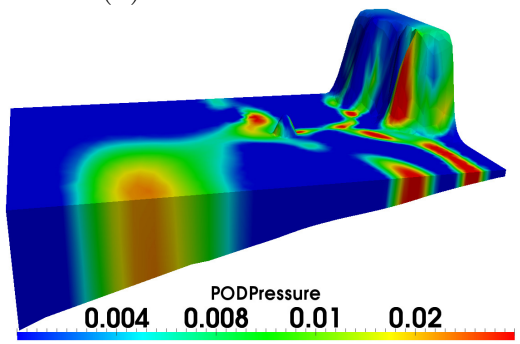
(c) the third POD bases



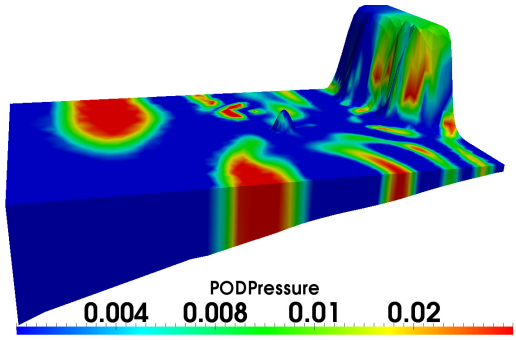
(d) the fourth POD bases



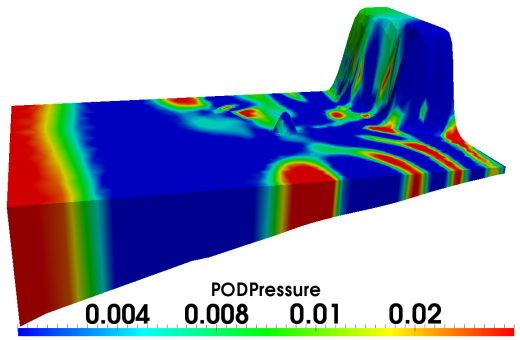
(e) the sixth POD bases



(f) the twelfth POD bases

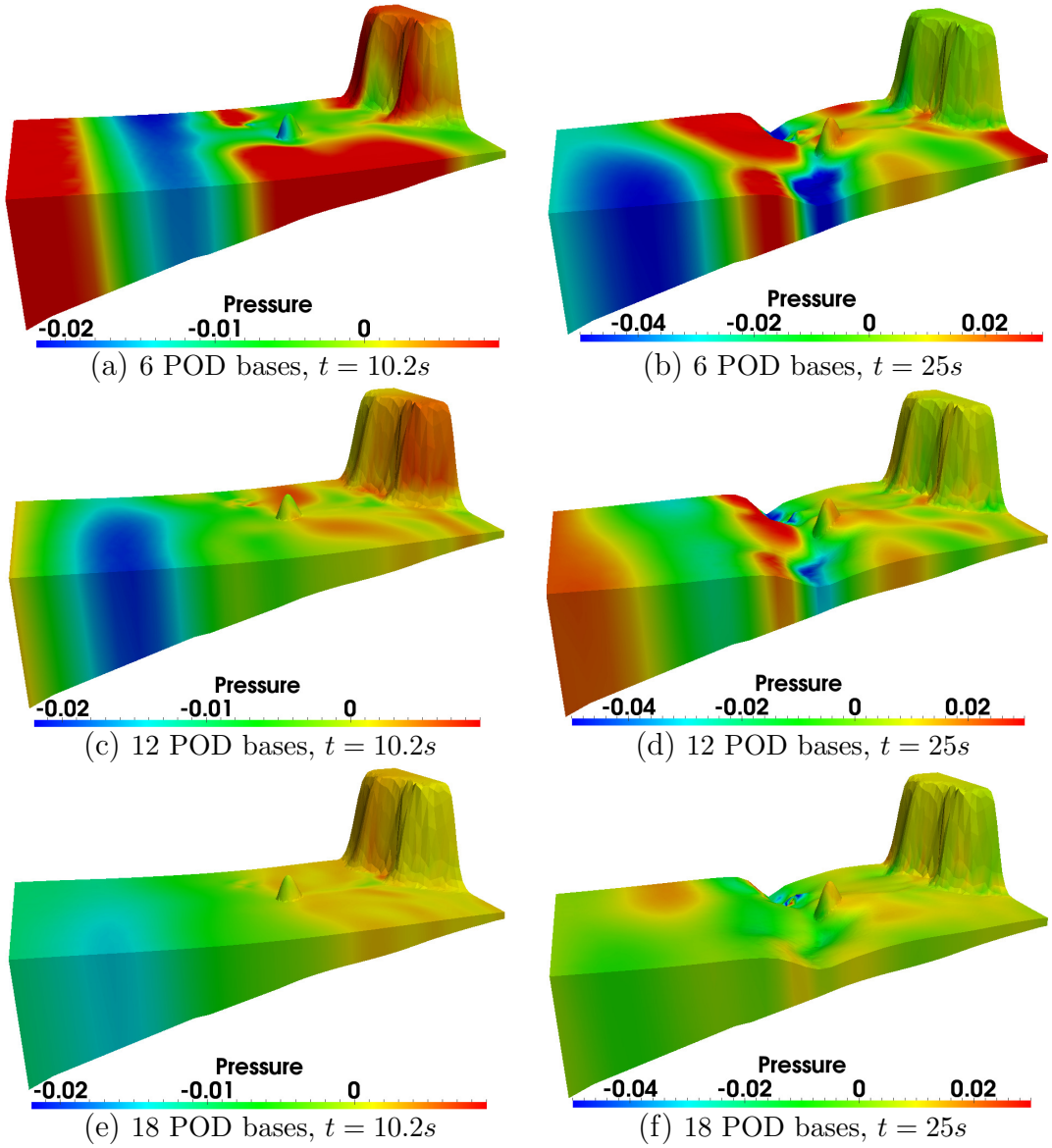


(g) the seventeenth POD bases



(h) the eighteenth POD bases

Figure 3.14: Okushiri tsunami case: The figures show the first 18 POD bases functions for pressure.



(a) 6 POD bases, $t = 10.2s$ (b) 6 POD bases, $t = 25s$

(c) 12 POD bases, $t = 10.2s$ (d) 12 POD bases, $t = 25s$

(e) 18 POD bases, $t = 10.2s$ (f) 18 POD bases, $t = 25s$

Figure 3.15: Okushiri tsunami case: The error of pressure solutions between the full model and NIROM, using 6, 12 and 18 POD basis at time instances 10.2 (left panel) and 25 (right panel) seconds.

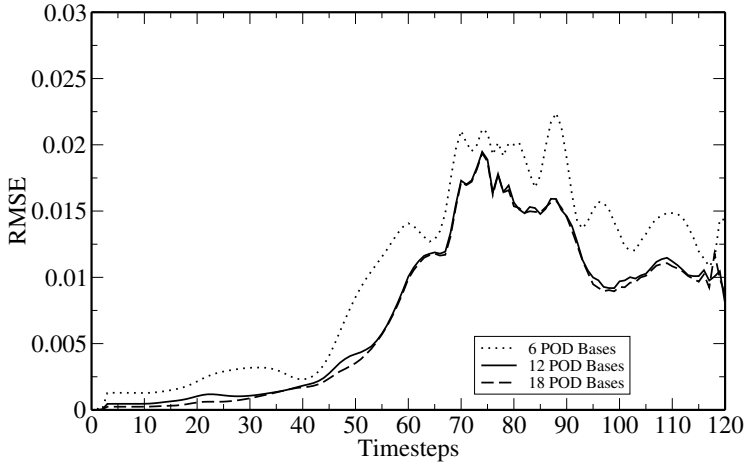


Figure 3.16: Okushiri tsunami case: The RMSE errors of pressure solutions between the full and non-intrusive reduced order models.

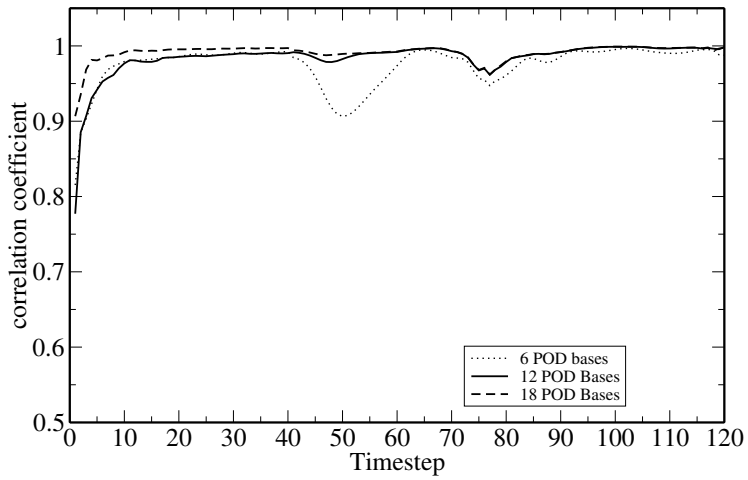


Figure 3.17: Okushiri tsunami case: The correlation coefficient of pressure solutions between the full and non-intrusive reduced order models.

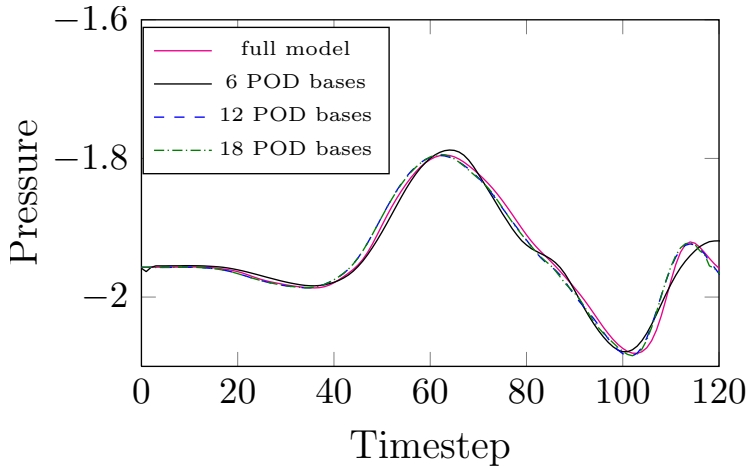


Figure 3.18: Okushiri tsunami case: The comparison of pressure solutions between the full model and NIROM model at location ($x = 0.6595, y = 1.63, z = -0.1995$).

3.6 Conclusions

In this chapter a non-intrusive reduced order model based on the Smolyak sparse grid method has been, for the first time, developed for 3D free surface flows and implemented under the framework of advanced 3D unstructured mesh finite element ocean model (FLUIDITY). The Smolyak sparse grid method is used to construct a set of interpolation functions representing the reduced system. The NIROM method is independent of the governing equations. The performance of the new POD-Smolyak 3D free surface flow NIROM is illustrated for two numerical test cases: Balzano test case and Okushiri tsunami case. To estimate the accuracy of NIROM, the results obtained from the free surface NIROM have been compared against those from the high fidelity free surface full model. It is shown that the accuracy of solutions from free surface flow NIROM is maintained while the CPU cost is reduced by several orders of magnitude. An error analysis has also been carried out for the validation of the new NIROM. The NIROM shows a good agreement with the high fidelity full model. It can be also shown that the accuracy can be improved by increasing the number of POD bases. Future work will investigate the effects of applying this new NIROM to more complex free surface flows (for example, urban flooding) and and for parametric non-intrusive cases.

Chapter

FOUR

Non-intrusive Reduced Order Modeling for multi-phase porous media flows

4.1 Abstract

A novel NIROM for multiphase flows in porous media has been developed in this chapter. The novelties introduced in this work are in (1) the first attempt of applying such a non-intrusive reduced order method to multiphase porous media simulation and 3D fluvial channel model, and (2) the first implementation of the non-intrusive ROM under the framework of a complex unstructured mesh control volume finite element (CVFEM) multiphase model.

The capability of this new NIROM has been numerically illustrated in two multiphase flow simulations in porous media: a two material layer case, a low permeability domain embedded in a high permeability domain case and a 3D fluvial channel model. By comparing the results of the POD-RBF ROM against the solutions obtained from the high fidelity full model, it is shown that this model can result in a large reduction in the CPU computation cost (by a factor of 2500) while much of the details of multiphase flow in porous media are captured.

This chapter is derived from and expands upon Xiao *et al.* (2015c).

4.2 Introduction

As we know, the simulations of multiphase flows in porous media are very important and have a wide range of applications, from groundwater production to radioactive waster and the extraction of oil and gas from the subsurface. However, the application of multiphase modelling in industry is not only computationally intensive, but also often suffers from significant uncertainties in the controlling parameters used as inputs when predicting the performance.

Recently, reduced order methods (*e.g*, POD, POD/DEIM, trajectory piecewise linearisation and bilinear approximation techniques) have been applied to reservoir modelling (see for instance, Heijn *et al.* (2004); Cardoso (2009); Cardoso *et al.* (2009); Chaturantabut & Sorensen (2011a); Yang *et al.* (2015b); Yoon *et al.* (2014); Ghasemi *et al.* (2014); Klie *et al.* (2013)). Heijn *et al.* (2004) and Cardoso (2009); Cardoso *et al.* (2009) first developed POD reduced order models for reservoir simulation. Chaturantabut & Sorensen (2011a), Yang *et al.* (2015b) and Yoon *et al.* (2014) further introduced DEIM into model reduction for non-linear flows (see Chaturantabut & Sorensen (2011a)). Again, these reduced order methods are intrusive and equations/codes dependent. There are very few studies in non-intrusive reduced order modelling in porous media flow simulation and the 3D fluvial channel problem. Klie first proposed a non-intrusive model reduction approach based on a three-layer neural network combined with POD and DEIM to predict the production of oil and gas reservoirs (see Klie *et al.* (2013)), where the RBF neural network is used for developing learning functions from input-output relationships. In this work, we used RBF as an interpolation method for constructing the time-dependent POD ROM.

The work in this chapter applies, a NIROM based on the POD-RBF method to generate reduced order model for multiphase flows in porous media and particularly the 3D fluvial channel problem. This has been implemented under the framework of a unstructured mesh finite element porous media flow model. The novelty of this work lies in the use of the RBF interpolation method combined with POD to represent the solution of the multiphase porous media equations on the reduced spaces. In this approach again, solutions to the full fidelity model are recorded (as

a sequence of snapshots), and from these snapshots POD bases are generated that optimally represent the porous media flow problem. The RBF interpolation method is then used to form a hypersurface interpolation function that approximates the time-dependent ROM. The capabilities of results from the POD-RBF multiphase flow model have been assessed by three multiphase flow test cases in porous media: a two material layer case, a low permeability domain embedded in a high permeability domain case and 3D fluvial channel case. Comparisons between the high fidelity full model and this non-intrusive ROM are made to investigate the accuracy of the POD-RBF formulation.

The structure of the chapter is as follows: section 4.3 presents the governing equations of the multiphase porous media flows; section 4.4 presents the construction of NIROM for multiphase porous media flows; section 4.5 illustrates the methodology derived by means of three numerical examples. The illustration consists of three test problems where a two material layer test case, a low permeability domain embedded in a high permeability domain case and 3D fluvial channel case are resolved. Finally in section 4.6, the conclusion is presented.

4.3 Governing equations

The governing equations used in the underlying multiphase model are given in this section. The darcy's law for immiscible multiphase flow in porous media has the form:

$$\mathbf{q}_\alpha = -\frac{\mathcal{K}_{r_\alpha}}{\mu_\alpha}\mathbf{K}\left(\nabla p_\alpha - \mathbf{s}_{u_\alpha}\right), \tag{4.1}$$

where $\mathbf{q}_\alpha$ is the α^{th} phase Darcy velocity. The $\mathcal{K}_{r_\alpha}$ is the relative permeability of the α^{th} phase, and it is a function that is denoted by $\mathcal{K}_{r_\alpha}(S_\alpha)$ corresponding to the phase saturation variable S_α. p_α is the pressure of the α^{th} phase, which may include capillary pressure. $\mathbf{K}$ is the absolute permeability tensor of the porous medium. μ_α and $\mathbf{s}_{u_\alpha}$ are the phase dynamic viscosity and source term respectively, which may include gravity.

A saturation-weighted Darcy velocity is introduced into the equation (4.1) and defined as

$$\mathbf{v}_\alpha = \frac{\mathbf{q}_\alpha}{S_\alpha}, \tag{4.2}$$

then equation (4.1) can be rewritten as follows:

$$\mathbf{u}_\alpha = \underline{\underline{\sigma}}_\alpha \mathbf{v}_\alpha = -\nabla p_\alpha + \mathbf{s}_{u\alpha}, \quad \underline{\underline{\sigma}}_\alpha = \mu_\alpha S_\alpha \left(\mathcal{K}_{r_\alpha}\mathbf{K}\right)^{-1} \tag{4.3}$$

where $\mathbf{u}_\alpha$ denotes the force per unit volume, which is defined as $\underline{\underline{\sigma}}_\alpha \mathbf{v}_\alpha$ and used as a prognostic variable in this approach. The $\underline{\underline{\sigma}}_\alpha$ represents the implicit linearisation of the viscous frictional forces.

The saturation equation can be written as:

$$\phi \frac{\partial S_\alpha}{\partial t} + \nabla \cdot (\mathbf{v}_\alpha S_\alpha) = s_{cty,\alpha}, \tag{4.4}$$

where ϕ denotes the porosity. The t is time and $s_{cty,\alpha}$ is a source term of the α^{th} phase. Finally, equation (4.4) is bounded by the constraint:

$$\sum_{\alpha=1}^{N_\alpha} S_\alpha = 1, \tag{4.5}$$

where N_α denotes the number of phases.

The discretisation of the above equations (4.1)-(4.5) at time level n can be written in a general form:

$$\mathbf{A}_v^n \mathbf{v}^n = \mathbf{s}_v^n, \quad \mathbf{A}_p^n \mathbf{p}^n = \mathbf{s}_p^n, \quad \mathbf{A}_S^n \mathbf{S}^n = \mathbf{s}_S^n \tag{4.6}$$

where $\mathbf{v}^n = (\mathbf{v}_1^n, \ldots, \mathbf{v}_\alpha^n, \ldots, \mathbf{v}_{N_\alpha}^n)^T$, and $\mathbf{v}_\alpha^n = (v_{\alpha,1}, \ldots, v_{\alpha,\mathcal{N}})^T$, $\mathbf{S}_\alpha^n = (S_{\alpha,1}, \ldots, S_{\alpha,\mathcal{N}})^T$, $\mathbf{p}^n = (P_{\alpha,1}, \ldots, P_{\alpha,\mathcal{N}})^T$ and $\mathcal{N}$ is the number of nodes.

4.4 Construction of the NIROM for multi-phase porous media problems

In this work, the radial basis function (RBF) interpolation has been used to construct the POD ROM in (7.2).

By applying the RBF method, a set of multidimensional functions $f_{v,j}^n$, $f_{p,j}^n$ and $f_{S,j}^n$ for each POD coefficient $\alpha_{v,r,j}^n$, $\alpha_{p,r,j}^n$ and $\alpha_{S,r,j}^n$ $(j \in \{1, 2, \ldots, M\})$ may be

approximately represented by the hypersurface interpolation function below:

$$\begin{aligned}
\alpha^n_{v,r,j} &= f_{v,j}(\alpha^{n-1}_{v,r}, \alpha^{n-1}_{p,r}, \alpha^{n-1}_{S,r}) = \sum_{i=1}^{N} w_{v,i,j} * \phi(r_i), \\
\alpha^n_{p,r,j} &= f_{p,j}(\alpha^{n-1}_{v,r}, \alpha^{n-1}_{p,r}, \alpha^{n-1}_{S,r}) = \sum_{i=1}^{N} w_{p,i,j} * \phi(r_i), \\
\alpha^n_{S,r,j} &= f_{S,j}(\alpha^{n-1}_{v,r}, \alpha^{n-1}_{p,r}, \alpha^{n-1}_{S,r}) = \sum_{i=1}^{N} w_{S,i,j} * \phi(r_i),
\end{aligned} \tag{4.7}$$

where $\phi(r_i)$ is the radial basis function whose values depend on the distance r_i from a collection data point, $(\hat{\alpha}_{v,r,i}, \hat{\alpha}_{p,r,i}, \hat{\alpha}_{S,r,i})$, where $i \in 1, 2, \ldots, N$ and weighted by $w_{v,i}$, $w_{v,i}$ and $w_{v,i}$. In this work, the multiquadratic functions are chosen:

$$\phi(r_i) = \sqrt{r_i^2 + \sigma^2} = \sqrt{\left\|(\alpha^{n-1}_{v,r}, \alpha^{n-1}_{p,r}, \alpha^{n-1}_{S,r}) - (\hat{\alpha}_{v,r,i}, \hat{\alpha}_{p,r,i}, \hat{\alpha}_{S,r,i})\right\|^2 + \sigma^2}, \tag{4.8}$$

where $r_i = \left\|(\alpha^{n-1}_{v,r}, \alpha^{n-1}_{p,r}, \alpha^{n-1}_{S,r}) - (\hat{\alpha}_{v,r,i}, \hat{\alpha}_{p,r,i}, \hat{\alpha}_{S,r,i})\right\|$ is a radius or the distance defined by the L_2 norm, $\sigma > 0$ is a shape parameter.

The weighting coefficients $w_{v,i}$, $w_{p,i}$ and $w_{S,i}$ are determined so as to ensure that the interpolation function values at the collection data point $(\hat{\alpha}_{v,r,k}, \hat{\alpha}_{p,r,k}, \hat{\alpha}_{S,r,k})$ match the given data $f_{v,k}$, $f_{p,k}$ and $f_{S,k}$. This can be expressed by,

$$A\mathbf{w}_{v,i} = \mathbf{f}_{v,i}, \quad A\mathbf{w}_{p,i} = \mathbf{f}_{p,i}, \quad A\mathbf{w}_{S,i} = \mathbf{f}_{S,i}, \quad i \in \{1, 2, \ldots, N\}, \tag{4.9}$$

where

- $\mathbf{w}_{v,i} = (w_{v,i,k})^T_{k=1,\ldots,N}$, $\mathbf{w}_{p,i} = (w_{p,i,k})^T_{k=1,\ldots,N}$ and $\mathbf{w}_{S,i} = (w_{S,i,k})^T_{k=1,\ldots,N}$,
- $\mathbf{f}_{v,i} = (w_{v,i,k})^T_{k=1,\ldots,N}$, $\mathbf{f}_{p,i} = (w_{p,i,k})^T_{k=1,\ldots,N}$ and $\mathbf{f}_{S,i} = (w_{S,i,k})^T_{k=1,\ldots,N}$,
- A is the interpolation matrix of elements $A_{k,l} = \phi(\|(\hat{\alpha}_{v,r,k}, \hat{\alpha}_{p,r,k}, \hat{\alpha}_{S,r,k}) - (\hat{\alpha}_{v,r,l}, \hat{\alpha}_{p,r,l}, \hat{\alpha}_{S,r,l})\|)$,
- $k, l \in \{1, 2, \ldots, N\}$, N is the number of data points.

The coefficients $w^{n-1}_{v,i} = (w_{v,i,j})_{j=1,\ldots,N}$, $w^{n-1}_{p,i} = (w_{p,i,j})_{j=1,\ldots,N}$ and $w^{n-1}_{S,i} = (w_{S,i,j})_{j=1,\ldots,N}$ are then determined by solving the linear system (4.9).

The process of constructing a NIROM using RBF-POD method for multi-phase porous media problem can be described as algorithm 3,

Algorithm 3: POD-RBF reduced order modelling

(1) **Offline calculation:** Construct the POD-RBF reduced order model

(a) POD bases

i. Generate the snapshots at time level $n = 1, \ldots, N_t$ by solving the full model (4.6);

ii. Construct the POD bases Φ_v, Φ_p and Φ_S using the SVD method;

(b) Construct a set of interpolation functions

i. Calculate the functional values $f_{v,i,k}$, $f_{p,i,k}$ and $f_{S,i,k}$ at the data point $(\hat{\alpha}_{v,r,k}, \hat{\alpha}_{p,r,k}, \hat{\alpha}_{S,r,k})$ through the solution from the full models, where $k \in \{1, 2, \ldots N\}$;

ii. Find the weights $\mathbf{w}_{v,i}$, $\mathbf{w}_{p,i}$ and $\mathbf{w}_{S,i}$ by solving (4.9) such that the interpolation functions $\mathbf{f}_{v,i}$, $\mathbf{f}_{p,i}$ and $\mathbf{f}_{S,i}$ pass through through the data points;

(2) **Online calculation:** The RBF interpolation function in (4.7) denotes a 3M-dimensional hyper surface. Once a set of interpolation functions $f_{v,j}$, $f_{p,j}$ and $f_{S,j}$ are constructed, they are then used to estimate the j^{th} POD coefficient $\alpha^n_{v,r,j}$, $\alpha^n_{p,r,j}$ and $\alpha^n_{S,r,j}$ at time level n.

Result: Write here the result
Initialization $\alpha^0_{v,r,j}$, $\alpha^0_{p,r,j}$ and $\alpha^0_{S,r,j}$;
for $n = 1$ *to* N_t **do**
  for $j = 1$ *to* m **do**

(i) **Inputs:** a complete set of POD coefficients for solution fields $\alpha_{\mathbf{u}}$, $\alpha_{\mathbf{p}}$ and $\alpha_{\mathbf{S}}$ at time step $n-1$:

$$\alpha^{n-1}_{v,r} = (\alpha^{n-1}_{v,r,j})^T_{j=1,\ldots,M}, \quad \alpha_{\mathbf{p}}{}^n = (\alpha^{n-1}_{p,r,j})^T_{j=1,\ldots,M}, \quad \alpha_{\mathbf{S}}{}^n = (\alpha^{n-1}_{S,r,j})^T_{j=1,\ldots,M},$$

(ii) **Outputs:** Estimate the POD coefficient $\alpha^n_{v,r,j}$, $\alpha^n_{p,r,j}$ and $\alpha^n_{S,r,j}$ at current time step n using the RBF interpolation (4.7);

$$\begin{aligned} \alpha^n_{v,r,j} &= f_{v,j}(\alpha^{n-1}_{v,r}, \alpha^{n-1}_{p,r}, \alpha^{n-1}_{S,r}), \\ \alpha^n_{p,r,j} &= f_{p,j}(\alpha^{n-1}_{v,r}, \alpha^{n-1}_{p,r}, \alpha^{n-1}_{S,r}), \\ \alpha^n_{S,r,j} &= f_{S,j}(\alpha^{n-1}_{v,r}, \alpha^{n-1}_{p,r}, \alpha^{n-1}_{S,r}), \end{aligned}$$

  endfor
  Obtain the solution of variables $\mathbf{v}^n$, $\mathbf{p}^n$ and $\mathbf{S}^n$ in (4.4) by projecting $\alpha^n_{v,r,j}$, $\alpha^n_{p,r,j}$ and $\alpha^n_{S,r,j}$ onto the full space (see (2.9)).

$$\mathbf{v}^n = \overline{\mathbf{v}} + \Phi_v^T \alpha^n_{u,r}, \quad \mathbf{p}^n = \overline{\mathbf{p}} + \Phi_p^T \alpha^n_{p,r}, \quad \mathbf{S}^n = \overline{\mathbf{S}} + \Phi_S^T \alpha^n_{S,r},$$

endfor

4.5 Numerical Examples

4.5.1 Introduction of an unstructured mesh multiphase fluid model

The POD-RBF reduced order modelling method has been implemented under the framework of an advanced 3D unstructured mesh multiphase fluid model, the Imperial College Finite Element Reservoir Simulator (IC-FERST). A control volume finite element method (CVFEM) is used to obtain the high-order fluxes on CV boundaries which are limited to yield bounded fields (*e.g.*, positive saturations). This method is combined with a family of FE pairs, originally introduced for geophysical fluid dynamics applications. In particular, the $P2DG - P1DG$ element pair (quadratic discontinuous polynomial FE basis function for velocity ($P2DG$) and linear discontinuous polynomial FE basis function for pressure, $P1DG$), is used to accurately represent sharp saturation changes between heterogeneous domains, see (Salinas *et al.* (2015); Su *et al.* (2015)).

4.5.2 General description of test cases

The waterflooding is a widely known technique in oil and gas reservoir engineering. It increases the production from oil reservoirs through injecting water into the reservoir. As illustrated in figure 4.1, the water is injected into the reservoir to increase the reservoir pressure, the oil is then displaced toward the production well. This phenomenon is also referred to the immiscible displacement in porous media.

In this section, the capability of the POD-RBF ROM has been demonstrated in three porous media flow problems: the two material layer test case, the low permeability domain embedded in a high permeability domain case and 3D fluvial channel case. These test cases are dimensionless and for simplicity no gravity has been considered. In all cases, the outlet boundary has a dimensionless pressure of 0, the whole domain is initially saturated with the non-wetting phase and the wetting phase at the irreducible saturation. The wetting phase is injected over the inlet boundary with a dimensionless velocity of 1. The viscosity ratio of the phases is 1. The Brooks-Corey model for the relative permeability, with an exponent of 2 and an end-point relative permeability of 1, is considered for both phases. The porosity is homogeneous and equal to 0.2. The immobile fraction of the wetting phase is set to 0.2 and 0.3 for

the non-wetting phase.

4.5.3 Two material layer test case

The first case for numerical illustration of the method proposed in this chapter is a two material layer test case. This problem domain consists of a rectangle of non-dimensional size 1×0.2. The domain is divided into two identical areas with a permeability of 4 within the top half part and 1 on the bottom half part.

The problem was resolved with a mesh of 984 nodes during the simulation time period $[0, 0.02]$. Fifty snapshots were taken from the pre-computed solution at regularly spaced time intervals $\Delta t = 0.0002$ and from these POD bases are generated for the solution variables v, p, S.

The first 18 POD bases are presented in figure 4.2. As shown in the figure, the first four POD bases capture most of flow features while the 5^{th}-18^{th} POD bases capture the details of small scale flow structures. Figure 4.3 shows the singular eigenvalues in order of decreasing magnitude. In general, the more POD bases and snapshots are chosen, the better the energy is represented. There is a trade-off between the accuracy and the CPU time. In this work, 18 POD bases with 50 snapshots are chosen resulting in 92% of 'energy' being captured.

Figure 4.4 shows the saturation solutions of the two material layer problem at time instances $t = 0.01$ and $t = 0.02$, as calculated using the full and non-intrusive POD-RBF models. It can be seen that both model solutions are in good agreement with each other. The POD-RBF model performs well in capturing the saturation shock-front.

Figure 4.5 shows the saturation solution at a particular position (0.026937, 0.16246). It is noted the results from the POD-RBF model using 6 and 12 POD bases become oscillatory after $t = 10$. By increasing the number of POD bases from 6 to 18, the POD-RBF modelling becomes stable and exhibits an overall good agreement with the full modelling.

The ability of the POD-RBF ROM is further highlighted in figure 4.6, which presents the saturation solution along a line parallel to the x-axies. We can see the POD-RBF model has a large error near the shock-front when using 6 POD bases. This can be significantly improved as the number of POD bases increases. Using 18 POD bases, the error of saturation solutions is decreased by $50\% - 97\%$ in comparison to that

using only 6 POD bases, and the shock-front is captured well.

To further validate the quality of the POD-RBF ROM, the corresponding error estimation of the POD ROM was carried out in this work. The accuracy of POD-RBF reduced order modelling was assessed. The correlation coefficient and RMSE of solutions between the full and POD-RBF models is computed for each time step.

The RMSE and correlation coefficient of saturation solutions between the full and POD-RBF models are presented in figure 4.7. With an increase in the number of POD bases, the RMSE in the saturation results decreases by about 50% while the correlation increases up to 98%.

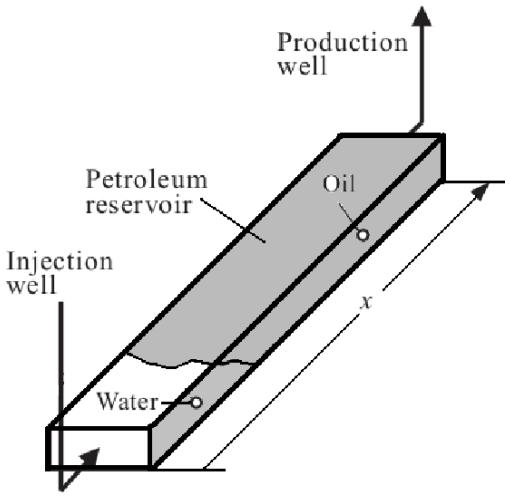
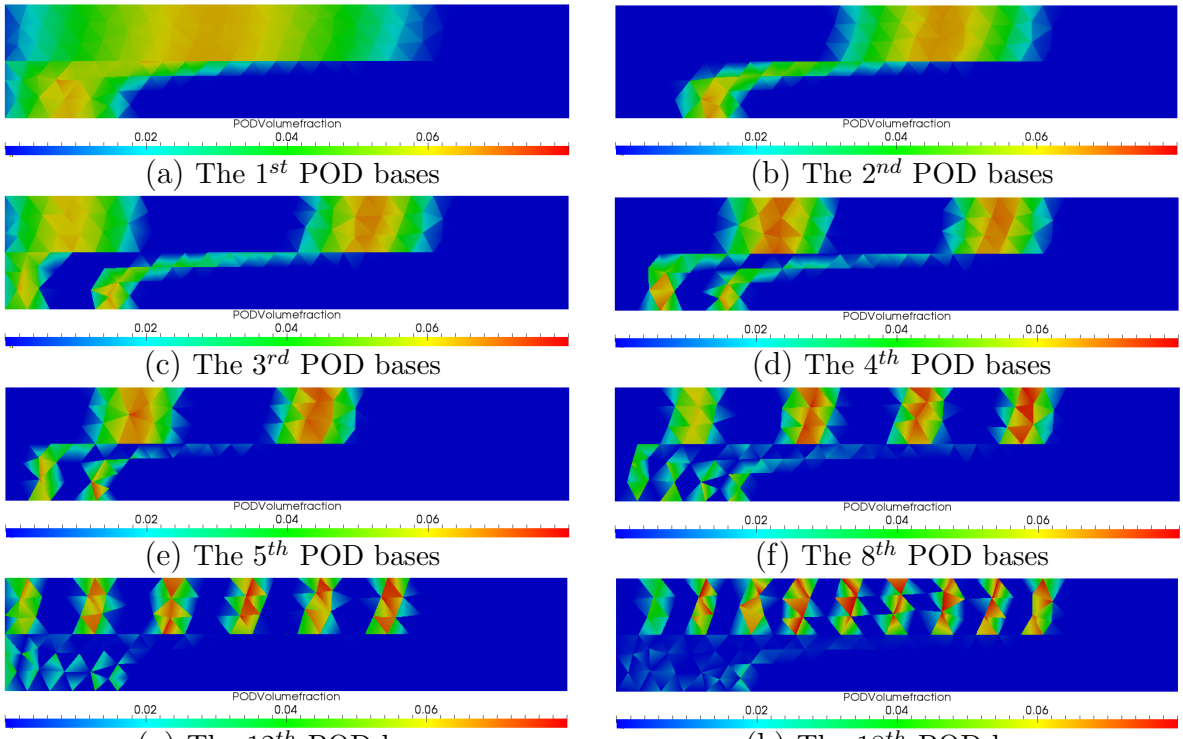


Figure 4.1: Waterflooding technique for oil production.



(a) The 1^{st} POD bases (b) The 2^{nd} POD bases

(c) The 3^{rd} POD bases (d) The 4^{th} POD bases

(e) The 5^{th} POD bases (f) The 8^{th} POD bases

(g) The 12^{th} POD bases (h) The 18^{th} POD bases

Figure 4.2: Two material layers case: the figures displayed the first 18 the POD bases functions of the 2D two material layer problem.

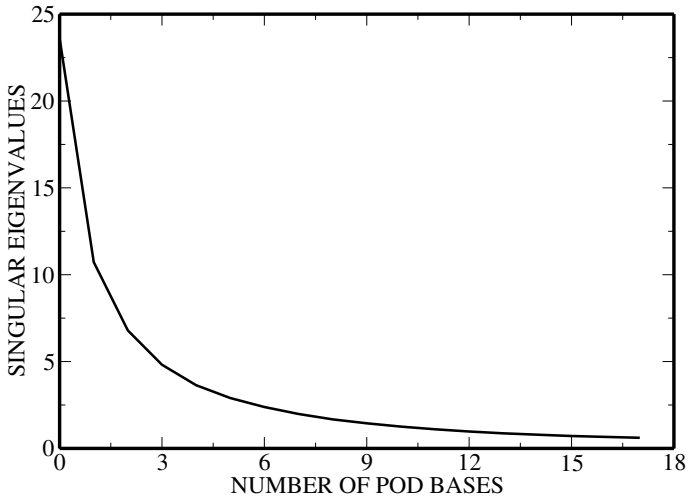
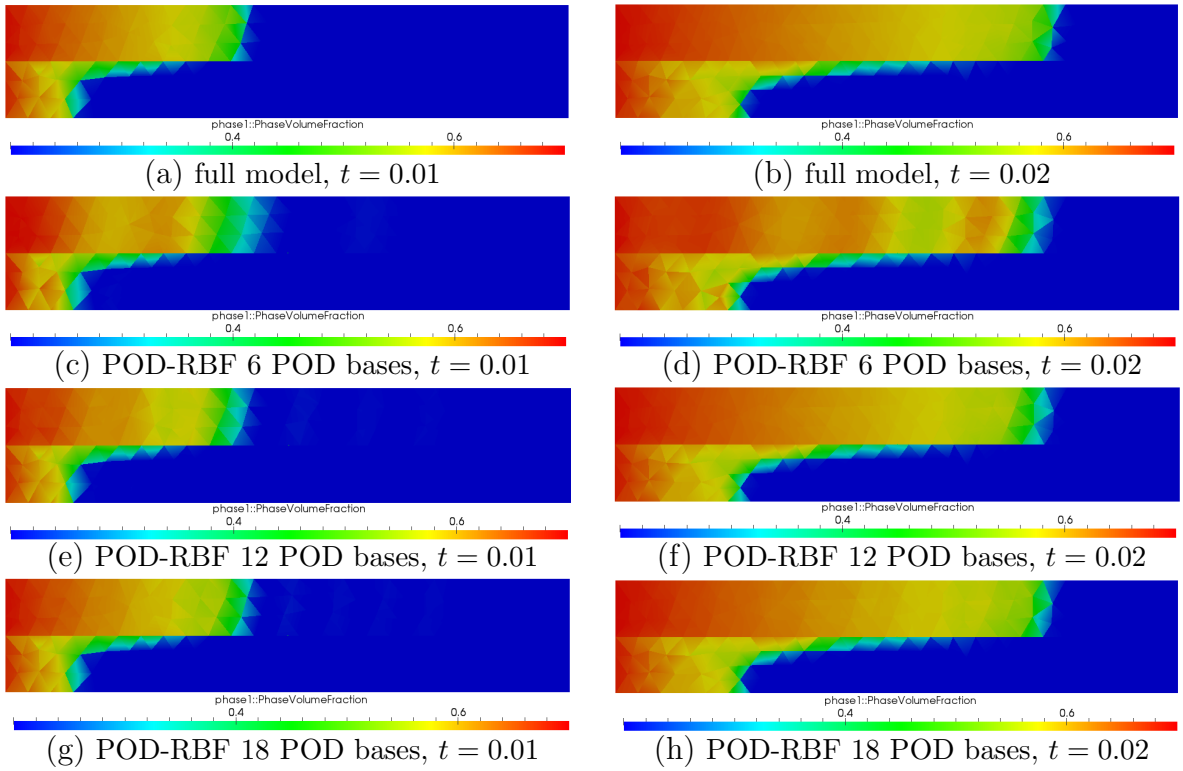


Figure 4.3: Two material layers case: the figure shows the singular eigenvalues in order of decreasing magnitude.



(a) full model, $t = 0.01$ (b) full model, $t = 0.02$

(c) POD-RBF 6 POD bases, $t = 0.01$ (d) POD-RBF 6 POD bases, $t = 0.02$

(e) POD-RBF 12 POD bases, $t = 0.01$ (f) POD-RBF 12 POD bases, $t = 0.02$

(g) POD-RBF 18 POD bases, $t = 0.01$ (h) POD-RBF 18 POD bases, $t = 0.02$

Figure 4.4: Two material layers case: the figures displayed above show the saturation solutions of the two material layer problem at time instances 0.01 and 0.02 (where 6, 12 and 18 POD bases are chosen with 50 snapshots). The permeability on the top half part is 4, and the bottom half part is 1.

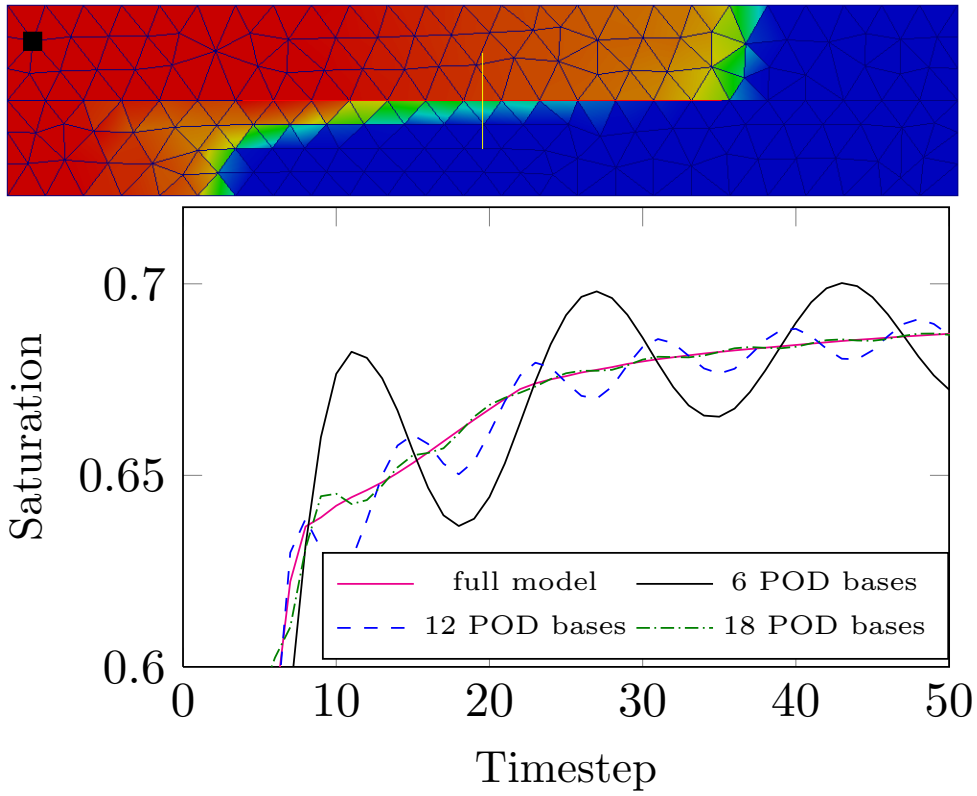
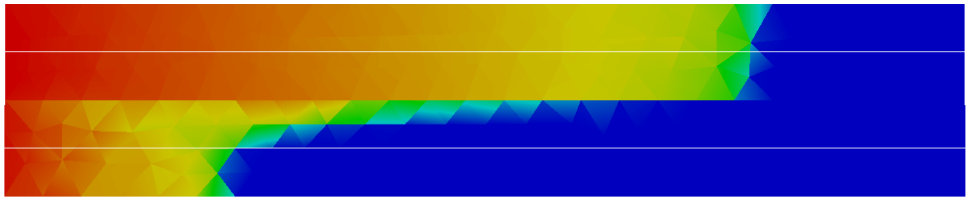
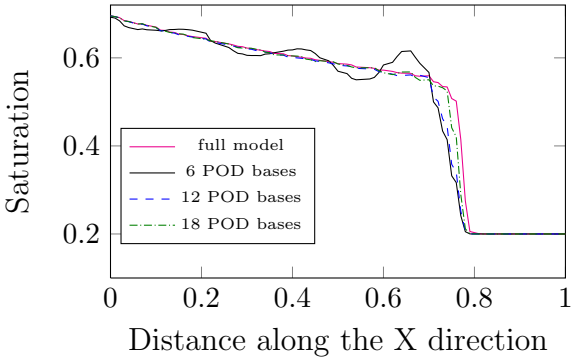


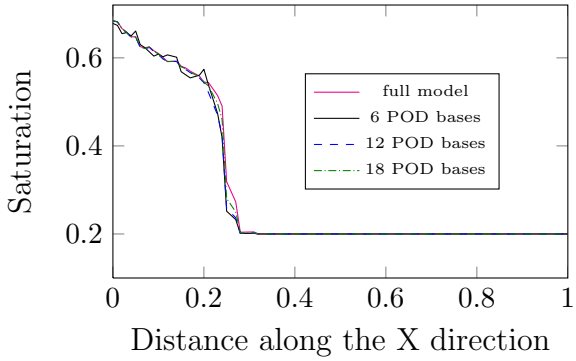
Figure 4.5: Two material layers case: the graph shows the solution saturations predicted by the full model and the POD-RBF ROM at a position (0.026937, 0.16246) (where 6, 12 and 18 POD bases are chosen with 50 snapshots)



(a) The cross section locations

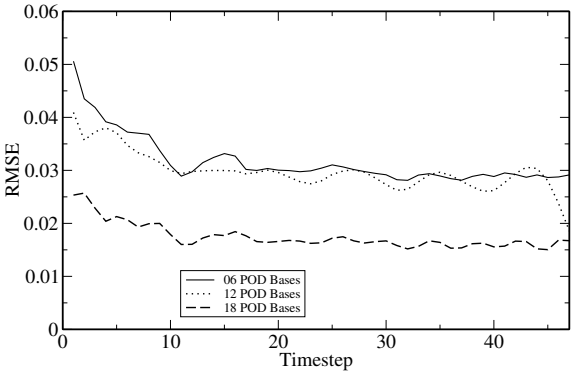


(b) Saturation at the cross section along the top line

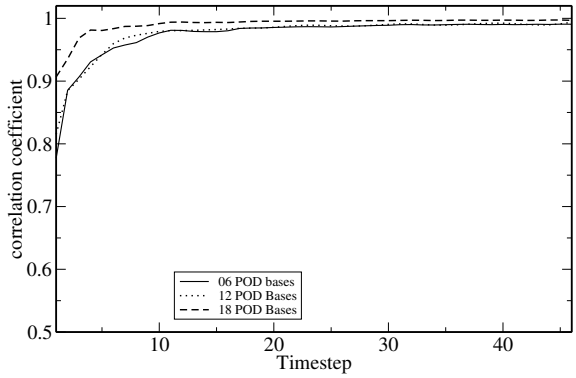


(c) Saturation at the cross section along the bottom line

Figure 4.6: Two material layers case: Saturation along lines parallel to the x axies.



(a) RMSE



(b) Correlation

Figure 4.7: Two material layers case: The graph shows the RMSE and correlation coefficient of solutions between the full and POD-RBF models.

4.5.4 Low permeability domain embedded in a high permeability domain

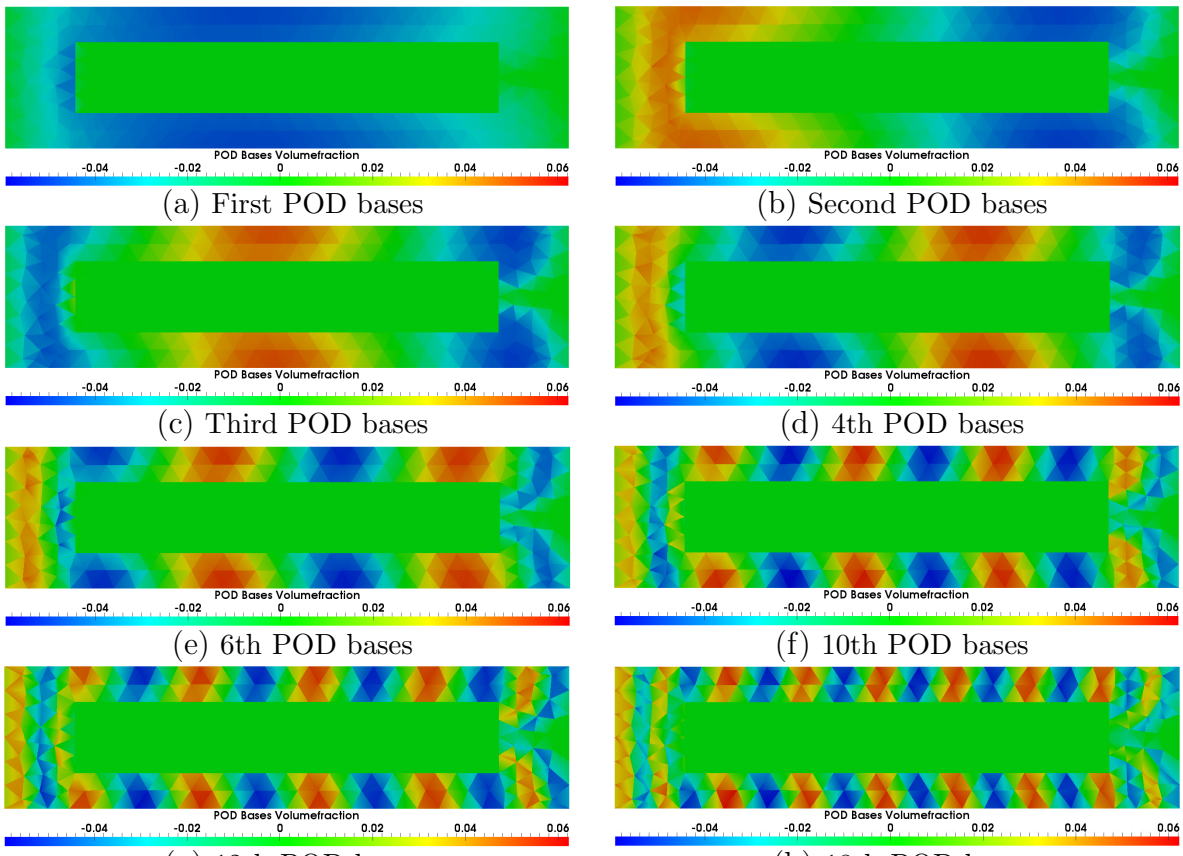
The second case involves a low permeability domain embedded in a higher permeability domain. The domain has a non-dimensional size 2×0.5. The low permeability is 0.001 and the high permeability is 1. The full model simulation with a mesh of 1386 nodes was run during the simulation period $[0, 0.1]$ with a time step size of 0.0001. Fifty snapshots of solutions were taken at regularly spaced time intervals $\Delta t = 0.02$ for each solution variable.

Figure 4.8 shows the first 18 leading POD bases functions of saturation. As shown in the figure, these leading POD bases capture the dominant characteristics of solutions. The POD bases corresponding to small eigenvalues, for example, the 12^{th} and 18^{th} POD bases, contain small scale flow features.

Evaluation of accuracy of the POD model was carried out through comparison of POD solutions with those from the full model. The saturation solutions at time instances 0.05 and 0.1 obtained from the full and POD-RBF models are presented in figure 4.9. Again, good agreement is observed between the two models. The POD-RBF model is able to capture the complex flow patterns around the block. Both the full and POD-RBF models provide almost identical details of local flows. For example, the separated flow forms downstream of the block.

To further demonstrate the ability of the POD-RBF model, the saturation solution at location $(0.58515, 0.43611)$ is presented in figure 4.10. It can be seen that the accuracy of solution can be improved by increasing the number of POD bases functions to 18. This is also be shown in figure 4.11, which illustrates the saturation along lines parallel to the x axies. Again the POD-RBF model performs very well in capturing the saturation shock-front when 18 POD bases are used.

To further assess the accuracy of the POD-RBF model, the absolute error in saturation solutions at time instances 0.05 and 0.1 is plotted in figure 4.12. It is shown that the error in the POD-RBF solution relative to the high fidelity full model decreases as the number of POD bases is increased.



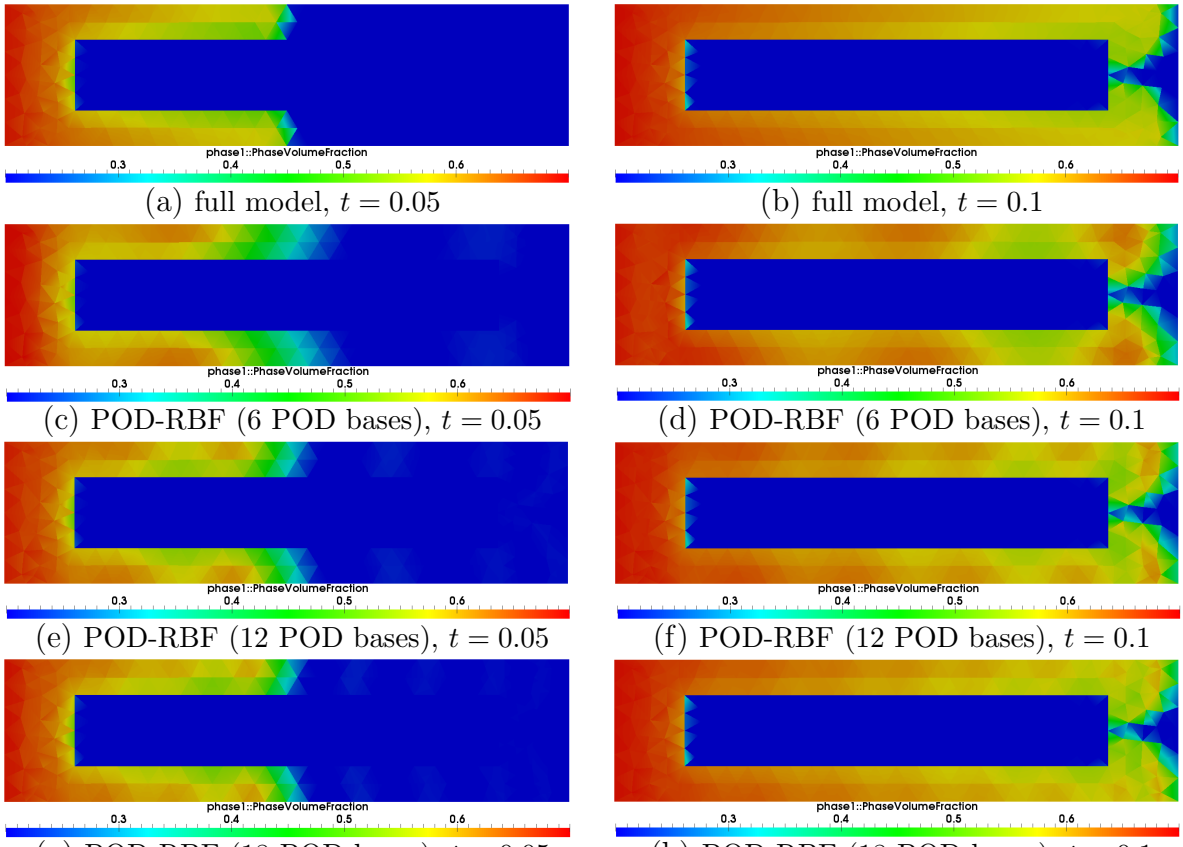
(a) First POD bases (b) Second POD bases

(c) Third POD bases (d) 4th POD bases

(e) 6th POD bases (f) 10th POD bases

(g) 12th POD bases (h) 18th POD bases

Figure 4.8: Low permeability domain embedded in a high permeability domain: the figures displayed above shows the leading POD bases functions of saturation. They are the 1^{st}, 2^{nd}, 3^{rd}, 4^{th}, 6^{th}, 10^{th}, 12^{th} and 18^{th} POD bases functions respectively.



(a) full model, $t = 0.05$ (b) full model, $t = 0.1$

(c) POD-RBF (6 POD bases), $t = 0.05$ (d) POD-RBF (6 POD bases), $t = 0.1$

(e) POD-RBF (12 POD bases), $t = 0.05$ (f) POD-RBF (12 POD bases), $t = 0.1$

(g) POD-RBF (18 POD bases), $t = 0.05$ (h) POD-RBF (18 POD bases), $t = 0.1$

Figure 4.9: Low permeability domain embedded in a high permeability domain: the figures displayed above show the saturation solutions of the low permeability domain embedded in a higher permeability domain problem at time instances 0.05 and 0.1. The solutions compare the predictions from the non-intrusive POD-RBF model with full model using 6, 12 and 18 POD bases functions. The low permeability is 0.001 and the high permeability is 1.

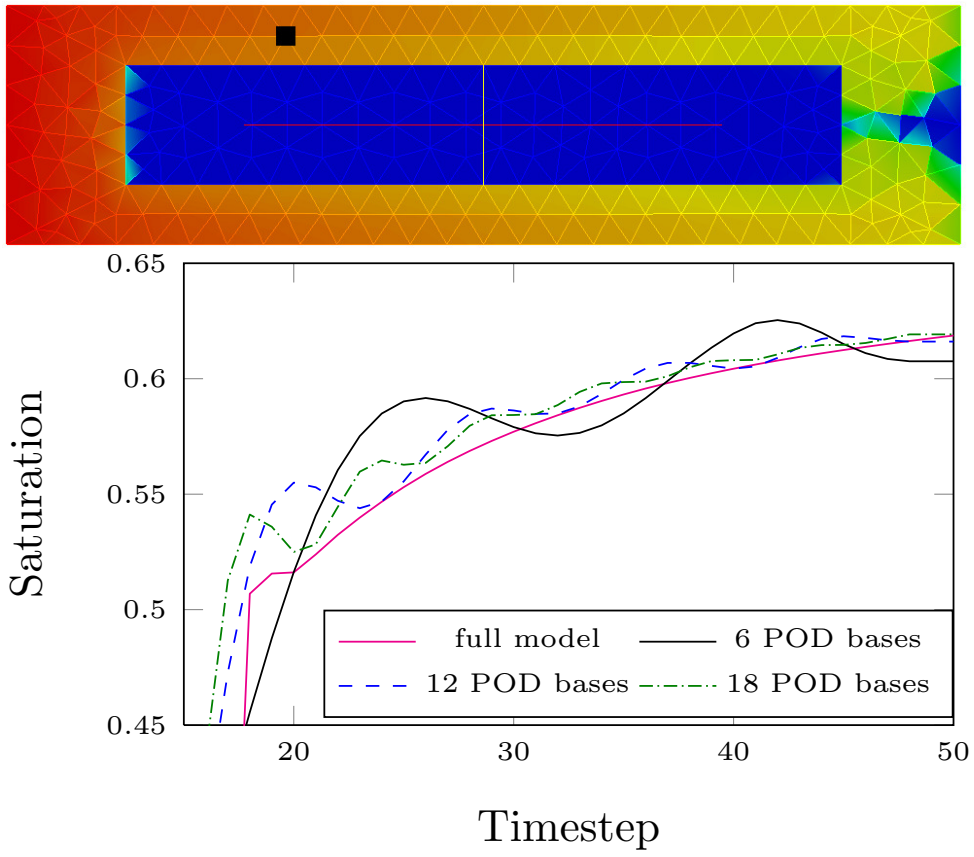
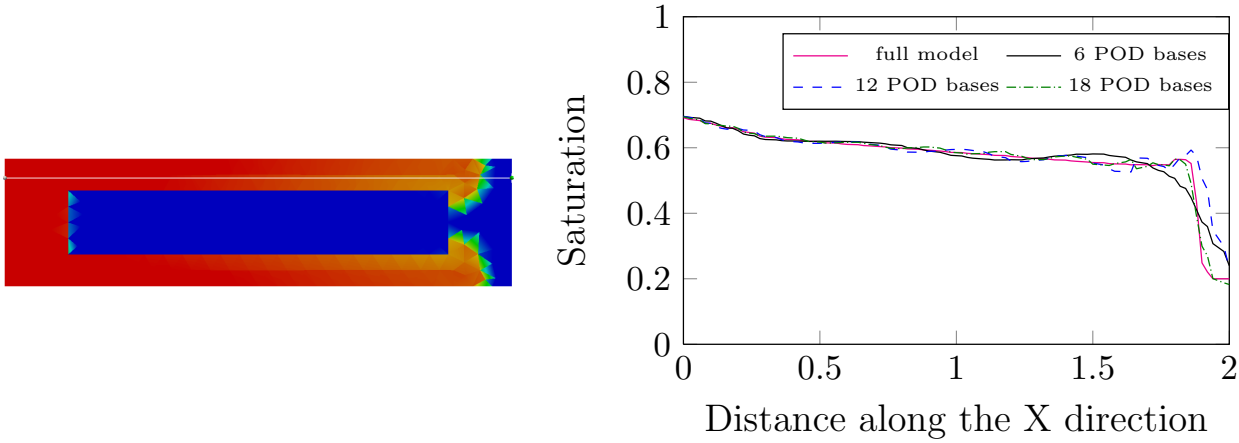
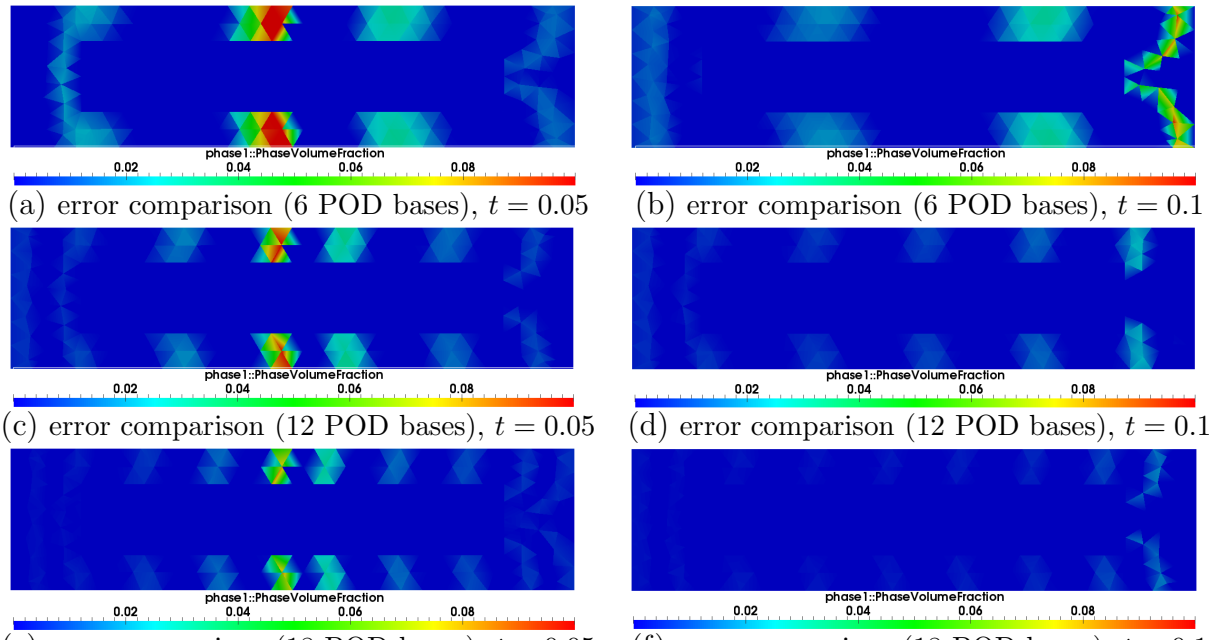


Figure 4.10: Low permeability domain embedded in a high permeability domain: the graph shows the solution saturations predicted by the full model and the POD-RBF ROM at a position: $x = 0.58515, y = 0.43611$ using 6, 12 and 18 POD bases.



(a) The cross section location (b Saturation solution at the cross section

Figure 4.11: Low permeability domain embedded in a high permeability domain: Saturation along lines parallel to the x axies.

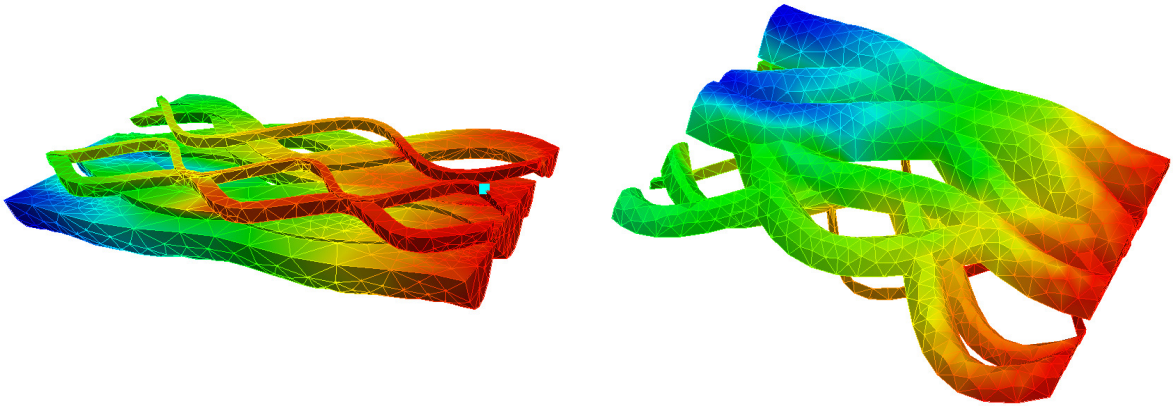


(a) error comparison (6 POD bases), $t = 0.05$ (b) error comparison (6 POD bases), $t = 0.1$

(c) error comparison (12 POD bases), $t = 0.05$ (d) error comparison (12 POD bases), $t = 0.1$

(e) error comparison (18 POD bases), $t = 0.05$ (f) error comparison (18 POD bases), $t = 0.1$

Figure 4.12: Low permeability domain embedded in a high permeability domain: the figures displayed above show the saturation error between full model and POD-RBF model of the low permeability domain embedded in a higher permeability domain problem at time instances 0.05 and 0.1 seconds using 6, 12 and 18 POD basis.

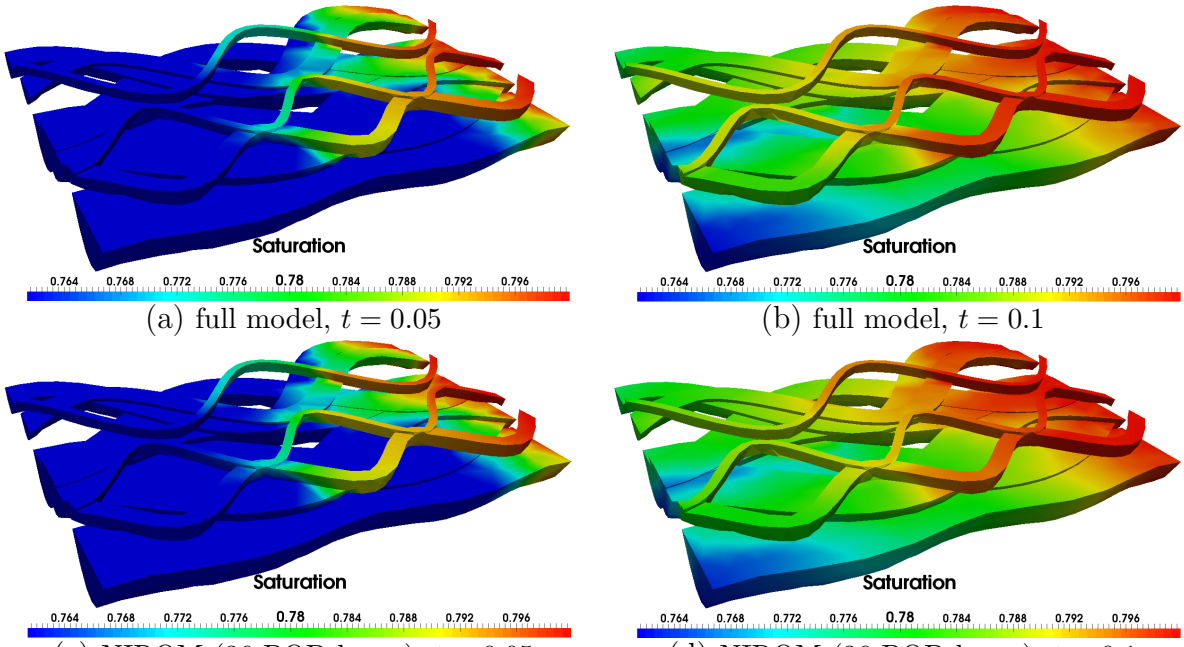


(a) water channel profile (b) inverted profile of (a)

Figure 4.13: 3D fluvial channel: the figures displayed above show the water channel profile.

4.5.5 3D fluvial channel case

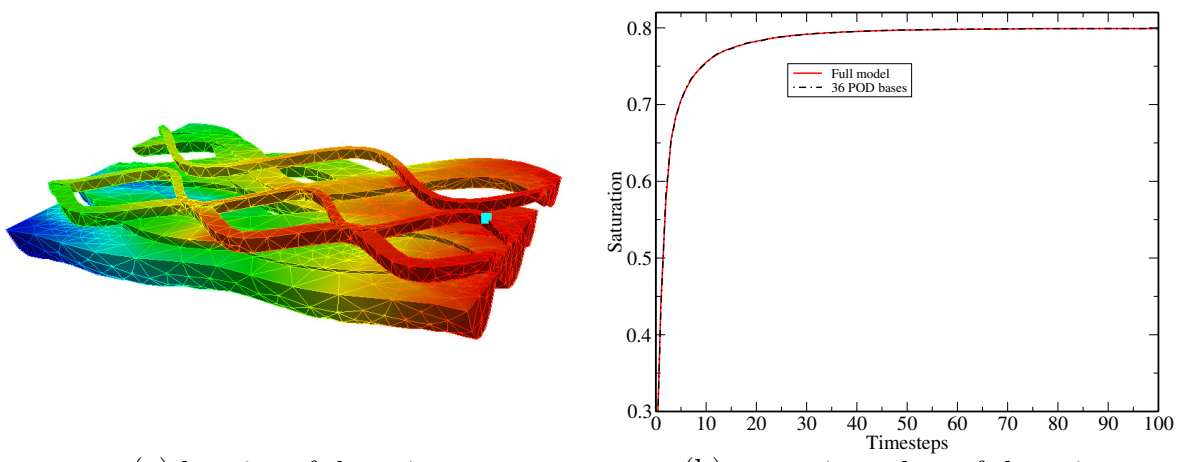
The third case is a three dimensional fluvial channel case. There is a set of channels in the computational domain which is composed of 31776 nodes–see figure 4.13. The domain is initially is filled with immovable water and movable oil and the saturations of oil and water are $S_{oil} = 0.8$ and $S_{water} = 0.2$, respectively. The water is then injected into the computational domain from the right side at constant pressure. The flow will pass through the channels from right side to the left side. All other sides are treated as barriers to flows except for the inlet side with a pressure of 55×10^6 (right side in figure 4.13) and outlet side with a pressure of 2×10^6 (right side in figure 4.13). The homogeneous porosity is set to be ϕ=0.2 and the saturations of the residual oil and irreducible water are set to be 0.2. The viscosities of the residual oil and irreducible water are set to be 0.004 and 0.001 respectively. The simulation was run during the time period $[0, 86400000]$ with a time step size of 864000. 100 snapshots of solutions were taken at regularly spaced time intervals $\Delta t = 864000$ for each solution variable. Figure 4.14 shows the saturation solutions obtained from the high fidelity full model and NIROM with 36 POD bases at time instances 43200000 and 69120000 seconds. It shows clearly that the results of NIROM are very close to that of high fidelity full model. The solutions of saturation at a particular point (figure 4.15 (a)) in the computational domain is presented in figure 4.15. The figure again shows that the NIROM using 36 POD bases has very good agreement with high fidelity full model.



(a) full model, $t = 0.05$ (b) full model, $t = 0.1$

(c) NIROM (36 POD bases), $t = 0.05$ (d) NIROM (36 POD bases), $t = 0.1$

Figure 4.14: 3D fluvial channel: the figures displayed above show the saturation of full model and NIROM of the 3D fluvial channel problem at time instances 43200000 and 69120000 seconds using 36 POD basis.



(a) location of the point (b) saturation values of the point

Figure 4.15: 3D fluvial channel: the figures displayed above show the values of saturation at a particular point in the mesh-see figure(a).

4.5.6 Computational efficiency of the POD-RBF model

Table 4.1 shows a comparison of the online CPU time required for running the full model and non-intrusive POD-RBF ROM. It can be seen that the online CPU time required for running the NIROM for multi-phase porous media problem is considerably less than that for the full model and is reduced by a factor of 2500. The simulation workstation has 12 processors and a 48GB random-access memory(RAM). The processor used in workstation is Intel(R) Xeon(R) CPU X5680 @ 3.33GHz. In this work only one single processor with frequency of 3.33GHz was used since the test cases were performed in serial.

Table 4.1: Comparison of the online CPU time (dimensionless) required for running the full model and POD-RBF NIROM during one time step.

Cases	Model	assembling and solving	projection	interpolation	total
Two material layers case	Full model	0.81605	0	0	0.81605
	NIROM	0	0.0003	0.0001	0.00040
High permeability domain embedding a low one	Full model	1.15607	0	0	1.15607
	NIROM	0	0.0003	0.0001	0.00040
3D fluvial channel	Full model	98.3998	0	0	98.3998
	NIROM	0	0.0003	0.0001	0.00040

4.6 Conclusion

A NIROM has been, for the first time, applied to porous media flows and developed for an advanced 3D unstructured mesh multiphase fluid model, the Imperial College Finite Element Reservoir Simulator (IC-FERST), which has the capabilities of using (1) anisotropic unstructured meshes to resolve fine scale flow feature; and (2) a novel control volume finite element method to resolve the high-order flux flows on CV boundaries. A RBF interpolation method is used to form a multi-dimensional interpolation function (hyper surface) that represents the solution of the multiphase porous media equations within the reduced space. The non-intrusive approach used here to construct the POD-RBF model is generic and does not require any information of the original source code or the model equations. It can be applied to any software or commercial codes. In addition, it avoids the instability of existing

Galerkin POD ROMs, the results might be smoothed by RBF (see Myers (1999)).

The capabilities of the newly developed POD-RBF multiphase porous media model are illustrated in three typical test cases in reservoir engineering. A comparison between the full and POD-EBF model results are made. An error analysis was also carried out for the validation and accuracy assessment of the POD-RBF model. It is shown that the POD-RBF model exhibits an overall good agreement with the high fidelity full model. An increase in the number of POD bases leads to an improvement in the accuracy of the POD-RBF model. The saturation shock-front can be captured with relatively few POD basis functions, 18 POD basis function(figure (h) of 4.4) in the examples.

In comparison to the full model, without compromising the accuracy of results the CPU time required for the POD-RBF model can be reduced by a factor of 2500. It is worth of mentioning that for large scale porous media flow simulation, an increase in the number of nodes used in the computational domain will result in a large increase of the CPU time in the full simulation, but has very little effect on that of the POD-RBF model.

Chapter

FIVE

Non-intrusive reduced order modeling of fluid-structure interactions

5.1 Abstract

A novel non-intrusive reduced order model (NIROM) for fluid-structure interaction (FSI) has been developed. The model is based on proper orthogonal decomposition (POD) and radial basis function (RBF) interpolation method. This is the first time that a NIROM was constructed for FSI phenomena using POD and RBF interpolation method. Another novelty of this work is the first implementation of the FSI NIROM under the framework of an unstructured mesh finite element multi-phase model (FLUIDITY) and a combined finite-discrete element method based solid model (Y2D).

The capability of this new NIROM for FSI is numerically illustrated in three coupling simulations: a one-way coupling case (flow past a cylinder), a two-way coupling case (a free-falling cylinder in water) and a vortex-induced vibrations of a elastic beam test case. It is shown that the FSI NIROM results in a large CPU time reduction by several orders of magnitude while the dominant details of the high fidelity model

are captured.

This chapter is derived from and expands upon (Xiao *et al.* (2016a)).

5.2 Introduction

The background of the NIROM for fluid-structure interaction problems can be found in section 1.3.3.3. The work described in this chapter uses, for the first time, the non-intrusive method to derive a reduced order model for fluid-structure interaction problems using the POD and RBF methods. This has been implemented under the framework of an unstructured mesh finite element model (FLUIDITY) and a combined finite-discrete element solid model (Y2D). The novelty of this work lies in the use of non-intrusive method to represent solutions of fluid-structure interaction problems on reduced spaces.

The structure of the chapter is as follows: section 5.3 presents the governing equations of fluid-structure interaction problems; section 5.4 derives the methods of constructing a non-intrusive reduced order model for fluid-structure interaction problems using the FSI NIROM method; section 5.5 demonstrates the capability of the derived methodology by three numerical examples: a one-way coupling test case(flow past a cylinder), a two-way coupling test case(a free-falling cylinder in water) and a vortex-induced vibrations of a elastic beam test case; Finally in section 5.6, summary and conclusions are presented.

5.3 Governing equations

In this section, the governing equations of the fluid-structure interaction are described, which consist of governing equations for fluid dynamics and solid dynamics.

5.3.1 Governing equations for fluid dynamics

The fluid dynamics is governed by the Navier-Stokes equations. In order to derive the coupling equations, the Navier-Stokes equations can also be written in the form

of,

$$\nabla \cdot \boldsymbol{u}_f = 0, \tag{5.1}$$

$$\rho_f \frac{D\boldsymbol{u}_f}{Dt} = \nabla \cdot \tau - \nabla p + \boldsymbol{B}_f, \tag{5.2}$$

where $\boldsymbol{u}_f$ denotes velocity vector of fluids, τ the viscous forces, p the pressure and $\boldsymbol{B_f}$ the body forces (*e.g.* gravity force). The ρ_f is the density of fluids.

5.3.2 Governing equations for solid dynamics

The governing equation of solid dynamics is the Newton's second law and has the discretised form as follows:

$$\boldsymbol{F}_{external} + \boldsymbol{F}_{viscosity} + \boldsymbol{F}_{pressure} + \boldsymbol{F}_{contact} - \boldsymbol{F}_{internal} = M\frac{\partial \boldsymbol{u}_s}{\partial t}, \tag{5.3}$$

where M denotes the mass matrix of nodes and it is given by $\boldsymbol{M} = \int_{V_0} \rho_0 \boldsymbol{N}\boldsymbol{N}^T dV$ (ρ_0 being the density of solids and $\boldsymbol{N}$ being finite element basis function), $\boldsymbol{F}_{internal}$ is the internal force and it is obtained by $\boldsymbol{F}_{internal} = \int_{v^{(n)}} \frac{\partial \boldsymbol{N}}{\partial \boldsymbol{x}} \boldsymbol{T} dv$ ($\boldsymbol{T}$ being the Cauchy stress). The $\boldsymbol{F}_{external}$ is the external force and derived by $\boldsymbol{F}_{external} = \int_{v^{(e)}} \boldsymbol{N}\boldsymbol{b} dv + \int_{v^{(e)}} \boldsymbol{N}\boldsymbol{t} dv$ ($\boldsymbol{b}$ being the body force, $\boldsymbol{t}$ being surface traction force). $\boldsymbol{F}_{viscosity}$ and $\boldsymbol{F}_{pressure}$ are viscous force and pressure at the fluid-solid interface respectively. In one way coupling, $\boldsymbol{F}_{viscosity} = 0$. The $\boldsymbol{F}_{contact}$ denotes the contact force between solids, for details, see Munjiza (2004).

5.3.3 Fluid-solid coupling equations

In this chapter, the Navier-Stokes equations are used for resolving the problem on the extended computational domain (Ω) comprised of the fluid Ω_f and solid Ω_s domains. In order to couple the fluid and solid, a supplementary equation is introduced:

$$\frac{\rho_f}{\Delta t}(\hat{\boldsymbol{u}}^f - \boldsymbol{u}_f^f) = \frac{\rho_f}{\Delta t}(\boldsymbol{u}_s^s - \boldsymbol{u}_f^s), \tag{5.4}$$

where $\boldsymbol{u}$ is the velocity, the subscripts denote material field (*i.e.* s denotes solid and f denotes fluid) while the superscripts denote material to which mesh is associated (*i.e.* s denotes values on the solid mesh and f denotes values on the fluid mesh) and

$\hat{\boldsymbol{u}}^f$ is the bulk velocity which has the following form:

$$\hat{\boldsymbol{u}}^f = \alpha_f \boldsymbol{u}_f^f + \alpha_s \boldsymbol{u}_s^f = \hat{\boldsymbol{u}}_f^f + \hat{\boldsymbol{u}}_s^f, \tag{5.5}$$

and

$$\hat{\boldsymbol{u}}^f = \begin{cases} \boldsymbol{u}_f^f & \text{if } \alpha_f = 1, \alpha_s = 0, \\ \boldsymbol{u}_s^f & \text{if } \alpha_f = 0, \alpha_s = 1, \end{cases} \tag{5.6}$$

where α_f and α_s are the volume fractions for the fluid and solid respectively, and $\alpha_f + \alpha_s$=1,

The continuity equation (5.1) on the extended computational domain ($\Omega = \Omega_f \cup \Omega_s$) then has the form of:

$$\nabla \cdot \hat{\boldsymbol{u}}^f = \nabla \cdot (\hat{\boldsymbol{u}}_f^f + \hat{\boldsymbol{u}}_s^f) = 0. \tag{5.7}$$

In order to obtain the solutions of the coupled system, the velocity of solids on the solid mesh, $\boldsymbol{u}_s^s$, is projected onto the fluid mesh, then it becomes $\hat{\boldsymbol{u}}_s^f$ (see Viré *et al.* (2015)).

To represent the impact of solid-fluid interactions on fluid solutions, a source term $\boldsymbol{s}_c^f$ is introduced into the momentum equation (5.2), that is:

$$\rho_f \frac{D\boldsymbol{u}_f}{Dt} = \nabla \cdot \tau - \nabla p + \boldsymbol{s}_c^f, \tag{5.8}$$

where σ_f denotes the total stress tensor which considers the contribution of pressure and $\boldsymbol{B_f}$ is the body forces (*e.g.* gravity force). $\boldsymbol{s}_c^f$ is the source term considering exchange forces between the fluid and solid for the sake of viscous terms and it consists of three components, that is, $\boldsymbol{s}_c^f = (\boldsymbol{s}_{c,x}^f, \boldsymbol{s}_{c,y}^f, \boldsymbol{s}_{c,z}^f)^T$, for details, see (Yang *et al.* (2015a)).

5.3.3.1 One way coupling

In one way coupling, the following equations are used:

$$\boldsymbol{F}_{pressure}^s = \int_{\Gamma_{solid}} \boldsymbol{N}_i \boldsymbol{n} \cdot (Ip) d\Gamma, \tag{5.9}$$

$$\boldsymbol{s}_c^f = (\boldsymbol{s}_{c,x}^f, \boldsymbol{s}_{c,y}^f, \boldsymbol{s}_{c,z}^f)^T = 0, \tag{5.10}$$

where N_i denotes the finite element basis function over element i. $\boldsymbol{n}$ is the unit normal vector on the solid surface $\boldsymbol{n} = (n_x, n_y, n_z)$. I is a unit diagonal matrix and p is pressure.

5.3.3.2 Two way coupling

The two way coupling uses the following equations:

$$\boldsymbol{F}^s_{viscosity} + \boldsymbol{F}^s_{pressure} = \int_{\Gamma_{solid}} \boldsymbol{N}_i \boldsymbol{n} \cdot (\underline{\underline{\tau}}_{solid} + Ip) d\Gamma, \tag{5.11}$$

where the $\underline{\underline{\tau}}_{solid}$ is the stress term caused by viscosity; Γ_{solid} is the solid surface; $\boldsymbol{F}^s_{viscosity} = (\boldsymbol{F}^s_{viscosity,u}, \boldsymbol{F}^s_{viscosity,v}, \boldsymbol{F}^s_{viscosity,w})$ and has the form of:

$$\begin{aligned}
\boldsymbol{F}^s_{viscosity,u} &= \textstyle\int_{V_{shell}} N_i(a_{xx}u_{sl} + a_{xy}v_{sl} + a_{xz}w_{sl})dV, \\
\boldsymbol{F}^s_{viscosity,v} &= \textstyle\int_{V_{shell}} N_i(a_{yx}u_{sl} + a_{yy}v_{sl} + a_{yz}w_{sl})dV, \\
\boldsymbol{F}^s_{viscosity,w} &= \textstyle\int_{V_{shell}} N_i(a_{zx}u_{sl} + a_{zy}v_{sl} + a_{zz}w_{sl})dV,
\end{aligned} \tag{5.12}$$

where V_{shell} denotes the mesh of a shell (a thin intermediate area between the solid and fluid (see Viré *et al.* (2015))); μ is the viscosity coefficient; Δr is the thickness of the shell; $\mathbf{u}_{sl}$ is the slip velocity which is the velocity difference between the solid velocity $\mathbf{u}_s = (u_{s,u}, u_{s,v}, u_{s,w})$ and fluid velocity $\mathbf{u}_f = (u_{f,u}, u_{f,v}, u_{f,w})$, that is,

$\mathbf{u}_{sl} = \mathbf{u}_s - \mathbf{u}_f$; and

$$
\begin{aligned}
a_{xx} &= \frac{\mu}{\Delta r \Delta x_{wall}}(n_x(2-\frac{2}{3})n_x + n_y n_y + n_z n_z),\\
a_{xy} &= \frac{\mu}{\Delta r \Delta x_{wall}}(-n_x\frac{2}{3}n_y + n_y n_x),\\
a_{xz} &= \frac{\mu}{\Delta r \Delta x_{wall}}(-n_x\frac{2}{3}n_z + n_z n_x),\\
a_{yx} &= \frac{\mu}{\Delta r \Delta x_{wall}}(n_x n_y - n_x\frac{2}{3}n_y),\\
a_{yy} &= \frac{\mu}{\Delta r \Delta x_{wall}}(n_x n_x + n_y(2-\frac{2}{3})n_y + n_z n_z),\\
a_{yz} &= \frac{\mu}{\Delta r \Delta x_{wall}}(-n_y\frac{2}{3})n_z + n_z n_y),\\
a_{zx} &= \frac{\mu}{\Delta r \Delta x_{wall}}(n_x(n_z - n_z\frac{2}{3}n_x),\\
a_{zy} &= \frac{\mu}{\Delta r \Delta x_{wall}}(n_y n_z - n_z\frac{2}{3}n_y),\\
a_{zz} &= \frac{\mu}{\Delta r \Delta x_{wall}}(n_x n_x + n_y n_y + n_z(2-\frac{2}{3})n_z).
\end{aligned}
$$

Once obtaining $\boldsymbol{F}^s_{viscosity}$ and $\boldsymbol{F}^s_{pressure}$, the velocity of the solid $\boldsymbol{u}_s$=(u_s, v_s, w_s) can be calculated by equation (5.3). The source term in (5.2) can then be obtained by (Yang *et al.* (2015a)):

$$
\begin{aligned}
\boldsymbol{s}^f_{c,x} &= a_{xx}u_s + a_{xy}v_s + a_{xz}w_s,\\
\boldsymbol{s}^f_{c,y} &= a_{yx}u_s + a_{yy}v_s + a_{yz}w_s,\\
\boldsymbol{s}^f_{c,z} &= a_{zx}u_s + a_{zy}v_s + a_{zz}w_s.
\end{aligned}
\tag{5.13}
$$

5.4 Construction of FSI NIROM using POD-RBF

In this section, the method of constructing NIROM for FSI problems using POD-RBF is described. The essence of this method lies in how to construct a set of interpolation functions or hyper surfaces that represent the reduced FSI system using POD-RBF non-intrusive reduced order modelling method (see Xiao *et al.* (2015e)). Table 5.1 lists the variables used in the formulation below.

The POD method is used to form a set of POD basis functions from the snapshots which are the solutions to the high fidelity model recorded in time. The POD

Variable	Definition
$\mathbf{u}^{POD}$	POD coefficients of coupled velocity components.
p^{POD}	POD coefficients of coupled pressure components.
v^{POD}	POD coefficients of coupled volume fraction components.
$\mathbf{u}$	Coupled velocity on full space.
p	Coupled pressure on full space.
v	Volume fraction on full space.
$\overline{\mathbf{u}}$	Mean of coupled velocities over the simulation period.
$\overline{v}$	Mean of coupled volumes fraction over the simulation period.
$\overline{p}$	Mean of coupled pressures over the simulation period.
$f_{\mathbf{u}}$	Hyper surface for the coupled velocity.
f_p	Hyper surface for the coupled pressure.
f_v	Hyper surface for the volume fraction .
ϕ	General radial basis functions.
$\Phi_{\mathbf{u}}$	POD basis functions of coupled velocity components.
Φ_p	POD basis functions of coupled pressure components.
Φ_v	POD basis functions of coupled volume fraction components.
N	Number of time steps.
M	Number of POD basis functions.

Table 5.1: Variables and definitions.

basis functions are optimal in the sense that they capture the most energy from the snapshots. This is achieved by performing the singular value decomposition (SVD) of the snapshots matrix A, that is, $A = E\Sigma F^T$ (E and F being orthogonal matrices, Σ being a diagonal matrix containing singular values arranged in a descending order). Then the POD basis functions Φ_i are the column of E, that is, $\Phi_j = E_{:,j}$, for $j \in \{1, 2 \dots m\}$. The solution of variables (velocity $\mathbf{u}$ for example) can be then expressed by a linear combination of the POD basis functions, $\mathbf{u} = \overline{\mathbf{u}} + \sum_{j=1}^{M} \Phi \mathbf{u}_j^{POD} (\mathbf{u}^{POD}$ being POD coefficients). For additional details of the POD theory, see (Tropea *et al.* (2007)).

The RBF interpolation method is used here to obtain the POD coefficients. The RBF interpolation method builds up a interpolation function $f_i(x)$ using a summation of N RBFs, each associated with a center $\mathbf{C}$ and weighted by an weighting coefficient w_i, that is, $f_i(x) = \sum_{i=1}^{N} w_i * \phi(\|\mathbf{x} - \mathbf{C}\|)$. A RBF is a function whose value rely on the distance from a center point $\mathbf{C}$, so that $\phi(x) = \phi(\|x - \mathbf{C}\|)$. The norm is commonly chosen as the Euclidean distance. Commonly used types of radial basis functions are multi-quadric, inverse quadratic, polyharmonic spline and Gaussian (see Xiao *et al.* (2015e)). In this work, the Gaussian RBF is chosen to

construct the approximate function. For additional details of the RBF interpolation theory, see (Wright (2003)).

The hyper surfaces of a FSI NIROM system which are used to calculate the POD coefficients have the following formulations:

$$\begin{aligned}
\mathbf{u}_j^{POD,n} &= f_{\mathbf{u},j}(\mathbf{u}^{POD,n-1}, p^{POD,n-1}, v^{POD,n-1}) = \sum_{i=1}^{N} w_{i,j} * \phi(r), \\
p_j^{POD,n} &= f_{p,j}(\mathbf{u}^{POD,n-1}, p^{POD,n-1}, v^{POD,n-1}) = \sum_{i=1}^{N} w_{i,j} * \phi(r), \\
v_j^{POD,n} &= f_{v,j}(\mathbf{u}^{POD,n-1}, p^{POD,n-1}, v^{POD,n-1}) = \sum_{i=1}^{N} w_{i,j} * \phi(r),
\end{aligned} \tag{5.14}$$

where $\mathbf{u}_j^{POD,n}, p_j^{POD,n}, v_j^{POD,n}$ are the POD coefficients of the coupled velocity, coupled pressure and volume fraction respectively (in which the subscript j denotes the j^{th} POD coefficient $j \in \{1, 2 \dots m$ and the superscript n denotes the time step); $f_{\mathbf{u},j}, f_{p,j}, f_{v,j}$ denote the hyper surfaces that represents the reduced FSI system; $w_{i,j}$ is the weight of radial basis functions; $\phi(r)$ is the radial basis function. In this work, the Gaussian radial basis function is chosen:

$$\phi(r) = e^{-(r/\sigma)^2} = e^{-((\left\|(\mathbf{u}^{POD,n-1}, p^{POD,n-1}, v^{POD,n-1}) - \mathbf{C}\right\|)/\sigma)^2}, \tag{5.15}$$

where r is a radius and $\sigma > 0$ is the shape parameter; and $\left\|(\mathbf{u}_j^{POD,n-1}, p^{POD,n-1}, v^{POD,n-1}) - \mathbf{C}\right\|$ is a scalar distance from a given center $\mathbf{C}$ defined by the L2 norm. The center $\mathbf{C}$ is chosen to be the origin of the input data. The weights $w_{i,j}$ are to be determined to ensure the hyper surface $f_{u,j}, f_{p,j}, f_{v,j}$ match the given data. The weight is obtained by solving the equation:

$$A\mathbf{w}_{i,j} = y, \tag{5.16}$$

where A is matrix associated with the radius r and $A_{k,l} = \phi(\left\|(u_k^{POD}, p_k^{POD}, v_k^{POD}) - \mathbf{C}\right\|)$, $k, l \in \{1, 2, \dots, N\}$, N is the number of data points. $y = \mathbf{u}^{POD,n}, p^{POD,n}, v^{POD,n}$ is a vector containing the POD coefficients one time step after input POD coefficients.

The FSI NIROM algorithms consist of both offline and online processes and can be described as follows:

Algorithm 4: Offline algorithm for forming FSI NIROM using POD-RBF

(1) Generate several snapshots over the time period $[0, T]$ by solving the full couple system;

(2) Form a number of POD basis functions $\Phi_{\mathbf{u}}$, Φ_p and Φ_v through POD method;

(3) Obtain the functional values y at the data point $\mathbf{u}^{POD,t}, p^{POD,t}, v^{POD,t}$ through the solution from the full models, where $t \in \{1, 2, \ldots T\}$;

(4) Calculate the weights $\mathbf{w}_{i,j}$ by solving (5.16);

(5) Obtain a set of hyper surfaces by substituting the weight values obtained in above step into equation (5.14);

The online algorithm 5 described below will be used for calculation of the values of coupled velocity $\mathbf{u}$, coupled pressure p and volume fraction v.

Algorithm 5: Online calculation of the POD coefficients for FSI NIROM

(1) Initialize $\mathbf{u}_j^{POD,0}$, $p_j^{POD,0}$ and $v_j^{POD,0}$;

(2) Calculate solutions at current time step using following loop:

for $n = 1$ *to* N **do**

for $j = 1$ *to* M **do**

Solving fluid process:

(i) Assign a complete set of POD coefficients $u^{POD,n-1}$, $p^{POD,n-1}$ and $v^{POD,n-1}$ at previous time step $n-1$ to equation:

$$\begin{aligned} f_{\mathbf{u},j} &\leftarrow (\mathbf{u}^{POD,n-1}, p^{POD,n-1}, v^{POD,n-1}), \\ f_{p,j} &\leftarrow (\mathbf{u}^{POD,n-1}, p^{POD,n-1}, v^{POD,n-1}), \\ f_{v,j} &\leftarrow (\mathbf{u}^{POD,n-1}, p^{POD,n-1}, v^{POD,n-1}), \end{aligned}$$

(ii) Calculate the POD coefficient $u^{POD,n}$, $p^{POD,n}$ and $v^{POD,n}$ at current time step n using the following equations:

$$\begin{aligned} \mathbf{u}_j^{POD,n} &= f_{\mathbf{u},j} = \sum_{i=1}^{N} w_{i,j} * \phi_{\mathbf{u}}(r), \\ p_j^{POD,n} &= f_{p,j} = \sum_{i=1}^{N} w_{i,j} * \phi_{p}(r), \\ v_j^{POD,n} &= f_{v,j} = \sum_{i=1}^{N} w_{i,j} * \phi_{v}(r), \end{aligned}$$

endfor

Obtain the solution $\mathbf{u}^n$, p^n and v^n on full space at current time step n by projecting $\mathbf{u}_j^{POD,n}$, $p_j^{POD,n}$ and $v_j^{POD,n}$ onto the full space.

$$\mathbf{u}^n = \overline{\mathbf{u}} + \sum_{i=1}^{M} \Phi_{\mathbf{u}} u_i^{POD,n}, \quad p^n = \overline{p} + \sum_{i=1}^{M} \Phi_p p_i^{POD,n}, \quad v^n = \overline{v} + \sum_{i=1}^{M} \Phi_v v_i^{POD,n},$$

Solving solid-fluid coupling:

If (one way coupling) then

$\boldsymbol{F}^s_{pressure} = \int_{\Gamma_{solid}} N_i n \cdot (Ip) d\Gamma, \quad \boldsymbol{s}_c^f = (\boldsymbol{s}_{c,x}^f, \boldsymbol{s}_{c,y}^f, \boldsymbol{s}_{c,z}^f)^T = 0.$

Else If (two way coupling)

$\boldsymbol{F}^s_{viscosity} + \boldsymbol{F}^s_{pressure} = \int_{\Gamma_{solid}} N_i n \cdot (\underline{\underline{\tau}}_{solid} + Ip) d\Gamma,$

obtain $\boldsymbol{s}_c^f = (\boldsymbol{s}_{c,x}^f, \boldsymbol{s}_{c,y}^f, \boldsymbol{s}_{c,z}^f)^T$ using equation (5.13).

End If

endfor

5.5 Illustrative numerical examples

The FSI NIROM has been implemented under the framework of a combined finite-discrete element solid model (Y2D) and an advanced 3D unstructured mesh multi-phase fluid model (FLUIDITY).

The solid model, Y2D, uses a finite-strain formulation to solve the structural dynamics equations and is capable of modelling fracture network with any stiffness and shapes, vibration modes and stresses (see for instance, Xiang *et al.* (2009); Latham *et al.* (2009); Lei *et al.* (2014, 2015)). It is coupled with the fluid multi-phase model FLUIDITY (see Pain *et al.* (2005)) to solve the fluid and solid coupling problem.

The fluid model, FLUIDITY, is capable of solving the Navier-Stoke equations and accompanying field equations on unstructured 1D, 2D and 3D finite element meshes. In order to obtain more accurate and stable solution from the high fidelity full model, a $P1_{DG}P2$ element pair is used in this work to accurately represent velocity and pressure changes between heterogeneous domains. The discontinuous Galerkin method is used for velocity while the continuous Galerkin method is used for pressure. One advantage of this FE pair is the mass matrix for velocity is a block diagonal matrix so that it can be trivially inverted. Another advantage is that it allows the order of the pressure to be increased to quadratic whilst maintaining Ladezinskya-Babuska-Brezzi (LBB) stability (see Cotter *et al.* (2009)). This element also has the ability represent very accurately the balance between the pressure or free surface gradients and the Coriolis force as well as buoyancy forces.

5.5.1 One way coupling test case - flow past a cylinder

The first case for numerical illustration of the method proposed in this chapter is a one-way coupling test case: flow past a solid cylinder case. This problem domain consists of a rectangle of non-dimensional size 2.2×0.41 and the radius of the solid cylinder is 0.05.

The problem was discretised with a mesh of 20058 nodes during the simulation time period $[0, 4]$ with a time step size of $\Delta t = 0.001$ which ensures the Courant number is smaller than 0.5. 100 snapshots were taken from the pre-computed solutions at regularly spaced time intervals 0.04 and a number of POD bases were generated for variables $\mathbf{u}, p, v$ through these snapshots.

Figure 5.1 shows the singular eigenvalues in order of decreasing magnitude. In general, the more POD bases are chosen, the more energy can be captured. In this case, as shown in figure 5.1, the singular eigenvalues decrease satisfying the Kolmogorov criterion drastically in the first 2 leading singular eigenvalues, which means the first 2 POD bases captured most energy (79.28%). This figure provides a criterion for choosing the number of POD bases.

Figure 5.2 shows the velocity solutions at time instances $t = 2.0$ and $t = 3.2$, as calculated using the high fidelity full model and FSI NIROM with 3, 6 and 20 POD bases. It can be seen that the FSI NIROM attains closer agreement to the full model as more POD bases are chosen. The FSI NIROM has captured 82.90%, 90.99%, 98.35% of energy in fluid dynamics using 3, 6 and 20 POD bases respectively in this example.

Figure 5.3 shows the error in velocity solutions predicted by the FSI NIROM using 3, 6 and 20 POD bases at time instances 2.0 and 3.2. The error in velocity solutions is decreased by 80% when the number of POD bases is increased from 3 to 20. The FSI NIROM with 20 POD bases exhibits an overall good agreement with the high fidelity full model.

To further assess the accuracy of the FSI NIROM, the velocity solution at a particular point ($x = 0.27543, y = 0.29336$) is displayed in figure 5.4. Again shown in this figure, an increase in the number of POD bases results in improved accuracy, which is consistent with the results shown in figure 5.2 and 5.3.

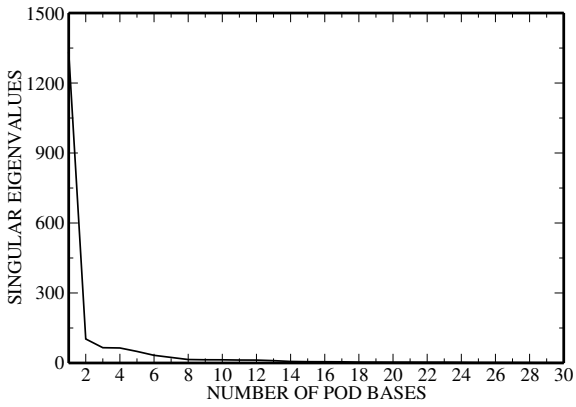
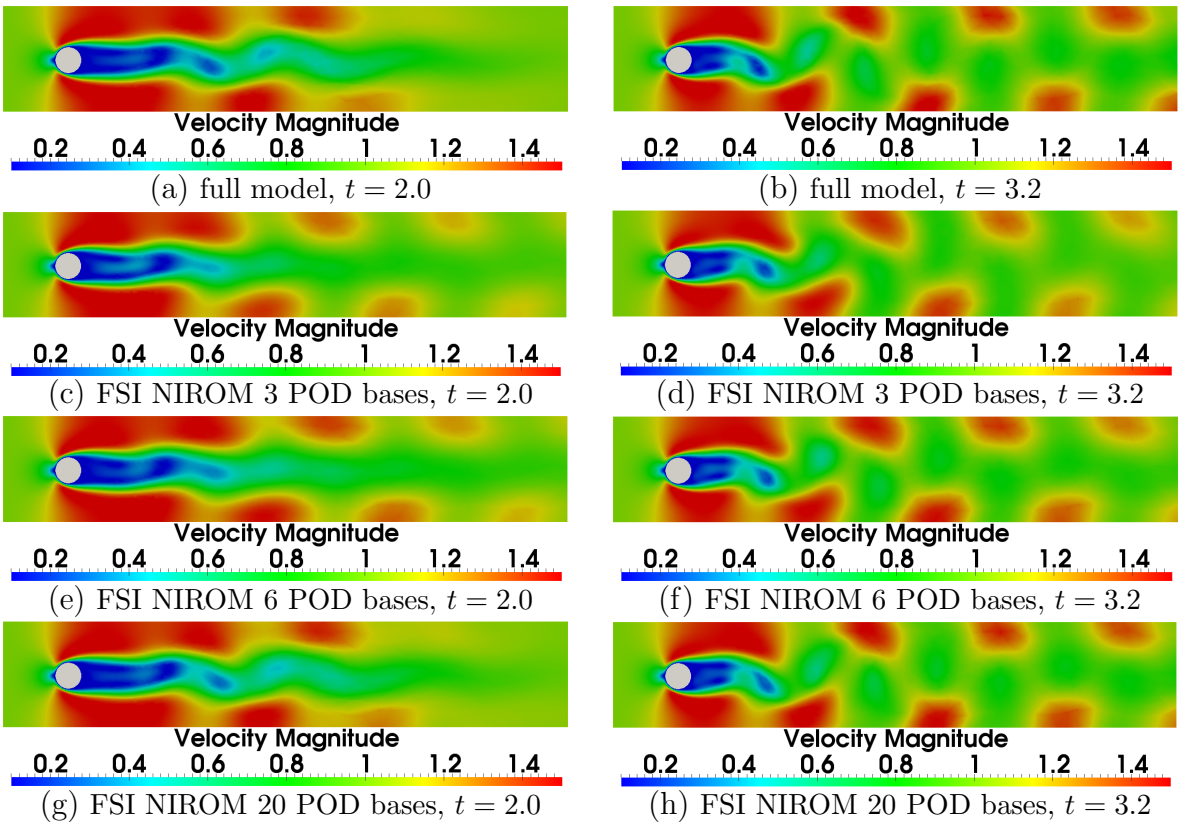


Figure 5.1: Flow past a cylinder: the figure shows the singular eigenvalues in order of decreasing magnitude.



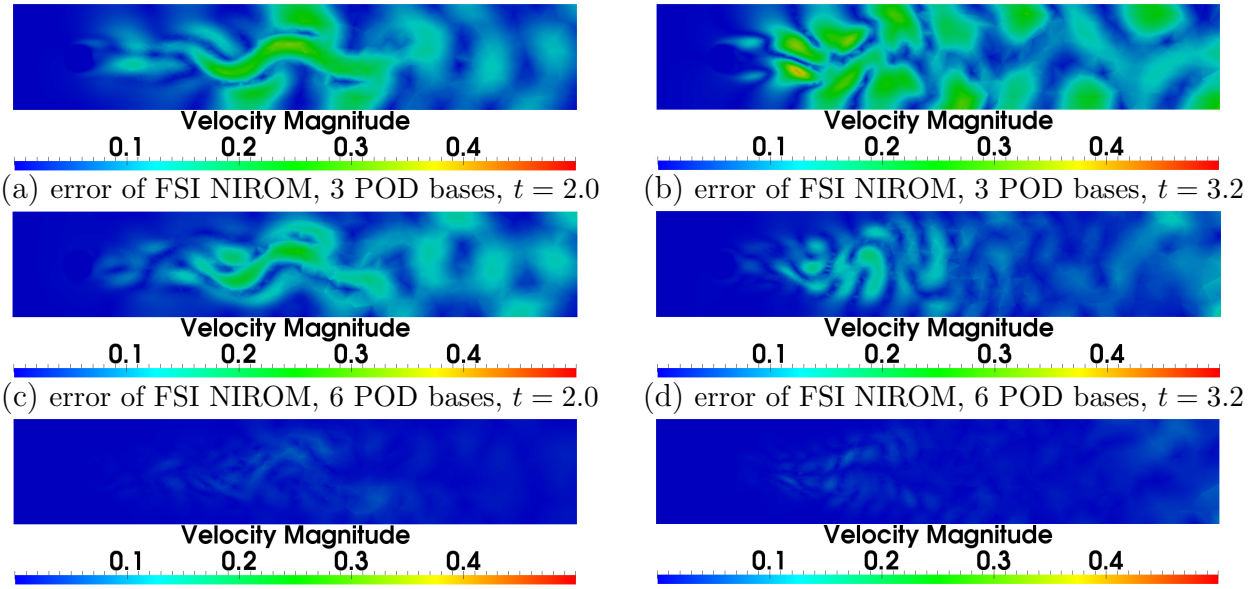
(a) full model, $t = 2.0$ (b) full model, $t = 3.2$

(c) FSI NIROM 3 POD bases, $t = 2.0$ (d) FSI NIROM 3 POD bases, $t = 3.2$

(e) FSI NIROM 6 POD bases, $t = 2.0$ (f) FSI NIROM 6 POD bases, $t = 3.2$

(g) FSI NIROM 20 POD bases, $t = 2.0$ (h) FSI NIROM 20 POD bases, $t = 3.2$

Figure 5.2: Flow past a cylinder: the figures displayed above show the velocity solutions at time instances 2.0 (left panel) and 3.2 (right panel). In NIROM, 3, 6 and 20 POD bases are chosen with 100 snapshots).



(a) error of FSI NIROM, 3 POD bases, $t = 2.0$ (b) error of FSI NIROM, 3 POD bases, $t = 3.2$

(c) error of FSI NIROM, 6 POD bases, $t = 2.0$ (d) error of FSI NIROM, 6 POD bases, $t = 3.2$

(e) error of FSI NIROM, 20 POD bases, $t = 2.0$ (f) error of FSI NIROM, 20 POD bases, $t = 3.2$

Figure 5.3: Flow past a cylinder: the figures displayed above show the solution difference between the full model and the FSI NIROM using 3, 6 and 20 POD bases at time instances 2.0 (left panel) and 3.2 (right panel).

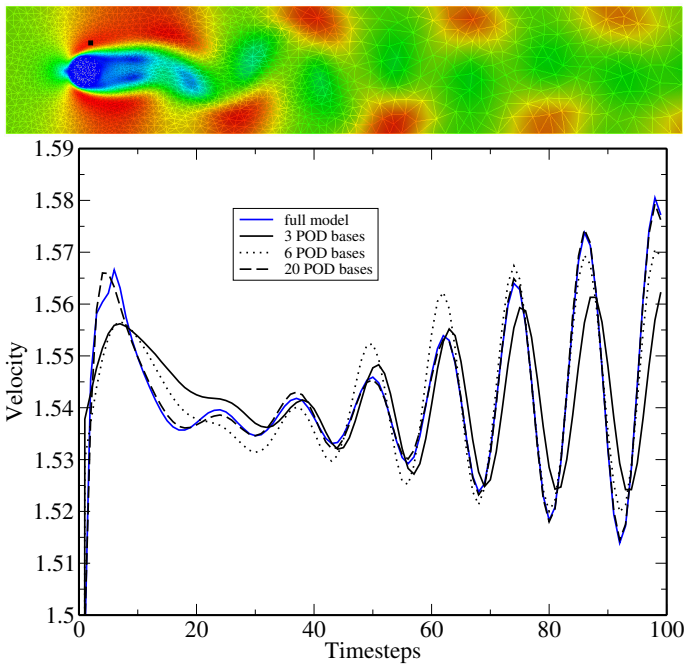


Figure 5.4: A 2D free-falling square in water: Velocity solution from high fidelity model and FSI NIROM using 3, 6 and 20 POD bases at point (x=0.27543, y=0.29336)

5.5.2 Two-way coupling case - a 2D free-falling square in water

The second illustrative case is a 2D free-falling case, that is, a square that falls through a vertical domain is subjected to the gravitational force. The domain has a non-dimensional size of 2.5×10 and the size of the solid square is 0.25×0.25. The number of nodes on the mesh is 93000. The length of the simulation time period is $2.5\,s$. The time step is set to $0.01\,s$ which ensures the Courant number is smaller than 0.5. 250 snapshots were recorded at each time step.

Figure 5.5 shows the singular eigenvalues in order of decreasing magnitude. Figure 5.6 shows the first 72 POD bases. It can be seen that most of flow features are captured within the first 12 leading POD bases while the small-scale flow features are represented by the 36^{th} - 72^{th} POD bases. The first few POD bases are capable of capturing most of the energy. In this work, 12, 36 and 72 POD bases are chosen to illustrate how to improve the accuracy of results by increasing the number of POD bases.

Figure 5.7 depicts the velocity solutions from the full model and NIROM at time instances $t = 1.0\,s$, $1.5\,s$, $2.0\,s$ and $2.5\,s$. It can be seen that the FSI NIROM performs well using 12 POD bases, better results are obtained by increasing the number of POD bases to 72, which captured almost 99% of the total energy.

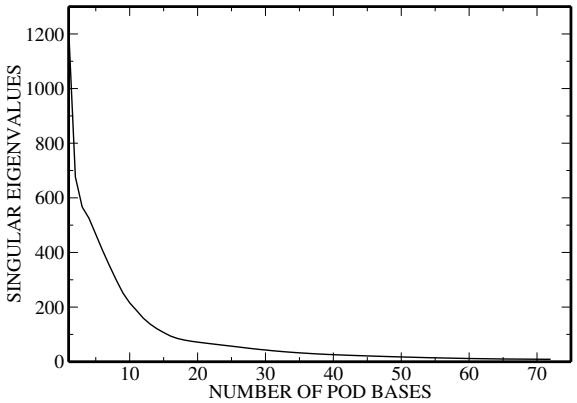
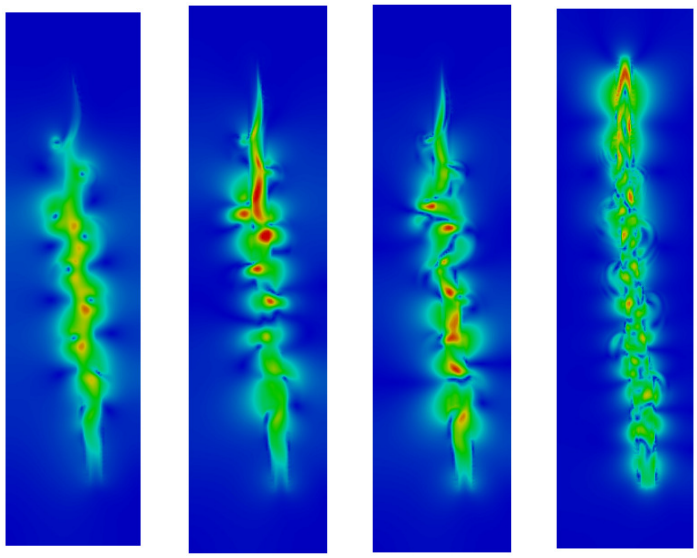
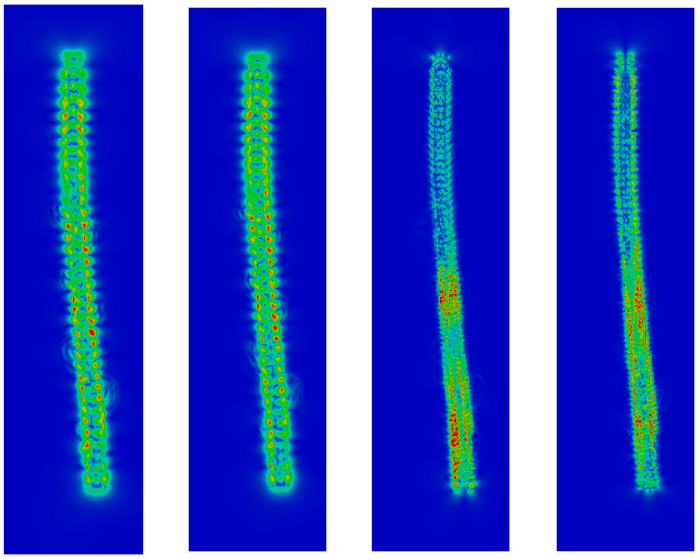


Figure 5.5: A 2D free-falling square in water: the figure shows the singular eigenvalues in order of decreasing magnitude.

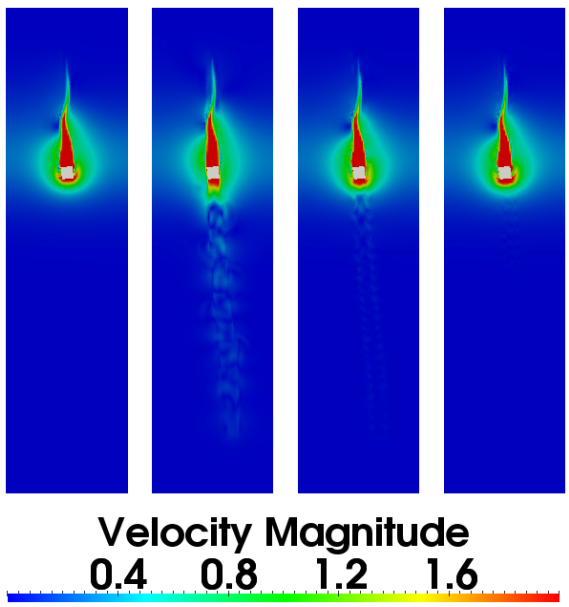


(a) 1st (b) 2nd (c) 3rd (d) 12th

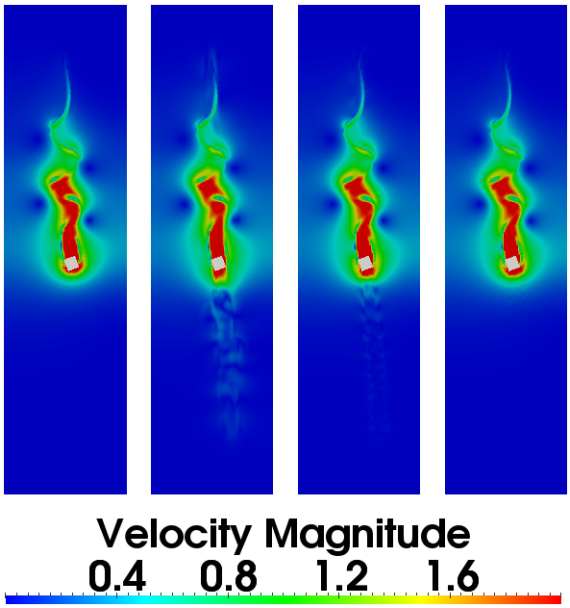


(a) 36th (b) 38th (c) 71st (d) 72th

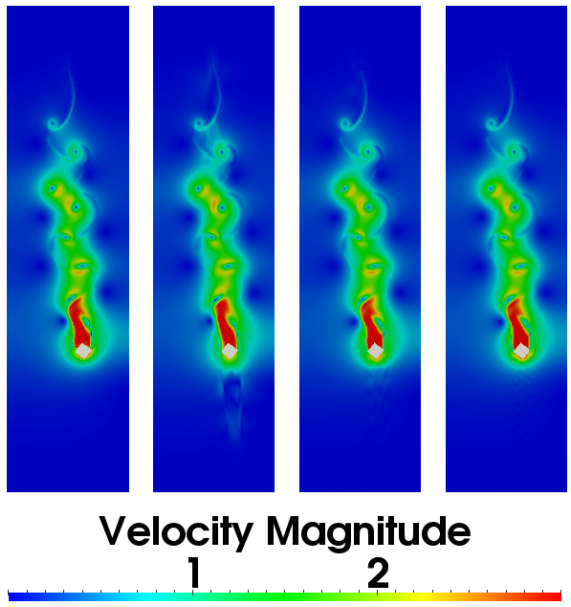
Figure 5.6: A 2D free-falling square in water: the figures displayed above show the first, second, third, $12^{th}, 36^{th}, 38^{th}, 71^{th}$ and 72^{th} POD bases.



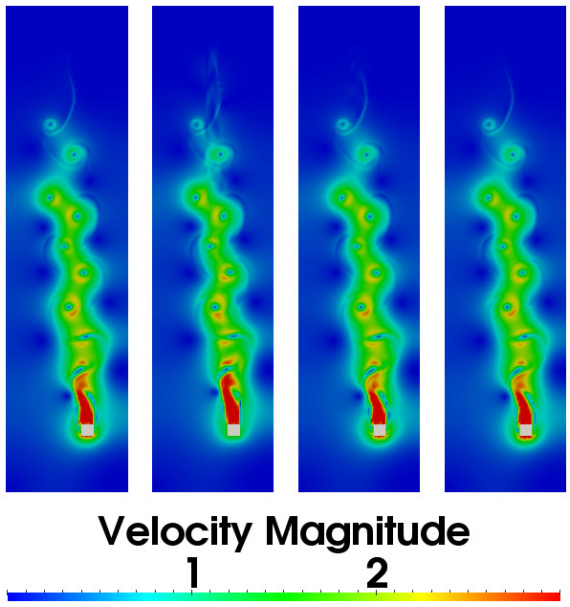
(a) Full model, NIROM with 12, 36 and 72 POD, $t = 1.0$



(b) Full model, NIROM with 12, 36 and 72 POD, $t = 1.5$



(c) Full model, NIROM with 12, 36 and 72 POD, $t = 2.0$



(d) Full model, NIROM with 12, 36 and 72 POD, $t = 2.5$

Figure 5.7: A 2D free-falling square in water: the figures displayed above show the solutions from full model and NIROM using 12, 36 and 72 POD bases at $t = 1.0$ (top left panel), $t = 1.5$ (top right panel), $t = 2.0$ (bottom left panel) and $t = 2.5$ (bottom right panel). In each panel, from left to right, full model, NIROM with 12, 36 and 72 POD basis functions, respectively.

5.5.3 Vortex-induced vibrations of an elastic beam

The third case is the vortex-induced vibrations of an elastic beam embedded in fluids. The computational domain is presented in figure 5.8 which has an elastic solid beam with a density of 100 enclosed within a rectangle computational domain. The rectangle computational domain has a non-dimensional size of 6×2. The elastic beam with a density of 100 has a size of 1×0.286 and is located on the bottom in the middle of the rectangle. A slip boundary condition is applied to the top, bottom and left sides, an open boundary condition applied to the right side. The inlet velocity at the left side is set to 20. The simulation period is $[0, 0.5]$ with a time step size of $\Delta t = 0.001$ which ensures the Courant number is smaller than 0.5.

The vortex-induced vibration problem was solved using an unstructured mesh of 28800 nodes illustrated in figure 5.8. 100 snapshots were taken at a regularly spaced time intervals 0.005. From these snapshots, a number of POD bases were generated.

Figure 5.9 presents the velocity solutions obtained from the high fidelity model and FSI NIROM with 6, 12 and 50 POD bases at time instances $t = 0.15$ and $t = 0.5$. It illustrates that the solutions from FSI NIROM are in close agreement with the high fidelity full model. It can be seen from the figure that only 6 POD bases already captured the velocity profiles well. The complex flow patterns are captured very well by using a larger number of POD bases − as shown in figures 5.9(g) and 5.9(h). It is also shown that the solution of FSI NIROM is closer to that of high fidelity full model as the number of POD bases is increased. This is illustrated by figure 5.10 which shows the error of velocity solutions predicted by the FSI NIROM with 6, 12 and 50 POD bases at time instances $t = 0.15$ and $t = 0.5$. It is evident that FSI NIROM with a larger number of POD bases exhibits less error.

Figure 5.11 presents the pressure profiles obtained from the high fidelity model and FSI NIROM with 6, 12 and 50 POD bases at time instances $t = 0.15$ and $t = 0.5$. It is shown that the FSI NIROM with 50 POD bases is in closer agreement with the high fidelity full model. In order to investigate the difference between the high fidelity model and FSI NIROM, the pressure solutions at a particular point $(x = 2, y = 1.05)$ in the computational domain are presented in figure 5.12. The figure shows that FSI NIROM with 12 and 50 POD bases exhibits a very good agreement with the high fidelity full model.

To validate the accuracy of FSI NIROM, the correlation coefficients and root mean

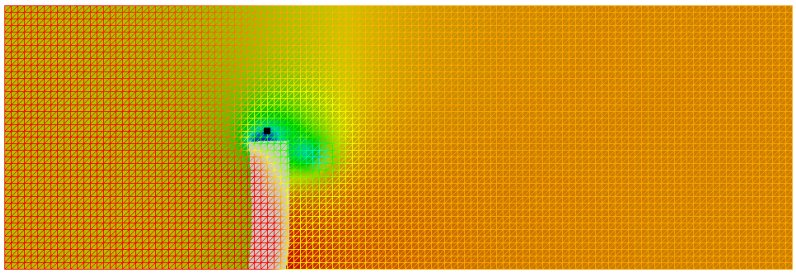
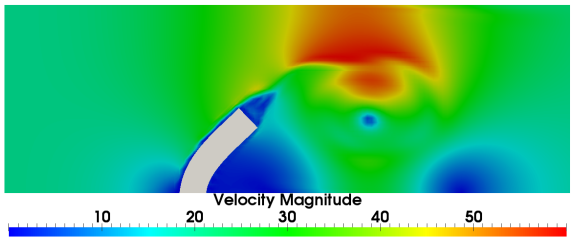
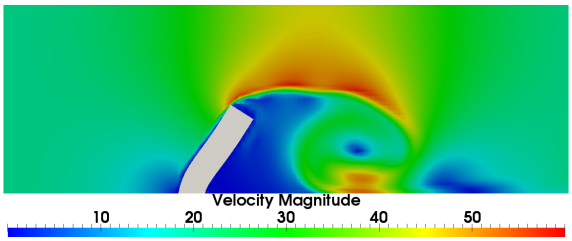


Figure 5.8: Vortex-induced vibrations: A comparison of pressure solutions between the high fidelity model and FSI NIROM at a particular point(x=2, y=1.05).

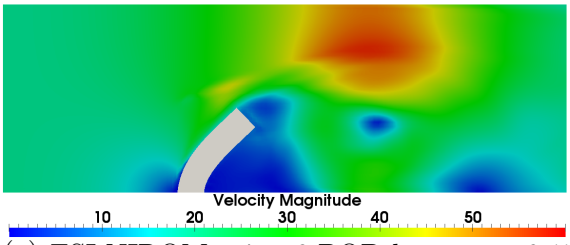
squared error (RMSE) of pressure solutions are provided in figure 5.13. It is seen that the FSI NIROM performs better when using a larger number of POD bases. Using 50 POD bases, the errors in pressure solutions are decreased by 30%-50% in comparison to that using 6 POD bases.



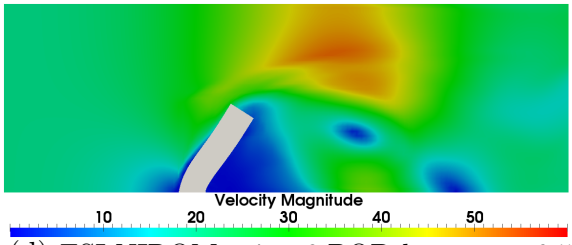
(a) full model, $t = 0.15$



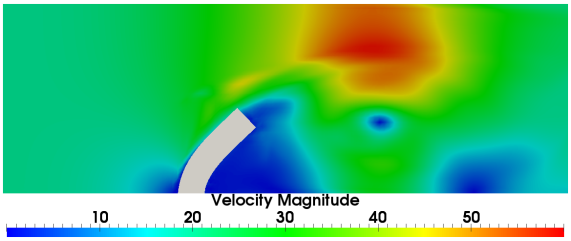
(b) full model, $t = 0.5$



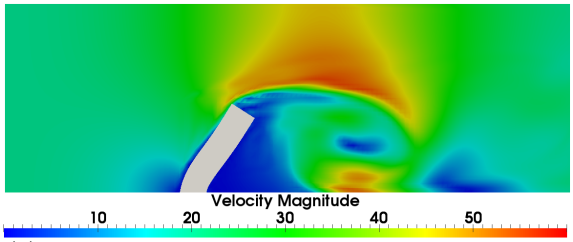
(c) FSI NIROM using 6 POD bases, $t = 0.15$



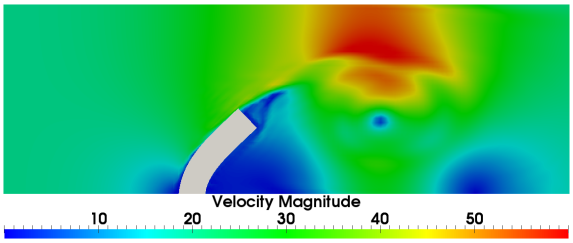
(d) FSI NIROM using 6 POD bases, $t = 0.5$



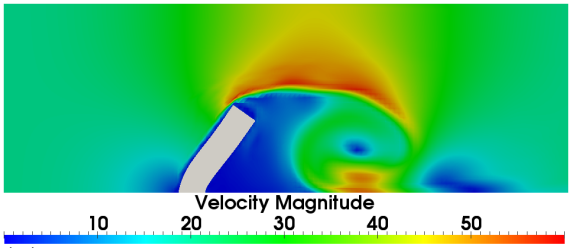
(e) FSI NIROM using 12 POD bases, $t = 0.15$



(f) FSI NIROM using 12 POD bases, $t = 0.5$

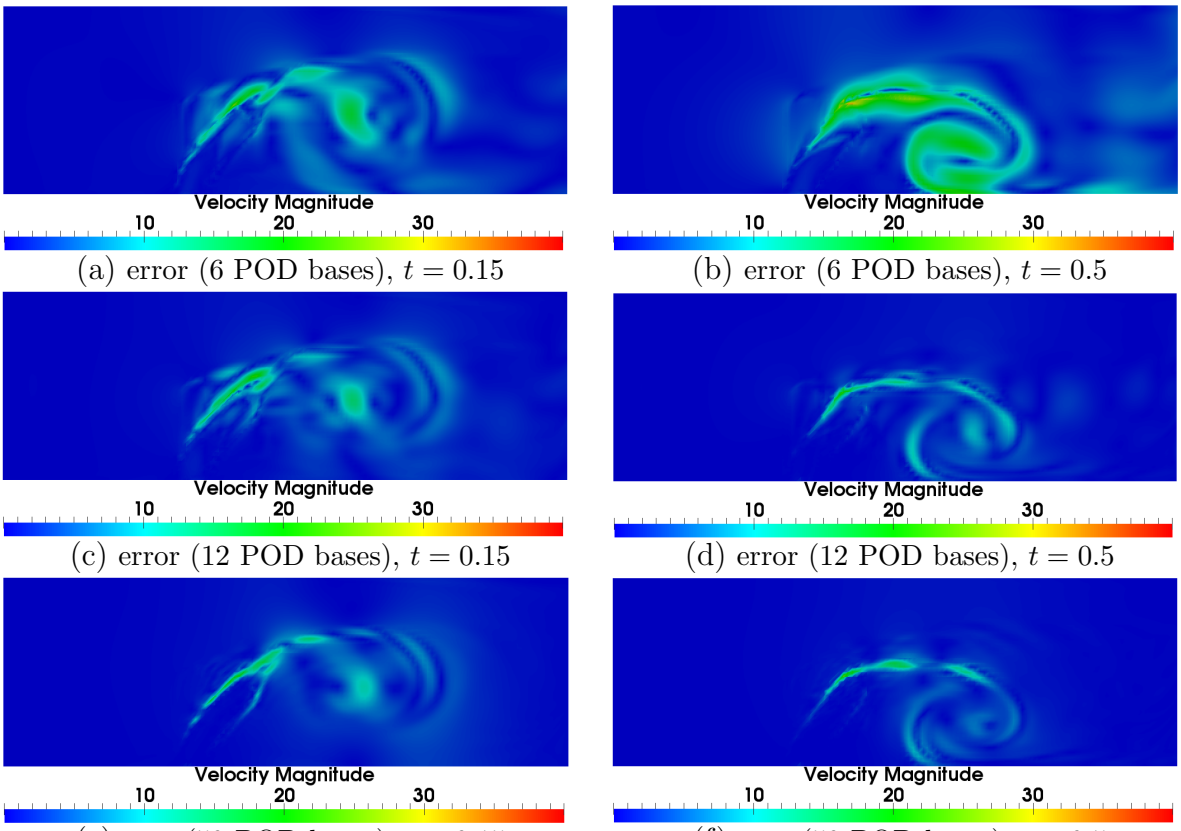


(g) FSI NIROM using 50 POD bases, $t = 0.15$



(h) FSI NIROM using 50 POD bases, $t = 0.5$

Figure 5.9: Vortex-induced vibrations: A comparison of velocity solutions between the high fidelity model and FSI NIROM with 6, 12 and 50 POD bases at time instances $t = 0.15$ (left panel) and $t = 0.5$ (right panel).



(a) error (6 POD bases), $t = 0.15$

(b) error (6 POD bases), $t = 0.5$

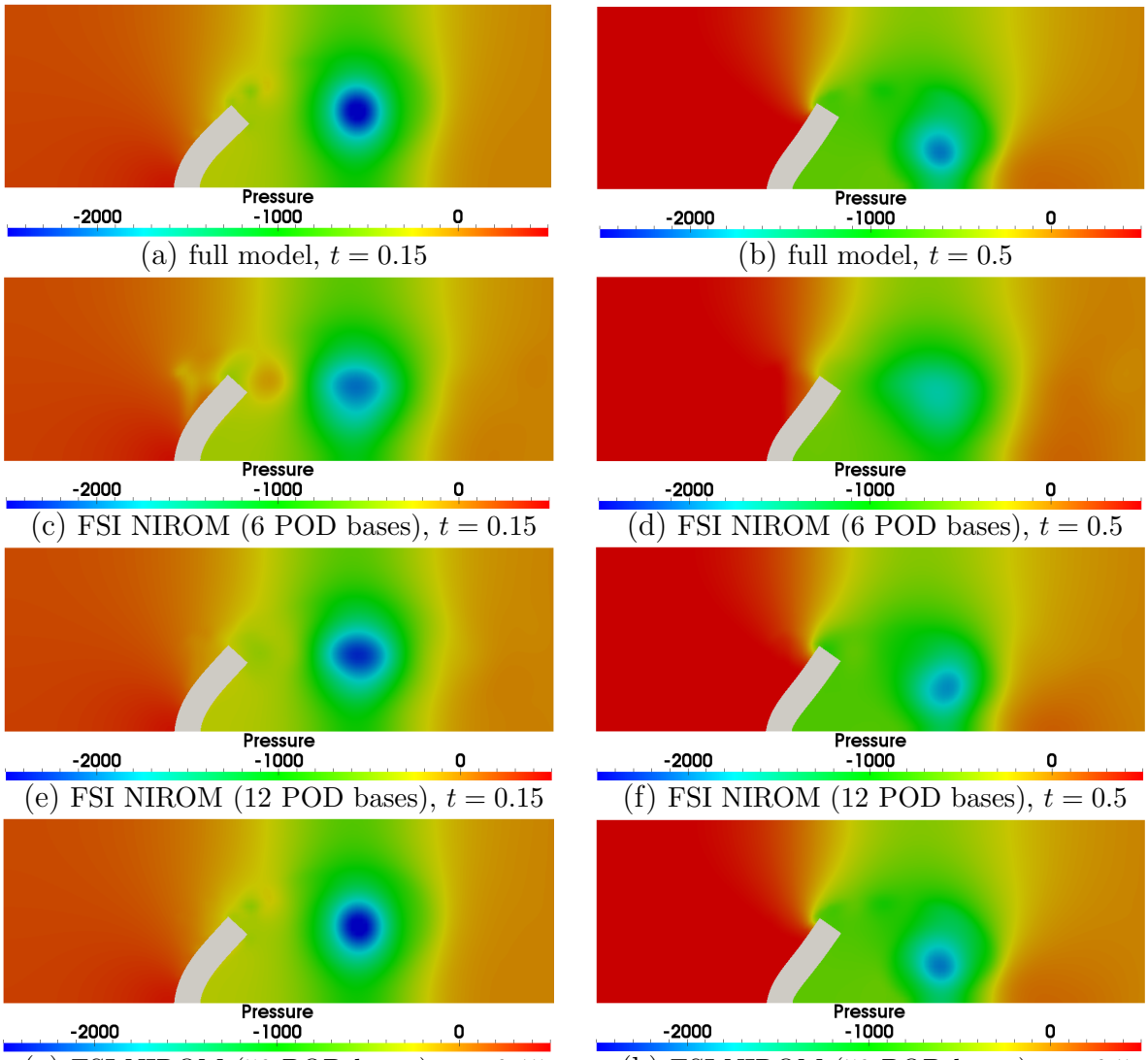
(c) error (12 POD bases), $t = 0.15$

(d) error (12 POD bases), $t = 0.5$

(e) error(50 POD bases), $t = 0.15$

(f) error(50 POD bases), $t = 0.5$

Figure 5.10: Vortex-induced vibrations: Error in velocity solutions obtained from FSI NIROM with 6, 12 and 50 POD bases at time instances $t = 0.15$ (left panel) and $t = 0.5$ (right panel).



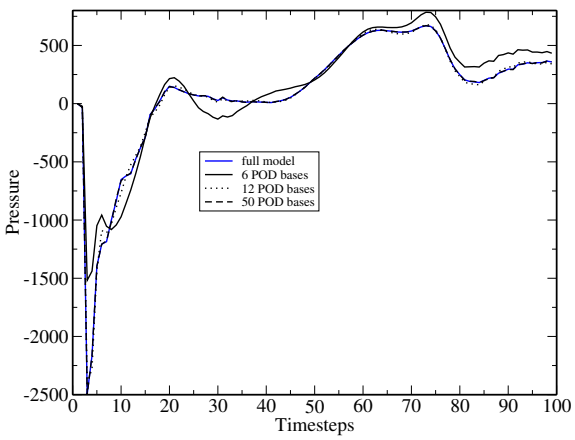
(a) full model, $t = 0.15$ (b) full model, $t = 0.5$

(c) FSI NIROM (6 POD bases), $t = 0.15$ (d) FSI NIROM (6 POD bases), $t = 0.5$

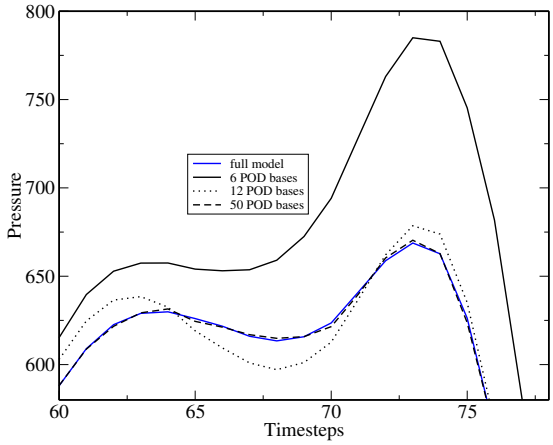
(e) FSI NIROM (12 POD bases), $t = 0.15$ (f) FSI NIROM (12 POD bases), $t = 0.5$

(g) FSI NIROM (50 POD bases), $t = 0.15$ (h) FSI NIROM (50 POD bases), $t = 0.5$

Figure 5.11: Vortex-induced vibrations: A comparison of Pressure solutions between the high fidelity model and FSI NIROM with 6, 12 and 50 POD bases at time instances $t = 0.15$ (left panel) and $t = 0.5$ (right panel).

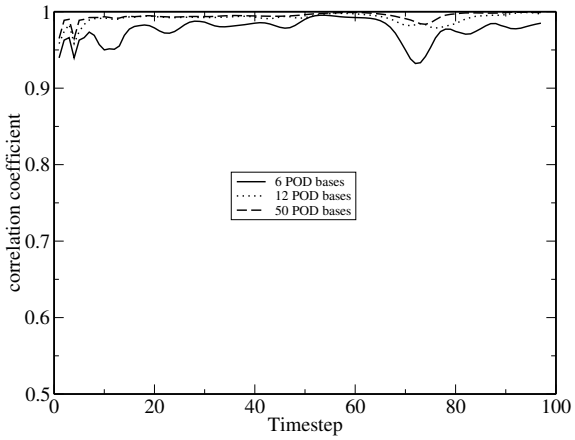


(a) Pressure solution

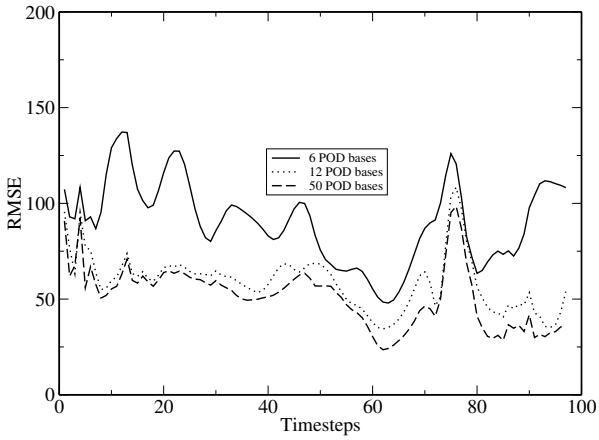


(b) Blowup of the pressure solution in (a)

Figure 5.12: Vortex-induced vibrations: A comparison of pressure solutions between the high fidelity model and FSI NIROM at a particular point(x=2, y=1.05).



(a) Correlation coefficient



(b) RMSE

Figure 5.13: Vortex-induced vibrations: RMSE and correlation coefficient of pressure solutions between the high fidelity and FSI NIROM with 6, 12 and 50 POD bases.

5.5.4 Computational efficiency of the FSI NIROM

In this section, the online computational cost required for running three test cases from the high fidelity full model and FSI NIROM is provided. The simulations were performed on 12 cores machine of an Intel(R) Xeon(R) X5680 processor with 3.3GHz and 48GB RAM. The test cases were run in serial, which means only one core was used when simulating. Table 5.2 shows the online CPU time (seconds) required for running the full model and FSI NIROM ROM at one time step for three test cases. The offline CPU cost including forming the POD bases and the interpolation functions is not listed here since they are not required for each time step.

Table 5.2: Online CPU time (seconds) required for running the full model and FSI NIROM one time step for three test cases.

Cases	Model	Assembling and Solving	Projection	Interpolation	Total
Flow past a cylinder	Full model	290.6667	0	0	290.6667
	FSI NIROM	0	0.0003	0.0001	0.00040
Free-falling square	Full model	29.2786	0	0	29.2786
	FSI NIROM	0	0.0003	0.0001	0.00040
Bending beam	Full model	102.6269	0	0	102.6269
	FSI NIROM	0	0.0003	0.0001	0.00040

Table 5.2 shows that the computational cost of FSI NIROM required for the test cases is reduced significantly by 5-6 orders of magnitude. Only interpolating the POD coefficients and projecting the POD coefficients back onto the full space are involved in the online calculation of FSI NIROM. In addition, the FSI NIROM is expected to gain more CPU savings if a finer mesh is used.

5.6 Conclusion

A POD-RBF method has been, for the first time, used to construct a non-intrusive reduced order model for the fluid-structure interactions (FSI) problem and developed under the framework of the combined finite-discrete element method based solid model (Y2D) and unstructured mesh finite element multi-phase model (FLUIDITY). A RBF multi-dimensional interpolation method is used to construct a set

of interpolated hyper surfaces representing the reduced FSI system. Due to non-intrusiveness, the novel FSI NIROM for fluid-solid coupling modelling is independent of the original system and source code for fluid and solid simulations, therefore, it is easy to be extended to future developments and applications.

The performance of the novel FSI NIROM has been demonstrated by three test coupling cases: a one-way coupling case (flow past a cylinder), two two-way coupling cases (a free-falling cylinder in water and a vortex-induced vibrations of an elastic beam case). A detailed comparison between the high fidelity model and FSI NIROM has been carried out. An accuracy assessment has also been made for the FSI NIROM. The numerical simulations show that the FSI NIROM exhibits comprehensive good agreement with the high fidelity model. The results of FSI NIROM can be improved by choosing a larger number of POD bases. A significant CPU speed-up has been obtained by the FSI NIROM method and additional speed-up can be expected as the number of nodes is increased.

Chapter

SIX

Model reduction for compressible fluid-solid coupling and its application to blasting

6.1 Abstract

An non-intrusive reduced order model (NIROM) based on POD-RBF is applied to compressible fluid and structure interactions. The first novelty of this chapter lies in its first development of NIROM for compressible fluid and structure interactions problems and fracture models. The second novelty is the application to a blasting test case. The performance of the NIROM for structure interacting with compressible fluid flows and fracture models is illustrated by two complex test cases: a bending beam forced by flows and a blasting test case. The numerical simulation results show that the NIROM is capable of capturing the details of compressible fluid and structure interactions and fractures and the CPU time is reduced by several orders of magnitude.

In addition, the mean subtraction issue before performing POD is discussed in this chapter. The results show that solutions without mean subtraction before performing POD are shown to be better than that with mean subtraction.

This chapter is derived from and expands upon Xiao *et al.* (2015b).

6.2 Introduction

The work described in this chapter, for the first time, apples the non-intrusive reduced order modelling method to compressible fluid and structure interaction problem and fracture problem. It is noteworthy that this work is the first work of building a reduced order model for the blasting test case. This model has been implemented under the framework of a combined finite-discrete element method based solid model (Y2D) and an unstructured mesh finite element model (FLUIDITY).

During the POD process, the mean of the snapshots is normally subtracted. The problem of mean subtraction was discussed in the work (Chen *et al.* (2012a); Müller (2008)). In their work, there are not much difference between the results with mean subtraction and results without mean subtraction. In this chapter, the solutions with mean subtraction and without mean subtraction are presented and discussed.

The performance of this compressible FSI NIROM without mean subtraction has been assessed by two test cases: a bending beam forced by flows and a blasting test case. Comparison between high fidelity full model and the compressible FSI NIROM without mean subtraction using different number of POD bases has been made to validate the accuracy.

The structure of the chapter is as follows: section 6.3 presents the compressible fluid and solid coupling problem; section 6.4 derives the formulation of a non-intrusive reduced order model for compressible fluid and structure interactions and fracture problems using POD-RBF method; section 6.5 demonstrates the capability of the derived methodology by two numerical examples: a bending beam forced by flows and a blasting test case. Finally in section 6.6, the conclusion is presented.

6.3 Description of compressible fluid and solid coupling problem

This work is carried out under the framework of an unstructured mesh multiphase fluid model (FLUIDITY) and a combined finite-discrete element solid model (Y2D),

therefore, the governing equations, coupling methods and fracture modelling methods used in those models are described in this section.

6.3.1 Governing equations for compressible fluids under the framework of FLUIDITY

"FLUIDITY" is a computational fluid dynamics open source model capable of numerically solving the 2-D and 3-D Navier-Stokes equation using finite element discretisation method, and the governing equations for compressible fluids in "Fluidity" have the following form Pain *et al.* (2005); AMCG & London (2015),

$$\frac{\partial \rho}{\partial t} + \nabla \cdot (\rho \mathbf{u}) = 0, \tag{6.1}$$

$$\frac{\partial}{\partial t}(\rho \mathbf{u}) + \nabla \cdot (\rho \mathbf{u}\mathbf{u} - \sigma) = \rho \mathbf{F}, \tag{6.2}$$

$$\frac{\partial}{\partial t}(\rho E) + \nabla \cdot (\rho E \boldsymbol{u} - \tau \boldsymbol{u} + \boldsymbol{q}) = \rho \boldsymbol{F} \boldsymbol{u}, \tag{6.3}$$

where ρ denotes the unknown density, $\mathbf{u}$ is the unknown velocity vector, t represents the time, σ is the stress tensor and $\sigma = \tau - p$, p being the unknown pressure, $\mathbf{F}$ is the volume or internal force per unit mass (*e.g.*, gravity). And $\boldsymbol{q}$ denotes the rate of volumetric heat addition per unit mass, $E = e + \mid \boldsymbol{u} \mid^2 /2$ is the total specific unknown energy. τ is the shear stress of fluid.

The density ρ is calculated by the equation of state, which is used to close the governing equation (6.3) Anderson & Wendt (1995):

$$p = \rho(\gamma - 1)e, \tag{6.4}$$

where p is the pressure, $\gamma = C_p/C_v$ is a heat capacity ratio (C_v and C_p being the specific heat at constant volume and at constant pressure respectively), $e = C_v T$ is the internal energy per unit mass ("the specific internal energy"), T being temperature.

6.3.2 Fracture modelling

The fracture model in the combined finite-discrete element method (FEMDEM) based solid model (Y2D) treats the whole domain as a multi-body system. Each

body is discretised into the finite element mesh. The fracture model is comprised of the finite element formulation and discrete element formulation. The finite element formulation is used to model continuum behaviour (*i.e.* calculation of stress and strain) before fractures are generated. If the failure criterion is met, the discrete element formulation is then used for modeling discontinuum behaviour (contact forces between discrete bodies and distribution of the contact force to nodes). The combination of the finite element formulation and discrete element formulation ensures the transition from continuum behaviour to discontinuum behaviour can be captured accurately. Combined single and smeared crack model with the Mohr-Coulomb failure criterion is used.

Algorithm 6: Fracturing simulation

(1) Input data (discontinuous solid meshes).
(2) Insert 4-noded joint elements between 3-node triangular elements, see Figure 6.1.
(3) Calculate stresses using the finite element formulation.
(4) Judge whether new fractures are generated using the Mohr-Coulomb failure criterion.
if new fractures are generated **then**
  add new contact couples.
else
  detect contact couples in DEM domain.
end if
(5) Calculate contact forces in DEM domain.
(6) Calculate velocity of each node through explicit time integration.
$u_{solid}^{t+1} = u_{solid}^{t} + u_{acceleration}\Delta t$
$u_{acceleration} = \frac{f_{external} - f_{internal}}{m}$
(7) Output data.
(8) Goto step (3): calculate stresses using the finite element formulation.
(9) Stop.

The overall fracture modelling algorithm based on FEMDEM is given in algorithm 6 (for details, see Guo *et al.* (2015); Munjiza *et al.* (1999)), where u_{solid}^{t} denotes the solid velocity vector at each node at the time step t, $u_{acceleration}$ is the acceleration, Δt is the time step, $f_{external}$ and $f_{internal}$ are the external and internal forces at each node respectively, and m is the mass of the node.

In fracture modelling, triangular elements and joint elements are introduced, as shown in Figure 6.1. The figure shows two 2-D solid discontinuous elements and a

inserted 4-noded joint element. The solid domain is firstly discretised by numerous 3-noded triangular elements, and those elements are treated as input data for the fracture modelling algorithm 6. A 4-noded joint element is then inserted between two triangular elements, and the stresses are calculated using FEM. The new fractures are judged by the Mohr-Coulomb criterion with a tension cut-off, see Figure 6.2. When the normal stress is less than the tensile strength, the shear stress in a joint element can be expressed by the equation (6.5) Guo *et al.* (2015).

$$\tau = c + \sigma tan\phi, \qquad \sigma_n < f_t, \tag{6.5}$$

where σ is the normal stress, ϕ is a internal friction angle, f_t is tensile strength and c is the cohesion.

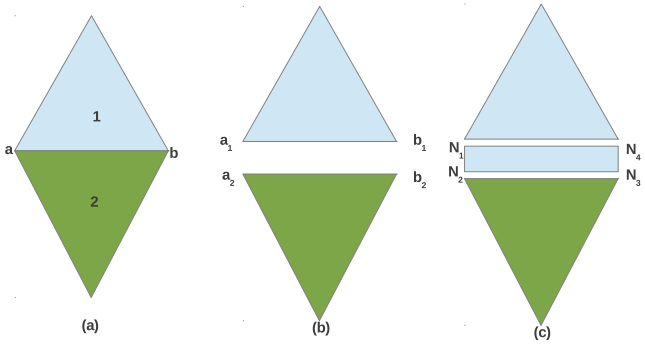


Figure 6.1: A 2-D solid discontinuous element with a 4-node joint element.

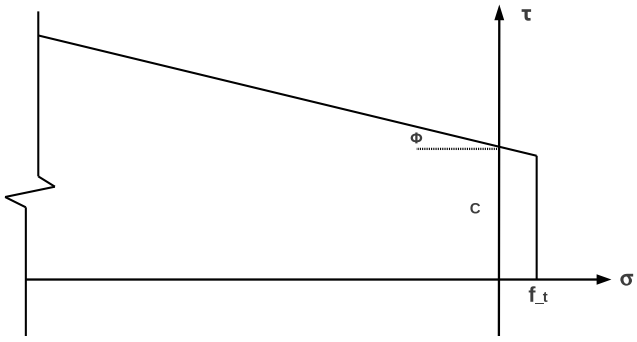


Figure 6.2: A Mohr-Coulomb failure criterion with a tension cut-off.

6.4 Model reduction schema

In this section, a NIROM is used for the modelling. The high fidelity model includes the interaction between solid and compressible fluid flows as well as crack initiation and propagation. Recently there have been a number of papers on reduced order modelling of compressive fluids,*e.g.* with shock waves Bourguet *et al.* (2007); Epureanuj & Heeg (1999); Dalle *et al.* (2010); Carlberg *et al.* (2011b); Lucia *et al.* (2001); Marley *et al.* (2015); F.Fang *et al.* (2013); White (2015). Most of existing ROMs for shock waves use the Galerkin (or Petrov-Galerkin) projection and POD approaches to generate the reduced order models. The challenge in using POD ROM for shock waves is to represent the shock front (moving discontinuities). Fang *et al.* F.Fang *et al.* (2013) introduced a Petrov-Galerkin approach for dealing with sharp or abrupt field changes in Discontinuous Galerkin ROM. Lucia Lucia *et al.* (2001) proposed a domain decomposition approach for isolating the region containing the moving shock wave for special treatment. The Gauss-Newton method with approximated tensors Carlberg *et al.* (2011b) and the clustering algorithm White (2015) were also developed for accurately capturing the shock front. In this work, a non-intrusive ROM using RBF is proposed for modelling the resulting abruptly changing (in space and time) fields. The POD bases are generated from solution snapshots where the details of the crack patterns (through the volume fraction and velocity of the solids) as well as the fluid velocity/pressure/density are included. The accuracy of the coupling NIROM results is sensitive to the number of snapshots chosen because of the rapidly changing fields. Due to the dissipative properties of RBF's representation of dynamics with NIROM, the oscillation issues associated with POD intrusive methods that use Bubnov-Galerkin methods are reduced.

In reduced order modelling, any variable can be expressed as a linear combination of a number of basis functions representing the original high fidelity modelling system in an optimal sense. It has the following form:

$$\varphi = \overline{\varphi} + \sum_{i=1}^{m} \alpha_i \Phi_i, \tag{6.6}$$

where φ denotes a variable to be solved (*e.g.* the velocity, pressure, density and solid concentration), $\overline{\varphi}$ is the mean of variable solutions over the simulation time period, α denotes the POD coefficients, m is the number of POD bases and Φ denotes the POD basis functions. Using POD, the basis functions can be calculated

from snapshots of variable solutions recorded at regular time intervals. The radial basis function interpolation method is used to calculate the POD coefficients. The procedure of POD is summarized in algorithm 7.

Algorithm 7: Proper Orthogonal Decomposition

(1) Compute solution of the coupled compressible fluid and solid system at time levels $1, ..., N_s$;

(2) Retrieve snapshots matrix A from the solutions obtained;

(3) Subtract the mean of snapshots matrix A, *i.e.* $A' = A - A_{mean}$;

(4) Perform Singular Value Decomposition (SVD) to snapshots matrix A or A', *i.e.* $A = E\Sigma F^T$;

(5) Choose the dimension of ROM, m ($m < N_s$);

(6) Obtain POD basis functions $\Phi_i = E_{:,i}$, for $i \in \{1, 2 \dots m\}$;

The radial basis function interpolation is used to determine the POD coefficients in (6.6). Commonly used RBFs are plate spline, multi-quadric, inverse multi-quadric and Gaussian. RBFs have been widely used in the context of multidimensional interpolation. An interpolation function $f(x)$ representing a physical problem can be approximated through a linear combination of the RBF ϕ centred at N points. In this work, the Gaussian RBF is used to construct the interpolation function $f(x)$. The Gaussian RBF has a form of $\phi(r) = e^{-(r/\sigma)^2}$ (r being the radius and σ being the shape parameter). In the following paragraph, a set of interpolation functions or hypersurfaces is derived through POD-RBF method. The POD-RBF NIROM method was first presented by Xiao *et al.* Xiao *et al.* (2015e). In this work this method is used to derive NIROM for the compressible fluids and fractured solids problem. The form of the equations used for solving the reduced system is:

$$\alpha^n_{\mathbf{z},j} = f_{p,j}(\alpha^{n-1}_{\mathbf{u}}, \alpha^{n-1}_p, \alpha^{n-1}_d, \alpha^{n-1}_c), \tag{6.7}$$

where α denotes POD coefficients, subscripts $\mathbf{u}$, p, d and c denote velocity, pressure, density and solid concentration components, $\mathbf{z}$ denotes one of the variables ($\mathbf{u}$, p, d and c), subscript j is the j^{th} POD coefficient of a complete set of POD coefficient $(\alpha_{\mathbf{u}}, \alpha_v, \alpha_d, \alpha_c)$, n is time step, f is a set of hypersurface functions representing the reduced system.

Algorithm 8: Constructing a set of hypersurface using POD-RBF

(1) Generate a number of snapshots over the time period $[0, T]$ by solving the compressible fluid/solid coupling problem and fracture model;

(2) Calculate POD basis functions $\Phi_{\mathbf{u}}$, Φ_p, Φ_d and Φ_c through a truncated SVD of the snapshots matrix;

(3) Obtain the functional values $y_{i,j}$ at the data point $\alpha^i_{\mathbf{u}}, \alpha^i_p, \alpha^i_d, \alpha^i_c$ via the solutions from the high fidelity full model, where $i \in \{1, 2, \dots N\}$ and $j \in \{1, 2, \dots m\}$;

(4) Obtain a set of hypersurfaces through the following loop:

for $j = 1$ *to* m **do**

(i) Calculate the weights $\mathbf{w}_{i,j}$ by solving (6.8);

$$A\mathbf{w}_{i,j} = y_{i,j}, \quad i \in \{1, 2, \dots, N\}, \tag{6.8}$$

(ii) Obtain a set of hyper surfaces $(f_{\mathbf{u},j}, f_{p,j}, f_{d,j}, f_{c,j})$ by substituting the weight values obtained in the above step into equation (6.9);

$$f_{\mathbf{z},j}(\alpha_{\mathbf{u}}, \alpha_p, \alpha_d, \alpha_c) = \sum_{i=1}^{N} w_{i,j}\phi_j(\left\|(\alpha_{\mathbf{u}}, \alpha_p, \alpha_d, \alpha_c) - (\alpha^i_{\mathbf{u}}, \alpha^i_p, \alpha^i_d, \alpha^i_c)\right\|), \tag{6.9}$$

endfor

The hypersurface functions are constructed using POD-RBF method, as described in algorithm 8, where N denotes the number of data points $(\boldsymbol{\alpha}^1, \boldsymbol{\alpha}^2, \cdots, \boldsymbol{\alpha}^N$, where $\boldsymbol{\alpha} = \alpha_{\mathbf{u}}, \alpha_p, \alpha_d, \alpha_c\ )$ and m denotes the number of POD basis functions and A is the matrix associated with the data point and centre $\mathbf{c}$ and $A_{i,j} = \phi(\left\|(\alpha^j_{\mathbf{u}}, \alpha^j_p, \alpha^j_d, \alpha^j_c) - \mathbf{c}^i\right\|)$, $i, j \in \{1, 2 \dots N\}$. The centre $\mathbf{c}$ is chosen to be the origin of the input data.

The online NIROM calculation for coupling of compressible fluids and fractured solids problems is described in algorithm 9. In the high-fidelity model, the solid−fluid movement is fully coupled, as explained in section 2. The coupling results are recorded and stored in the snapshots. The POD bases are then generated from the snapshots where the details of the fracture patterns (through the volume fraction

and velocity of the solids) as well as the fluid velocity/pressure/density are included. However, this information is interpolated onto the fluids mesh which is then used to form the NIROM model. Thus the solids volume fractions and solids velocity are calculated within the NIROM. For clarification, we superimpose the full model solids positions onto all results - both reduced order and full model. The accuracy

of the coupling NIROM results is dependent on the number of snapshots chosen.

Algorithm 9: Online NIROM calculation for compressible fluids and fractured solids problems

(1) Initialisation.

for $j = 1$ *to* m **do**

Initialize $\alpha^0_{\mathbf{u},j}$, $\alpha^0_{p,j}$, $\alpha^0_{d,j}$ and $\alpha^0_{c,j}$;

endfor

(2) Calculate solutions at current time step:

for $n = 1$ *to* T **do**

for $j = 1$ *to* m **do**

Solving fluid process:

(i) Evaluate the hypersurfaces f at the previous time step $n-1$ by using the complete set of POD coefficients $\alpha^{n-1}_{u,j}$, $\alpha^{n-1}_{p,j}$, $\alpha^{n-1}_{d,j}$ and $\alpha^{n-1}_{c,j}$:

$$f_{\mathbf{z},j} \leftarrow (\alpha^{n-1}_{\mathbf{u}}, \alpha^{n-1}_{v}, \alpha^{n-1}_{d}, \alpha^{n-1}_{c}),$$

(ii) Calculate the POD coefficients $\alpha^n_{\mathbf{u}}$, α^n_p, α^n_d and α^n_c at the current time step n using the following equations:

$$\alpha^n_{\mathbf{z},j} = \sum_{i=1}^{N} w_{i,j}\phi_{i,j}(r),$$

endfor

Calculate the solution $\mathbf{u}^n$, p^n, d^n and c^n on the full space at current time step n by projecting $\alpha^n_{\mathbf{u},j}$, $\alpha^n_{p,j}$, $\alpha^n_{d,j}$ and $\alpha^n_{c,j}$ onto the full space.

$$\mathbf{u}^n = \sum_{j=1}^{m} \alpha^n_{\mathbf{u},j}\Phi_{\mathbf{u},j}, \quad p^n = \sum_{j=1}^{m} \alpha^n_{p,j}\Phi_{p,j}, \quad d^n = \sum_{j=1}^{m} \alpha^n_{d,j}\Phi_{d,j}, \quad c^n = \sum_{j=1}^{m} \alpha^n_{c,j}\Phi_{c,j},$$

.

endfor

6.5 Application to compressible fluid and solid problems

The fluid and fracture solid coupling NIROM has been implemented under the framework of an advanced 3D unstructured mesh multi-phase fluid model (Fluidity) and a combined finite-discrete element method based solid model (Y2D). The compressible fluid and fracture solid coupling NIROM is first validated by an immersed wall in a fluid, then further validated by a more complex case: blasting.

6.5.1 Case 1: an immersed wall in a fluid

The first case is an immersed wall in a fluid test case, which name after the work of Wang *et al.* (2008). In this case, a solid beam is embedded in fluids with subject to a high pressure wave. The domain consists of a rectangle of non-dimensional size of 4×2 with 7500 nodes. The beam is located at the bottom center and has a size of 0.286×1. The initial pressure at the area ($0 < \mathrm{x} < 1.5$) with a non-dimensional density of 8 is set as 516.5 and the rest of the domain with a density of 1.5 is set as 1. A slip boundary condition is applied on the left, bottom and the top sides. The open boundary condition is applied on the right side. The density of the solid is 100.

The high fidelity full model was simulated during the time period $[0, 0.8]$ with a time step size of $\Delta t = 0.001$. 800 snapshots were taken at a regularly spaced time interval of 0.001. From these snapshots, the POD bases were formed in two ways: either subtracting the mean of snapshots or not before the singular value decomposition (SVD) is performed.

6.5.1.1 Case 1a: fluid and fracture solid coupling NIROM results with mean subtraction before constructing the POD basis

The fluid and fracture solid coupling NIROM was first formed with mean subtraction before constructing the POD basis. In this case, 30 POD bases representing almost 99.5% of energy in the original dynamic system were chosen to form the fluid and fracture solid coupling NIROM. The logarithm of the singular eigenvalues of velocity, pressure, density and solid concentration associated to the chosen 30 POD bases are given in Figure 6.3.

The pressure and velocity results from both the high fidelity model and fluid and fracture solid coupling ROM are shown in Figures 6.4 and 6.5 respectively. It is illustrated that these fluid and fracture solid coupling NIROM results are not good in comparison with those from the high fidelity model. To further assess the quality of the fluid and fracture solid coupling NIROM with mean subtraction before constructing the POD basis, the error analysis is carried out. The root mean square error (RMSE) and correlation coefficient of results between the fluid and fracture solid coupling NIROM and the fidelity model are shown in Figure 6.6. It can be seen that the RMSE of results is around 39.59 while the correlation coefficient is mostly less than 0.6. The RMSE reflects the differences of the two models. As shown in the Figure 6.6, the RMSE varies between time 0 and 0.5s and the difference values are around 39.59, which means the two models are not similar. This is also reflected by the correlation coefficient curve, which varies big between the time $0-0.5s$. The accuracy of fluid and fracture solid coupling NIROM results therefore, is low and needs to be improved.

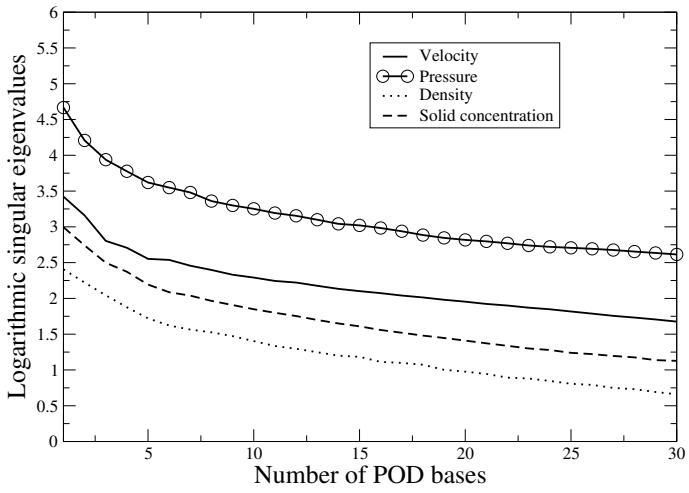
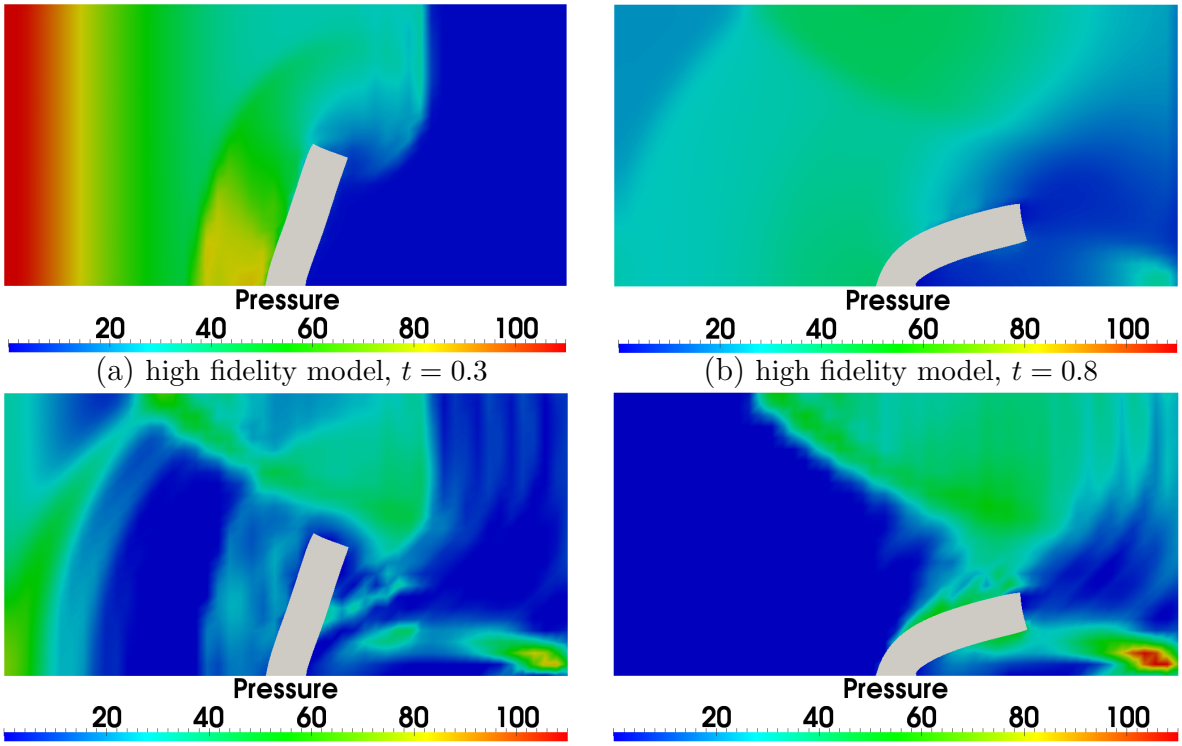


Figure 6.3: Case 1a: the figure shows the logarithm of the singular eigenvalues of velocity, pressure, density and solid concentration in order of decreasing magnitude with mean subtraction before constructing the POD basis.



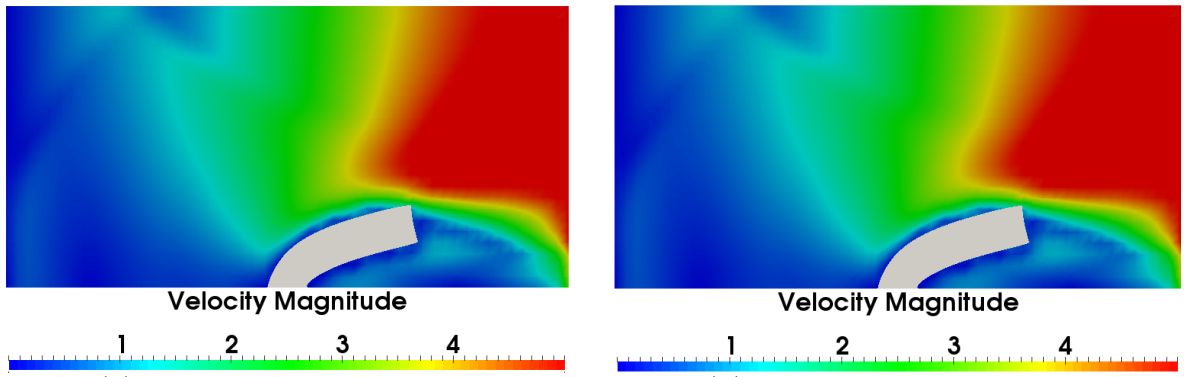
(a) high fidelity model, $t = 0.3$

(b) high fidelity model, $t = 0.8$

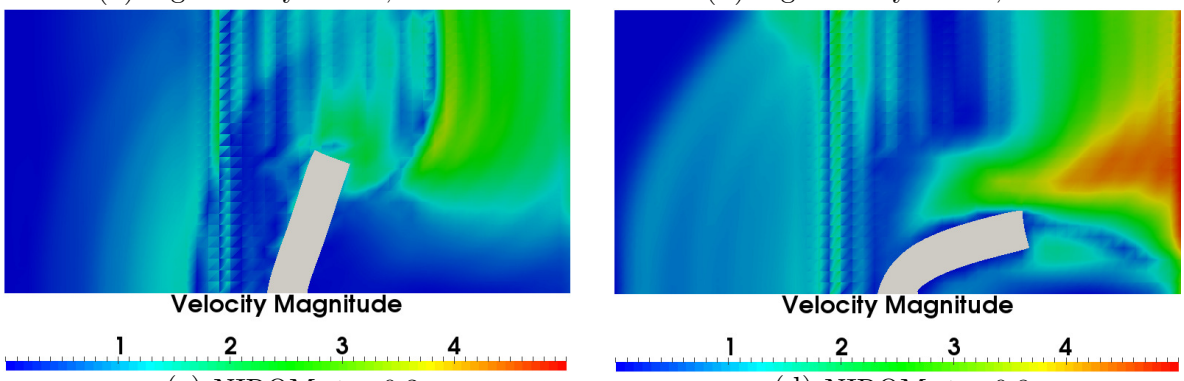
(c) NIROM, $t = 0.3$

(d) NIROM, $t = 0.8$

Figure 6.4: Case 1a: a comparison of pressure solutions between the full model and fluid and fracture solid coupling NIROM using 30 POD bases at time instances $t = 0.3$ and $t = 0.8$. The mean is not used to construct the POD basis functions.

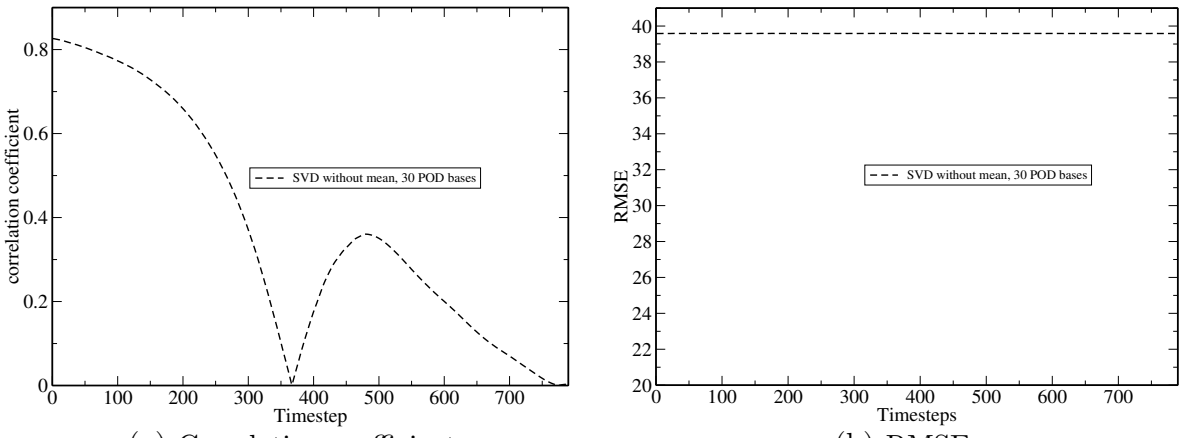


(a) high fidelity model, $t = 0.3$ (b) high fidelity model, $t = 0.8$



(c) NIROM, $t = 0.3$ (d) NIROM, $t = 0.8$

Figure 6.5: Case 1a: a comparison of velocity solutions between the full model and fluid and fracture solid coupling NIROM using 30 POD bases at time instances $t = 0.3$ and $t = 0.8$. The mean is not used to construct the POD basis functions.



(a) Correlation coefficient (b) RMSE

Figure 6.6: Case 1a: the correlation coefficient and RMSE of pressure solutions between the high fidelity and fluid and fracture solid coupling NIROM using 30 POD bases, where the mean is not used to construct the POD basis functions.

6.5.1.2 Case 1b: the fluid and fracture solid coupling NIROM results without mean subtraction before constructing the POD basis

In this subsection, the fluid and fracture solid coupling NIROM results without mean subtraction before constructing the POD basis are given and discussed. Figure 6.7 presents the logarithm of the singular eigenvalues of velocity, pressure, density and solid concentration in order of decreasing magnitude without mean subtraction before constructing the POD basis.

Figure 6.8 shows a comparison of pressure solutions between the full model and fluid and fracture solid coupling NIROM with the use of 12, 18 and 30 POD bases at time instances $t = 0.3$ and $t = 0.8$. We can see the fluid and fracture solid coupling NIROM results are in agreement with those from the high fidelity model. The front is captured well even when only 12 POD bases are used. The accuracy of NIROM results is improved with the increased number of POD bases. The absolute error of pressure solutions between high fidelity model and fluid and fracture solid coupling NIROM using different numbers of POD bases at time instances $t = 0.3$ and $t = 0.8$ is given in Figure 6.10. The figure clearly shows that the error of the fluid and fracture solid coupling NIROM relative to the high fidelity model becomes smaller as the number of POD bases is increased. Velocity solutions of both the high fidelity model and the NIROM with 30 POD bases at time instances $t = 0.3$ and $t = 0.8$ is given in Figure 6.9.

To further validate the accuracy of the fluid and fracture solid coupling NIROM without mean subtraction, the correlation coefficient and RMSE of pressure results between the high fidelity model and fluid and fracture solid coupling NIROM are used for error analysis, see figure 6.10. It is shown in this figure that the correlation coefficient is larger than 0.9955 while the RMSE is smaller than 2 when 12 POD bases are used and the error is further decreased as the number of POD bases is increased. It is illustrated that the accuracy of fluid and fracture solid coupling NIROM results can be improved significantly if the mean of snapshots are considered in SVD process, where the correlation coefficient increases from 0.4 to 0.9955 while the RMSE decreases from 39.6 to 2 in comparison with results shown in Figure 6.6.

The initial errors of four variables between the full model and NIROM with mean

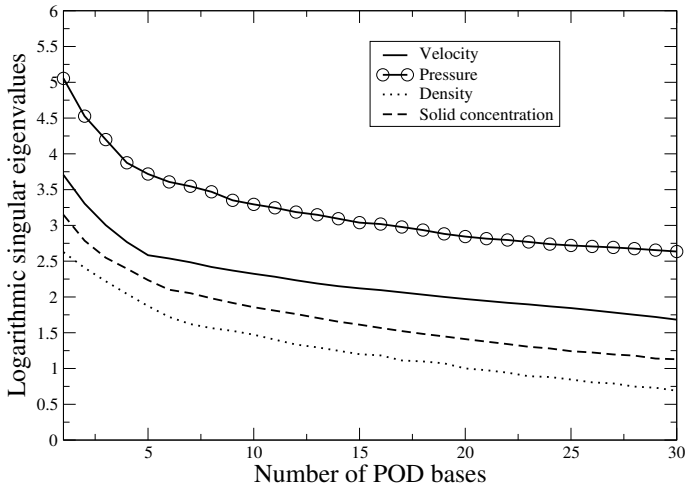


Figure 6.7: Case 1b : the figure shows the logarithm of the singular eigenvalues of velocity, pressure, density and solid concentration in order of decreasing magnitude without mean subtraction before constructing the POD basis.

subtraction and without mean subtraction are listed in table 6.1. The calculation formula considering all nodes is given below:

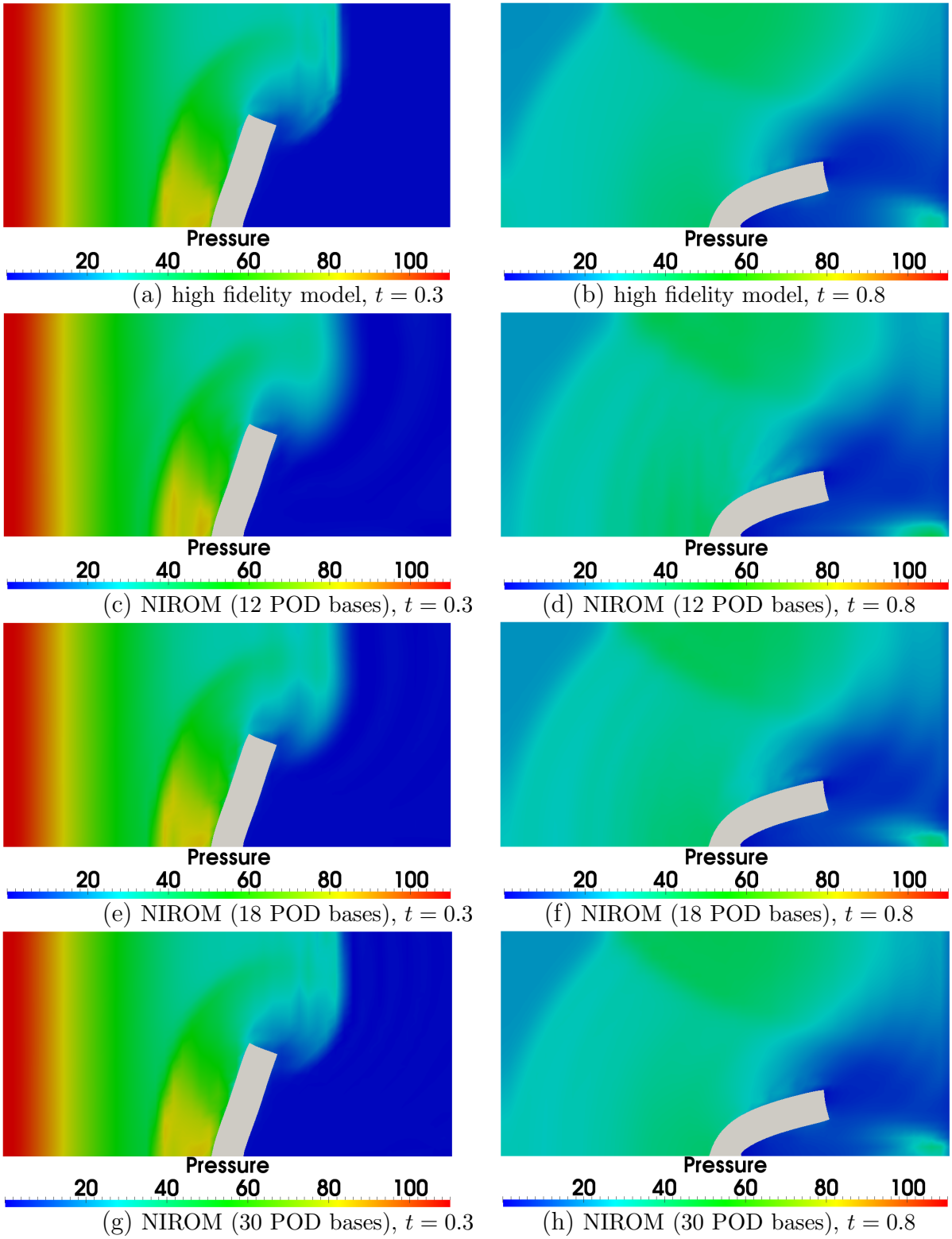
$$\sum_{i=1}^{N_{nodes}} ({\varphi_0}^i - \Phi\Phi^T {\varphi_0}^i)^2, \tag{6.10}$$

where N_{nodes} is the number of nodes on the mesh.

Table 6.1: Case 1: comparison of $|| \varphi_0 - \Phi\Phi^T\varphi_0 ||_2$ (where φ_0 being the initial solutions of full model) for four variables between NIROM with mean subtraction and NIROM without mean subtraction.

Variable errors	case 1a all nodes	case 1b all nodes	case 1a each node	case 1b each node	nodes
velocity	163.3	9.8	0.02	0.0013	7500
pressure	3428.4	63.1	0.4571	0.0084	7500
density	1.12	0.02	0.0001	0	7500
solid concentration	37.3	0.54	0.0049	0	7500

It is seen in table 6.1 that the error in the NIROM constructed with the mean subtracted from the snapshots is about 16 57 times larger than that from the NIROM without mean subtraction, which thus results in a large error in the simulated results from the NIROM with mean subtraction.



(a) high fidelity model, $t = 0.3$

(b) high fidelity model, $t = 0.8$

(c) NIROM (12 POD bases), $t = 0.3$

(d) NIROM (12 POD bases), $t = 0.8$

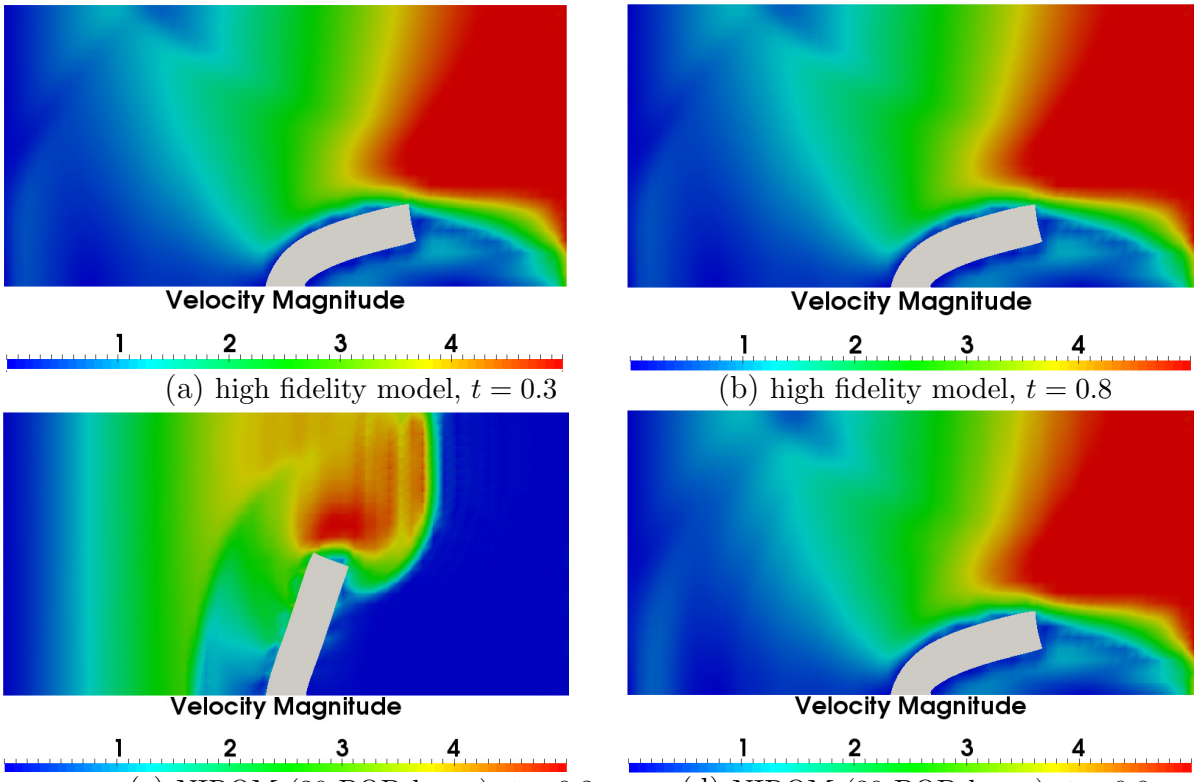
(e) NIROM (18 POD bases), $t = 0.3$

(f) NIROM (18 POD bases), $t = 0.8$

(g) NIROM (30 POD bases), $t = 0.3$

(h) NIROM (30 POD bases), $t = 0.8$

Figure 6.8: Case 1b: a comparison of pressure solutions between the full model and fluid and fracture solid coupling NIROM with 12, 18 and 30 POD bases at time instances $t = 0.3$ and $t = 0.8$, where the mean is used to construct the POD basis functions.



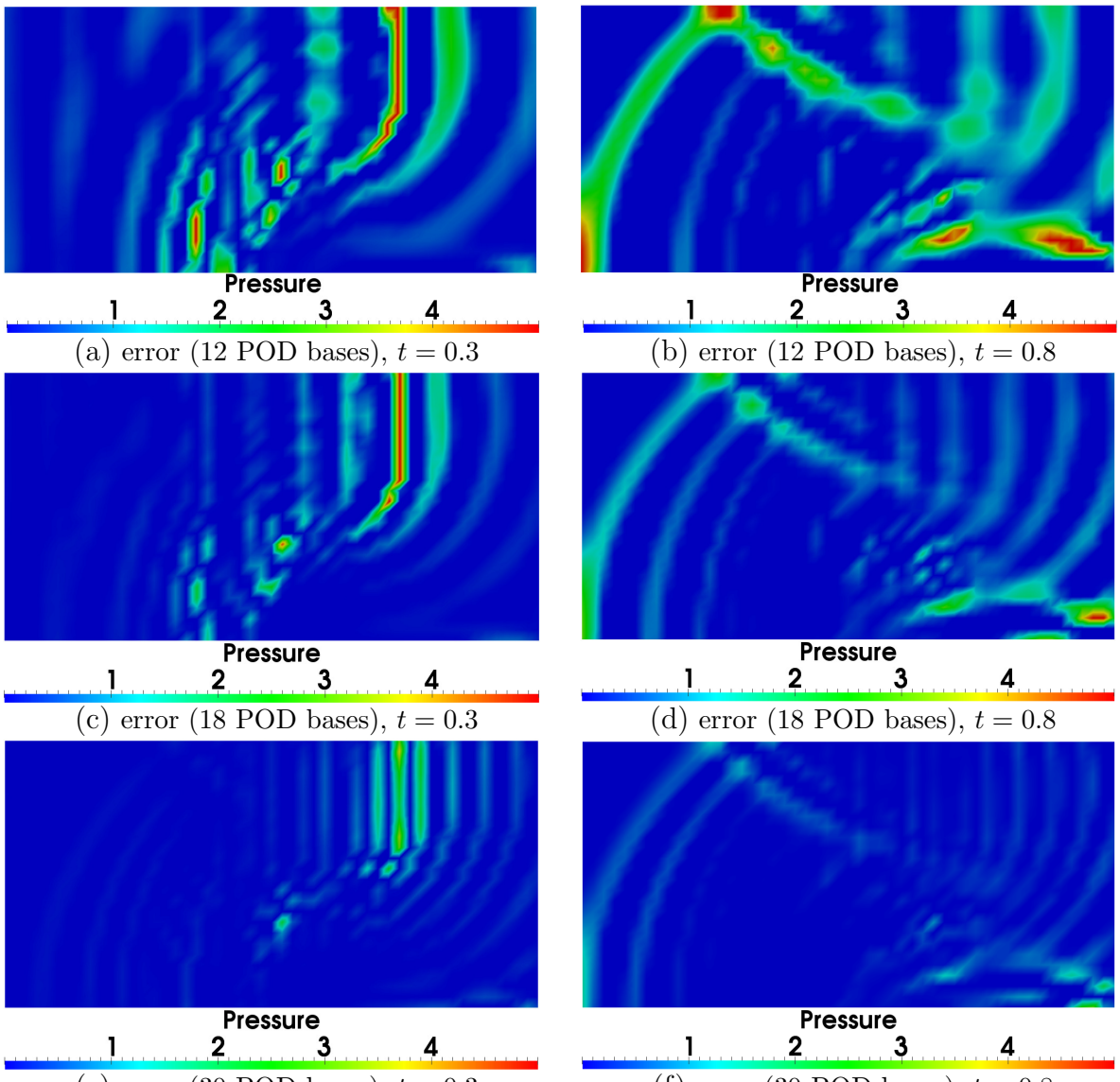
(a) high fidelity model, $t = 0.3$

(b) high fidelity model, $t = 0.8$

(c) NIROM (30 POD bases), $t = 0.3$

(d) NIROM (30 POD bases), $t = 0.8$

Figure 6.9: Case 1b: a comparison of velocity solutions between the full model and fluid and fracture solid coupling NIROM with 30 POD bases at time instances $t = 0.3$ and $t = 0.8$, where the mean is used to construct the POD basis functions.



(a) error (12 POD bases), $t = 0.3$

(b) error (12 POD bases), $t = 0.8$

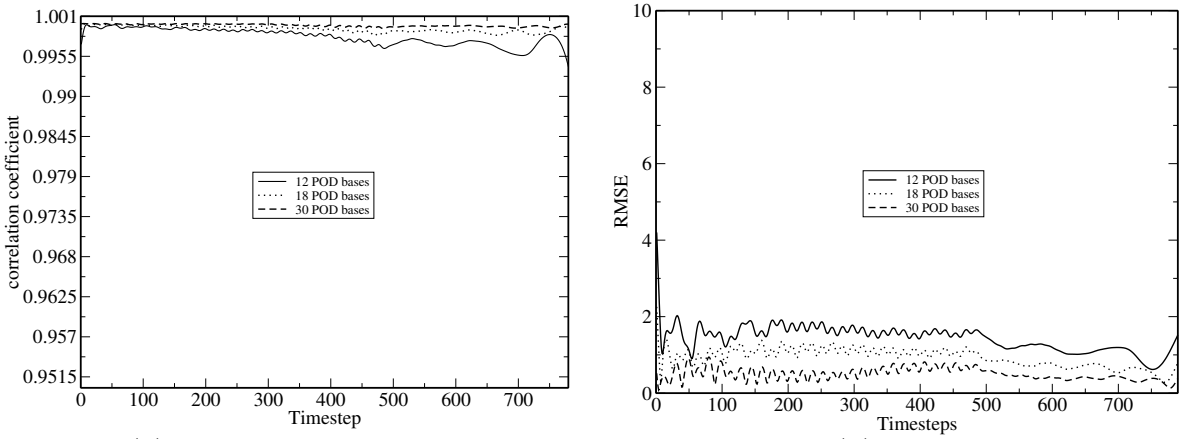
(c) error (18 POD bases), $t = 0.3$

(d) error (18 POD bases), $t = 0.8$

(e) error (30 POD bases), $t = 0.3$

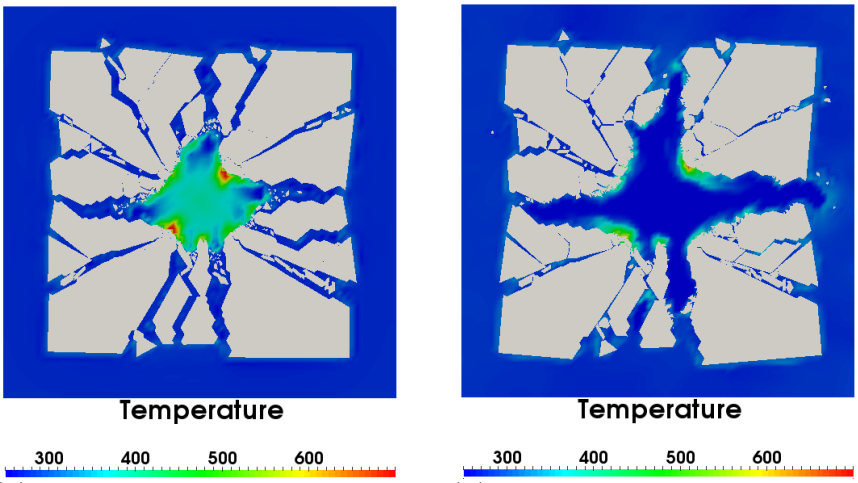
(f) error (30 POD bases), $t = 0.8$

Figure 6.10: Case 1b: error between the high fidelity model and fluid and fracture solid coupling NIROM with 12, 18 and 30 POD bases at time instances $t = 0.3$ and $t = 0.8$, where the mean is used to construct the POD basis functions.



(a) Correlation coefficient (b) RMSE

Figure 6.11: Case 1b: RMSE and correlation coefficient of pressure solutions between the high fidelity and fluid and fracture solid coupling NIROM with 12, 18 and 30 POD bases, where the mean is used to construct the POD basis functions.



(a) high fidelity model, $t = 0.04\,s$ (b) high fidelity model, $t = 0.16\,s$

Figure 6.12: Case 2a: temperature solutions obtained from the full model at time levels $t = 0.04\,s$ and $t = 0.16\,s$.

6.5.2 Case 2: blasting test case

To demonstrate the capability of the fluid and fracture solid coupling NIROM, the model is further applied to a high nonlinear flow: blasting-induced fracture test case. The computational domain is presented in Figure 6.21, which includes a solid square block with a size of $2 \times 2\,m$ embedded within a compressible gas rectangle area with a size of $3 \times 3\,m$. The explosion point lies at the center of the computational domain with a diameter of $0.2\,m$ and a very high initial pressure. The initial high pressure of the explosion point is set to be $10^8\,Pa$ and the initial high temperature is $1000\,Kelvin$. The background area (excluding the explosion point) has an initial pressure of 101325 Pa and an initial temperature of 273.26 Kelvin. The viscosity μ is $0.1\,Pa \cdot s$. The solid with a density of $2340\,kg/m^3$ has a penalty number of 2.0×10^{10} and a Youngs modulus E of 2.66×10^{10}. The tensile strength and the shear strength are 4×10^6 Pa and 1.4×10^7 Pa respectively. The energy decrease rate is 200.

The high fidelity model was simulated with a finite element mesh of 48600 nodes during the time period $[0, 0.2]\,s$ with a time step size of $\Delta t = 0.00008\,s$. 250 snapshots were taken at a regularly spaced time intervals of $\Delta t = 0.0008\,s$. The temperature solutions solved by the energy equation at time levels $t = 0.04\,s$ and $t = 0.16\,s$ are given in Figure 6.12.

6.5.2.1 Case 2a: fluid and fracture solid coupling NIROM results with mean subtraction before constructing the POD basis

In this section, the results from NIROM with mean subtraction before constructing the POD basis are presented. Figure 6.13 shows the logarithm of the singular eigenvalues of velocity, pressure, density and solid concentration in order of decreasing magnitude with mean subtraction before constructing the POD basis. At some stage, the eigenvalue increases where it should decrease. This can explain why the results shown below have a large error in comparison to those from the high fidelity model. Figure 6.14 presents the velocity solutions from the high fidelity model and fluid and fracture solid coupling NIROM with 100 POD bases at time instances $t = 0.04\,s$ and $t = 0.16\,s$. It is shown that the structure of flows obtained from the fluid and fracture solid coupling NIROM is similar to that from the high fidelity model, but there are some large errors in velocity values. Figure 6.15 shows the pressure solutions from the high fidelity model and fluid and fracture solid coupling NIROM with 100 POD bases at time instances $t = 0.04\,s$ and $t = 0.16\,s$. It is seen that there is a large error in the NIROM results. This is caused by the large error in the initial conditions. We found the error in the initial pressure in the NIROM with mean subtraction is about 1000 times larger than that of the NIROM without mean subtraction.

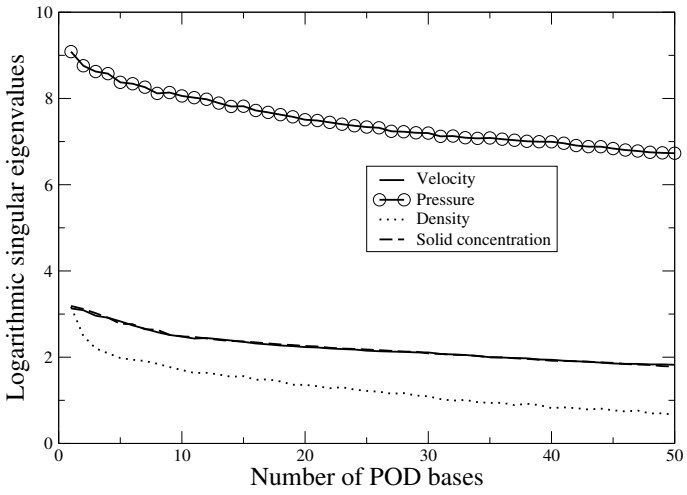
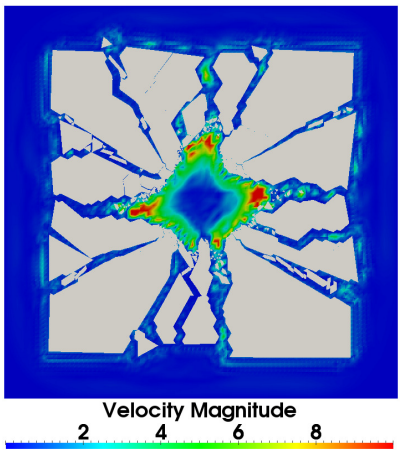
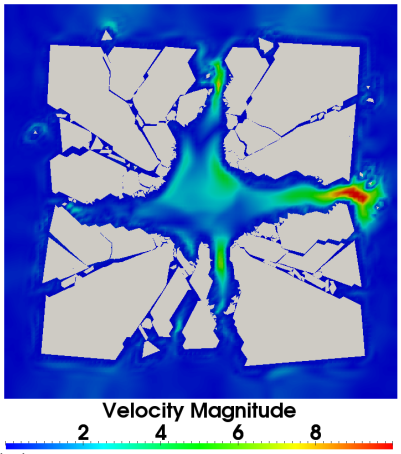


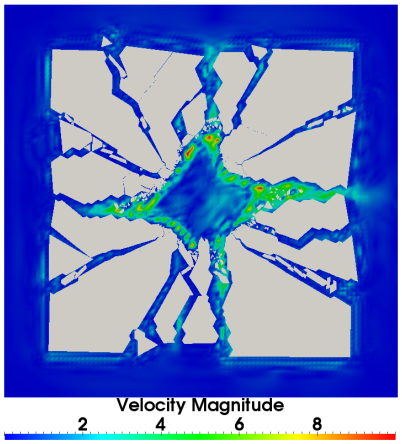
Figure 6.13: Case 2a: The logarithm of the singular eigenvalues of velocity, pressure, density and solid concentration in order of decreasing magnitude with mean subtraction before constructing the POD basis.



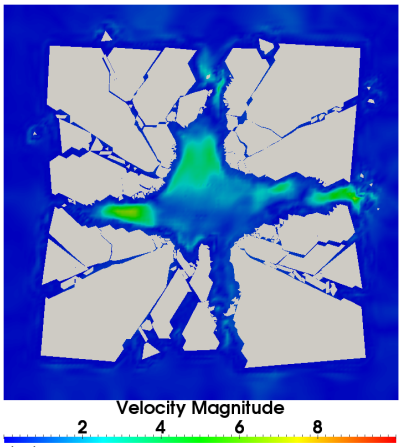
(a) high fidelity model, $t = 0.04\,s$



(b) high fidelity model, $t = 0.16\,s$

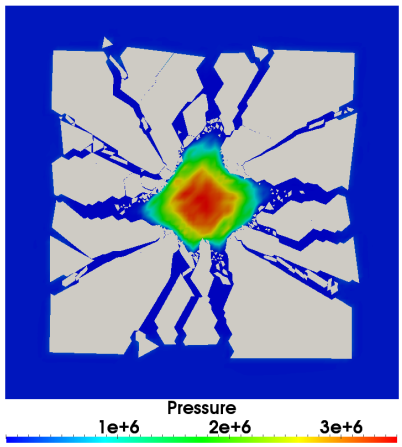


(c) (100 POD bases), $t = 0.04\,s$

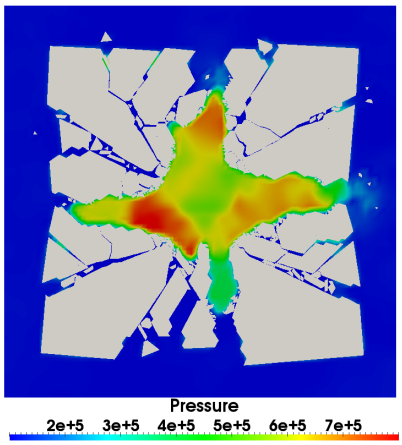


(d) (100 POD bases), $t = 0.16\,s$

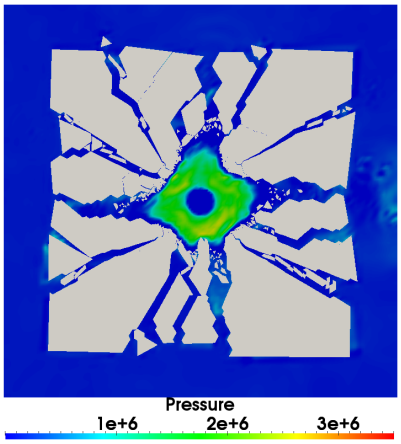
Figure 6.14: Case 2a: a comparison of velocity solutions between the full model and fluid and fracture solid coupling NIROM using 100 POD bases at time instances $t = 0.04\,s$ and $t = 0.16\,s$, where the mean is not used to construct the POD basis functions.



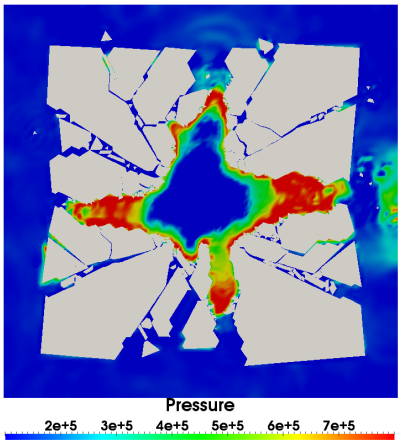
(a) high fidelity model, $t = 0.04\,s$



(b) high fidelity model, $t = 0.16\,s$



(c) NIROM (100 POD bases), $t = 0.04\,s$



(d) NIROM (100 POD bases), $t = 0.16\,s$

Figure 6.15: Case 2a: a comparison of pressure solutions between the full model and NIROM with 100 POD bases at time instances $t = 0.04\,s$ and $t = 0.16\,s$, where the mean is not used to construct the POD basis functions.

6.5.2.2 Case 2b: fluid and fracture solid coupling NIROM solutions without mean subtraction before constructing the POD basis

In this section, the fluid and fracture solid coupling NIROM solutions without mean subtraction before constructing the POD basis are given. Figure 6.16 show the logarithm of the singular eigenvalues of velocity, pressure, density and solid concentration in order of decreasing magnitude without mean subtraction before constructing the POD basis.

Figure 6.17 shows a comparison of velocity solutions between the full model and fluid and fracture solid coupling NIROM using 6, 12 and 50 POD bases at time instances $t = 0.04\,s$ and $t = 0.16\,s$. It is evident that the fluid and fracture solid coupling NIROM with only 6 POD bases performs well when the mean of snapshots is not subtracted before constructing the POD basis, even better than the solutions from fluid and fracture solid coupling NIROM with 100 POD bases when the mean is subtracted before SVD − as shown in Figure 6.14. Figure 6.17 also shows that shock front of the blast wave is captured very well by increasing the number of POD bases from 6 to 50. There is no visible difference between the high fidelity model and fluid and fracture solid coupling NIROM with 50 POD bases. The difference of pressure solutions between the high fidelity model and fluid and fracture solid coupling NIROM with 6, 12 and 50 POD basis functions at time instances $t = 0.04$ and $t = 0.16\,s$ is presented in Figure 6.18. It is evident that a higher accuracy is obtained by choosing a larger number of POD bases.

Figure 6.19 presents a comparison of pressure solutions between the full model and fluid and fracture solid coupling NIROM using 6, 12 and 50 POD bases at time instances $t = 0.04\,s$ and $t = 0.16\,.$ The pressure solutions from fluid and fracture solid coupling NIROM using 6 POD bases are not as good as velocity solutions from fluid and fracture solid coupling NIROM using the same number of POD bases. In this case, there are visible differences between the high fidelity model and fluid and fracture solid coupling NIROM using 6 and 12 POD bases, which is evident at the time instance $t = 0.16\,s$. The errors between the high fidelity model and fluid and fracture solid coupling NIROM with 6, 12 and 50 POD basis functions at time instances $t = 0.04\,s$ and $t = 0.16\,s$ are plotted in Figure 6.20. It is evident that the error is decreased by choosing more POD basis functions.

In order to assess the performance of the fluid and fracture solid coupling NIROM, the velocity solution obtained from the high fidelity model and fluid and fracture

solid coupling NIROMs at a point ($x = 1.5\,m, y = 1.6333\,m$) near the explosion point over the simulation time period is plotted in Figure 6.21. The reason that we choose the point around the explosion centre is that there is an abrupt change around the explosion point. Figure 6.21 illustrates that fluid and fracture solid coupling NIROM with a small number of POD basis functions perform well when there are no abrupt changes, whereas fluid and fracture solid coupling NIROM with 50 POD basis functions captures the abrupt changes very well.

The accuracy of the fluid and fracture solid coupling NIROM is validated by the RMSE and correlation coefficients of pressure solutions between the high fidelity model and fluid and fracture solid coupling NIROM. It is shown in Figure 6.22 that the RMSE of pressure results decreases as the number of POD bases increases. The correlation coefficients from fluid and fracture solid coupling NIROMs are over 0.935, indicating that the high fidelity model and fluid and fracture solid coupling NIROMs are highly correlated. The fluid and fracture solid coupling NIROM gets more closer agreement to the high fidelity model as the number of POD basis functions increases.

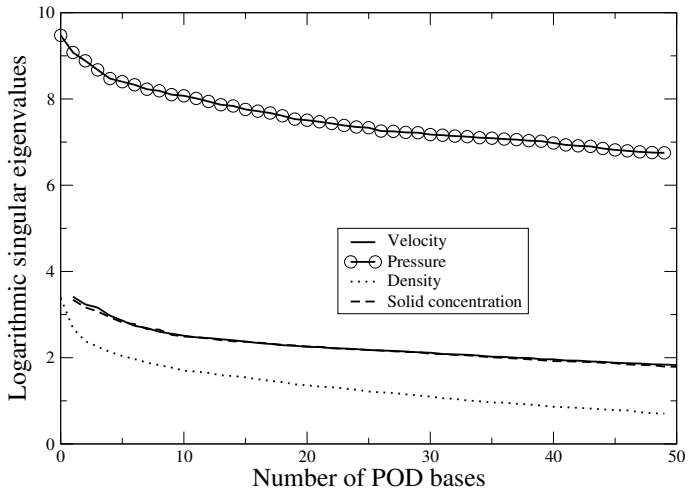
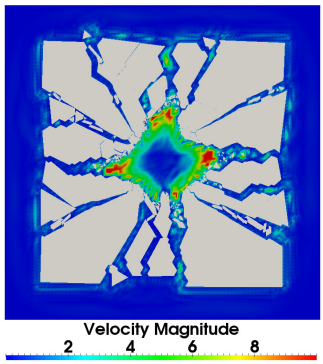
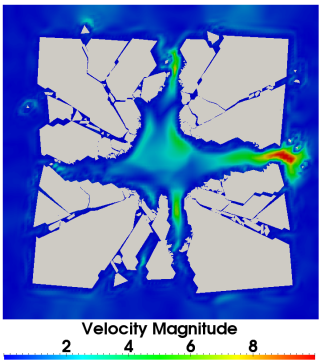


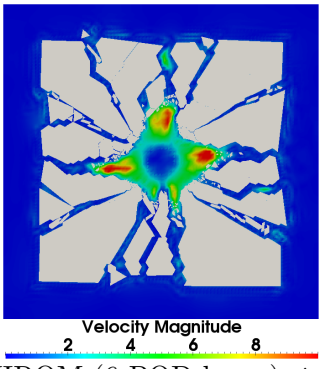
Figure 6.16: Case 2b: The logarithm of the singular eigenvalues of velocity, pressure, density and solid concentration in order of decreasing magnitude without mean subtraction before constructing the POD basis.



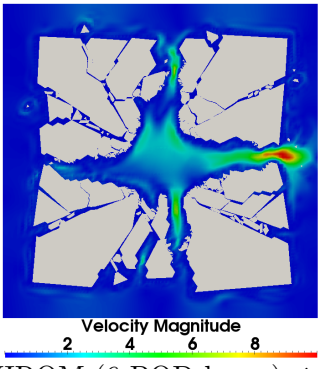
(a) high fidelity model, $t = 0.04\,s$



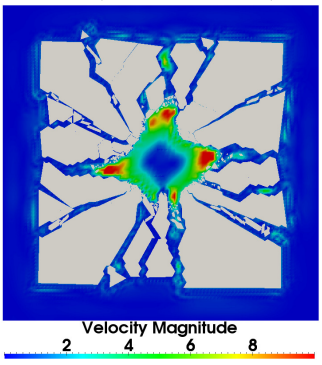
(b) high fidelity model, $t = 0.16\,s$



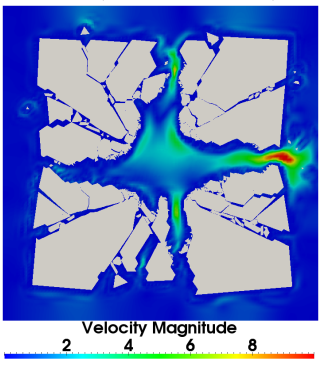
(c) NIROM (6 POD bases), $t = 0.04$



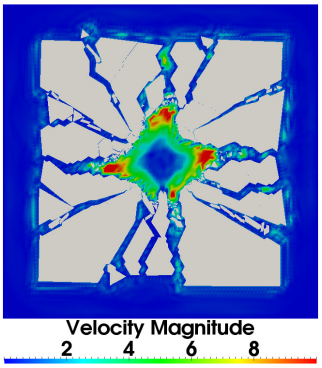
(d) NIROM (6 POD bases), $t = 0.16$



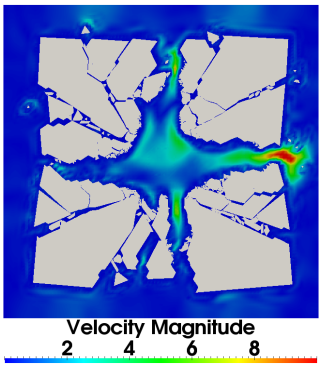
(e) NIROM (12 POD bases), $t = 0.04\,s$



(f) NIROM (12 POD bases), $t = 0.16\,s$

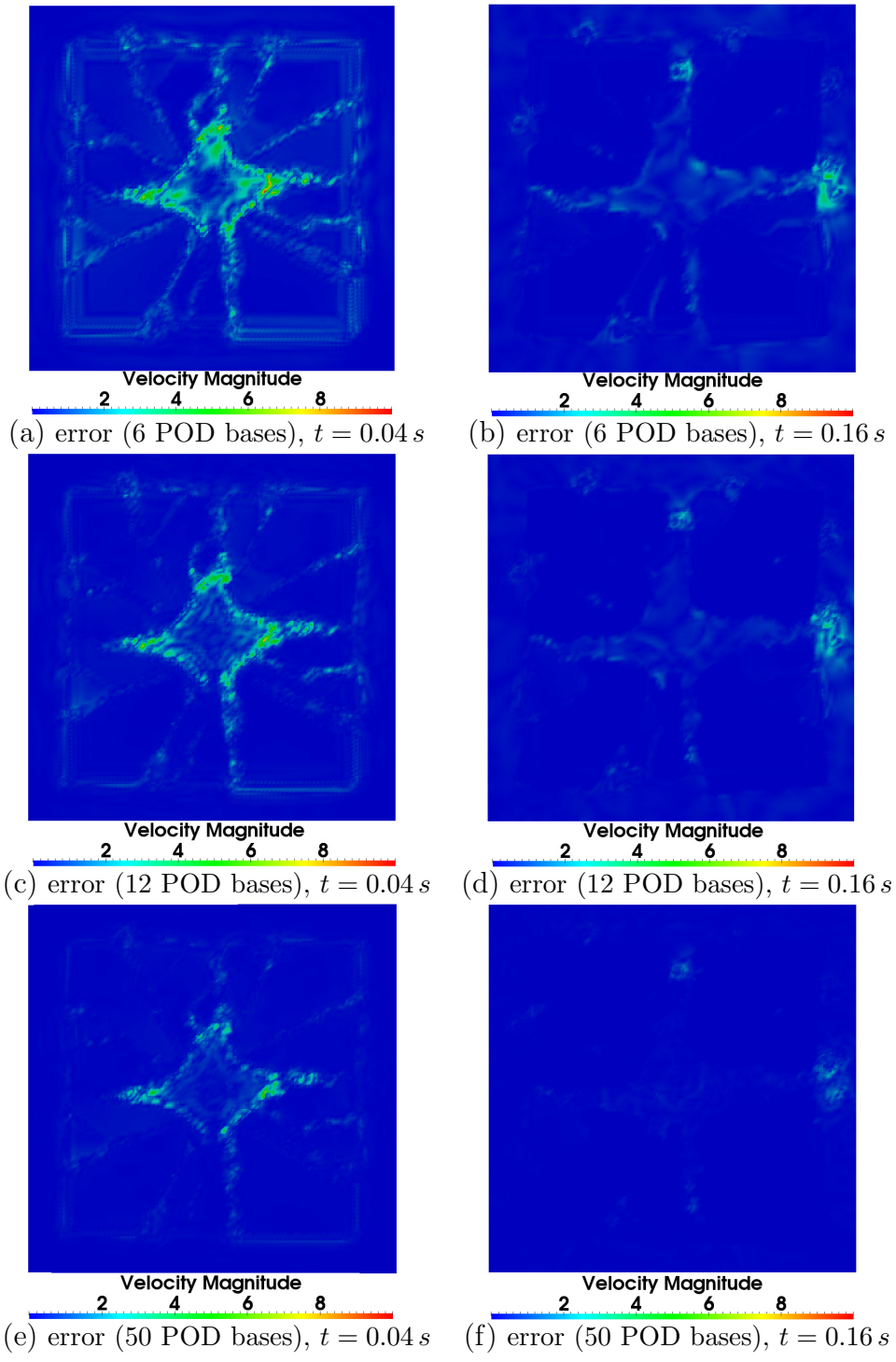


(g) NIROM (50 POD bases), $t = 0.04\,s$



(h) NIROM (50 POD bases), $t = 0.16\,s$

Figure 6.17: Case 2b: A comparison of velocity solutions between the full model and fluid and fracture solid coupling NIROM with 6, 12 and 50 POD bases at time instances $t = 0.04\,s$ and $t = 0.16\,s$, where the is used to construct the POD basis functions.

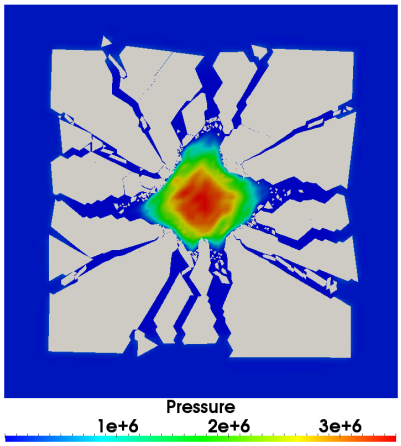


(a) error (6 POD bases), $t = 0.04\,s$ (b) error (6 POD bases), $t = 0.16\,s$

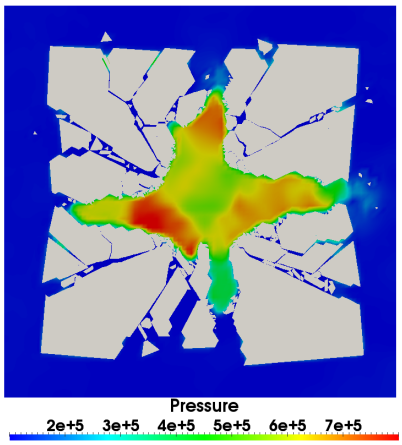
(c) error (12 POD bases), $t = 0.04\,s$ (d) error (12 POD bases), $t = 0.16\,s$

(e) error (50 POD bases), $t = 0.04\,s$ (f) error (50 POD bases), $t = 0.16\,s$

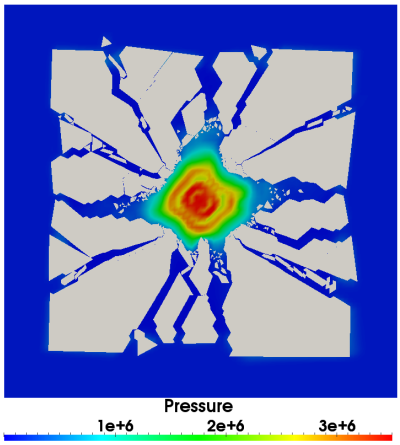
Figure 6.18: Case 2b: the difference of velocity solutions between the high fidelity model and fluid and fracture solid coupling NIROM using 6, 12 and 50 POD bases at time instances $t = 0.04\,s$ and $t = 0.16\,s$, where the mean is used to construct the POD basis functions.



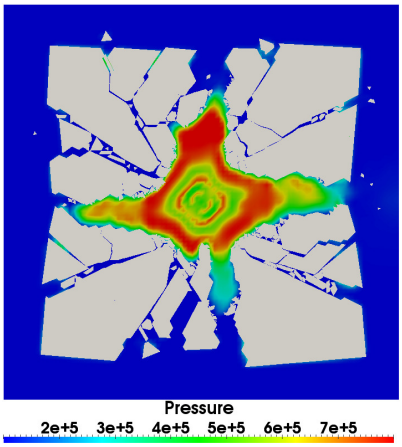
(a) high fidelity model, $t = 0.04\,s$



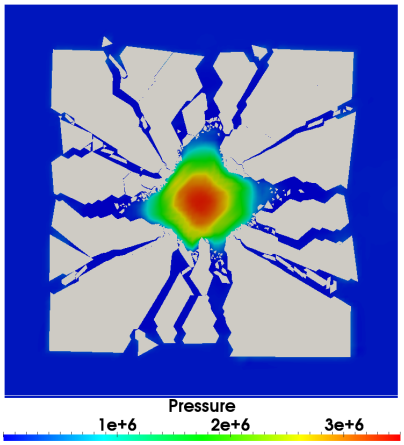
(b) high fidelity model, $t = 0.16\,s$



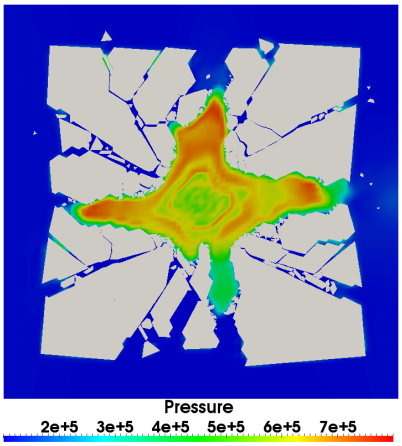
(c) NIROM (6 POD bases), $t = 0.04\,s$



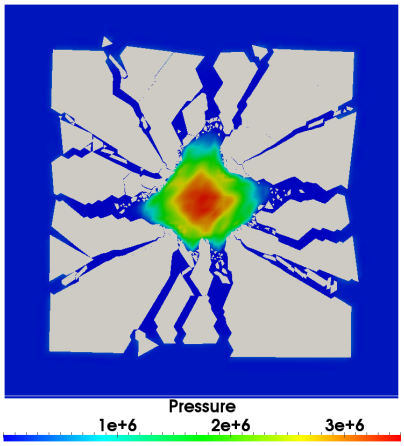
(d) NIROM (6 POD bases), $t = 0.16\,s$



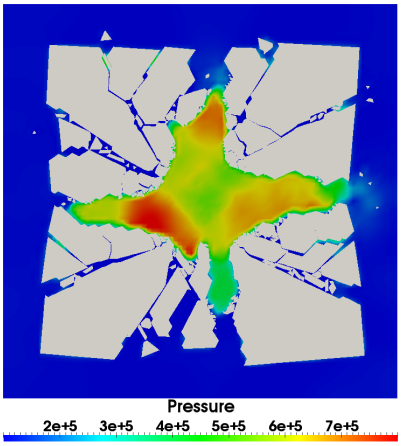
(e) NIROM (12 POD bases), $t = 0.04\,s$



(f) NIROM (12 POD bases), $t = 0.16\,s$

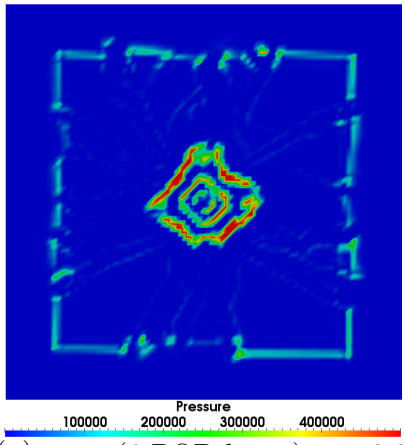


(g) NIROM (50 POD bases), $t = 0.04\,s$

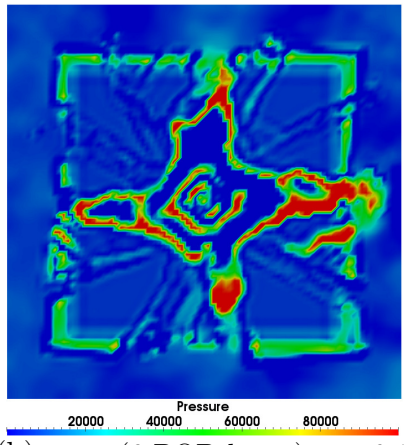


(h) NIROM (50 POD bases), $t = 0.16\,s$

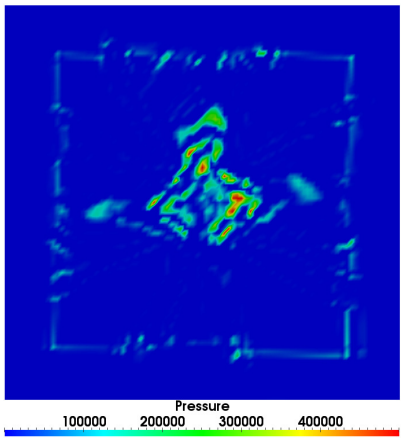
Figure 6.19: Case 2b: a comparison of pressure solutions between the full model



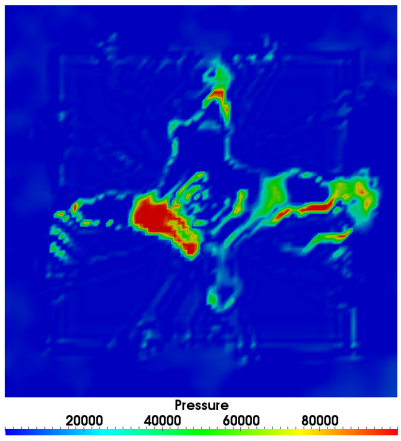
(a) error (6 POD bases), $t = 0.04$



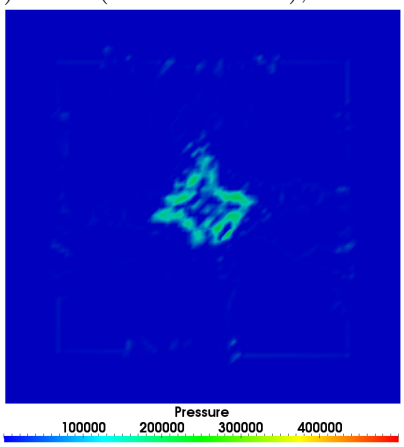
(b) error (6 POD bases), $t = 0.16$



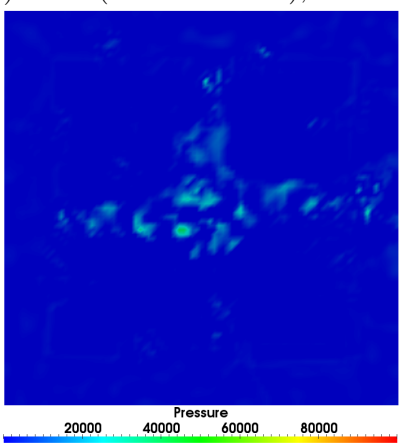
(c) error (12 POD bases), $t = 0.04\,s$



(d) error (12 POD bases), $t = 0.16\,s$



(e) error (50 POD bases), $t = 0.04\,s$



(f) error (50 POD bases), $t = 0.16\,s$

Figure 6.20: Case 2b: the difference of pressure solutions between the high fidelity model and fluid and fracture solid coupling NIROM with 6, 12 and 50 POD bases at time instances $t = 0.04\,s$ and $t = 0.16\,s$, where the mean is not used to construct the POD basis functions.

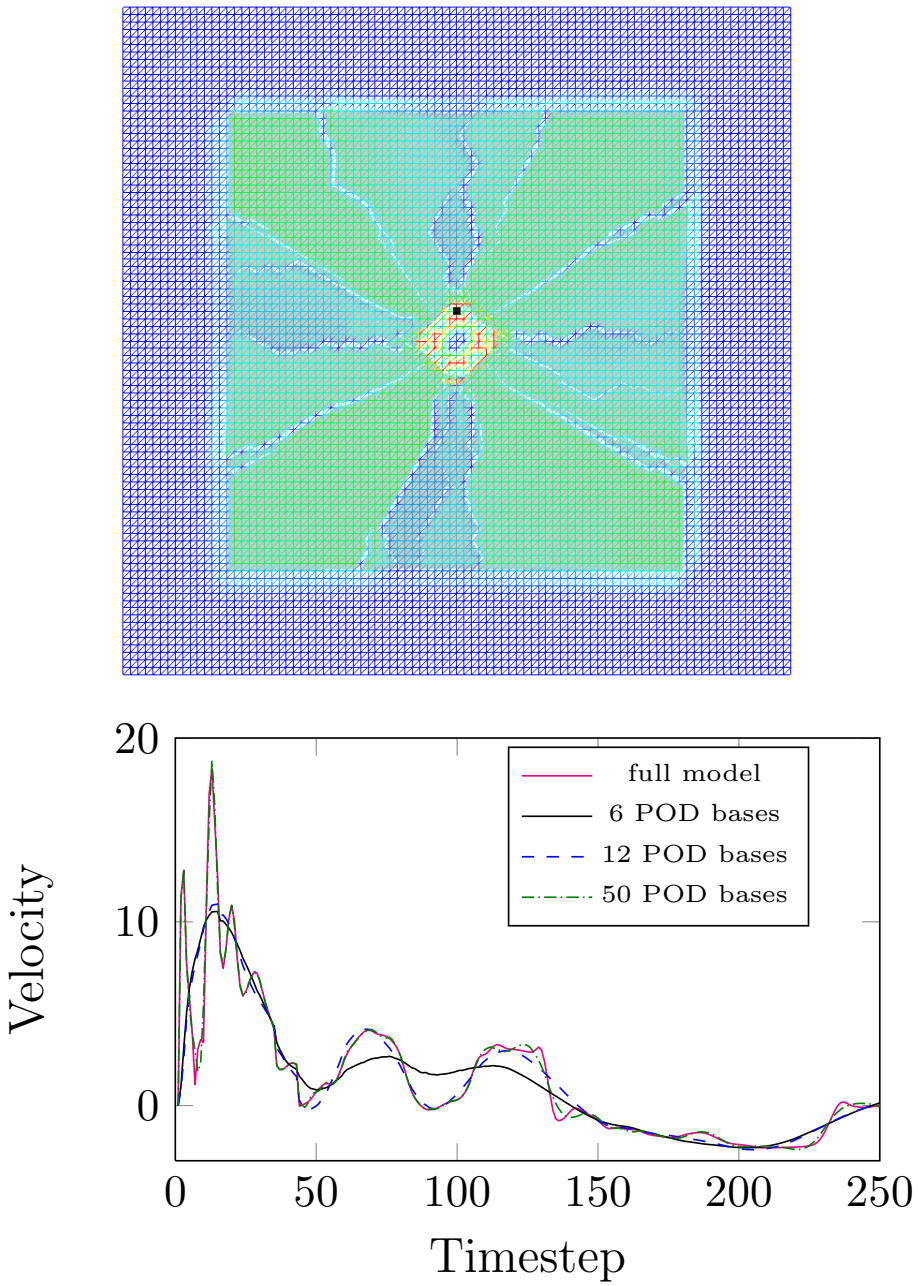
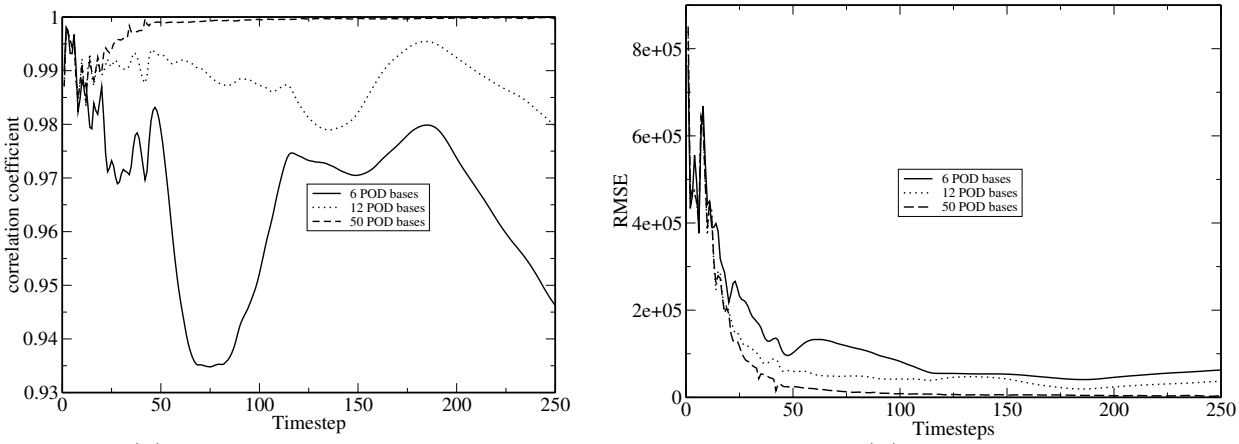


Figure 6.21: Case 2b: velocity comparison at a point ($x = 1.5\,m, y = 1.6333\,m$), where the mean is used to construct the POD basis functions.



(a) Correlation coefficient (b) RMSE

Figure 6.22: Case 2b: the correlation coefficient and RMSE of pressure solutions between the high fidelity and fluid and fracture solid coupling NIROM with 6, 12 and 50 POD bases, where the mean is used to construct the POD basis functions.

6.5.3 Efficiency of the POD-RBF model

In this section, the online and offline computational costs are given. The offline cost can be defined as the time for precomputing while the online cost involves the simulation time when running the NIROM. The online computational time required for running the fluid and fracture solid coupling NIROM and high fidelity model are compared in table 6.2, which includes the time required for the computational process in algorithm 9. The simulations were carried out on a 12 cores (Intel(R) Xeon(R) X5680) workstation with 48GB RAM. During the simulations, only one core with 3.3GHz was used. The CPU time for constructing a set of hypersurfaces (see algorithm 8) is offline, therefore, it is not listed in the table. As shown in table 6.2, the computational time required for running the NIROM is decreased drastically in comparison with the high fidelity model. For example, in blasting test case with 48600 nodes, the CPU time for NIROM is reduced by 5 orders of magnitude.

Table 6.2: Comparison of the online CPU cost (unit second) required for running the high fidelity model and NIROM during one snapshot.

Cases	Model	Assembling and Solving	Projection	Interpolation	Total
an immersed wall	Full model	4.95120	0	0	4.95120
	NIROM	0	0.0003	0.0001	0.00040
Blasting	Full model	224.47059	0	0	224.47059
	NIROM	0	0.0003	0.0001	0.00040

The offline computational cost required for forming the NIROM includes the time for forming the POD basis functions and the hypersurfaces of the system dynamics. The time for forming the hypersurfaces can be ignored as it is negligable. The CPU cost required for forming the POD basis functions is related to the number of POD bases, nodes and snapshots. Table 6.3 lists the offline CPU cost required for forming the basis functions using different numbers of POD bases. Table 6.4 lists the offline computational cost required for constructing POD basis functions using different number of snapshots. As shown in the tables the relationship between the offline CPU cost and the number of POD bases, nodes and snapshots is linear.

Table 6.3: Offline computational cost (seconds) required for constructing POD basis functions using different numbers of POD bases

Number of POD bases	12	18	30	nodes	snapshots
An immersed wall	17.93	18.11	18.53	7500	200
Number of POD bases	6	12	50	nodes	snapshots
Blasting	146.85	150.65	166.66	48600	200

Table 6.4: Offline computational cost (seconds) required for constructing POD basis functions using different numbers of snapshots

Number of snapshots	50	100	200	nodes	number of POD bases
An immersed wall	1.25	4.41	17.93	7500	12
Blasting	9.39	38.40	150.65	48600	12

6.6 Conclusions

A POD-RBF NIROM has been, for the first time, applied to compressible fluids and fractured solids problem and implemented under the framework of a combined finite-discrete element method based solid model (Y2D) and an unstructured mesh finite element model (Fluidity). The model is independent of the governing equations and the source code, therefore, it is easy to modify. The performance of the NIROM for compressible fluids and fractured solids problem is numerically illustrated in two test cases: an immersed wall in a fluid and a blasting case. The issue whether or not the mean of snapshots is subtracted before constructing the POD basis is addressed by comparing the fluid and fracture solid coupling NIROM results with those from the high fidelity model. An error analysis has been also carried out to validate and assess the newly NIROM. It is found that the fluid and fracture solid coupling NIROM without subtraction the mean can perform much better than that with subtracting the mean. The numerical results show that the NIROM performs well and exhibits a good agreement with high fidelity model if the mean is used to construct the POD basis functions. The front of shock waves is captured well using only a small number of POD bases without mean subtraction beforehand. The online computational cost of the NIROM has been compared against that required for the high fidelity full model. The online CPU cost required for NIROM is reduced by a factor of several orders of magnitude.

Chapter

SEVEN

Variable parametric non-intrusive reduced order modelling of Navier-Stokes equations

7.1 Abstract

A variable-parameter non-intrusive reduced order model (NIROM) based on proper orthogonal decomposition (POD) and radial basis function (RBF) methods have been developed for Navier-Stokes equations. The new variable-parameter NIROM is based on two level radial basis function interpolation. The first level RBF representing the material properties such as initial conditions is constructed through RBF interpolation method, and the data points used to construct the RBF approximation function are chosen by Smolyak sparse grid. The second level RBF represents the time-dependent fluid dynamics. The novelties of this work are (1) the use of two-level RBF interpolation method to represent variable-parametric Navier−Stokes equations; (2) the use of Smolyak sparse grid to determine the distribution of data points representing the material property; (3) the first implementation of such a NIROM under the framework of an unstructured mesh finite element ocean model. The capability of this NIROM has been illustrated numerically by two test cases:

flow past a cylinder and lock exchange case. The results show that this NIROM captured the quasi-totality of the details of the flow with CPU speedup of three orders of magnitude.

This chapter is derived from and expands upon Xiao *et al.* (2016c)

7.2 Introduction

In this chapter, we further extend the NIROMs to varying parameter problems. In this approach a two-level RBF interpolation is used to represent the variable parameter fluid dynamics. The first level RBF interpolation is used to represent the parameter space, and the training data points are determined by the Smolyak sparse grid. The second level RBF interpolation is a set of RBF hyper-surfaces representing the fluid dynamics. This has been implemented under the framework of an unstructured mesh finite element model (FLUIDITY).

In this approach, each variable parameter denotes one dimension, a Smolyak sparse grid is constructed from a tensor product grid obtained from all variable parameters. Each node at the Smolyak sparse grid has a simulation representing the fluid dynamics of a parameter set and solutions to the simulations are recorded. From these snapshots at each node, a set of POD bases are generated in an optimal sense that represents the fluid dynamics. A set of POD bases at an undetermined node can be obtained by the first level RBF interpolation. The second level RBF interpolation is then used to construct a set of hyper-surfaces representing the time-dependent fluid dynamics. After the hyper-surface is obtained, the solution of the ROM at current time level can be obtained by giving POD coefficients of earlier time levels into the hyper-surface. The capabilities of this new NIROM have been assessed for two test cases: a flow past a cylinder case and a 2-D lock exchange case. Comparisons have been made between the high fidelity model and the NIROM to investigate the accuracy of the NIROM methodology.

The structure of the chapter is as follows: section 7.3 presents the reduced order modelling method using Smolyak-RBF-POD method; section 7.4 illustrates the NIROM method derived by means of two numerical examples: flow past a cylinder and lock exchange problem. Finally in section 7.5, summary and conclusions are presented.

7.3 Variable parametric non-intrusive model reduction methodology

In this section, the method of constructing variable parametric NIROM is described. The key idea underpinning the approach is to use a two-level RBF interpolation. The first level RBF interpolation is used to represent parameter space and the second level interpolation is used to represent the fluid dynamics. In the first level RBF, the RBF interpolation method is used to construct a surface representing the varying parameter space *i.e.* initial conditions and boundary conditions. In the second level RBF, a set of hyper-surfaces is constructed to represent the reduced system.

7.3.1 Construction of basis functions

In this work, the variable vectors velocity $\mathbf{u}$, pressure $\mathbf{p}$ and temperature $\mathbf{D}$ at time level n can be written as:

$$\mathbf{u}^n = \alpha_{\mathbf{u}}\Phi_{\mathbf{u}}^T \quad \mathbf{p}^n = \alpha_{\mathbf{p}}\Phi_{\mathbf{p}}^T, \quad \mathbf{D}^n = \alpha_{\mathbf{D}}\Phi_{\mathbf{D}}^T, \tag{7.1}$$

where $\alpha_{\mathbf{u}}$, $\alpha_{\mathbf{p}}$ and $\alpha_{\mathbf{D}}$ denote the velocity, pressure and temperature solution vector of reduced order model respectively, $\alpha_{\mathbf{u}} = (\alpha_{\mathbf{u},1}, \alpha_{\mathbf{u},2}, \cdots, \alpha_{\mathbf{u},m})$, $\alpha_{\mathbf{p}} = (\alpha_{p,1}, \alpha_{p,2}, \cdots, \alpha_{p,m})$ and $\alpha_{\mathbf{D}} = (\alpha_{D,1}, \alpha_{D,2}, \cdots, \alpha_{D,m})$. $\Phi_{\mathbf{u}}^T$, $\Phi_{\mathbf{p}}^T$ and $\Phi_{\mathbf{D}}^T$ denote basis function vectors for velocity, pressure and temperature respectively, and $\Phi_{\mathbf{u}} = (\Phi_{u,1}, \ldots, \Phi_{u,M})$, $\Phi_p = (\Phi_{p,1}, \ldots, \Phi_{p,m})$, $\Phi_D = (\Phi_{D,1}, \ldots, \Phi_{D,m})$.

The general form of the NIROM can be described as follows,

$$\begin{aligned} \mathbf{u}_j^n &= f_{\mathbf{u},j}(\mathbf{u}^{n-1}, \mathbf{p}^{n-1}, \mathbf{D}^{n-1}), \\ \mathbf{p}_j^n &= f_{p,j}(\mathbf{u}^{n-1}, \mathbf{p}^{n-1}, \mathbf{D}^{n-1}), \\ \mathbf{D}_j^n &= f_{D,j}(\mathbf{u}^{n-1}, \mathbf{p}^{n-1}, \mathbf{D}^{n-1}), \end{aligned} \tag{7.2}$$

subject to the initial condition

$$\mathbf{u}_j^0 = (\mathbf{u}_j^0, \Phi_{\mathbf{u},j}), \quad \mathbf{p}_j^0 = (\mathbf{p}_j^0, \Phi_{p,j}), \quad \mathbf{D}_j^0 = (\mathbf{D}_j^0, \Phi_{D,j}), \tag{7.3}$$

where $(\mathbf{u}^{n-1}, \mathbf{p}^{n-1}, \mathbf{D}^{n-1})$ denote a complete set of POD coefficients at time level

$n-1$ ($n \in \{1, 2, \ldots, N_t\}$), N_t is the total number of time levels in the computational period.

7.3.2 Smolyak sparse grid representing the parameter space

In this section, the method of representing the parameter space using Smolyak sparse grid and RBF interpolation is described. The aim of this method is to construct a surface representing the varying parameters using a RBF interpolation method. The number of training data used to construct this surface is determined by Smolyak sparse grids, which find the optimal number of training data. A number of random data points can be chosen to be training data points for the first level RBF interpolation. However, the accuracy of the interpolation function will be reduced if too few data points are chosen. The computational cost will be more intensive if too many data points are chosen. To this end, a sparse grid is used to determine the number of training simulations. Each training data represents a set of basis functions derived from a run of high fidelity full model.

In Smolyak sparse grid interpolation, there is a parameter, called approximation level, that controls how many nodes on the full tensor-product grid are selected. The higher the approximation level is chosen, the larger number of nodes will be used and higher approximation quality will be obtained, for more details, see Smolyak (1963); Judd *et al.* (2014). Smolyak presented a rule that selects nodes from tensor product grid. The construction process of the sparse grid can be summarised as follows:

Let $Q_l^1 f$ be a quadrature rule on dimension 1 with N_l points, it has the form of,

$$Q_l^1 f = \sum_{i=1}^{N_l} f(\xi_l^i).\eta_l^i, \tag{7.4}$$

where l denotes the approximation level of sparse grid and f is the function on the interval [0,1] to be approximated. The η denotes the weight corresponding the point ξ_l^i and i denotes the i^{th} points on the dimension.

In order to construct the sparse grid, a multi-index I is introduced and has the following form of,

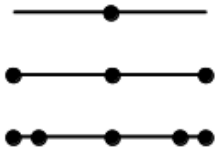


Figure 7.1: Example of 1-D grid: the graph shows the 1-D smolyak grid with level 0, level 1 and full tensor product grid (top to bottom) respectively.

$$I = \sum_{i=1}^{d} l_i. \tag{7.5}$$

Using the multi-index, the d-dimensional sparse grid quadrature formulation $Q_l^d f$ on the space $[0,1]^d$ then can be defined as,

$$Q_l^d f = \sum_{|\mathbf{l}| \leq l+d-1} (\Delta_{l_1}^1 \otimes \cdots \otimes \Delta_{l_d}^d) f, \tag{7.6}$$

where $\triangle_l^1$ is a difference quadrature rule, and is defined as,

$$\triangle_l^1 = (Q_l^1 - Q_{l-1}) f, \tag{7.7}$$

with

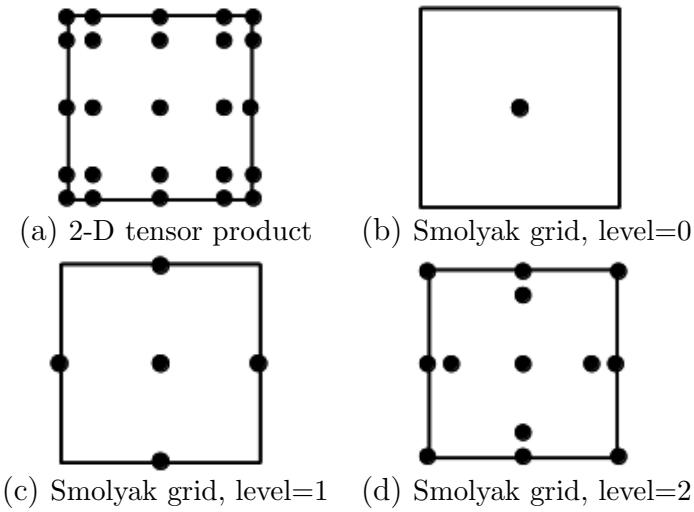
$$Q_0^1 f = 0. \tag{7.8}$$

The Smolyak sparse grid satisfies the following condition:

$$d \leqslant i_1 + i_2 + \cdots + i_d \geqslant d + level, \tag{7.9}$$

where d denotes a dimension size, i_1, i_2 and i_d are indices corresponding to dimension 1, 2 and d respectively, and each one varies from 1 to the number of points in one dimension. For example, in one dimension case, if there are three points on the dimension, then $i_1 \subset 1, 2, 3$. The level is the approximation level. Examples of Smolyak sparse grids of approximation levels 0, 1, 2 with dimension size 1 and 2 are illustrated in figures 7.1 and 7.2.

As can be seen in the figures 7.1 and 7.2 the Smolyak sparse grid has a considerably decreased number of nodes. In the one-dimensional case, see figure7.1, the full tensor product has 5 nodes while the Smolyak sparse grid has only 1 or 3 nodes depending on the level one or two. In two-dimensional case, see figure 7.2, the full



(a) 2-D tensor product (b) Smolyak grid, level=0

(c) Smolyak grid, level=1 (d) Smolyak grid, level=2

Figure 7.2: Examples of grids: the figures displayed above shows the full tensor product grid and 2-D smolyak sparse grid with level 0, 1 and 2.

tensor product has 25 nodes (5×5), while the Smolyak sparse grids with levels 0, 1 and 2 only have 1, 9 and 13 nodes respectively. It is worth noting that the number of nodes ratio for the full tensor product and Smolyak sparse grid increases as the dimension size increases. More details regarding the construction of Smolyak sparse grid can be found in Gerstner & Griebel (1998); Judd *et al.* (2014). In this work, each varying parameter constitutes one dimension in the parameter space which can be a high dimension space.

After obtaining a number of data points, RBF interpolation method is used to construct a parameter surface through the data points. A RBF is a function that its value depends on the distance from the origin or some other points. The RBF is commonly used to approximate a function. The RBF interpolation method constructs an approximation function through a number of random data points.

Let $H(\xi)$ denote the function representing the varying parameter space, and has the form of,

$$H(\xi) = \sum_{i=1}^{G} w_i \, \phi(\|\xi - \xi_i\|), \tag{7.10}$$

where $H(\xi)$ denotes the approximating function (parameter surface), and is a sum of G radial basis functions ϕ, each RBF associated with a different center ξ_i, and weighted by a coefficient w_i. G is the number of training data points. The norm

$\|\|$is usually chosen to be Euclidean distance. For a given data point ξ_j, it has a form of,

$$H(\xi_j) = \sum_{i=1}^{G} w_i \, \phi(\|\xi_j - \xi_i\|), j \in \{1, 2, \ldots, G). \tag{7.11}$$

The frequently used RBFs can be either multi-quadric, inverse quadratic, Gaussian, plate spline or inverse multi-quadric. In this work, Gaussian RBF is chosen. The Gaussian RBF has a form of $\phi(r) = e^{-(r/\sigma)^2}$(r being radius and σ being the shape parameter). The weights can be obtained by solving the linear equation (7.12),

$$Aw_i = b, \tag{7.12}$$

where b is a vector consists of real functional values of the data points, and

$$A = \begin{bmatrix} \phi\left(\|\boldsymbol{\xi}_1 - \boldsymbol{\xi}_1\|_2\right) & \phi\left(\|\boldsymbol{\xi}_1 - \boldsymbol{\xi}_2\|_2\right) & \cdots \phi\left(\|\boldsymbol{\xi}_1 - \boldsymbol{\xi}_G\|_2\right) \\ \phi\left(\|\boldsymbol{\xi}_2 - \boldsymbol{\xi}_1\|_2\right) & \phi\left(\|\boldsymbol{\xi}_2 - \boldsymbol{\xi}_2\|_2\right) & \cdots \phi\left(\|\boldsymbol{\xi}_2 - \boldsymbol{\xi}_G\|_2\right) \\ \vdots & \vdots & \vdots \\ \phi\left(\|\boldsymbol{\xi}_G - \boldsymbol{\xi}_1\|_2\right) & \phi\left(\|\boldsymbol{\xi}_G - \boldsymbol{\xi}_2\|_2\right) & \cdots \phi\left(\|\boldsymbol{\xi}_G - \boldsymbol{\xi}_G\|_2\right) \end{bmatrix}. \tag{7.13}$$

The process of constructing a set of surfaces for the parameter space can be summarised as,

Algorithm 10: Constructing a set of surfaces for the parameter space

(1) Choose the varying parameters and find the maximum and minimum values of the varying parameters. The varying parameters constitute a tensor product grid;

(2) Generate a Smolyak sparse grid for the varying parameters, and obtain the number of nodes N_s on the Smolyak sparse grid;

(3) Generate a number of snapshots over the time period $[0, T]$ for each node at the Smolyak sparse grid by solving the high fidelity model;

(4) Calculate POD basis functions $\Phi_{\mathbf{u}}$, Φ_p or Φ_D for each node through a truncated SVD of the snapshots matrix;

(5) Calculate POD basis functions for a new arbitrary point within the domain of the tensor product grid through the interpolation surface using the following loop:

for $j = 1$ *to* m **do**

(i) Calculate the weights $\mathbf{w}_{i,j}$ by solving;

$$A\mathbf{w}_{i,j} = \Phi_{i,j}, \quad i \in \{1, 2, \ldots, N\},$$

(ii) Obtain a set of surfaces $(H_{\mathbf{u},j}, H_{p,j}, H_{D,j})$ by substituting the weights into following equations,

$$H(\xi) = \sum_{i=1}^{G} w_i \, \phi(\|\xi - \xi_i\|),$$

(iii) Obtain POD basis functions for a new arbitrary point using the equation,

$$H(\xi_k) = \sum_{i=1}^{G} w_j \phi_j(\|(\xi_k) - (\xi_j)\|).$$

endfor

7.3.3 Constructing the second level RBF interpolation

In this section, a process of constructing the second level RBF interpolation representing fluid dynamics is described. That is, this section describes a process how to construct a set of hyper-surfaces. This set of hyper-surfaces is associated with an undetermined point at Smolyak sparse grid.

Algorithm 11: Constructing hyper-surfaces for fluid dynamics

(1) Obtain the functional values y_i at the data point $\boldsymbol{\alpha}^t = (\alpha^t_{\mathbf{u}}, \alpha^t_p, \alpha^t_D)$ via the solutions from the high fidelity model, where $t \in \{1, 2, \dots N_t\}$;

(2) Obtain a set of hyper surfaces through the following loop:

for $j = 1$ *to* m **do**

(i) Calculate the weights $\mathbf{w}_{i,j}$ by solving;

$$\begin{bmatrix} \phi\left(\|\boldsymbol{\alpha}_1 - \boldsymbol{\alpha}_1\|_2\right) & \phi\left(\|\boldsymbol{\alpha}_1 - \boldsymbol{\alpha}_2\|_2\right) & \cdots \phi\left(\|\boldsymbol{\alpha}_1 - \boldsymbol{\alpha}_{N_t}\|_2\right) \\ \phi\left(\|\boldsymbol{\alpha}_2 - \boldsymbol{\alpha}_1\|_2\right) & \phi\left(\|\boldsymbol{\alpha}_2 - \boldsymbol{\alpha}_2\|_2\right) & \cdots \phi\left(\|\boldsymbol{\alpha}_2 - \boldsymbol{\alpha}_{N_t}\|_2\right) \\ \vdots & \vdots & \vdots \\ \phi\left(\|\boldsymbol{\alpha}_{N_t} - \boldsymbol{\alpha}_1\|_2\right) & \phi\left(\|\boldsymbol{\alpha}_{N_t} - \boldsymbol{\alpha}_2\|_2\right) & \cdots \phi\left(\|\boldsymbol{\alpha}_{N_t} - \boldsymbol{\alpha}_{N_t}\|_2\right) \end{bmatrix} \begin{pmatrix} w_1 \\ w_2 \\ \vdots \\ w_{N_t} \end{pmatrix} = \begin{pmatrix} y_1 \\ y_2 \\ \vdots \\ y_{N_t} \end{pmatrix}$$

(ii) Obtain a set of hyper-surfaces $(f_{\mathbf{u},j}, f_{p,j}, f_{D,j})$ by substituting the weights obtained in the above equation into following equations,

$$f_{\mathbf{u},j}(\alpha_{\mathbf{u}}, \alpha_p, \alpha_D) = \sum_{i=1}^{N_t} w_{i,j}\phi_j(\left\|(\alpha_{\mathbf{u}}, \alpha_p, \alpha_D) - (\alpha^i_{\mathbf{u}}, \alpha^i_p, \alpha^i_D)\right\|),$$

$$f_{p,j}(\alpha_{\mathbf{u}}, \alpha_p, \alpha_D) = \sum_{i=1}^{N_t} w_{i,j}\phi_j(\left\|(\alpha_{\mathbf{u}}, \alpha_p, \alpha_D) - (\alpha^i_{\mathbf{u}}, \alpha^i_p, \alpha^i_D)\right\|),$$

$$f_{D,j}(\alpha_{\mathbf{u}}, \alpha_p, \alpha_D) = \sum_{i=1}^{N_t} w_{i,j}\phi_j(\left\|(\alpha_{\mathbf{u}}, \alpha_p, \alpha_D) - (\alpha^i_{\mathbf{u}}, \alpha^i_p, \alpha^i_D)\right\|),$$

endfor

7.3.4 Calculating the undetermined POD coefficients

After obtaining a set of hyper-surfaces in algorithm 11, then it can be used to calculate the ROM. In this section, a process of calculating the undetermined POD coefficients is described.

Algorithm 12: Online calculation of the undetermined POD coefficients (solutions of ROM)

(1) Initialisation.

for $j = 1$ *to* m **do**

Initialize $\alpha^0_{\mathbf{u},j}$, $\alpha^0_{p,j}$ and $\alpha^0_{D,j}$;

endfor

(2) Calculate solutions of current time step:

for $n = 1$ *to* N_t **do**

for $j = 1$ *to* m **do**

(i) Assign a complete set of POD coefficients $\alpha^{n-1}_{u,j}$, $\alpha^{n-1}_{p,j}$ and $\alpha^{n-1}_{D,j}$ at previous time level $n-1$ into the hyper-surface $f = (f_{\mathbf{u},j}, f_{p,j}, f_{D,j})$:

$$f_{\mathbf{u},j} \leftarrow (\alpha^{n-1}_{\mathbf{u}}, \alpha^{n-1}_{v}, \alpha^{n-1}_{D}), \quad f_{p,j} \leftarrow (\alpha^{n-1}_{\mathbf{u}}, \alpha^{n-1}_{v}, \alpha^{n-1}_{D}), \quad f_{D,j} \leftarrow (\alpha^{n-1}_{\mathbf{u}}, \alpha^{n-1}_{v}, \alpha^{n-1}_{D}),$$

(ii) Calculate the POD coefficient $\alpha^n_{\mathbf{u}}$, α^n_p and α^n_D at current time level n using the equations:

$$\alpha^n_{\mathbf{u},j} = \sum_{i=1}^{N_t} w_{i,j}\phi_{i,j}(r), \quad \alpha^n_{p,j} = \sum_{i=1}^{N_t} w_{i,j}\phi_{i,j}(r), \quad \alpha^n_{D,j} = \sum_{i=1}^{N_t} w_{i,j}\phi_{i,j}(r),$$

endfor

Compute the solution $\mathbf{u}^n$, p^n and D^n on full space at current time level n by projecting $\alpha^n_{\mathbf{u},j}$, $\alpha^n_{p,j}$ and $\alpha^n_{D,j}$ onto the full space using the equations,

$$\mathbf{u}^n = \sum_{j=1}^{m} \alpha^n_{\mathbf{u},j}\Phi_{\mathbf{u},j}, \quad p^n = \sum_{j=1}^{m} \alpha^n_{p,j}\Phi_{p,j}, \quad D^n = \sum_{j=1}^{m} \alpha^n_{D,j}\Phi_{D,j}.$$

endfor

7.4 Numerical Examples

Two examples are presented in this section to show the capabilities of the NIROM in resolving flow problem governed by Navier-Stokes equations. In the first example a flow past a cylinder is solved. This is used to demonstrate the capabilities of varying boundary condition (inlet velocity). In the second example a 2-D lock exchange problem is solved. This example involves varying the initial conditions (initial temperature distribution). Both examples were simulated under the framework of an advanced unstructured mesh finite element model (FLUIDITY) (see Pain *et al.* (2005)).

7.4.1 Flow past a cylinder

In this example a 2 dimensional flow past a cylinder is numerically simulated. The problem domain is presented in figure 7.7 which shows a cylinder with a radius of 0.12 units at location (0.2, 0.2) embedded within a rectangle with 2 non-dimensional units length and 0.4 non-dimensional units width. The fluid dynamics of the flow are driven by an inlet velocity, which enters from the left boundary of the domain. The fluid is allowed to flow past through the right boundary of the domain. No slip and zero outward flow conditions are applied to the lower and upper edges and the Dirichlet boundary conditions are applied to the cylinder's wall. The Reynolds number used in this example is set to be $Re = 4000$. The simulation time period is 6 seconds$[0s - 6s]$, and the time step size is $\Delta t = 0.01$. 300 snapshots were captured at equal time intervals $\Delta t = 0.02$ between the time period $[0s - 6s]$. The computational domain consists of 3213 nodes.

The NIROM was constructed from snapshots of three simulations from the full model. For each of these training simulations, the inlet velocity was varied between 0.45 and 0.55. The varying value of inlet velocity of training simulation is determined by the Smolyak sparse grid. The number of training simulations is dependent on the dimension size and the level of the Smolyak sparse grid, see Smolyak (1963). A varying inlet velocity of 0.46, having different values from the three training simulations, is chosen to show the capability of the NIROM.

The singular values are presented in figure 7.3. It can be seen that there is a sharp drop in the first five singular values, and then they continue to decrease at a steady rate, which means a larger singular value is associated with a basis function

capturing more energy. This can be confirmed on inspection of the basis functions graph 7.4 which shows that of the first, second and third basis functions capture most of the energy and the $16^{th}, 35^{th}$ and 36^{th} basis functions capture less energy. The first basis function captures the largest energy of the system while the 36^{th} one captures the least energy. The singular values decay graph 7.3 provides us a clear indication how to choose the number of basis functions to represent the system.

In this example NIROM with 6, 12 and 36 basis functions are selected to demonstrate the increasing accuracy resulting from choosing larger number of basis functions. Figure 7.5 presents velocity profile of exact high fidelity model, as well as NIROMs using 6, 12 and 36 basis functions at time levels $t = 3$ and $t = 6$. Whilst there are visual differences in the NIROM with smaller number of basis function, in comparison to the exact high fidelity model's solution, the NIROM has still captured the dominant flow profile. Unlike the NIROM with 6 basis functions, the NIROM with 12 basis functions well captured the flow on the right half part of the computational domain. When the number of basis functions were increased to 36, the NIROM has captured the details of the flow very well- namely there are few clear differences with exact solutions. This can be confirmed on inspection of the error graph 7.6, which presents errors between the exact solutions with NIROMs with 6, 12 and 36 basis functions. The error is evidently decreased when the number of basis function is increased to 36. Figure 7.7 compares the velocity solutions of high fidelity with NIROM using 6, 12 and 36 basis functions at a particular point (x=0.89514, y=0.32519) on the computational domain. It clearly shows that the NIROM with 36 basis functions is in close agreement with the exact solutions.

The figures 7.5 and 7.6 show that the new NIROM is capable of predicting unseen variable parameters. In this paragraph, the error of NIROM is analysed. This is achieved by root-mean-square error (RMSE) and correlation coefficient, which considers all the computational nodes on the mesh and all the simulation time levels. Figure 7.8 shows the RMSE and correlation coefficient between the high fidelity model and NIROMs with 6, 12 and 36 basis functions. This figure shows again that the NIROM with more basis functions exhibits more prediction accuracy.

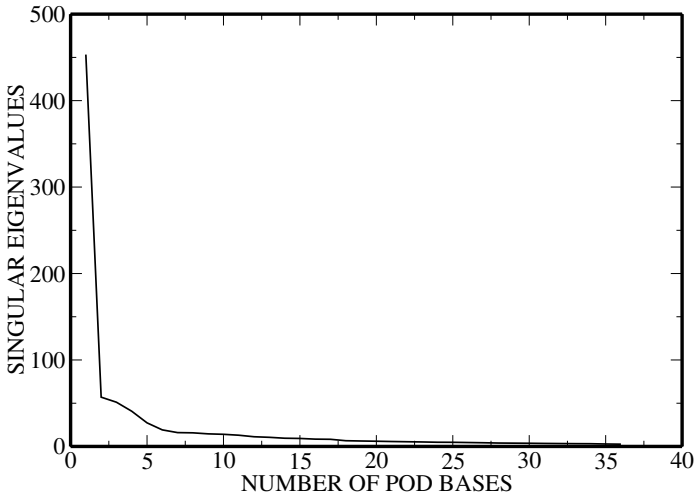
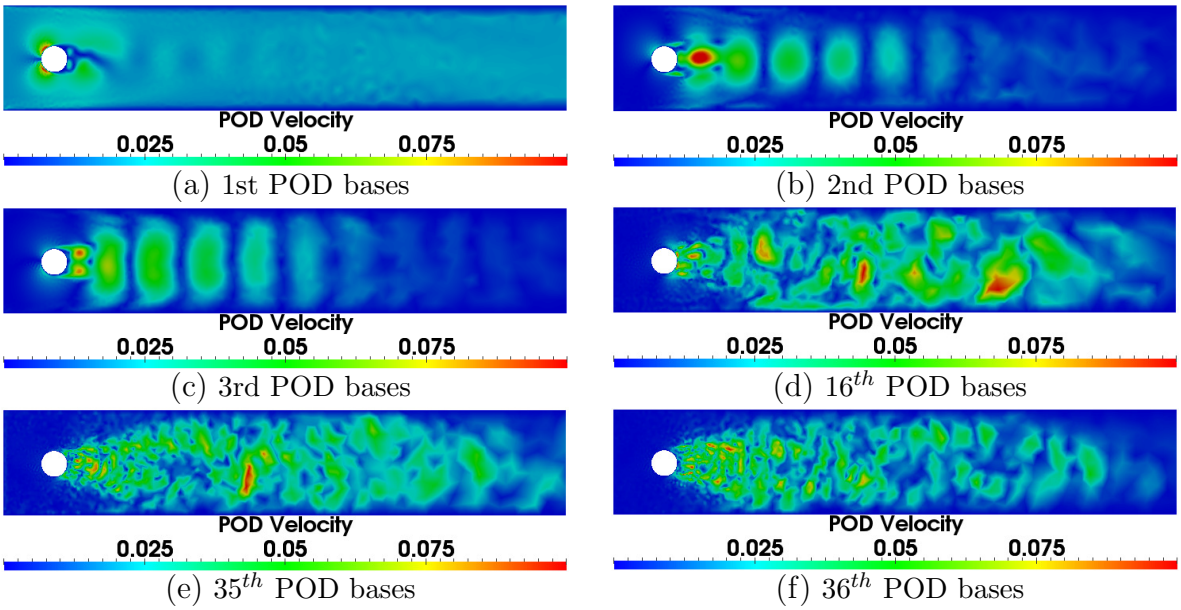


Figure 7.3: Flow past a cylinder: the graph shows the first 36 eigenvalues in a decreasing order.

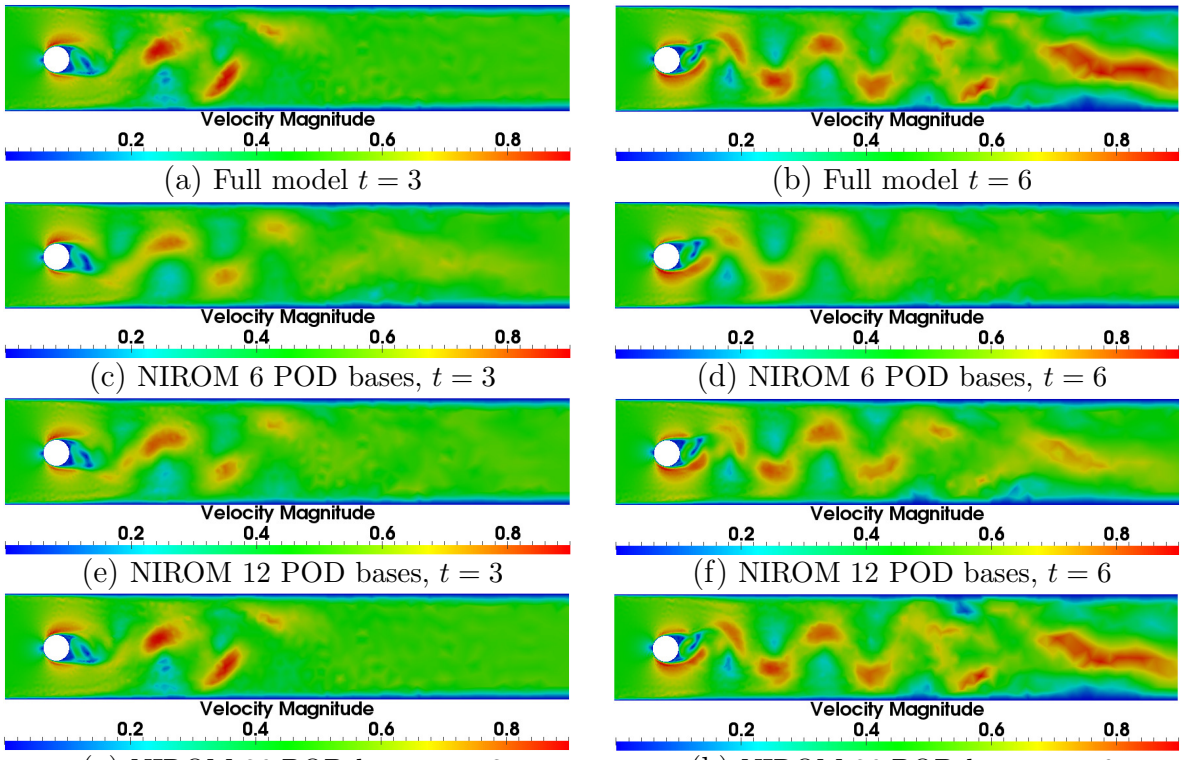


(a) 1st POD bases (b) 2nd POD bases

(c) 3rd POD bases (d) 16^{th} POD bases

(e) 35^{th} POD bases (f) 36^{th} POD bases

Figure 7.4: Flow past a cylinder: the figures show the some of the first 36 POD bases functions of flow past a cylinder test case.



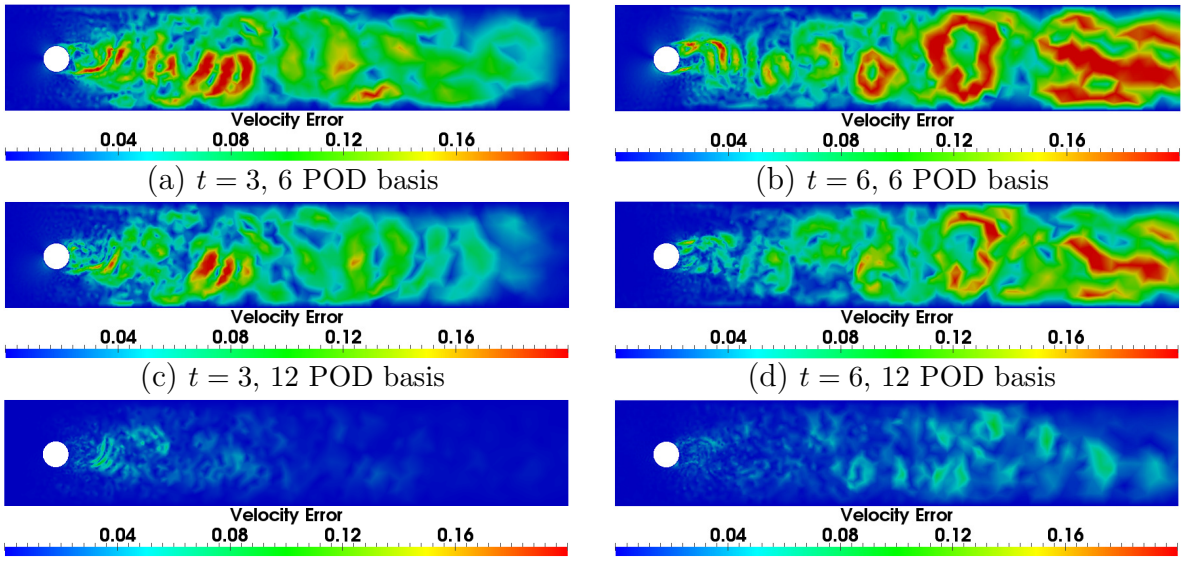
(a) Full model $t = 3$ (b) Full model $t = 6$

(c) NIROM 6 POD bases, $t = 3$ (d) NIROM 6 POD bases, $t = 6$

(e) NIROM 12 POD bases, $t = 3$ (f) NIROM 12 POD bases, $t = 6$

(g) NIROM 36 POD bases, $t = 3$ (h) NIROM 36 POD bases, $t = 6$

Figure 7.5: Flow past a cylinder: the figures displayed above shows the velocity from full model and the NIROM with 6, 12 and 36 POD bases at time instances 3 and 6.



(a) $t = 3$, 6 POD basis

(b) $t = 6$, 6 POD basis

(c) $t = 3$, 12 POD basis

(d) $t = 6$, 12 POD basis

(e) $t = 3$, 36 POD basis

(f) $t = 6$, 36 POD basis

Figure 7.6: Flow past a cylinder: the figures show the velocity error between high fidelity model and NIROM with 6, 12 and 36 POD basis at time instances 3 and 6.

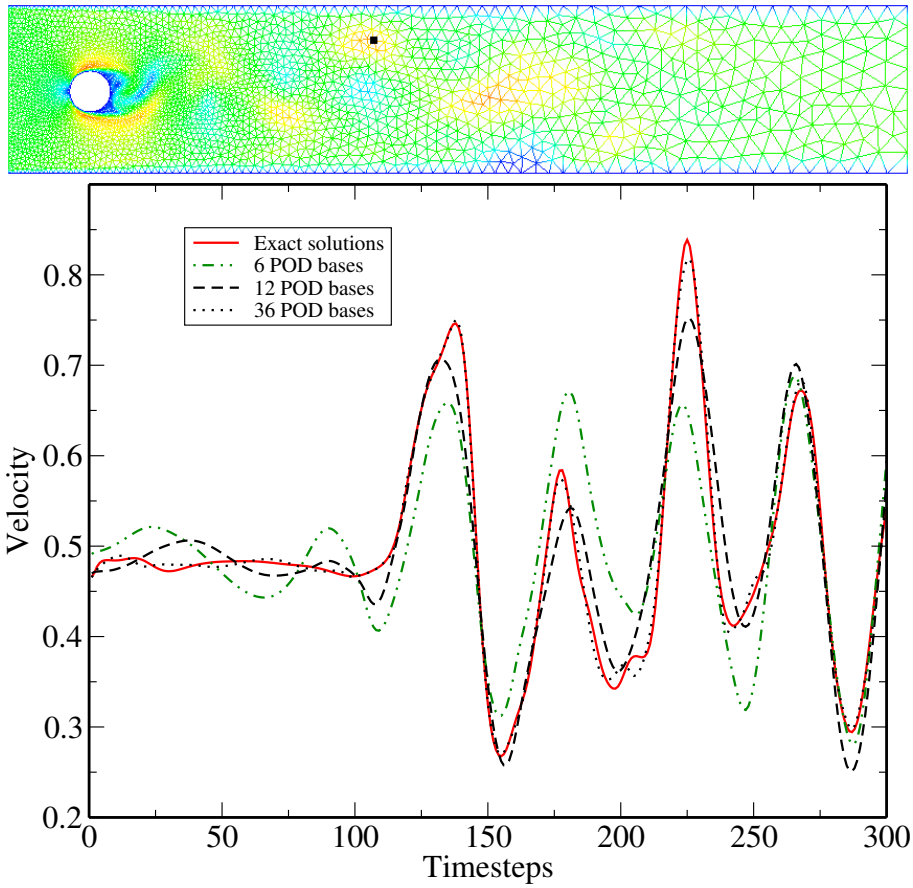


Figure 7.7: Flow past a cylinder: the graph shows the velocity solutions from high fidelity model, NIROM with 6, 12 and 36 basis functions at location (x=0.89514, y=0.32519).

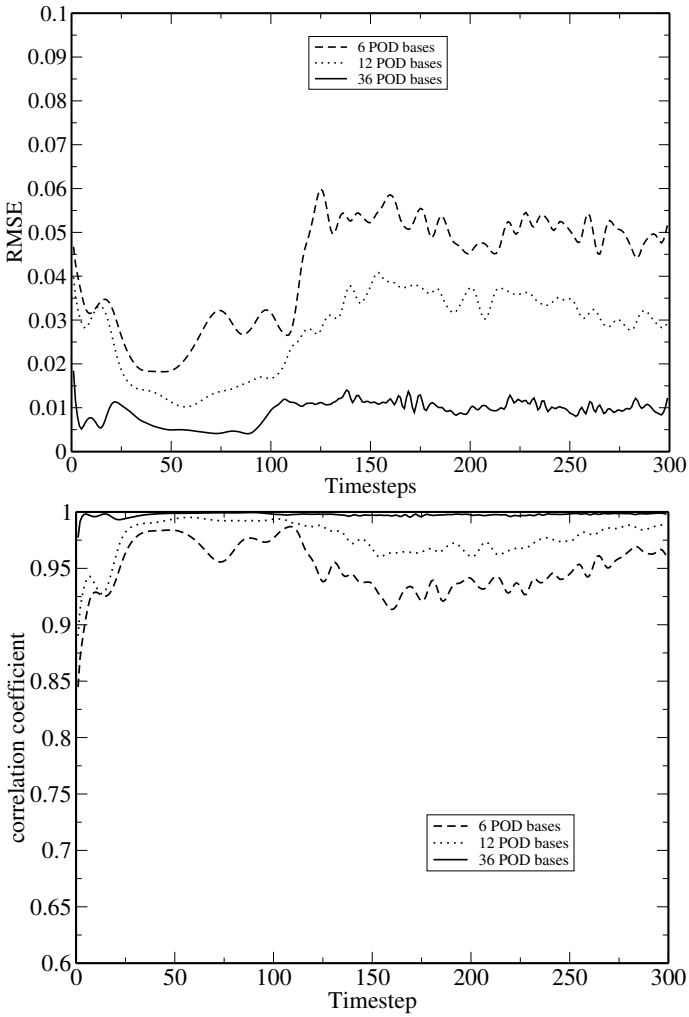


Figure 7.8: Flow past a cylinder: the graph shows the root mean squared error(RMSE) and correlation coefficient between full model and NIROM with 6, 12 and 36 POD bases.

7.4.2 Lock exchange

This section solves a lock exchange problem which involves two fluids of different temperature and density separated by a lock. When the lock is removed, two currents propagate along the tank horizontally. This laboratory-scale set up incorporates dynamics observed in gravity currents over a range of scales (see Benjamin (1968)). The problem computational domain is presented in figure 7.9 which consists of a non-dimensional rectangle (0.8×0.1). The initial conditions for the velocities and pressure are $\mathbf{u} = 0$ and $p = 0$, respectively. The isotropic value of viscosity is 1×10^{-10}. The Crank-Nicolson method was applied in the temporal discretisation. The problem was resolved using the mesh with 4242 nodes, and 120 snapshots were obtained at regularly spaced time intervals during the time period $[0 - 30]$ from each simulation. The NIROM was constructed from snapshots of three simulations from the high fidelity full model. Each simulation has a different initial condition for the non-dimensional temperature. The initial condition for the temperature is T. It is set to be $-T$ for the cold fluid at the left side of the lock T for the hot fluid at the right side of the lock. T was varied between 0.45 to 0.55. According to the Smolyak sparse grid, the T for the three training data points are set to be 0.45, 0.5 and 0.55, respectively. A initial temperature ($T = 0.46$) is chosen here to show the capabilities of the NIROM, that is, the initial temperature of hot fluid is set to be -0.46 and the cold is set to be 0.46.

Figure 7.10 presents the singular values of the problem in a decreasing order. In this problem, the reduction in the first 10 singular values is very fast, which means the first 10 basis functions corresponding to these 10 singular values captured most of the energy. Some of the first 36 basis functions are presented in figure 7.11, which shows the first few basis functions are capturing the general profile while the last few basis functions are capturing the minor details of the profile. In other words, the basis functions resulting from the larger singular value captures the larger energy of the system. In this example 6, 12 and 36 basis functions were chosen to show the capabilities of the NIROM.

Figure 7.12 presents the temperature solutions obtained from high fidelity model, NIROM with 6, 12 and 36 basis functions. In comparison to the solution from high fidelity model, the NIROMs appear to be minor visual differences between all the temperature solutions. However, temperature solutions predicted from NIROM with 6 and 12 basis functions are shown to be diffusing a little bit slower than

NIROM with 36 basis functions at the time level ($t = 30$). Using larger number of basis functions results in greater accuracy of the NIROM. The NIROM with 36 basis functions is almost identical to the high fidelity model. This can be confirmed by inspection of the error figure 7.13, which shows the solution differences between exact solutions and NIROM with 6, 12 and 36 basis functions. It can be seen that the error of NIROM with 36 basis functions is too small to notice. The error of NIROM is also analysed by RMSE and correlation coefficients analysis, which is presented in figure 7.14. It can be seen that the RMSE curve and correlation coefficient curve of NIROM with 36 basis functions are flat at this scale, and the RMSE is close to 0 and the correlation coefficient is very close to 1. This means that in this case NIROM using 36 basis functions has captured almost 99.99% energy of the system.

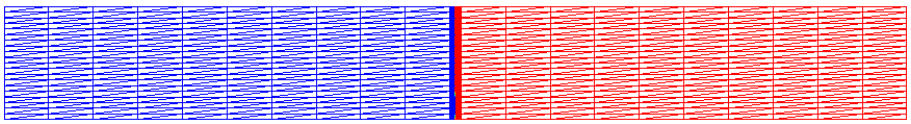


Figure 7.9: Lock exchange: the graph shows the computational domain of the 2-D lock exchange problem.

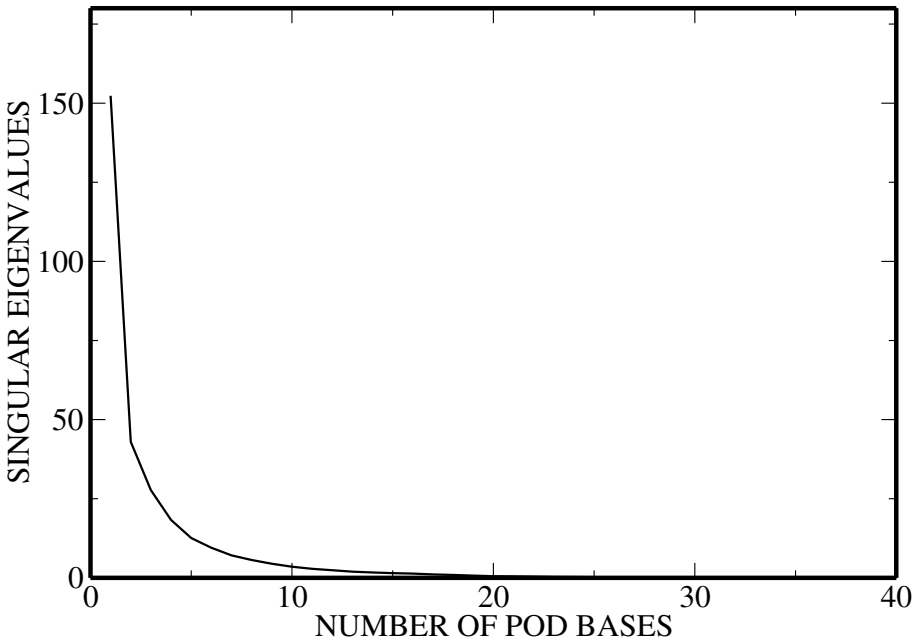
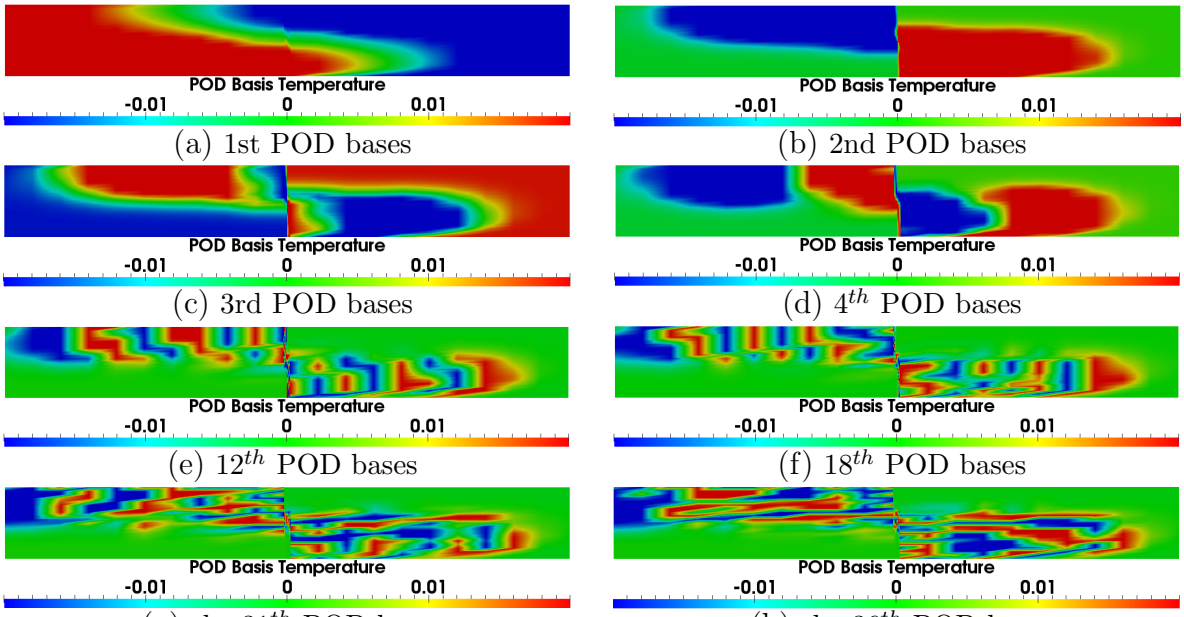


Figure 7.10: Lock exchange: the graph shows the singular values of the 2-D lock exchange problem.



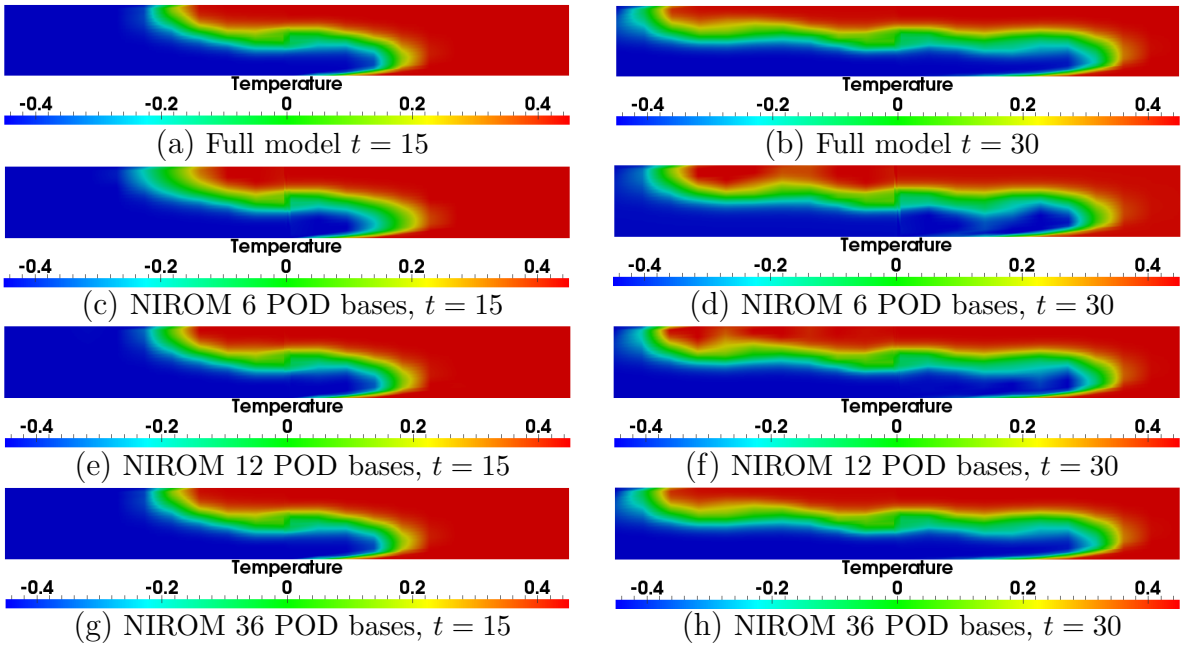
(a) 1st POD bases (b) 2nd POD bases

(c) 3rd POD bases (d) 4^{th} POD bases

(e) 12^{th} POD bases (f) 18^{th} POD bases

(g) the 31^{th} POD bases (h) the 36^{th} POD bases

Figure 7.11: Lock exchange: the figure shows some of the first 36 basis functions of the problem.



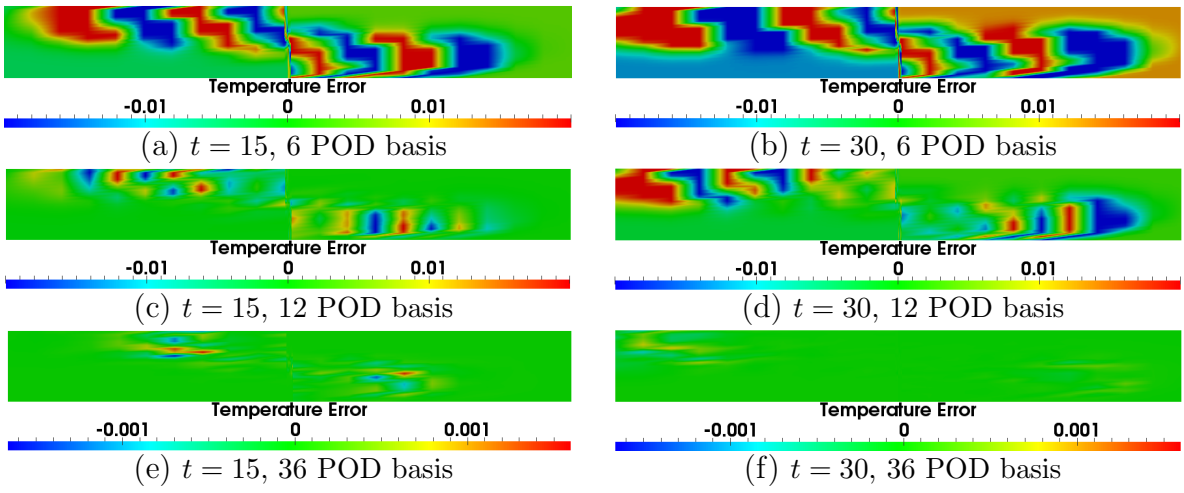
(a) Full model $t = 15$ (b) Full model $t = 30$

(c) NIROM 6 POD bases, $t = 15$ (d) NIROM 6 POD bases, $t = 30$

(e) NIROM 12 POD bases, $t = 15$ (f) NIROM 12 POD bases, $t = 30$

(g) NIROM 36 POD bases, $t = 15$ (h) NIROM 36 POD bases, $t = 30$

Figure 7.12: Lock exchange: the figures displayed above shows the temperature from full model and the NIROM of 6, 12 and 36 POD bases at time instances 15 and 30.



(a) $t = 15$, 6 POD basis (b) $t = 30$, 6 POD basis

(c) $t = 15$, 12 POD basis (d) $t = 30$, 12 POD basis

(e) $t = 15$, 36 POD basis (f) $t = 30$, 36 POD basis

Figure 7.13: Lock exchange: the figures show the temperature error between high fidelity model and NIROM with 6, 12 and 36 POD basis at time instances 15 and 30.

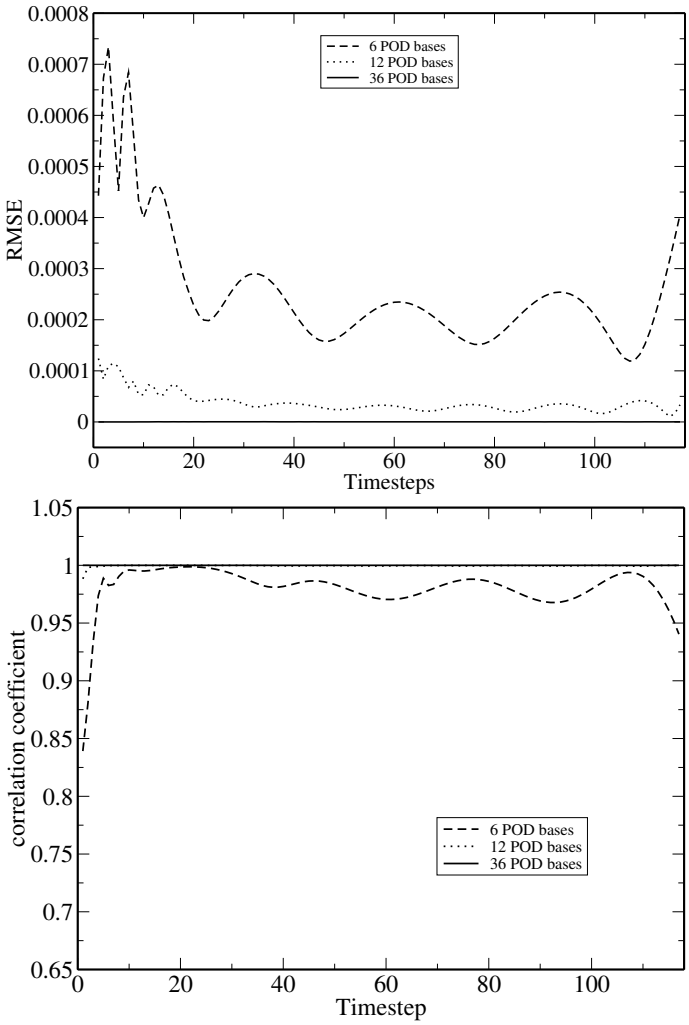


Figure 7.14: Lock exchange: the graph shows the root mean squared error(RMSE) and correlation coefficient between full model and NIROM with 6, 12 and 36 POD bases.

7.4.3 Efficiency of the NIROM model

This section compares the online computational cost required by high fidelity model and the NIROM. The specifications of the machine for simulations are: 4 cores with a frequency of 2.00GHz($Intel$® $Core^{TM}$ i7-3537U CPU @ 2.00GHz 4); a 8GB memory. One core was used when running the simulations since the test cases were simulated in serial.

Table 7.1 lists the online CPU cost required for simulating the flow past a cylinder and lock exchange test cases using the full model and NIROM. The offline cost involving constructing the basis functions is not listed in this table.

Table 7.1: Online CPU cost required for simulating the two test cases using the full model and NIROM during one time step.

Cases	Model	assembling and solving	projection	interpolation	total
Flow past a cylinder	Full model	0.5891	0	0	0.6002
	NIROM	0	0.0003	0.0001	0.0004
Lock exchange	Full model	0.9489	0	0	0.95003
	NIROM	0	0.0003	0.0001	0.0004

As shown in the table that the online CPU time required for the NIROM is substantially less than that for high fidelity model. The reduction in CPU time is dependent on the complexity of problem.

7.5 Conclusion

This chapter has presented a new NIROM for variable parameter Navier-Stokes equations. It forms two level RBF interpolation. The first level RBF interpolation is a set of surfaces representing parameter space such as initial conditions and boundary conditions. The second level RBF interpolation is a set of hyper-surfaces that represent fluid dynamics of the system. A unique aspect of the NIROM is that the training data points of the first level RBF interpolation is determined by the Smolyak sparse grid, resulting in optimal number of simulations.

Two numerical examples were chosen to demonstrate the capabilities of the NIROM.

In the first numerical example, flow past a cylinder was solved, which the NIROM was trained upon a small number of simulations determined by the Smolyak sparse grid and then tested on a new varying parameter. It was shown that the NIROM was accurate while the computational time was reduced by three orders of magnitude. In the second example, a lock exchange problem was solved. The prediction capabilities of the NIROM was carried out by specifying a new varying initial condition. It was shown that the problem was well predicted with a significantly efficient computational cost. An error analysis was undertaken through RMSE and correlation coefficient.

Future work will include applying the NIROM to more complex cases, realistic problems and problems with more complex varying parameters set, for example, several initial conditions, boundary conditions and other parameters were varied simultaneously.

Chapter

EIGHT

Variable-material non-intrusive reduced order modelling of multi-phase porous media flows

8.1 Abstract

A novel variable-material non-intrusive reduced order model (NIROM) based on a Smolyak sparse grid interpolation method, a radial basis function (RBF) method and proper orthogonal decomposition (POD) has been developed for multiphase flows in porous media. This novel NIROM is constructed by using a Smolyak grid or RBF interpolation methods to represent the material properties and a RBF method to represent the time-dependent POD equations. The novelties of this work are in (1) the use of the newly presented Smolyak gird and RBF interpolation method to construct variable-material NIROM; (2) the first attempt of applying such a NIROM to multiphase porous media simulation; (3) the first implementation of such a NIROM under the framework of a unstructured mesh control volume finite element (CVFEM) multiphase model.

The capability of this new NIROM has been numerically illustrated in three multiphase flows in porous media: a four material layer case, a reservoir with four baffles

and a reservoir with eight baffles case. By comparing the results of the novel NIROM against the solutions obtained from the high fidelity full model, it is shown that this model can result in a large reduction in the CPU cost (by about three orders) while much of the details of multiphase flow in porous media are captured.

This chapter is derived from and expands upon Xiao *et al.* (2016b).

8.2 Introduction

In this chapter a novel NIROM for variable-material multi-phase porous media flows is described and numerically illustrated. The newly NIROM is capable of solving multi-phase porous media problems with variable input parameters with considerable enhanced computational efficiency. An unseen material property set can be obtained by interpolating from the Smolyak material property grid the RBF hypersurface. At each node in the Smolyak material grid there is a set of RBF hypersurfaces for POD coefficients. The difference between this model and one presented in previous chapter 7 (two-level RBF interpolation model) lies in the first-level interpolation. This model constructs a set of surface representing the material properties directly using Smolyak sparse grid.

The structure of this chapter is as follows:

section 8.3 presents the methodology of constructing the NIROM for variable-material multi-phase porous media flows; section 8.4 illustrates the methodology derived by means of four numerical examples. The illustration consists of four test problems where a four material layers, reservoir with four and eight baffles and a 3D fluvial channel case are resolved. Finally in section 8.5, the conclusion is presented.

8.3 Methodology of constructing the NIROM for variable-material multi-phase porous media flows

This section describes the methodology of construction of two-level interpolation representing the varying material property multi-phase porous media problems. The first level interpolation is achieved by the Smolyak sparse interpolation or RBF interpolation. The second level interpolation is through POD-RBF method, as described in 2.7. In this approach, a number of simulations are run firstly, and each

simulation has a set of varying material properties. The values of varying material properties in each simulation are determined by the Smolyak sparse grid. Then, a set of Smolyak sparse grids is constructed to represent those material properties. Those sets of Smolyak sparse grids are essentially a set of surfaces. After obtaining the surfaces, a set of new basis functions can be obtained by inputting a new arbitrary point ξ. A set of hyper surfaces is then constructed to represent the fluid dynamics of multi-phase porous media problem. This process is described in algorithm 11. After this process, the new results can be obtained by the on-line algorithm 12. In algorithms 11 and 12, the subscript D denotes density. In this chapter, it can be changed to denote saturation.

8.3.1 Material property surfaces based on Smolyak sparse grid

The algorithm of constructing a set of Smolyak sparse grids for permeabilities can be described as the following algorithm 13,

8.3.2 Permeability distribution surfaces based on radial basis functions

The radial basis function interpolation method can also be used to construct a set of surfaces representing the permeability space. The radial basis function interpolation method is an efficient method to approximate a function using a number of scattered data points. The radial basis functions interpolation method constructs functional approximations in the form of

$$H(\mathbf{k}) = \sum_{i=1}^{N} w_i \, \phi(\|\mathbf{k} - \mathbf{k}_i\|), \tag{8.2}$$

where the interpolation function $f(\mathbf{k})$ is represented as a linear combination of N radial basis functions(ϕ). Each RBF is associated with a different center $\mathbf{k}_i$ (other points), and weighted by a coefficient w_i. $\|\mathbf{k} - \mathbf{k}_i\|$ is a scalar distance defined by the L_2 norm.

In the RBF interpolation problem, the weight coefficients w_i are determined by ensuring that the interpolation function values $f(\mathbf{k})$ will match the given data y

Algorithm 13: Constructing surfaces for permeabilities space using a Smolyak sparse grid

(1) Determine d material property variables $\{k_1, k_2, \cdots, k_d\}$ where d is the number of varying rock types or permeability regions and calculate the minimum and maximum values of those variables. Each material property variable constitute one dimension of the Smolyak sparse grid;

(2) Construct a Smolyak sparse grid for the material property variables;

(3) Obtain values for each Smolyak sparse grid node $\mathbf{k}^i = \{k_1^i, k_2^i, \cdots, k_d^i\}, i \in (1, 2, \cdots, N_s)$;

(4) Generate N_s sets of snapshots over the time period $[0, T]$ for each Smolyak sparse grid node by running the high fidelity model. Each Smolyak sparse grid node is associated with a set of snapshots;

(5) Generate N_s sets of POD basis functions $\{\Phi_{\mathbf{u}}^1, \Phi_p^1, \Phi_S^1\}$, $\{\Phi_{\mathbf{u}}^2, \Phi_p^2, \Phi_S^2\}$, $\cdots$, $\{\Phi_{\mathbf{u}}^{N_s}, \Phi_p^{N_s}, \Phi_S^{N_s}\}$ for each Smolyak sparse grid node $k^i, i \in (1, 2, \cdots, N_s)$ by performing a truncated SVD of the snapshots matrix obtained from corresponding set of snapshots;

(6) Obtain a number of basis functions for a new material property point k^i within the domain of the tensor product grid via Smolyak sparse grid interpolation method. A tensor product grid has a total number of nodes of O^d where there are O points used in each dimension and d is the size of dimensionality):

for $j = 1$ *to* m **do**

(i) Obtain a set of surfaces by using the Smolyak sparse grid interpolation formulation,

$$\hat{A}(k, d) = \sum_{max(d,l+1) \leq |\mathbf{l}| \leq d+l} (-1)^{d+l-|\mathbf{l}|} \cdot \begin{pmatrix} d-1 \\ d+l-|\mathbf{l}| \end{pmatrix} (U^{l_1} \otimes \cdots \otimes U^{l_d}), \quad (8.1)$$

where $|\mathbf{l}| = l_1 + \cdots + l_d$, $(U^l)(f) = \sum_{i=1}^{O_l} f(k_i^l).(H_i^l(k))$,

endfor

(basis functions) exactly. This is achieved by enforcing $f(\mathbf{k}) = y$, which produces a linear equation

$$Aw = y, \tag{8.3}$$

where

$$A = \begin{bmatrix} \phi\left(\|k_1 - k_1\|_2\right) & \phi\left(\|k_1 - k_2\|_2\right) & \cdots \phi\left(\|k_1 - k_n\|_2\right) \\ \phi\left(\|k_2 - k_1\|_2\right) & \phi\left(\|k_2 - k_2\|_2\right) & \cdots \phi\left(\|k_2 - k_n\|_2\right) \\ \vdots & \vdots & \vdots \\ \phi\left(\|k_n - k_1\|_2\right) & \phi\left(\|k_n - k_2\|_2\right) & \cdots \phi\left(\|k_n - k_n\|_2\right) \end{bmatrix}, \tag{8.4}$$

$$w = [w_1, w_2, ..., w_n]^T, y = [y_1, y_2, ..., y_n]^T \tag{8.5}$$

The weight coefficients w_j are then determined by solving the linear system (8.3) $Aw = y$. The process of constructing a set of surfaces for the parameter space can be summarised as,

Algorithm 14: Constructing a set of surfaces for permeability distribution space based on RBF interpolation

(1) Choose the varying parameters and find the maximum and minimum values of them. The varying parameters constitute a tensor product grid;

(2) Generate randomly a number of nodes G on the tensor product grid;

(3) Generate a number of snapshots over the time period $[0, T]$ for each node by solving the high fidelity model;

(4) Calculate POD basis functions $\Phi_{\mathbf{u}}$, Φ_p or Φ_S for each node through a truncated SVD of the snapshots matrix;

(5) Calculate POD basis functions for a new arbitrary point within the domain of the tensor product grid through the interpolation surfaces using the following loop:

for $j = 1$ *to* m **do**

(i) Calculate the weights $\mathbf{w}_{i,j}$ by solving;

$$A\mathbf{w}_{i,j} = \Phi_{i,j}, \quad i \in \{1, 2, \ldots, N\},$$

(ii) Obtain a set of surfaces $(H_{\mathbf{u},j}, H_{p,j}, H_{S,j})$ by substituting the weights into following equations,

$$H(\mathbf{k}) = \sum_{i=1}^{G} w_i \, \phi(\|\mathbf{k} - \mathbf{k}_i\|),$$

(iii) Obtain POD basis functions for a new arbitrary point using the equation,

$$H(k_k) = \sum_{i=1}^{G} w_j \phi_j(\|(k_k) - (k_j)\|).$$

endfor

8.4 Numerical Examples

8.4.1 Four material layers test case

The first example for numerical illustration of the method proposed in this chapter is a four material layer test case. This problem domain consists of a rectangle of non-dimensional size 0.75×0.2, as shown in figure 8.3. The domain is divided into four identical areas with permeabilities between 1 and 2. The viscosity of oil and water are 1. The porosity of each layer is 0.2. Initial saturation of water and oil are set to be 0.2 and 0.8 respectively. The injection is driven by constant pressure inlet boundary condition with a dimensionless value of 1.

The problem was resolved with a mesh of 864 nodes during the simulation time period $[0, 0.03]$ with a time step size of 0.00005. 60 snapshots were taken from the pre-computed solution at regularly spaced time intervals $\Delta t = 0.0005$ and from these POD bases are generated for the solution variables u, p, s.

The NIROM is constructed from a number of training simulations. For each of these training simulations, the permeability sets of the four areas in the computational domain were varied, the permeability sets are listed in table 8.1-labelled E1-E9. The permeabilities of four areas of each training simulation are determined by the Smolyak sparse grid. In this case the Smolyak sparse grid has a dimension size of four and a approximation level of one. In order to test the NIROM, an unseen case -labelled P1 in table 8.1, with a permeability set of (2.000, 1.500, 2.000, 1.550) was predicted.

In this example 6, 12 and 18 POD basis functions were chosen to show the capabilities of the NIROM. Figure 8.1 shows the saturation from the high fidelity model and NIROM with 6, 12 and 18 POD bases at time instances 0.01 and 0.025. It can be seen that the NIROM with 6 POD bases captured the general magnitude of the flows well, however, saturation at some local small areas, for example, the front area were not fully captured. This can be improved by increasing the number of POD bases. As it is shown in the figure that the NIROM with 18 POD bases have a good agreement with high fidelity model. There is not too much visual difference between the high fidelity full model and NIROM with 18 POD basis functions.

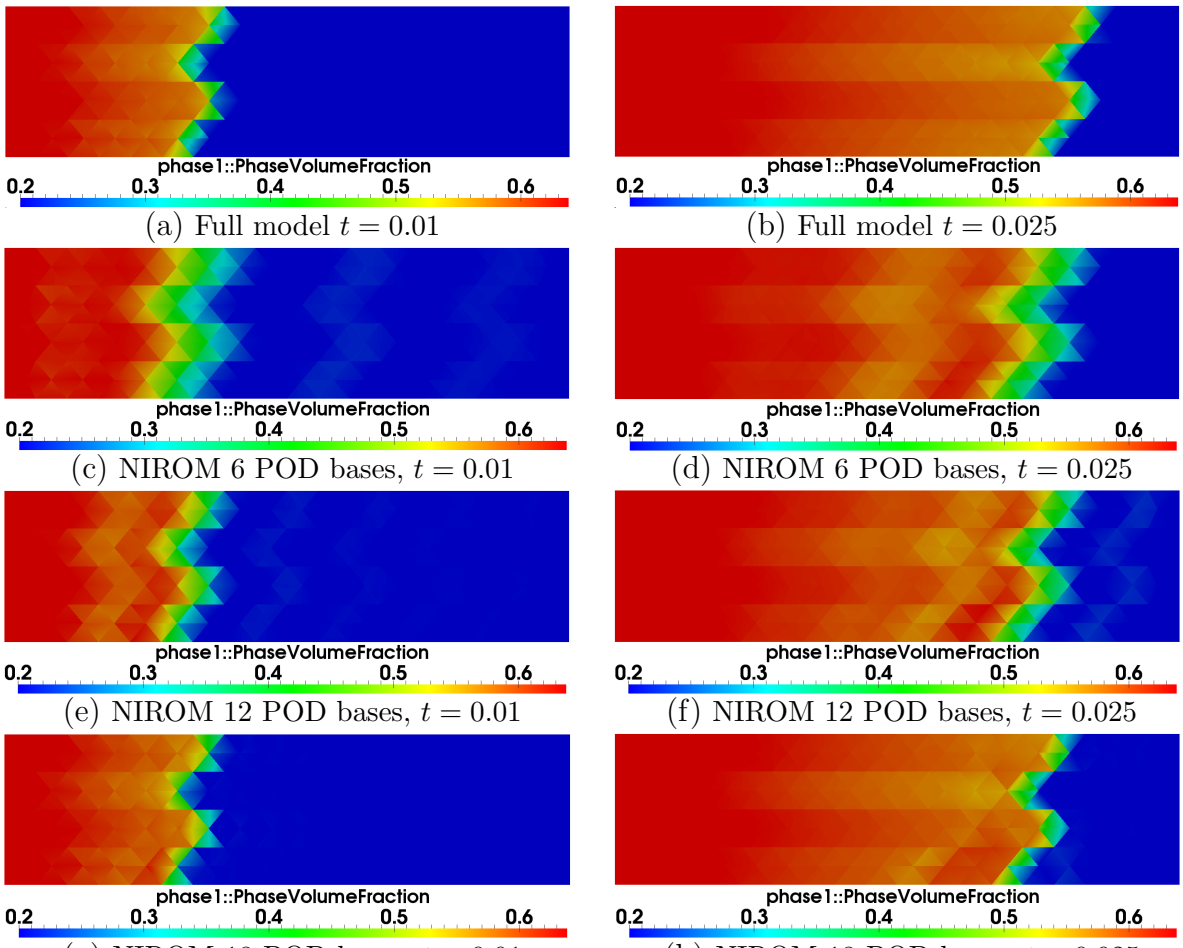
Generally, the POD basis functions represent energy of the system. The larger number of POD basis functions are used, the more energy will be captured. Some

of the first 18 POD basis functions are presented in figure 8.2, which shows the first POD basis function captures the most of the energy of the system, while the last POD basis captures the minor detailed energy of the system. The energy captured by the POD basis functions from the first one to last one is in a decreasing order.

The comparison of saturation solutions at a particular point on the computational domain between the high fidelity full model and NIROM with 6, 12 and 18 POD basis functions is presented in figure 8.3. The location of that particular point on the domain is shown in the top of figure 8.3. It is evident in the figure that the saturation solutions of NIROM with 18 POD basis functions are more closer to high fidelity model than NIROM with 6 and 12 POD basis functions.

Table 8.1: Permeability specifications for four-layer case

Cases	Layer 1	Layer 2	Layer 3	Layer 4
E1	1.500	1.500	1.500	1.500
E2	1.000	1.500	1.500	1.500
E3	2.000	1.500	1.500	1.500
E4	1.500	1.000	1.500	1.500
E5	1.500	2.000	1.500	1.500
E6	1.500	1.500	1.000	1.500
E7	1.500	1.500	2.000	1.500
E8	1.500	1.500	1.500	1.000
E9	1.500	1.500	1.500	2.000
P1	2.000	1.500	2.000	1.550



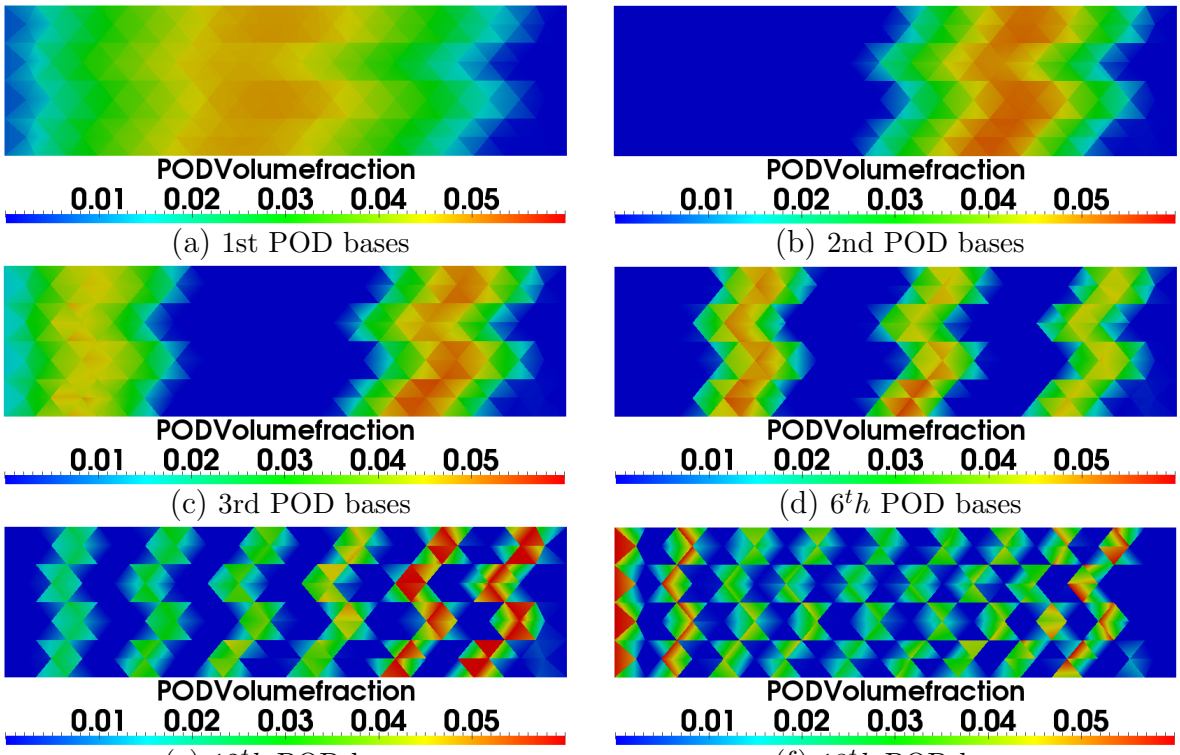
(a) Full model $t = 0.01$ (b) Full model $t = 0.025$

(c) NIROM 6 POD bases, $t = 0.01$ (d) NIROM 6 POD bases, $t = 0.025$

(e) NIROM 12 POD bases, $t = 0.01$ (f) NIROM 12 POD bases, $t = 0.025$

(g) NIROM 18 POD bases, $t = 0.01$ (h) NIROM 18 POD bases, $t = 0.025$

Figure 8.1: Four material layers test case: the figures displayed above shows the saturation from the high fidelity model and NIROM with 6, 12 and 18 POD bases at time instances 0.01 and 0.025.



(a) 1st POD bases (b) 2nd POD bases

(c) 3rd POD bases (d) 6^th POD bases

(e) 12^th POD bases (f) 18^th POD bases

Figure 8.2: Four material layers test case: the figures show the some of the first 18 POD bases functions of the four material layers test case.

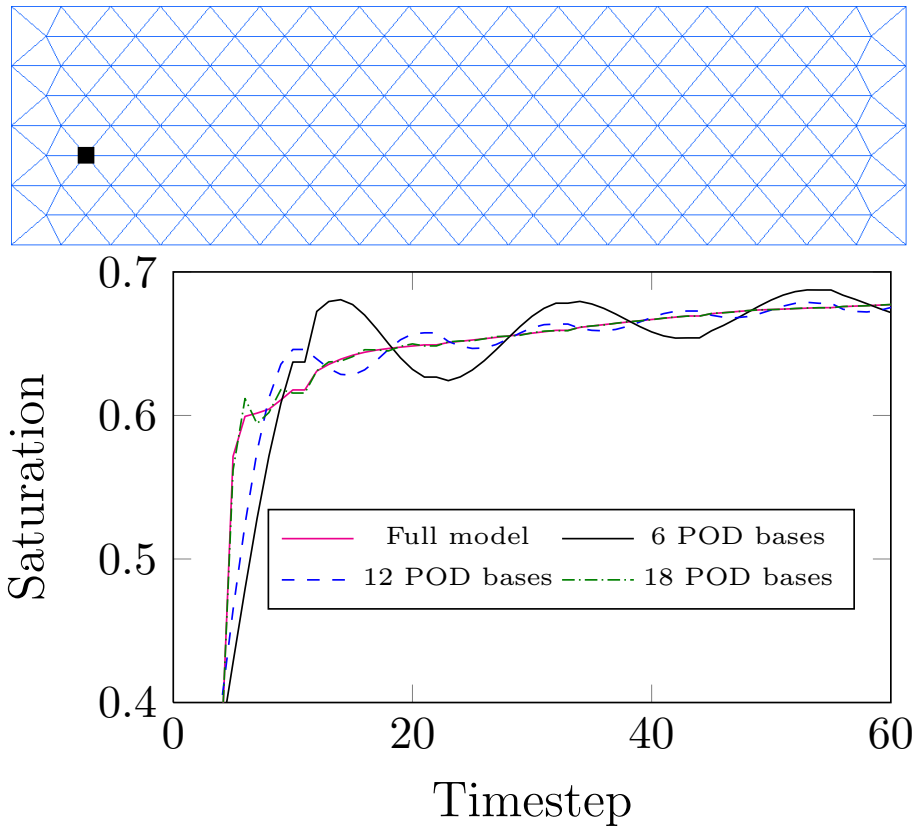


Figure 8.3: Four material layers test case: the graph shows the saturation solutions predicted by the full model and the NIROM using 6, 12 and 18 POD bases at a position (x= 0.0625 y=0.075).

8.4.2 Reservoir with four baffles

The second case is comprised of four low permeability barriers embedded in a higher permeability domain as illustrated in figure 8.4. The domain has a non-dimensional size of 10 × 10 with 2646 nodes. The permeability of the four barriers in this test case are between 0.1 and 0.5, and the permeability of the background is 10. The porosity is 0.2 and the injection was controlled by constant inlet velocity of (x=1, y=1).

The full model simulation with a mesh of 2646 nodes was run during the simulation period $[0, 5]$ with a time step size of 0.01. 50 snapshots of solutions were collected at regularly spaced time intervals $\Delta t = 0.1$ for each solution variable.

Similar to the first example, a number of training simulations are used for constructing the NIROM. The number of training simulations are determined by the Smolyak sparse grid. In this example, Smolyak sparse grid with level one and two were used to demonstrate the performance of NIROM. The Smolyak sparse grid with level one and dimensional size of four has 9 nodes and the Smolyak sparse grid with level two has 41 nodes. The permeability of each barrier constitutes one dimension of the Smolyak sparse grid. The quadrature rule used in this Smolyak sparse grid is a Clenshaw-Curtis rule. Each node is associated with a training simulation and each training simulation has a varied permeability combinations, see table 8.2, which lists permeability combinations of the four-barrier case using level one for training simulations -labelled E1-E9.

Table 8.2: Permeability combinations for four-barrier case with level one

Cases	Barrier 1	Barrier 2	Barrier 3	Barrier 4
E1	0.300	0.300	0.300	0.300
E2	0.100	0.300	0.300	0.300
E3	0.500	0.300	0.300	0.300
E4	0.300	0.100	0.300	0.300
E5	0.300	0.500	0.300	0.300
E6	0.300	0.300	0.100	0.300
E7	0.300	0.300	0.500	0.300
E8	0.300	0.300	0.300	0.100
E9	0.300	0.300	0.300	0.500
P1	0.100	0.500	0.500	0.500

An unseen Smolyak sparse grid node(0.1,0.5,0.5,0.5)-labelled P1 was predicted to show the capabilities of the NIROM. Figure 8.5 presents the solutions of saturation from high fidelity model and the NIROM with 6, 12 and 24 POD bases at time instances 1.5 and 4.0 using smolyak level one. It can be seen that the NIROM with only 6 POD bases captured almost all the energy, and it only has some small errors at the front area, as shown in figure 8.5(c). These errors were decreased by using larger number of POD bases. There is no much visual difference between the NIROMs with 12 and 24 POD bases and high fidelity model since larger number of POD bases results in more captured energy from the system. Some of the first 24 POD basis functions are presented in figure 8.6. It can be seen that the first few basis functions are capturing the main energy, while the last few ones are capturing the minor detailed informations.

A level two of the Smolyak sparse grid is also used to demonstrate the capabilities of the NIROM. There are 41 nodes in this Smolyak sparse grid with level two. Permeability combinations of the four barriers of 32 more nodes excluding 9 nodes of level one are listed in table 8.3 and 8.4-labelled E10-E41. The solutions of saturation of the unseen node (0.1,0.5,0.5,0.5) using level two are presented in figure 8.7. This figure compares the saturation solutions of the high fidelity model, NIROM with 6, 12 and 24 POD bases at time instances 1.5 and 4.0 using smolyak level two. These results of level two are very close to that of level one. A point which is next to the barrier one (lowest permeability area in the domain), see figure 8.8(top), and it represents the most difficult location in the domain to capture. The figure 8.8 shows the saturation solutions from high fidelity model and NIROM with 6, 12 and 24 POD bases using level one(middle) and level two(bottom). The results of NIROM using level one and two are very close, therefore, they are shown in separate figures(middle and bottom in figure 8.8). It can be seen in the figure that the NIROM with level two performs a little bit better than that of level two. This is only one node which is located in the most difficult area to capture from the 2646 nodes in the computational domain. The performance of overall nodes in the domain is analysed by correlation coefficient and root mean square error(RMSE), which are presented in figure 8.9. This figure again shows that NIROMs are overall very close to the fidelity model and the errors are decreased by choosing larger number of POD basis functions.

Table 8.3: Permeability sets for the 4 barrier case with level two excluding level one–part I

Cases	Barrier 1	Barrier 2	Barrier 3	Barrier 4
E10	0.15857	0.300	0.300	0.300
E11	0.44142	0.300	0.300	0.300
E12	0.100	0.100	0.300	0.300
E13	0.500	0.100	0.300	0.300
E14	0.100	0.500	0.300	0.300
E15	0.500	0.500	0.300	0.300
E16	0.300	0.15857	0.300	0.300
E17	0.300	0.44142	0.300	0.300
E18	0.100	0.300	0.100	0.300
E19	0.500	0.300	0.100	0.300
E20	0.100	0.300	0.500	0.300
E21	0.500	0.300	0.500	0.300
E22	0.300	0.100	0.100	0.300
E23	0.300	0.500	0.100	0.300
E34	0.300	0.100	0.500	0.300
E25	0.300	0.500	0.500	0.300
E26	0.300	0.300	0.15857	0.300

Table 8.4: Permeability sets for the 4 barrier case with level two excluding level one–part II

Cases	Barrier 1	Barrier 2	Barrier 3	Barrier 4
E27	0.300	0.300	0.44142	0.300
E28	0.100	0.300	0.300	0.100
E29	0.500	0.300	0.300	0.100
E30	0.100	0.300	0.300	0.500
E31	0.500	0.300	0.300	0.500
E32	0.300	0.100	0.300	0.100
E33	0.300	0.500	0.300	0.100
E34	0.300	0.100	0.300	0.500
E35	0.300	0.500	0.300	0.500
E36	0.300	0.300	0.100	0.100
E37	0.300	0.300	0.500	0.100
E38	0.300	0.300	0.100	0.500
E39	0.300	0.300	0.500	0.500
E40	0.300	0.300	0.300	0.15857
E41	0.300	0.300	0.300	0.44142
P1	0.100	0.500	0.500	0.500

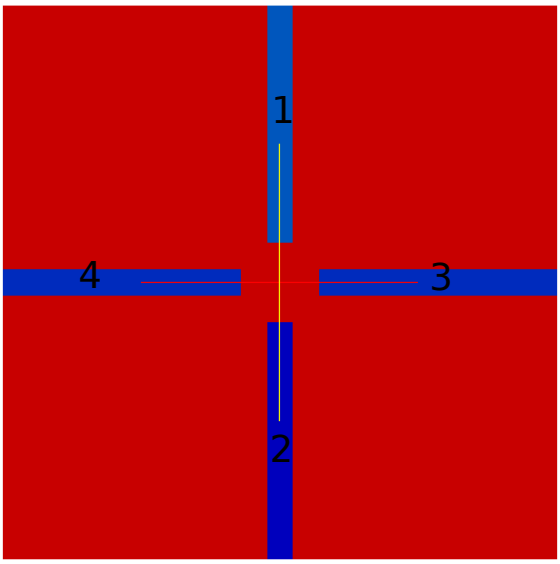
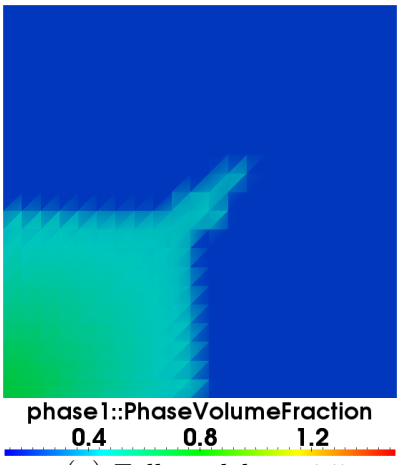
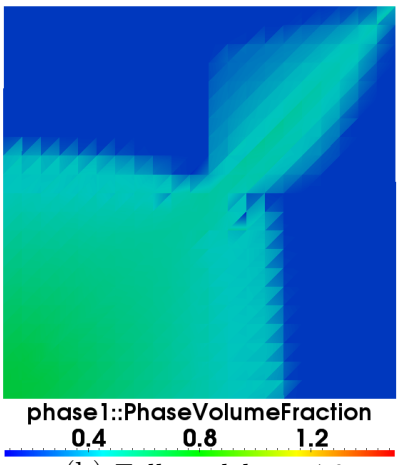


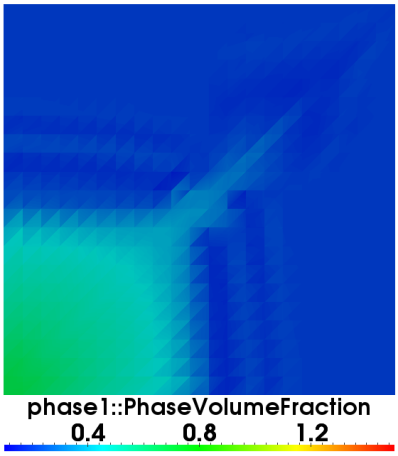
Figure 8.4: Four baffles case: distribution of permeabilities in the domain, the permeability of the four barriers(barrier 1: top; barrier 2: bottom; barrier 3: right; barrier 4: left) are between 0.1 and 0.5, and the permeability of the background is 10.



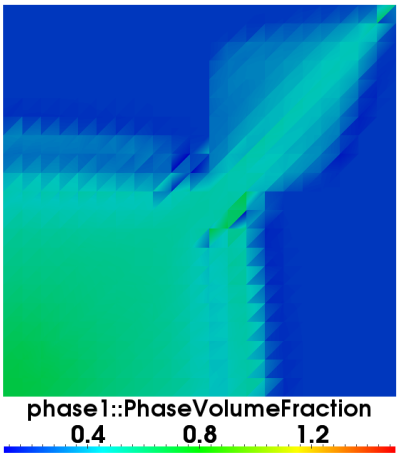
(a) Full model $t = 1.5$



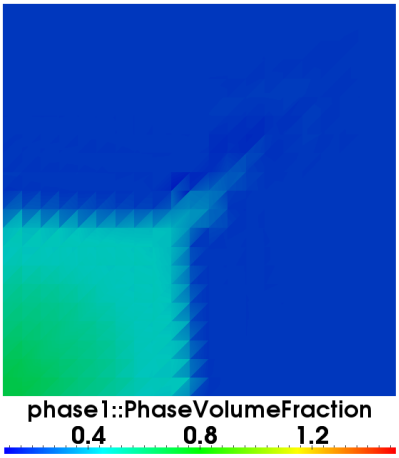
(b) Full model $t = 4.0$



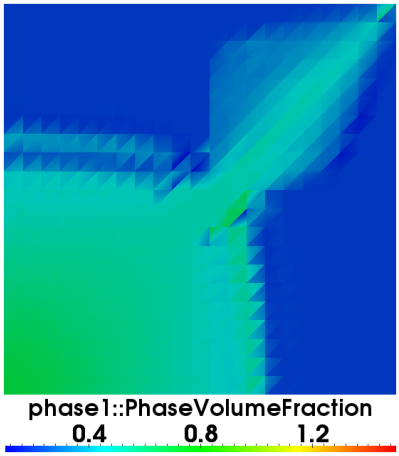
(c) NIROM 6 POD bases, $t = 1.5$



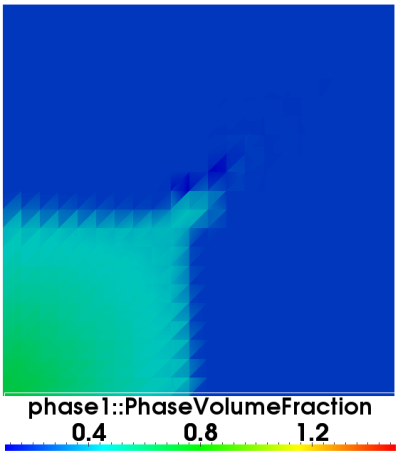
(d) NIROM 6 POD bases, $t = 4.0$



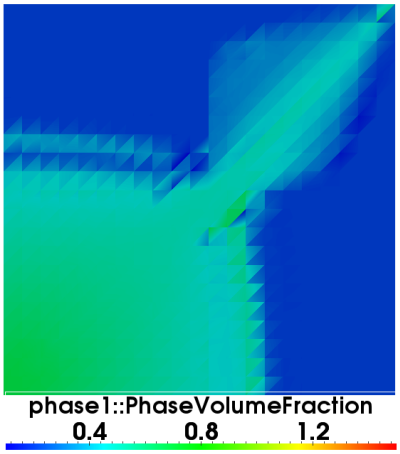
(e) NIROM 12 POD bases, $t = 1.5$



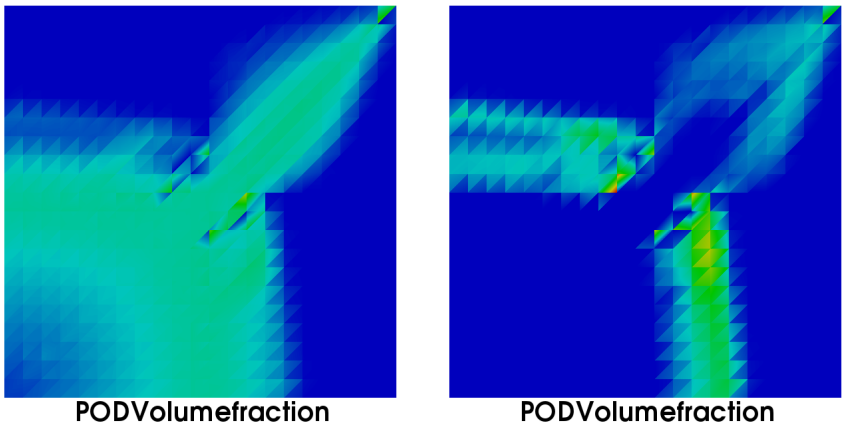
(f) NIROM 12 POD bases, $t = 4.0$



(g) NIROM 24 POD bases, $t = 1.5$

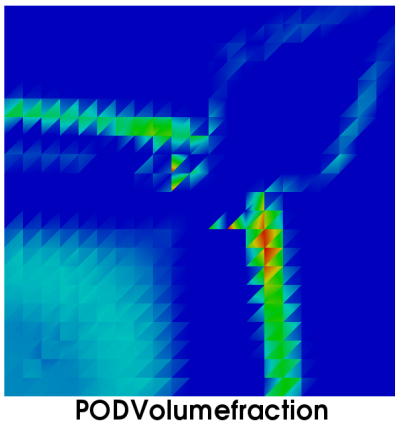


(h) NIROM 24 POD bases, $t = 4.0$

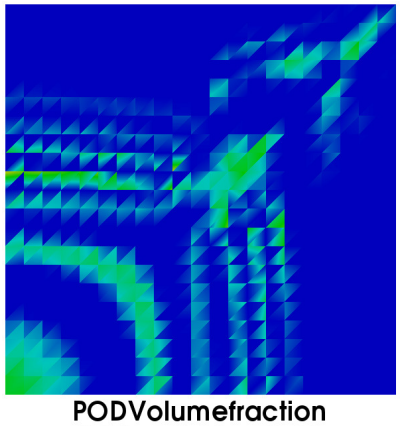


(a) the first POD bases

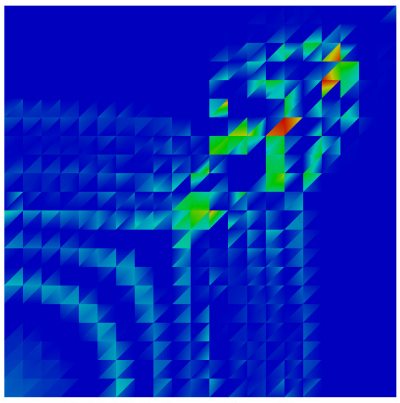
(b) the second POD bases



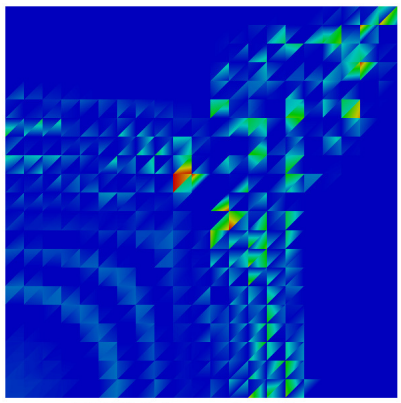
(c) the third POD bases



(d) the twelfth POD bases

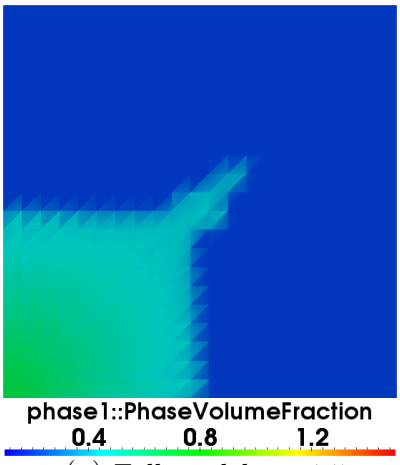


(e) the twentieth POD bases

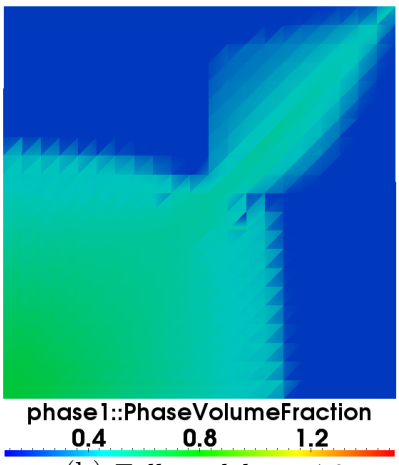


(f) the twenty-fourth POD bases

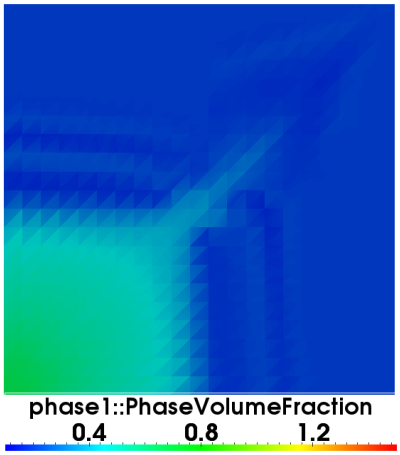
Figure 8.6: Four baffles case: some of the first 24 POD basis functions of the reservoir with four baffles.



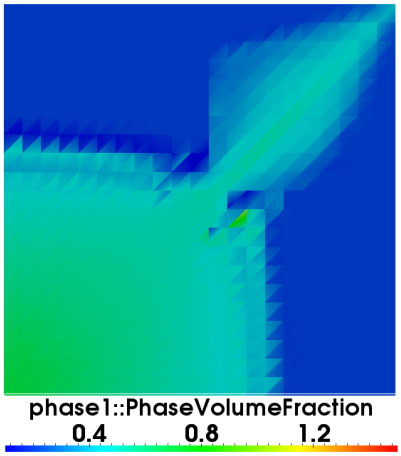
(a) Full model $t = 1.5$



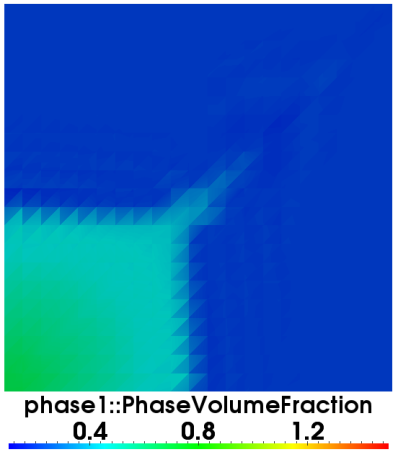
(b) Full model $t = 4.0$



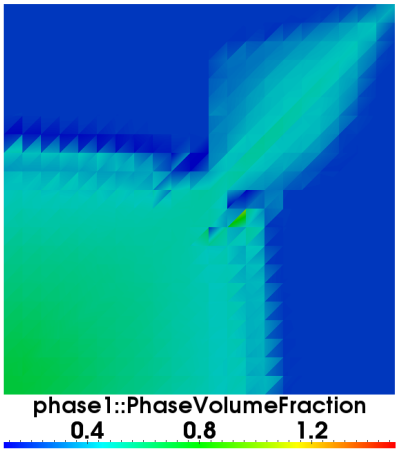
(c) NIROM 6 POD bases, $t = 1.5$



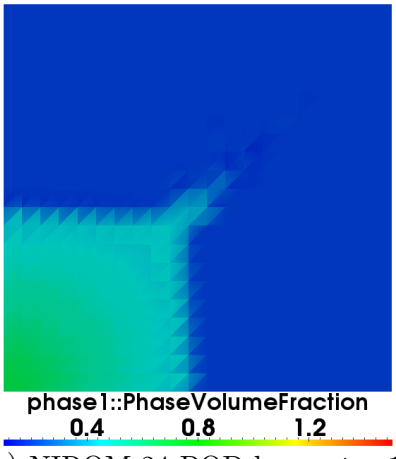
(d) NIROM 6 POD bases, $t = 4.0$



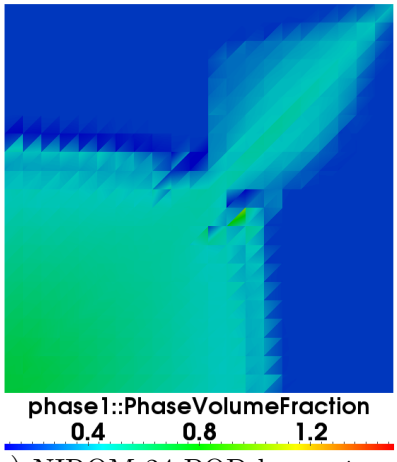
(e) NIROM 12 POD bases, $t = 1.5$



(f) NIROM 12 POD bases, $t = 4.0$



(g) NIROM 24 POD bases, $t = 1.5$



(h) NIROM 24 POD bases, $t = 4.0$

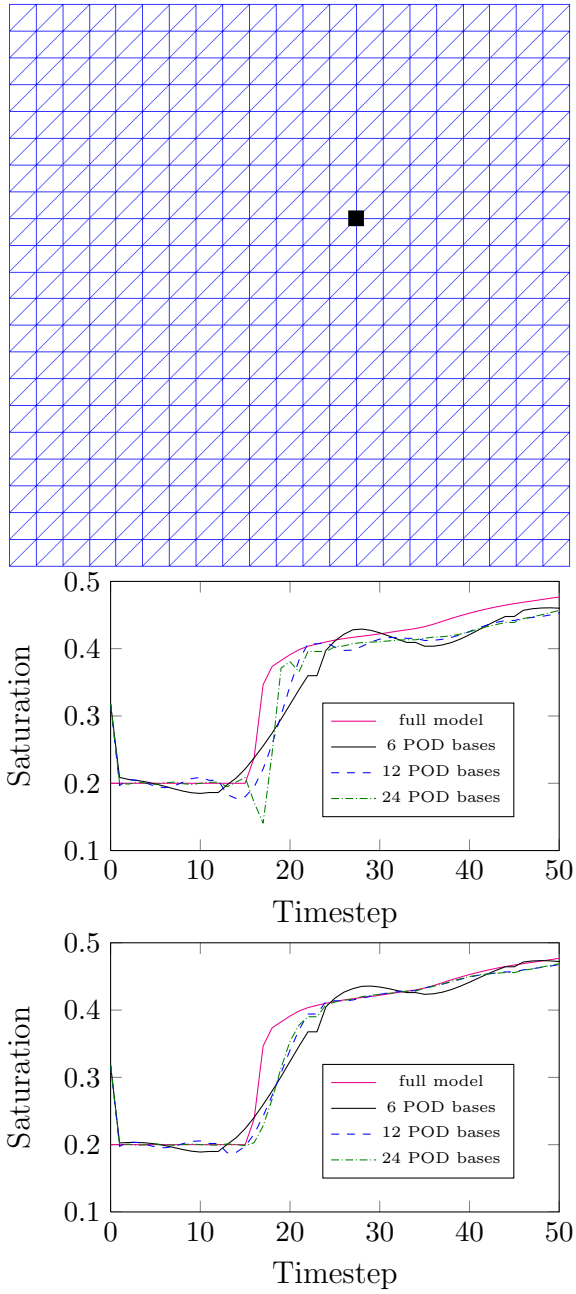


Figure 8.8: Four baffles case: the graphs show the solution velocities predicted by the full model, and the NIROM with level one (middle) and level two (bottom) at location (6.1905, 6.1905).

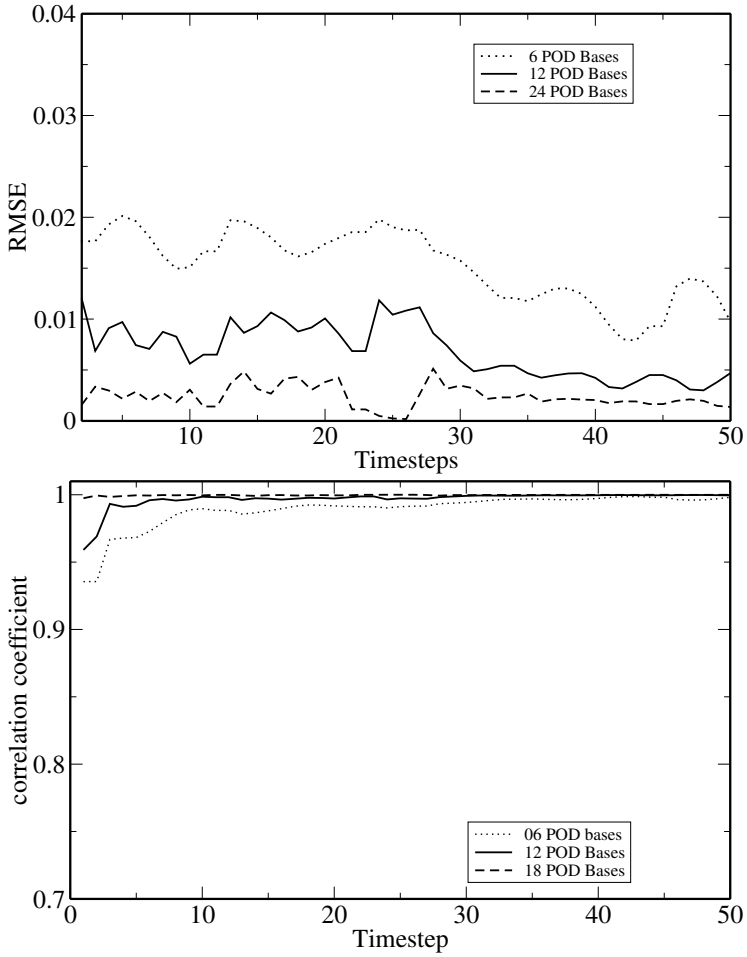


Figure 8.9: Four baffles case: the graph shows the RMSE errors and correlation coefficient calculated for the NIROMs of the four barriers case.

8.4.3 Reservoir with eight baffles

The third case is comprised of eight low permeability barriers embedded in a higher permeability domain as illustrated in figure 8.10. The domain has a non-dimensional size 10×10. The permeability of the eight barriers in this test case are between 0.1 and 0.5, and the permeability of the background is 10. The full model simulation with a mesh of 2646 nodes was run during the simulation period $[0, 5]$ with a time step size of 0.01. 50 snapshots of solutions were collected at regularly spaced time intervals $\Delta t = 0.1$ for each solution variable. The porosity is 0.2 and the injection was controlled by constant inlet velocity of (x=1, y=1).

In this example, the Smolyak sparse grid has a dimensional size of eight, and there are 17 nodes in the sparse grid in terms of level one. Table 8.5 lists permeability combinations of the eight-barrier case using level one-labelled E1-E17. An unseen Smolyak sparse node (0.1,0.5,0.5,0.5,0.1,0.5,0.5,0.5)-labelled P1 is chosen to show the capabilities of the NIROM.

Table 8.5: Permeability combinations for eight-barrier case with level one

Cases \ Barriers	1	2	3	4	5	6	7	8
E1	0.3	0.3	0.3	0.3	0.3	0.3	0.3	0.3
E2	0.1	0.3	0.3	0.3	0.3	0.3	0.3	0.3
E3	0.5	0.3	0.3	0.3	0.3	0.3	0.3	0.3
E4	0.3	0.1	0.3	0.3	0.3	0.3	0.3	0.3
E5	0.3	0.5	0.3	0.3	0.3	0.3	0.3	0.3
E6	0.3	0.3	0.1	0.3	0.3	0.3	0.3	0.3
E7	0.3	0.3	0.5	0.3	0.3	0.3	0.3	0.3
E8	0.3	0.3	0.3	0.1	0.3	0.3	0.3	0.3
E9	0.3	0.3	0.3	0.5	0.3	0.3	0.3	0.3
E10	0.3	0.3	0.3	0.3	0.1	0.3	0.3	0.3
E11	0.3	0.3	0.3	0.3	0.5	0.3	0.3	0.3
E12	0.3	0.3	0.3	0.3	0.3	0.1	0.3	0.3
E13	0.3	0.3	0.3	0.3	0.3	0.5	0.3	0.3
E14	0.3	0.3	0.3	0.3	0.3	0.3	0.1	0.3
E15	0.3	0.3	0.3	0.3	0.3	0.3	0.5	0.3
E16	0.3	0.3	0.3	0.3	0.3	0.3	0.3	0.1
E17	0.3	0.3	0.3	0.3	0.3	0.3	0.3	0.5
P1	0.1	0.5	0.5	0.5	0.1	0.5	0.5	0.5

Figure 8.11 shows the solutions of saturation from full model and the NIROM with

6, 12 and 24 POD bases at time instances 1.5 and 4.0 using smolyak level one. It can be seen that the NIROMs has captured most of the energy. The NIROM with 24 POD bases is more closer to high fidelity model than NIROMs with 6 and 12 POD bases. The solutions obtained from the high fidelity model and NIROMs at a particular point in the domain are presented in figure 8.12. It again shows that the saturation solutions from NIROMs with 6, 12 and 24 POD bases are close to high fidelity full model, and in the meantime, NIROM with larger number of POD basis functions has higher accuracy than that of with smaller number of POD basis functions. This is confirmed by the inspection of the RMSE and correlation coefficient figures 8.13.

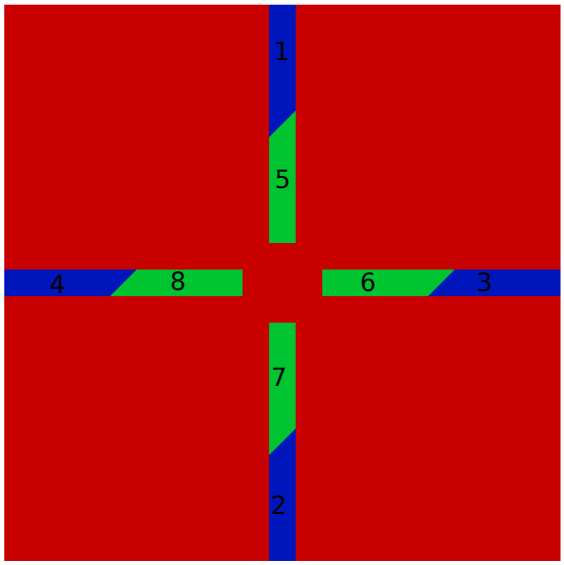
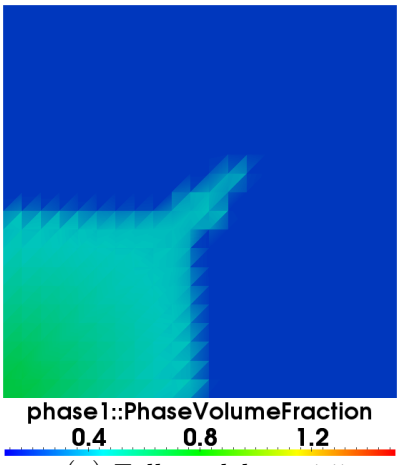
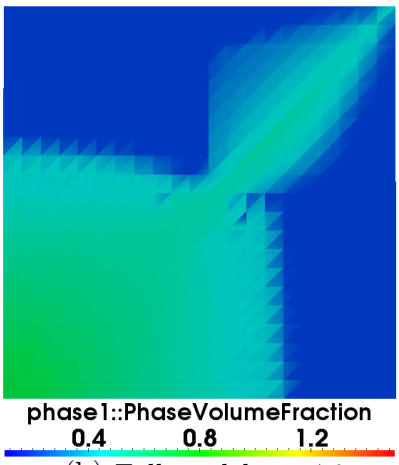


Figure 8.10: Eight baffles case: distribution of permeability in the domain, the permeability of the eight barriers are between 0.1 and 0.5, and the permeability of the background is 10.

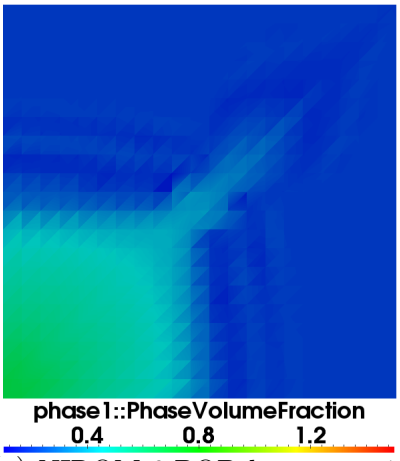
In order to compare the performance of NIROMs using Smolyak sparse grid and RBF, the saturation profile and saturation values comparison at a particular point (x=1.9048, y=2.381) are presented in figure 8.14 and 8.15, respectively. The figure 8.14 shows the saturation profile of the high fidelity model, NIROM with Smolyak sparse grid using 24 POD basis functions and NIROM with RBF using 24 POD basis functions. Visually, the saturation of NIROM with RBF is more closer to the full model than that of NIROM with Smolyak sparse grid. This can also be seen from the figure 8.15, the two NIROMs perform well at the particular point (x=1.9048,



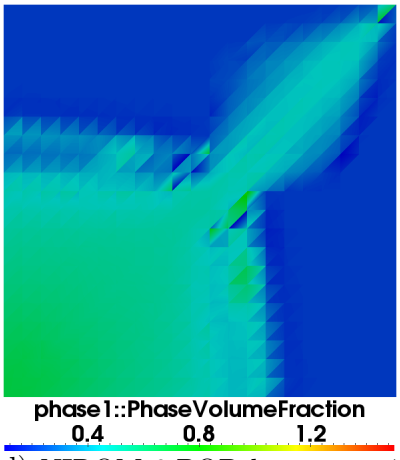
(a) Full model $t = 1.5$



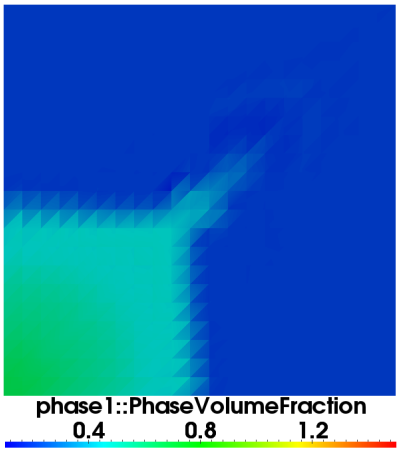
(b) Full model $t = 4.0$



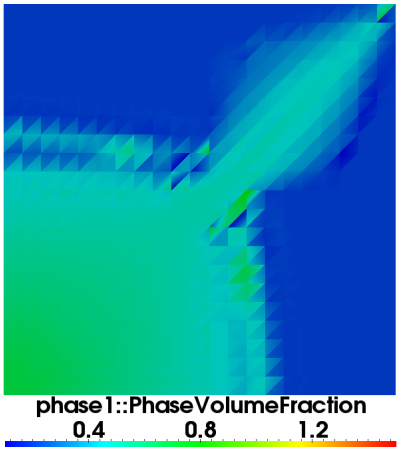
(c) NIROM 6 POD bases, $t = 1.5$



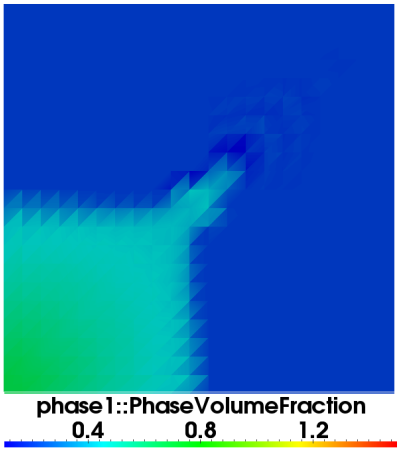
(d) NIROM 6 POD bases, $t = 4.0$



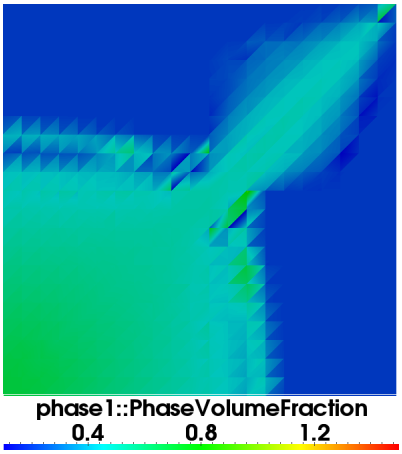
(e) NIROM 12 POD bases, $t = 1.5$



(f) NIROM 12 POD bases, $t = 4.0$



(g) NIROM 24 POD bases, $t = 1.5$



(h) NIROM 24 POD bases, $t = 4.0$

y=2.381) and NIROM with RBF performs better than NIROM with Smolyak sparse grid.

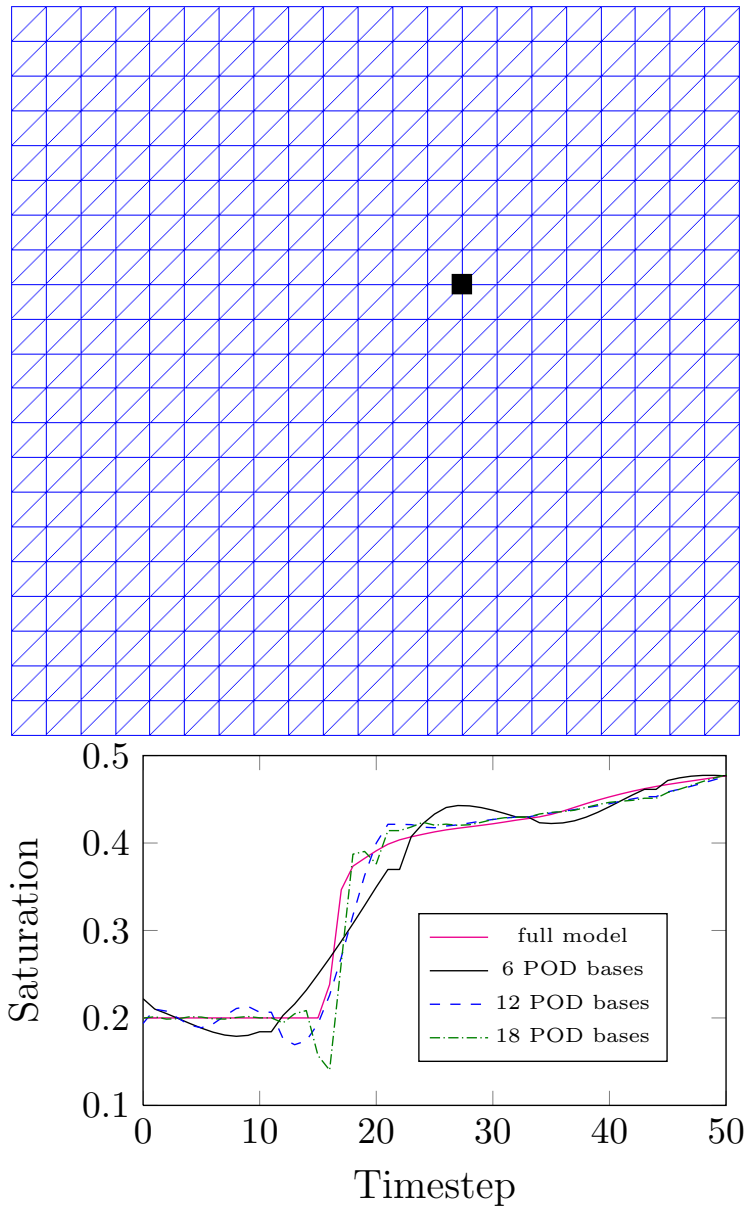


Figure 8.12: Eight baffles case: the graphs show the solution velocities predicted by the full model, and the NIROM at position (6.1905 6.1905).

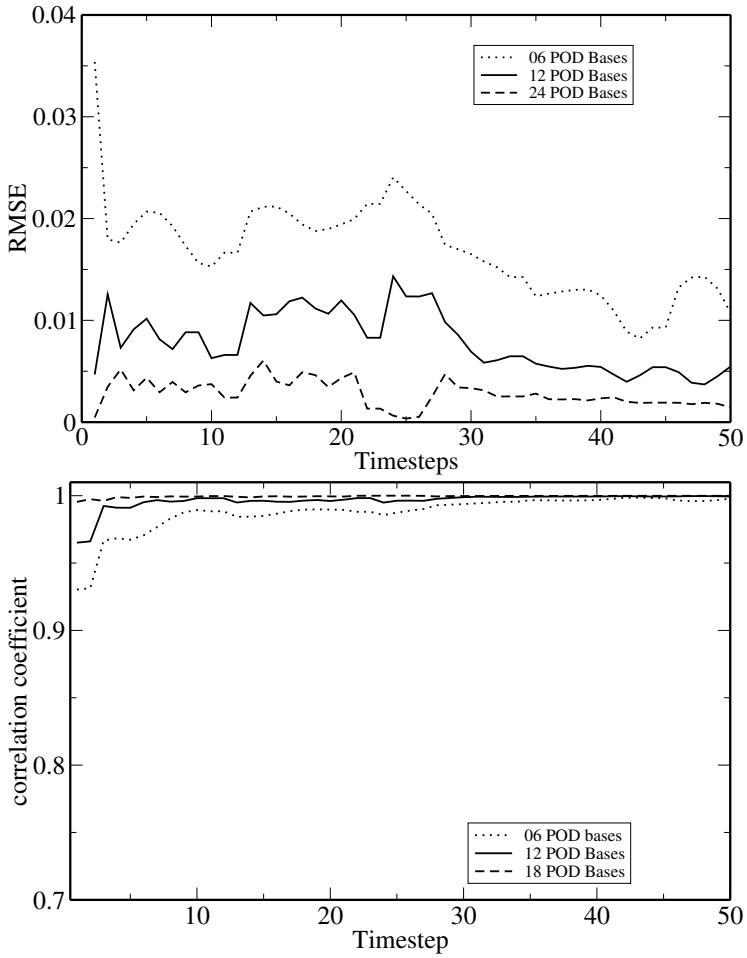
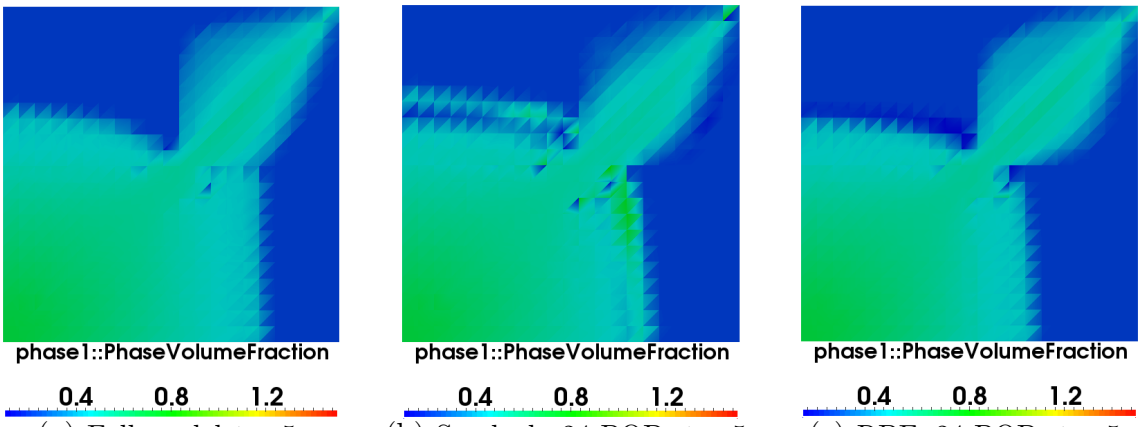
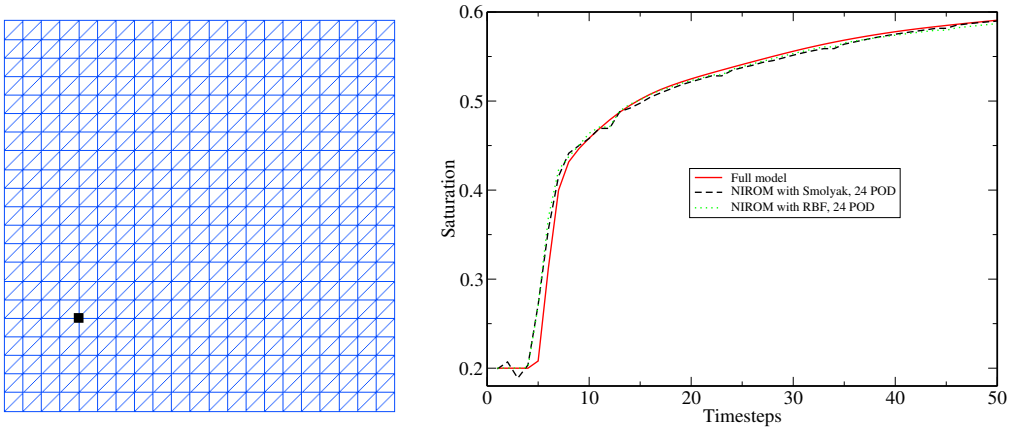


Figure 8.13: Eight baffles case: the graph shows the RMSE errors and correlation coefficient calculated for the NIROM model for the 8 layers case.



(a) Full model $t = 5$ s (b) Smolyak, 24 POD, $t = 5$ s (c) RBF, 24 POD, $t = 5$ s

Figure 8.14: 8 baffles case: saturation comparison between the high fidelity full model, NIROM with Smolyak sparse grid and NIROM with RBF at time level $t = 5$ s.



(a) Location (b) Saturation comparision

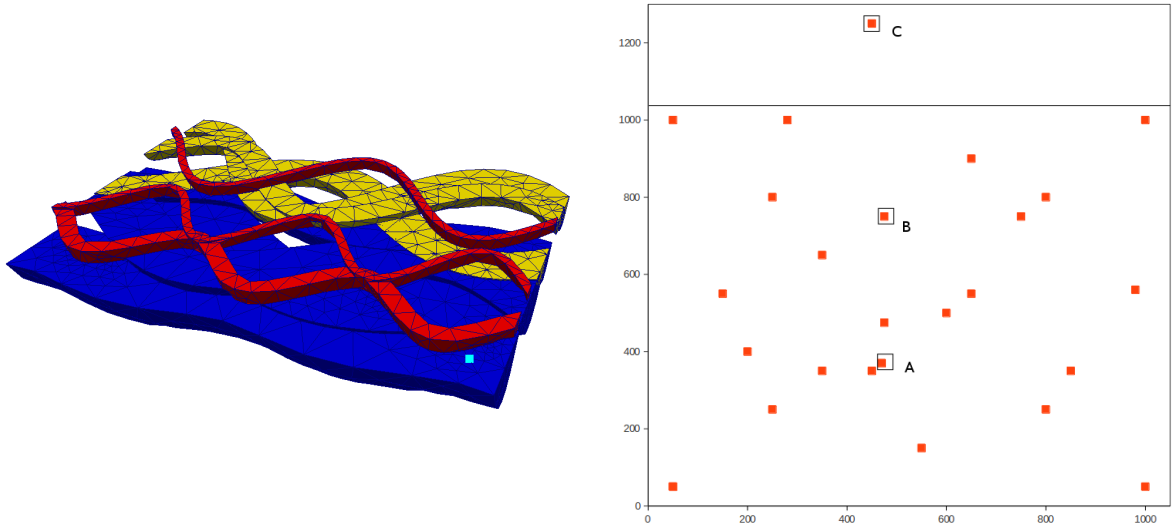
Figure 8.15: 8 baffles case: saturation values comparison between the full model, NIROM with Smolyak grid and RBF using 24 POD basis functions at a particular point (x=1.9048, y=2.381) on the domain.

8.4.4 3D fluvial channel case

The fourth case examined is a 3D model of a reservoir containing a number of high permeability channels. There are three types of channels in the reservoir and each type has a different permeability and associated uncertainty. The computational domain was composed of 31776 nodes (figure 8.16). The different channel types are shown in different colors blue, yellow and red. The water is injected into the computational domain from the right side at constant pressure. The flow passes through the channels from right to left. The porosity is set to be ϕ=0.2 throughout the model. The viscosities of the residual oil and irreducible water are set to be 0.004 and 0.001 Pa.s respectively. The simulation was run over the simulation period $[0, 1000days]$ with a time step size of 10 days. 20 snapshots of solutions were taken at regularly spaced time intervals $\Delta t = 5$ days for each solution variable (pressure saturation and velocity).

In this test case, 23 training simulations were used to construct the NIROM. In order to test the capability of the NIROM, three new cases with different permeabilities were simulated. In each of the 23 training simulations, the permeabilities of two channels (the blue and the red channels in figure 8.16(b) were modified randomly. The distribution of the 23 simulations with the different permeabilities used is shown in figure 8.16. The permeabilities were varied between 50 mD (milli-Darcy) and 1000 mD. The three new test simulations are points A, B and C in the figure 8.16 (a). Point A is the closest point to the training points, and point B is a little bit further from the training points. Point C is outside the training domain $[50 - 1000]$.

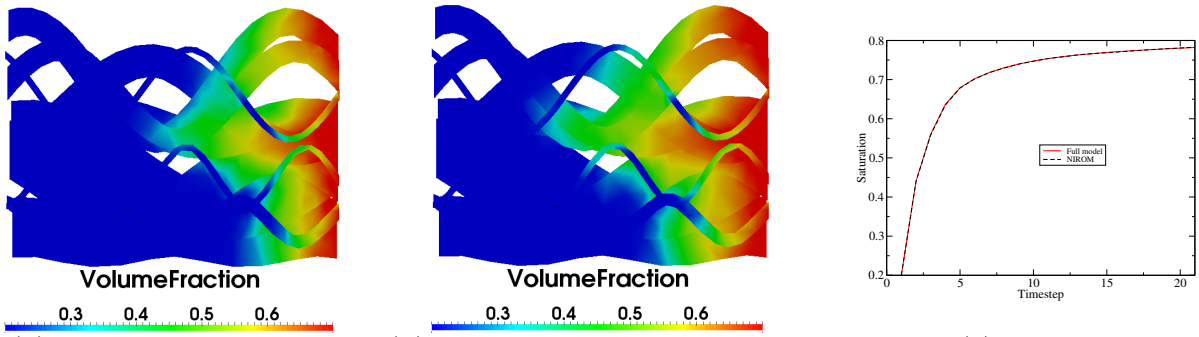
Figure 8.17 shows the saturation obtained from the full model and NIROM at time 15 days at point A (460, 360). Figure (c) compares the saturation obtained from two models at a particular location $x = 184.25, y = 110$ in the computational domain, see figure 8.16 (b). As can be seen in the figure, the results of the NIROM using permeability values close to those used in the training set agree well with results from the full physics model. Figure 8.18 shows the saturation profile from the full model and the NIROM at time 25 days at point B (475, 750). The saturation obtained from the two models at a particular location $x = 184.25, y = 110$ in the computational domain, see figure 8.16 (b), is given in the sub-figure (c). The NIROM results agree less well with the simulation shown in the point of A. Figure 8.19 compares the saturation profile of the full model and NIROM after time 30 days at point C (450, 1250). Figure 8.19 (c) compares the saturation value obtained by the two models at



(a) (b)

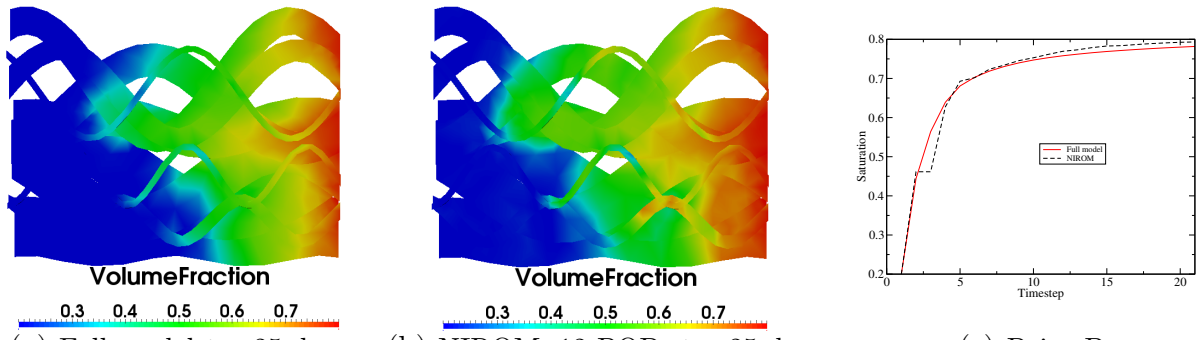
Figure 8.16: (a) the different channel types (wide channels: blue), (medium width channels: yellow) and (small channels: red) ; (b) the distribution of permeabilities used for the red and blue channels

$x = 184.25, y = 110$ in the computational domain. The permeabilities of the widest channel and narrowest channel are [450,1250], which are outside the domain of the training points. The NIROM performed less well in this case.



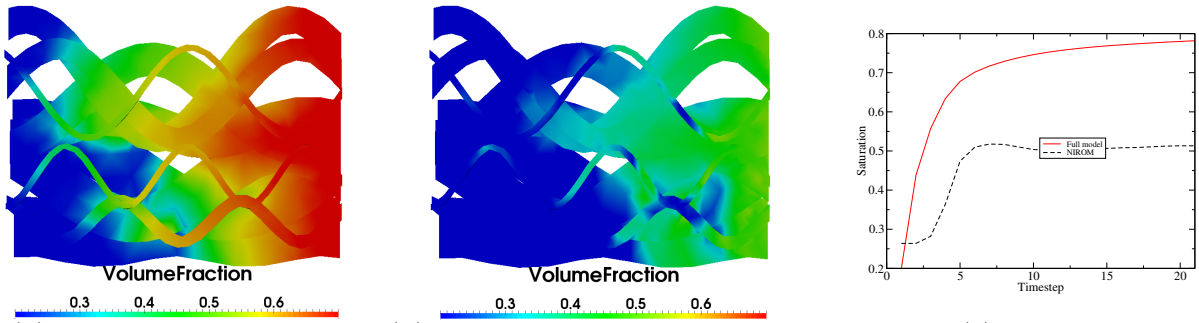
(a) Full model $t = 15$ days (b) NIROM, 12 POD, $t = 15$ days (c) Point A

Figure 8.17: Channel case: the saturation distribution obtained from the full physical model and NIROM with 12 POD basis functions at time level $t = 15$ days for the permeabilities shown at point A (460, 360) in Figure 8.16 (b). Figure (c) shows a comparison of the saturation value at $x = 184.25, y = 110$ in the computational domain, see figure 8.16 (a).



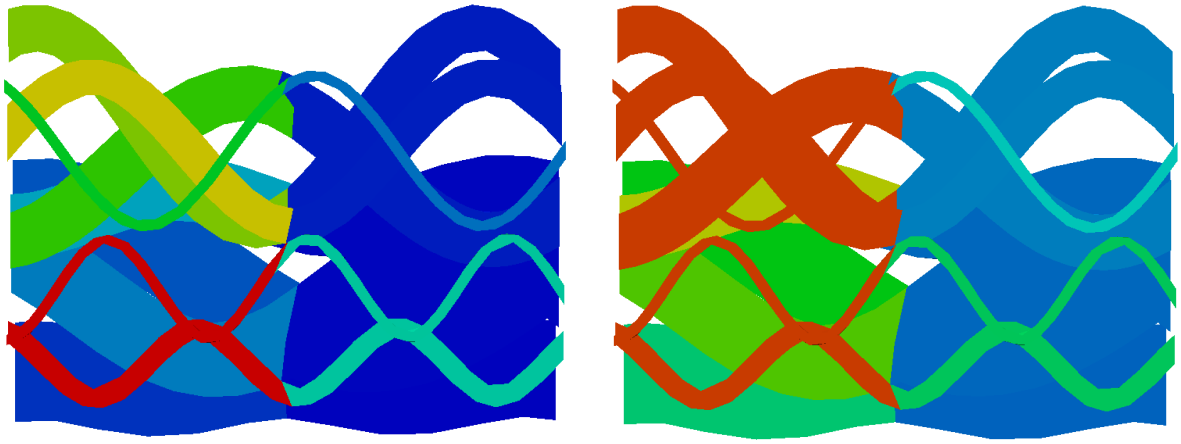
(a) Full model $t = 25$ days (b) NIROM, 12 POD, $t = 25$ days (c) Point B

Figure 8.18: Channel case: the saturation distribution obtained from the full physical model and NIROM with 12 POD basis functions at time level $t = 25$ days at location B in figure 8.16 (b).



(a) Full model $t = 30$ days (b) NIROM, 12 POD, $t = 30$ days (c) Point C

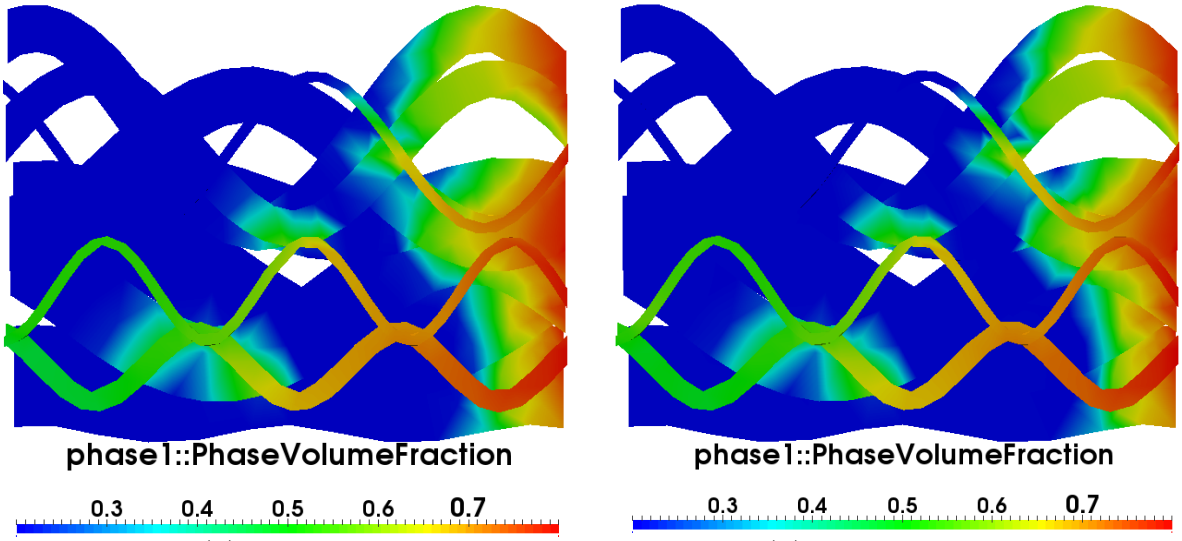
Figure 8.19: Channel case: the saturation distribution obtained from the full physical model and NIROM with 12 POD basis functions at time level $t = 30$ days at location C in figure 8.16 (a).



(a) (b)

Figure 8.20: two examples of 22 different channel types.

In order to test the capabilities of the NIROM for larger number of varying parameters, the reservoir was divided into 22 types of channels and each channel has a different permeability and associated uncertainty. 49 training simulations were used in this example. Two of the permeability combinations among those 49 training simulations are presented in figure 8.20. The saturation solutions at an untrained point from full model and NIROM with 22 varying input permeabilities are presented in figure 8.21. From the figures, there are not too much visual difference. In order to see the difference, the saturation values at a particular point (x=-18.378, y=184.25, z=110) on the domain from both the high fidelity model and NIROM are presented in figure 8.22. It can be seen from the figures, the NIROM predict well for the large number of varying parameter inputs.



(a) Full model (b) NIROM, 12 POD

Figure 8.21: Channel case: Saturation solutions at an untrained point from full model and NIROM with 22 varying input permeabilities.

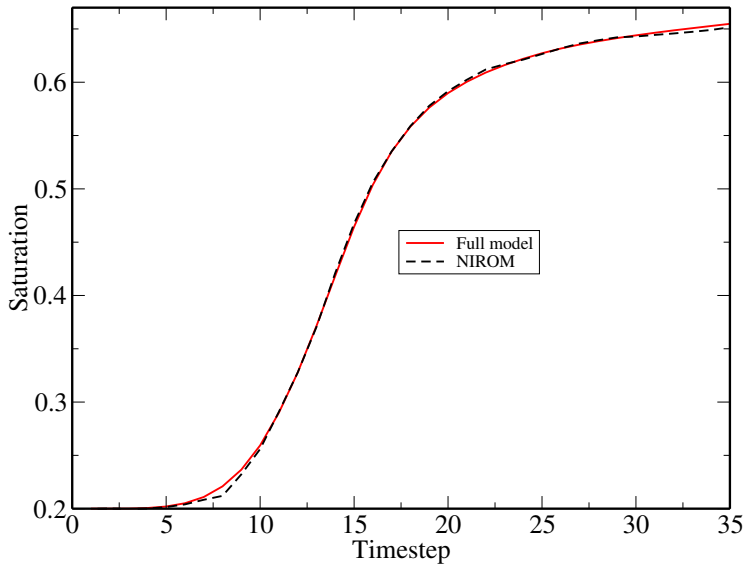


Figure 8.22: Reservoir with 22 types of channels: the graph shows the saturation comparison between the full model and NIROM at an unseen point based on 49 training simulations particular point (x=-18.378, y=184.25, z=110).

8.4.5 Efficiency of the NIROM

Table 8.6 shows a comparison of the online CPU time required for running the full model and non-intrusive Smolyak-RBF-POD ROM. The simulations were performed on 12 cores machine of an Intel® Xeon® X5680 processor with 3.3GHz and 48GB RAM. The test cases were run in serial, which means only one core was used when simulating. It can be seen that the online CPU time required for running the Smolyak-RBF-POD model is considerably less than that for the full model and is reduced by a factor of 2500. It is worth noting that as the number of nodes increases the CPU time required for the full model increases rapidly while the CPU time for the Smolyak-RBF-POD model almost remains the same.

8.5 Conclusion

In this chapter a new non-intrusive reduced order model for varying material properties is presented. It was constructed by using a Smolyak sparse grid for the material properties and a set of hyper-surfaces for the fluid dynamics, which is a unique aspect of this work. Another uniqueness is the non-intrusiveness, that is, it is independent on the governing equations and source code. This non-intrusiveness results in this

Table 8.6: Comparison of the online CPU time (dimensionless) required for running the full model and Smolyak-RBF-POD ROMs during one time step.

Cases	Model	assembling and solving	projection	interpolation	total
Four material layers test case	Full model	0.6000	0	0	0.6001
	NIROM	0	0.0003	0.000	0.0004
Reservoir with four baffles	Full model	1.730	0	0	1.731
	NIROM	0	0.0003	0.0001	0.00040
Reservoir with eight baffles	Full model	1.730	0	0	1.731
	NIROM	0	0.0003	0.0001	0.00040
Channels	Full model	74.9200	0	0	74.920
	NIROM	0	0.0003	0.0001	0.00040

new ROM is easy to implement, modify and extend. This model was firstly implemented under the framework of a 3D unstructured mesh multiphase model, Imperial College Finite Element Reservoir Simulator (IC-FERST) and firstly applied to multiphase flows in porous media problems. The results of numerical examples show that the NIROM solves accurately the varying material properties multiphase porous media problems with a high degree of computational efficiency. The errors of the NIROM is analysed by RMSE and correlation coefficient. It would be interesting to apply this approach to commercial software, such as ECLIPSE (reservoir simulator). It would be also interesting to apply this approach to uncertainty quantification and sensitivity analysis.

Chapter

NINE

Conclusions and future work

9.1 Conclusions

In this thesis, I have presented three new non-intrusive reduced order modelling methods: POD/Taylor series expansion, POD/ Smolyak sparse grid interpolation and POD/RBF. These methods have been used to constructed NIROMs for free surface, multi-phase porous media flows and fluid-solid coupling problems. In addition, two variable material non-intrusive ROMs have been proposed. One uses a two level RBF interpolation. In this method, the first level interpolation function represents the material properties and the second level interpolation function represents the time-dependent fluid dynamics. The second variable material NIROM is based on a Smolyak sparse grid and RBF interpolation. This model is also constructed by two level interpolation functions. The first level interpolation function is constructed via Smolyak sparse grid to represent the material properties and the second level (dynamic system representation) is constructed by RBF method. The methods presented in this thesis have been illustrated by numerical test cases on a finite element unstructured mesh fluid model (Fluidity). It is demonstrated that accuracy of solutions from the non-intrusive models is maintained whilst online CPU times are reduced by several orders of magnitude in comparison to the high fidelity models. The benefits of the NIROMs presented here is that they do not require any

modifications to the source code, due to the fact that they are independent of the governing equations.

Chapter 2 presents three novel NIROMs. Rather than standard intrusive ROM, the three NIROMs use Smolyak sparse grid interpolation method, radial basis function method and a Taylor series expansion method respectively to calculate the POD coefficients. The idea of the Smolyak sparse grid method and RBF method lies in constructing a set of hyper-surfaces that representing the reduced space. The Taylor expansion method uses a second order Taylor expansion to capture the quadratic non-linearities in the Navier-Stokes equations. The methods have been numerically compared against the high fidelity full model on three flow problems: flow past a cylinder, lock exchange and wind driven gyre problems. The three non-intrusive methods gave accurate solutions. Taylor series expansion method perform poorly for higher Reynolds numbers. The Smolyak sparse grid and RBF methods are then used to construct NIROMs for more complex problems in the following chapters.

Chapter 3 presents a NIROM for three-dimensional (3D) free surface flows using POD-Smolyak. This is the first time Smolyak sparse grid based non-intrusive ROMs have been applied to 3D free surface flow and implemented under the framework of an advanced 3D unstructured mesh finite element ocean model (Fluidity). The Smolyak sparse grid method is used to construct a set of hyper-surfaces representing the reduced dynamic system. The performance of the new POD-Smolyak 3D free surface flow NIROM is illustrated for two numerical test cases: the Balzano test case and the Okushiri tsunami test case. The results obtained from the free surface NIROM have been compared against those from the high fidelity free surface full model. It is shown that the accuracy of solutions from free surface flow NIROM is maintained while the CPU cost is reduced by several orders of magnitude. An error analysis has also been carried out for the validation of the new NIROM.

Chapter 4 presents a NIROM for multi-phase porous media flows using POD-RBF. This is the first porous media flow non-intrusive reduced order model and this NIROM is developed for an advanced 3D unstructured mesh multiphase fluid model, the Imperial College Finite Element Reservoir Simulator (IC-FERST). A RBF interpolation method is used to form a hyper surface that represents the solution of the multiphase porous media equations within the reduced space. The capabilities of the newly developed multiphase porous media NIROM are illustrated in two reservoir engineering test cases. A comparison between the full and POD-RBF model results are made. An error analysis was also carried out for the validation and accuracy

assessment of the POD-RBF model. The saturation shock-front can be captured with relatively few POD basis functions, 18 POD basis function in the examples. In comparison to the full model, without compromising the accuracy of results the CPU time required for the POD-RBF model can be reduced by a factor of 2500.

Chapter 5 presents a NIROM for incompressible fluid-structure problem. This is the first non-intrusive incompressible fluid-structure reduced order model. It is developed under the framework of the combined finite-discrete element method based solid model (Y2D) and unstructured mesh finite element multi-phase model (Fluidity). A RBF multi-dimensional interpolation method is used to construct a set of interpolation hyper surfaces representing the reduced FSI dynamic system. The performance of the NIROM has been demonstrated by applying to three coupling test cases: a one-way coupling case (flow past a cylinder), two two-way coupling cases (a free-falling cylinder in water and a vortex-induced vibrations of an elastic beam case). The numerical simulations show that the FSI NIROM exhibits good agreement with the high fidelity model.

Chapter 6 presents a NIROM for compressible fluid and fractured solid coupling problems. This is the first compressible fluids and fractured solids NIROM. It has also been implemented under the framework of a combined finite-discrete element method based solid model (Y2D) and an unstructured mesh finite element model (Fluidity). The performance of the NIROM for compressible fluids and fractured solids problem is numerically illustrated in two test cases: a bending beam forced by flows and a blasting case. Interestingly, the results obtained from NIROM with mean subtraction beforehand are found to be poor. In this chapter, the issue whether or not the mean of snapshots is subtracted before performing POD is studied by comparing the fluid and fracture solid coupling NIROM results with those from the high fidelity model. An error analysis has been also carried out to validate and assess the newly NIROM. It is found that the fluid and fracture solid coupling NIROM without subtraction the mean can perform much better than that with subtracting the mean from the snapshots that are used to help form the POD basis functions. The numerical results show that the NIROM performs well and exhibits a good agreement with the high fidelity model. The front of shock waves is captured well using only a small number of POD basis functions.

Chapter 7 presents a new variable parameters NIROM for the Navier-Stokes equations using two-level RBF interpolation. In this model, the first level RBF interpolation is a set of surfaces representing the parameter space such as initial and

boundary conditions. The second level RBF interpolation is a set of hyper-surfaces that represents the dynamics of the system. A unique aspect of the NIROM is that the training data points of the first level RBF interpolation is determined by the Smolyak sparse grid, resulting in optimal number of running of simulations. Two numerical examples were chosen to demonstrate the capabilities of the NIROM: flow past a cylinder and a lock exchange problem. The prediction capabilities of the NIROM was investigated by specifying the initial and boundary conditions with the sparse grid. It was shown that the problem was well predicted with a greatly reduced computational CPU cost. An error analysis was also undertaken.

Chapter 8 presents a new variable material NIROM for multi-phase porous media flows using Smolyak and RBF interpolation methods. Unlike the variable parameter NIROM presented in the chapter 7, which uses a RBF interpolation method to represent the material properties, this model uses a Smolyak sparse grid to construct the material properties surfaces. The model was also implemented under the framework of a 3D unstructured mesh multiphase model, the Imperial College Finite Element Reservoir Simulator (IC-FERST). It has been applied to multiphase flows in porous media problems. The results of numerical examples show that the NIROM solves accurately the varying material properties in multiphase porous media problems with a high degree of computational efficiency. The errors of the NIROM is analysed by RMSE and correlation coefficient.

9.2 Future work

While the new NIROMs and their applications have been implemented and demonstrated in this work, there are some possible extensions.

9.2.1 Possible extensions and applications

It would be interesting to apply the NIROMs to uncertainty analysis, sensitivity analysis and optimisation where many runs of models are required. Data assimilation is also an interesting research field. We applied the NIROM to free surface problems, multiphase porous media problems and coupling problems in chapters 3, 4, 5 and 6. In the future, it will be interesting to apply the NIROM to more complex problems such as urban flooding, realistic blasting cases and urban pipe

problems. In chapters 4 and 8, we demonstrated our results within the platform of Fluidity. In the future, we can also apply this method to build a NIROM for some commercial software, such as ECLIPSE (reservoir simulator). Error analysis methods such as posteriori error analysis may also be developed in future work, see figure 9.1. The deep learning method is a new research topic in machine learning LeCun *et al.* (2015). It allows models to use multiple layers to represent the physical system. The powerful capabilities of deep learning has been demonstrated in a wide range of application areas such as information processing, speech recognition, object detection and text processing. It would be interesting to use a deep learning method to construct a set of hypersurfaces representing the time-dependent fluid dynamics for complex problems in reduced space.

9.2.2 Subdomain based reduced order model

It would also be interesting to develop a novel domain decomposed based reduced order reservoir model. This ROM can be formed by dividing up the domain into subdomains and performing either intrusive or non-intrusive reduced modelling within each of these subdomains and linking their solutions to obtain the overall solution. Due to the local behavior of the subdomain ROM it is expected to scale much better to large multi-scale problems (hyper-reduction) and require fewer basis functions compared to the global POD basis function method normally used. Figure 9.1 shows a schematic of a possible hyper-reduction or sub-grid-scale reservoir model framework.

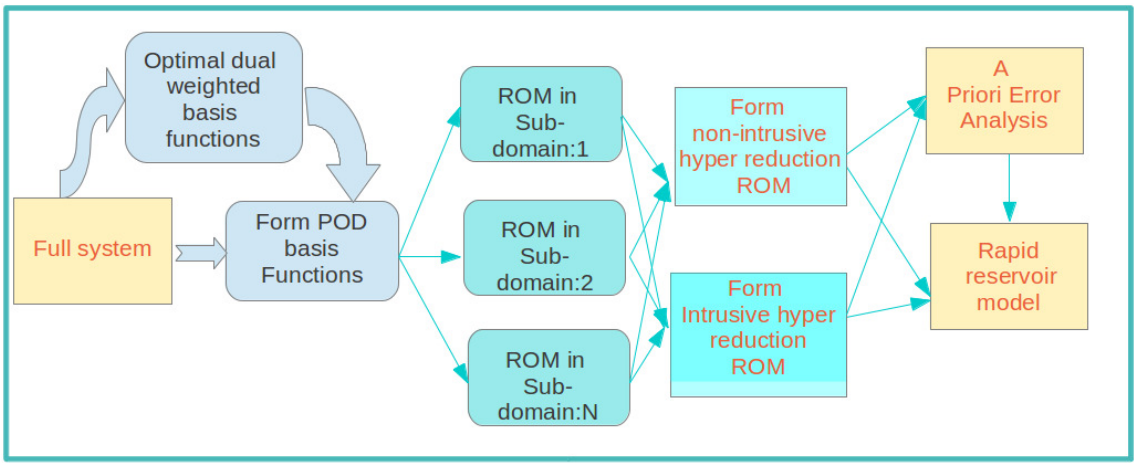


Figure 9.1: Framework for hyper-reduction and sub-grid-scale reservoir modelling.

To form this model, we can use i) Proper Orthogonal Decomposition (POD) methods to form the basis functions, combined with ii) methods that treat the non-linear terms efficiently (*e.g.* Residual DEIM (Xiao *et al.* (2014)) - forming the non-linear approximations implicitly in time, Localized DEIM (Ghasemi & Gildin (2015); Peherstorfer *et al.* (2014)) - forming the non-linear terms using DEIM local to regions, Matrix DEIM (Wirtz *et al.* (2014)) - forming the ROM matrix equation by DEIM interpolation of parts of the forward model matrix centred at the DEIM points), iii) the use of dual weighted basis functions in order to form POD basis in the optimal sense of calculating a key modelling goal(s) like oil production rate, iv) the use of subdomains in order to localize the ROM and enable it to be applied to large scale problems and v) the use of response surfaces such as RBF and Smolyak sparse grid methods in order to form non-intrusive ROM's that require no modification of the forward model to construct. The combination of these methods will result in a unique tool that offers substantial improvements in computational efficiency, ease of use (NIROM) and accuracy compared to traditional ROM. This will enable very detailed embedded solutions to be formed for detailed processes (e.g. flow through fractures) occurring in reservoir modelling and provide improved analysis (to what is currently available) of multi-scale and multi-phase dynamics for use in prediction, design optimisation and data assimilation. The hypothesis is that its fine-multi-scale modelling may thus act as a highly sophisticated sub-grid-scale model that can be truncated at any level of refinement/sophistication.

9.2.3 Non-intrusive ROM for problems with adaptive meshes

The adaptive mesh is widely used technology in modelling. The non-intrusive ROM will be applicable to more engineering areas if it is capable of dealing with problems with adaptive meshes. A spatial location inconsistency of nodes will arised when forming the POD basis functions. One possible way of incorporating the adaptive mesh technology into non-intrusive ROM is through supermesh technologies (Farrell *et al.* (2009)).

Bibliography

Ahuja, Sunil, & Rowley, Clarence W. 2010. Feedback control of unstable steady states of flow past a flat plate using reduced-order estimators. *Journal of fluid mechanics*, **645**, 447–478.

Akhtar, Imran. 2008. *Parallel Simulation, Reduced-Order Modeling, and Feedback Control of Vortex Shedding using Fluidic Actuators*. Ph.D. thesis, Virginia Polytechnic Institute and State University.

Akhtar, Imran, Marzouk, Osama A, & Nayfeh, Ali H. 2009. A van der Pol–Duffing oscillator model of hydrodynamic forces on canonical structures. *Journal of Computational and Nonlinear Dynamics*, **4**(4), 041006.

Altaf, MU, El Gharamti, Mohamad, Heemink, Arnold W, & Hoteit, Ibrahim. 2013. A reduced adjoint approach to variational data assimilation. *Computer Methods in Applied Mechanics and Engineering*, **254**, 1–13.

AMCG, & London, Imperial. College. 2015. Fluidity manual v4.1.12. figshare. *https://dx.doi.org/10.6084/m9.figshare.1387713.v2*, 1–329.

Amsallem, David, Zahr, Matthew J, & Farhat, Charbel. 2012. Nonlinear model order reduction based on local reduced-order bases. *International Journal for Numerical Methods in Engineering*, **92**(10), 891–916.

Anderson, John David, & Wendt, J. 1995. *Computational fluid dynamics*. Vol. 206. Springer.

Ansari, Esmail. 2014. Development of a surrogate simulator for two-phase subsurface flow simulation using trajectory piecewise linearization. *Journal of Petroleum Exploration and Production Technology*, **4**(3), 315–325.

Ardjmandpour, N, Pain, CC, Fang, F, Buchan, AG, Singer, J, Player, MA, Xu, Xu, Navon, IM, & Carter, J. 2014. Reduced order borehole induction modelling. *International Journal of Computational Fluid Dynamics*, **28**(3-4), 140–157.

Aubry, Nadine, Holmes, Philip, Lumley, John L, & Stone, Emily. 1988. The dynamics of coherent structures in the wall region of a turbulent boundary layer. *Journal of Fluid Mechanics*, **192**, 115–173.

Audouze, C, De Vuyst, F, & Nair, PB. 2009. Reduced-order modeling of parameterized PDEs using time–space-parameter principal component analysis. *International journal for numerical methods in engineering*, **80**(8), 1025–1057.

Awan, Anwar R, Teigland, Rune, Kleppe, Jon, *et al.* . 2008. A survey of North Sea enhanced-oil-recovery projects initiated during the years 1975 to 2005. *SPE Reservoir Evaluation & Engineering*, **11**(03), 497–512.

Baghalian, Sara, Bonakdari, Hossein, Nazari, Foad, & Fazli, Majid. 2012. Closed-form solution for flow field in curved channels in comparison with experimental and numerical analyses and artificial neural network. *Engineering Applications of Computational Fluid Mechanics*, **6**(4), 514–526.

Bagheri, Shervin, Brandt, Luca, & Henningson, Dan S. 2009. Input–output analysis, model reduction and control of the flat-plate boundary layer. *Journal of Fluid Mechanics*, **620**, 263–298.

Ballabrera-Poy, Joaquim, Busalacchi, Antonio J, & Murtugudde, Ragu. 2001. Application of a reduced-order Kalman filter to initialize a coupled atmosphere-ocean model: Impact on the prediction of El Nino. *Journal of climate*, **14**(8), 1720–1737.

Balzano, Andrea. 1998. Evaluation of methods for numerical simulation of wetting and drying in shallow water flow models. *Coastal Engineering*, **34**(1), 83–107.

Barbagallo, Alexandre, Sipp, Denis, & Schmid, Peter J. 2009. Closed-loop control of an open cavity flow using reduced-order models. *Journal of Fluid Mechanics*, **641**, 1–50.

Barker, John W, & Dupouy, Philippe. 1999. An analysis of dynamic pseudo-relative permeability methods for oil-water flows. *Petroleum Geoscience*, **5**(4), 385–394.

Barker, John W, Thibeau, Sylvain, *et al.* . 1997. A critical review of the use of pseudorelative permeabilities for upscaling. *SPE Reservoir Engineering*, **12**(02), 138–143.

Barone, Matthew F, Kalashnikova, Irina, Brake, Matthew R, & Segalman, Daniel J. 2009. Reduced order modeling of fluid/structure interaction. *Sandia National Laboratories Report, SAND No*, **7189**.

Barrault, M., Maday, Y., Nguyen, N.C., & Patera, A.T. 2004. An empirical interpolation method: application to efficient reduced-basis discretization of partial differential equations. *C. R. Acad. Sci. Paris, Ser*, **339**, 667–672.

Barthelmann, Volker, Novak, Erich, & Ritter, Klaus. 2000. High dimensional polynomial interpolation on sparse grids. *Advances in Computational Mathematics*, **12**(4), 273–288.

Batycky, RP, Blunt, Martin J, Thiele, Marco R, *et al.* . 1997. A 3D field-scale streamline-based reservoir simulator. *SPE Reservoir Engineering*, **12**(04), 246–254.

Baumann, Manuel M. 2013. *Nonlinear Model Order Reduction using POD/DEIM for Optimal Control of Burgers' Equation*. Ph.D. thesis, TU Delft, Delft University of Technology.

Baur, Ulrike, & Benner, Peter. 2008. Cross-Gramian based model reduction for data-sparse systems. *Electronic Transactions on Numerical Analysis*, **31**(256-270), 27.

Baur, Ulrike, Beattie, Christopher, Benner, Peter, & Gugercin, Serkan. 2011. Interpolatory projection methods for parameterized model reduction. *SIAM Journal on Scientific Computing*, **33**(5), 2489–2518.

Bechtold, Tamara, Striebel, Michael, Mohaghegh, K, & ter Maten, EJW. 2008. Nonlinear model order reduction in nanoelectronics: combination of POD and TPWL. *PAMM*, **8**(1), 10057–10060.

Benjamin, T.B. 1968. Gravity currents and related phenomena. *Journal of Fluid Mechanics*, **31**, 209–248.

Bergmann, Michel, Cordier, Laurent, & Brancher, Jean-Pierre. 2005. Optimal rotary control of the cylinder wake using proper orthogonal decomposition reduced-order model. *Physics of Fluids (1994-present)*, **17**(9), 097101.

Berkooz, Gal, Holmes, Philip, & Lumley, John L. 1993. The proper orthogonal decomposition in the analysis of turbulent flows. *Annual review of fluid mechanics*, **25**(1), 539–575.

Bistrian, D.A., & Navon, I.M. 2015. An improved algorithm for the shallow water equations model reduction: Dynamic Mode Decomposition vs POD. *International Journal for Numerical Methods in Fluids*.

Bodnár, Tomáš, Galdi, Giovanni P, & Nečasová, Šárka. 2014. *Fluid-Structure Interaction and Biomedical Applications*. Springer.

Bond, Bradley N, & Daniel, Luca. 2008. Guaranteed stable projection-based model reduction for indefinite and unstable linear systems. *Pages 728–735 of: Proceedings of the 2008 IEEE/ACM International Conference on Computer-Aided Design*. IEEE Press.

Borggaard, Jeff, Stoyanov, Miroslav, & Zietsman, Lizette. 2010. Linear feedback control of a von Kármán street by cylinder rotation. *Pages 5674–5681 of: American Control Conference (ACC), 2010*. IEEE.

Bourguet, Rémi, Braza, Marianna, & Dervieux, Alain. 2007. Reduced-order modeling for unsteady transonic flows around an airfoil. *Physics of Fluids (1994-present)*, **19**(11), 111701.

Boyaval, S, Bris, C Le, Lelivre, T, Maday, Y, Nguyen, NC, & Patera, AT. 2010. Reduced Basis Techniques for Stochastic Problems. *Arch Comput Methods Eng*, **17**(4), 435–454.

Buchan, AG, Calloo, AA, Goffin, MG, Dargaville, S, Fang, F, Pain, CC, & Navon, IM. 2015. A POD reduced order model for resolving angular direction in neutron/photon transport problems. *Journal of Computational Physics*, **296**, 138–157.

Buffoni, Marcelo, & Willcox, Karen. 2010. Projection-based model reduction for reacting flows. *Page 5008 of: 40th Fluid Dynamics Conference and Exhibit*.

Buhmann, Martin, & Dyn, Nira. 1993. Spectral convergence of multiquadric interpolation. *Proceedings of the Edinburgh Mathematical Society (Series 2)*, **36**(02), 319–333.

Bui, D., Hamdaoui, M., & De Vuyst, F. 2013. PODISAT: An efficient POD-based surrogate approach with adaptive tabulation and fidelity regions for parametrized steady-state PDE discrete solutions. *International Journal for Numerical Methods in Engineering*, **94**(7), 648–671.

Bungartz, Hans-Joachim, & Schäfer, Michael. 2006. *Fluid-structure interaction: modelling, simulation, optimisation*. Vol. 1. Springer Science & Business Media.

Buzzard, Gregery T, & Xiu, Dongbin. 2011. Variance-based global sensitivity analysis via sparse-grid interpolation and cubature. *Communications in Computational Physics*, **9**(3), 542–567.

Cao, Y., Zhu, J., Luo, Z., & Navon, I.M. 2006. Reduced order modeling of the upper tropical Pacific Ocean model using proper orthogonal decomposition. *Computers & Mathematics with Applications*, **52**, 1373–1386.

Cao, Y., Zhu, J., Navon, I.M., & Luo, Z. 2007. A reduced order approach to four dimensional variational data assimilation using proper orthogonal decomposition. *International Journal for Numerical Methods in Fluids*, **53**, 1571–1583.

Cardoso, MA, Durlofsky, LJ, & Sarma, P. 2009. Development and application of reduced-order modeling procedures for subsurface flow simulation. *International journal for numerical methods in engineering*, **77**(9), 1322–1350.

Cardoso, Marco Antonio. 2009. *Development and application of reduced-order modeling procedures for reservoir simulation*. ProQuest.

Carlberg, Kevin, Bou-Mosleh, Charbel, & Farhat, Charbel. 2011a. Efficient nonlinear model reduction via a least-squares Petrov–Galerkin projection and compressive tensor approximations. *International Journal for Numerical Methods in Engineering*, **86**(2), 155–181.

Carlberg, Kevin, Cortial, Julien, Amsallem, David, Zahr, Matthew, & Farhat, Charbel. 2011b. The GNAT nonlinear model reduction method and its application to fluid dynamics problems. *Pages 2011–3112 of: 6th AIAA Theoretical Fluid Mechanics Conference, Honolulu, Hawaii, June*, vol. 2730.

Carlberg, Kevin, Farhat, Charbel, Cortial, Julien, & Amsallem, David. 2013. The GNAT method for nonlinear model reduction: effective implementation and application to computational fluid dynamics and turbulent flows. *Journal of Computational Physics*, **242**, 623–647.

Carstens, Volker, Kemme, Ralf, & Schmitt, Stefan. 2003. Coupled simulation of flow-structure interaction in turbomachinery. *Aerospace Science and Technology*, **7**(4), 298–306.

C.Audouze, F.D.Vuyst, & P.B.Nair. 2013. Nonintrusive reduced-order modeling of parametrized time-dependent partial differential equations. *Numerical Methods for Partial Differential Equations*, **29**(5), 1587–1628.

Chang, Gary Han, & Modarres-Sadeghi, Yahya. 2015. A reduced order model for fluid-structure interaction of thin shell structures conveying fluid for physiological applications. *Bulletin of the American Physical Society*, **60**.

Chaturantabut, S. 2008. *Dimension Reduction for Unsteady Nonlinear Partial Differential Equations via Empirical Interpolation Methods.* M.Phil. thesis, Rice university.

Chaturantabut, S., & Sorensen, D.C. 2010. Nonlinear model reduction via discrete empirical interpolation. *SIAM J. Sci. Comput*, **32**, 2737–2764.

Chaturantabut, S., & Sorensen, D.C. 2012. A state space error estimate for POD-DEIM nonlinear model reduction. *SIAM Journal on Numerical Analysis*, **50**, 46–63.

Chaturantabut, Saifon, & Sorensen, Danny C. 2011a. Application of POD and DEIM on dimension reduction of non-linear miscible viscous fingering in porous media. *Mathematical and Computer Modelling of Dynamical Systems*, **17**(4), 337–353.

Chaturantabut, Saifon, & Sorensen, Danny C. 2011b. Error Analysis for Nonlinear Model Reduction using POD-DEIM Technique. *Page 46 of: Householder Symposium XVIII on Numerical Linear Algebra.*

Chen, Hao, Reuss, David L, & Sick, Volker. 2012a. On the use and interpretation of proper orthogonal decomposition of in-cylinder engine flows. *Measurement Science and Technology*, **23**(8), 085302.

Chen, X., Navon, I.M., & Fang, F. 2011. A dual-weighted trust-region adaptive POD 4D-VAR applied to a finite-element shallow-water equations model. *International Journal for Numerical Methods in Fluids*, **65**(5), 520–541.

Chen, X., Akella, S., & Navon, I.M. 2012b. A dual-weighted trust-region adaptive POD 4-D Var applied to a finite-volume shallow water equations model on the sphere. *International Journal for Numerical Methods in Fluids*, **68**(3), 377–402.

Cheng, Mulin. 2013. *Adaptive methods exploring intrinsic sparse structures of stochastic partial differential equations.* Ph.D. thesis, California Institute of Technology.

Chiu, Tai-Yih. 1996. Model reduction by the low-frequency approximation balancing method for unstable systems. *Automatic Control, IEEE Transactions on*, **41**(7), 995–997.

Chu, Yunfei, Serpas, Mitchell, & Hahn, Juergen. 2011. State-preserving nonlinear model reduction procedure. *Chemical engineering science*, **66**(17), 3907–3913.

Coelho, Rajan Filomeno, Breitkopf, Piotr, & Knopf-Lenoir, Catherine. 2008. Model reduction for multidisciplinary optimization-application to a 2D wing. *Structural and multidisciplinary optimization*, **37**(1), 29–48.

Cohen, Kelly, Siegel, Stefan, McLaughlin, Thomas, & Gillies, Eric. 2003. Feedback control of a cylinder wake low-dimensional model. *AIAA journal*, **41**(7), 1389–1391.

Conrard, P. R., & Marzouk, Y. M. 2013. Adaptive Smolyak pseudospectral approximations. *SIAM J. Sci. Comput.*, **35(6)**, 26432670.

Costin, WJ, & Allen, CB. 2013. Numerical study of radial basis function interpolation for data transfer across discontinuous mesh interfaces. *International Journal for Numerical Methods in Fluids*, **72**(10), 1076–1095.

Cotter, Colin J, Ham, David A, Pain, Christopher C, & Reich, Sebastian. 2009. LBB stability of a mixed Galerkin finite element pair for fluid flow simulations. *Journal of Computational Physics*, **228**(2), 336–348.

Crommelin., D.T., & Majda, A.J. 2004. Strategies for model reduction: Comparing different optimal bases. *Journal of the Atmospheric Sciences*, **61**, 2206–2217.

Daescu, Dacian N, & Navon, IM. 2007. Efficiency of a POD-based reduced second-order adjoint model in 4D-Var data assimilation. *International Journal for Numerical Methods in Fluids*, **53**(6), 985–1004.

Daescu, D.N., & Navon, I.M. 2008. A Dual-Weighted Approach to Order Reduction in 4D-Var Data Assimilation. *Monthly Weather Review*, **136**(3), 1026–1041.

Dalle, Derek J, Fotia, Matthew L, & Driscoll, James F. 2010. Reduced-order modeling of two-dimensional supersonic flows with applications to scramjet inlets. *Journal of Propulsion and Power*, **26**(3), 545–555.

De Giorgi, MG, Bello, D, & Ficarella, A. 2014. An artificial neural network approach to investigate cavitating flow regime at different temperatures. *Measurement*, **47**, 971–981.

Degroote, Joris, Vierendeels, Jan, & Willcox, Karen. 2010. Interpolation among reduced-order matrices to obtain parameterized models for design, optimization and probabilistic analysis. *International Journal for Numerical Methods in Fluids*, **63**(2), 207–230.

Dehghan, Mehdi, & Shokri, Ali. 2009. A meshless method for numerical solution of the one-dimensional wave equation with an integral condition using radial basis functions. *Numerical Algorithms*, **52**(3), 461–477.

Dimitriu, Gabriel, Apreutesei, Narcisa, & Ştefănescu, Răzvan. 2010. Numerical simulations with data assimilation using an adaptive POD procedure. *Pages 165–172 of: Large-Scale Scientific Computing*. Springer.

Dimitriu, Gabriel, Navon, Ionel M, & Ştefănescu, Răzvan. 2014. Application of POD-DEIM Approach for Dimension Reduction of a Diffusive Predator-Prey System with Allee Effect. *Pages 373–381 of: Large-Scale Scientific Computing*. Springer.

Dong, Ning, & Roychowdhury, Jaijeet. 2003. Piecewise polynomial nonlinear model reduction. *Pages 484–489 of: Design Automation Conference, 2003. Proceedings*. IEEE.

Du, J., Fang, F., Pain, C.C., Navon, I.M., Zhu, J., & Ham, D.A. 2013a. POD reduced-order unstructured mesh modeling applied to 2D and 3D fluid flow. *Computers and Mathematics with Applications*, **65**, 362–379.

Du, Juan, Fang, Fangxin, Pain, Christopher C, Navon, I.M., Zhu, Jiang, & Ham, David A. 2013b. POD reduced-order unstructured mesh modeling applied to 2D and 3D fluid flow. *Computers and Mathematics with Applications*, **65**(3), 362–379.

Du, Juan, Navon, IM, Zhu, Jiang, Fang, Fangxin, & Alekseev, AK. 2013c. Reduced order modeling based on POD of a parabolized Navier–Stokes equations model II: Trust region POD 4D VAR data assimilation. *Computers & Mathematics with Applications*, **65**(3), 380–394.

Durlofsky, Louis J, & Chen, Yuguang. 2012. Uncertainty quantification for subsurface flow problems using coarse-scale models. *Pages 163–202 of: Numerical Analysis of Multiscale Problems*. Springer.

Eftang, JL, Knezevic, DJ, & Patera, AT. 2011. An hp Certified Reduced Basis Method for Parametrized Parabolic Partial Differential Equations. *Math Comput Model Dyn Syst*, **17**(4), 395–422.

E.Iuliano, & D.Quagliarella. 2013. Aerodynamic Shape Optimization via non-intrusive POD-based Surrogate Modelling. *2013 IEEE Congress on Evolutionary Computation Cancn, Mxico*, 1–8.

Eldred, M. S., & Burkardt, J. 2009. Comparison of Non-Intrusive Polynomial Chaos and Stochastic Collocation Methods for Uncertainty Quantification. *American Institute of Aeronautics and Astronautics*, **20090976**, 1–20.

Elsayed, Khairy, & Lacor, Chris. 2013. CFD modeling and multi-objective optimization of cyclone geometry using desirability function, artificial neural networks and genetic algorithms. *Applied Mathematical Modelling*, **37**(8), 5680–5704.

Epureanuj, Bogdan I, & Heeg, Jennifer. 1999. Reduced order models in unsteady aerodynamics.

Er, Meng Joo, Wu, Shiqian, Lu, Juwei, & Toh, Hock Lye. 2002. Face recognition with radial basis function (RBF) neural networks. *Neural Networks, IEEE Transactions on*, **13**(3), 697–710.

Fang, F, Pain, CC, Navon, IM, Piggott, MD, Gorman, GJ, Farrell, PE, Allison, PA, & Goddard, AJH. 2009a. A POD reduced-order 4D-Var adaptive mesh ocean modelling approach. *International Journal for Numerical Methods in Fluids*, **60**(7), 709–732.

Fang, F., Pain, C.C., Navon, I.M., Piggott, M.D., Gorman, G.J., Allison, P.A., & Goddard, A.J.H. 2009b. Reduced-order modelling of an adaptive mesh ocean model. *International journal for numerical methods in fluids*, **59**(8), 827–851.

Fang, F, Pain, C.C., Navon, I.M., Gorman, GJ, Piggott, MD, Allison, PA, & Goddard, AJH. 2010. A POD goal-oriented error measure for mesh optimization. *International Journal for Numerical Methods in Fluids*, **63**(2), 185–206.

Fang, F, Zhang, T, Pavlidis, D, Pain, C.C., Buchan, AG, & Navon, I.M. 2014. Reduced order modelling of an unstructured mesh air pollution model and application in 2D/3D urban street canyons. *Atmospheric Environment*, **96**, 96–106.

Farrell, PE, Piggott, MD, Pain, CC, Gorman, GJ, & Wilson, CR. 2009. Conservative interpolation between unstructured meshes via supermesh construction. *Computer Methods in Applied Mechanics and Engineering*, **198**(33), 2632–2642.

F.Casenave, A.Ern, & T.Lelivre. 2014. A nonintrusive reduced basis method applied to aeroacoustic simulations. *Advances in Computational Mathematics*, 1–26.

Feriedoun Sabetghadam, Alireza Jafarpour. 2012. α Regularization of the POD-Galerkin Dynamical Systems of the Kuramoto-Sivashinsky Equation. *Applied Mathematics and Computation*, **218**, 6012–6026.

F.Fang, C.Pain, Navon, I.M., Elsheikh, A.H., Du, J., & D.Xiao. 2013. Non-Linear Petrov-Galerkin Methods for Reduced Order Hyperbolic Equations and Discontinuous Finite Element Methods. *Journal of Computational Physics*, **234**, 540–559.

Fink, Davina, & Ehlers, Wolfgang. 2015. Application and modification of the POD method and the POD-DEIM for model reduction in porous-media simulations. *PAMM*, **15**(1), 385–386.

Fornberg, Bengt, & Flyer, Natasha. 2005. Accuracy of radial basis function interpolation and derivative approximations on 1-D infinite grids. *Advances in Computational Mathematics*, **23**(1-2), 5–20.

Forti, Davide, & Rozza, Gianluigi. 2014. Efficient geometrical parametrisation techniques of interfaces for reduced-order modelling: application to fluid–structure interaction coupling problems. *International Journal of Computational Fluid Dynamics*, **28**(3-4), 158–169.

Fosas de Pando, Miguel, Schmid, Peter J, & Sipp, Denis. 2013. Nonlinear model-order reduction for oscillator flows using POD-DEIM. *Page 25006 of: APS Meeting Abstracts*, vol. 1.

Franca, Leopoldo P., & Frey, Sergio L. 1992a. Stabilized finite element methods: II. The incompressible Navier-Stokes equations. *Computer Methods in Applied Mechanics and Engineering*, **99**(2-3), 209–233.

Franca, Leopoldo P, & Frey, Sérgio L. 1992b. Stabilized finite element methods: II. The incompressible Navier-Stokes equations. *Computer Methods in Applied Mechanics and Engineering*, **99**(2), 209–233.

Frangos, M, Marzouk, Y, Willcox, K, & van Bloemen Waanders, B. 2010. Surrogate and reduced-order modeling: A comparison of approaches for large-scale statistical inverse problems. *Large-Scale Inverse Problems and Quantification of Uncertainty*, **123149**.

Fukunaga, K. 1990. Introduction to Statistical Recognition(2nd edn). *Computer Science and Scientific Computing Series*, **Academic Press,Academic Press: Boston, MA.**, 5–33.

Funke, S.W., Pain, C.C., Kramer, S.C., & Piggott, M.D. 2011. A wetting and drying algorithm with a combined pressure/free-surface formulation for non-hydrostatic models. *Advances in Water Resources*, **34**(11), 1483–1495.

Galbally, David, Fidkowski, K, Willcox, K, & Ghattas, O. 2010. Non-linear model reduction for uncertainty quantification in large-scale inverse problems. *International journal for numerical methods in engineering*, **81**(12), 1581–1608.

Ganapathysubramanian, Baskar, & Zabaras, Nicholas. 2007. Sparse grid collocation schemes for stochastic natural convection problems. *Journal of Computational Physics*, **225**(1), 652–685.

Garcke, Jochen, & Griebel, Michael. 2013. *Sparse grids and applications*. Springer.

Gavilan Gonzalez, Angel, & Rojas, Juan A. 2009. Solving Portfolio Problems with the Smolyak-Parameterized Expectations Algorithm.

Gerstner, T., & Griebel, M. 1998. Numerical integration using sparse grids. *Numerical algorithms*, **18**(3-4), 209–232.

Ghasemi, Mohamadreza, & Gildin, Eduardo. 2015. Localized Model Reduction in Porous Media Flow. *IFAC-PapersOnLine*, **48**(6), 242 – 247. 2nd {IFAC} Workshop on Automatic Control in Offshore Oil and Gas Production {OOGP} 2015Florianpolis, Brazil, 2729 May 2015.

Ghasemi, Mohammadreza. 2015. *Model order reduction in porous media flow simulation and optimization*. Ph.D. thesis.

Ghasemi, Mohammadreza, Ibrahim, Ashraf, Gildin, Eduardo, *et al.* . 2014. Reduced Order Modeling in Reservoir Simulation Using the Bilinear Approximation Techniques. *In: SPE Latin America and Caribbean Petroleum Engineering Conference*. Society of Petroleum Engineers.

Ghasemi, Mohammadreza, Yang, Yanfang, Gildin, Eduardo, Efendiev, Yalchin, Calo, Victor, *et al.* . 2015. Fast Multiscale Reservoir Simulations using POD-DEIM Model Reduction. *In: SPE Reservoir Simulation Symposium*. Society of Petroleum Engineers.

Gholami, Azadeh, Bonakdari, Hossein, Zaji, Amir Hossein, & Akhtari, Ali Akbar. 2015. Simulation of open channel bend characteristics using computational fluid dynamics and artificial neural networks. *Engineering Applications of Computational Fluid Mechanics*, **9**(1), 355–369.

Ghoman, Satyajit S, Wang, Zhicun, Chen, PC, & Kapania, Rakesh K. 2012. A POD-based reduced order design scheme for shape optimization of air vehicles. *AIAA Paper*, **1808**.

Ghommem, Mehdi, Gildin, Eduardo, Ghasemi, Mohammadreza, *et al.* . 2015. Complexity Reduction of Multiphase Flows in Heterogeneous Porous Media. *SPE Journal*.

Gildin, Eduardo, Ghasemi, Mohammadreza, Romanovskay, Anastasiya, Efendiev, Yalchin, *et al.* . 2013. Nonlinear complexity reduction for fast simulation of flow in heterogeneous porous media. *In: SPE Reservoir Simulation Symposium*. Society of Petroleum Engineers.

Ginevra Di Donato, SPE, Wenfen Huang, SPE, & Martin Blunt, SPE. 2003. Streamline-Based Dual Porosity Simulation of Fractured Reservoirs.

Goss, Jennifer, & Subbarao, Kamesh. 2008. Inlet shape optimization based on POD model reduction of the Euler equations. *AIAA*, **5809**, 2008.

Goyal, Siddharth, & Barooah, Prabir. 2012. A method for model-reduction of nonlinear thermal dynamics of multi-zone buildings. *Energy and Buildings*, **47**, 332–340.

Graham, WR, Peraire, J, & Tang, KY. 1999a. Optimal control of vortex shedding using low-order models. Part IIModel-based control. *International journal for numerical methods in engineering*, **44**(7), 973–990.

Graham, WR, Peraire, J, & Tang, KY. 1999b. Optimal control of vortex shedding using low-order models. Part Iopen-loop model development. *International Journal for Numerical Methods in Engineering*, **44**(7), 945–972.

Guénot, Marc, Lepot, Ingrid, Sainvitu, Caroline, Goblet, Jordan, & Coelho, Rajan Filomeno. 2013. Adaptive sampling strategies for non-intrusive POD-based surrogates. *Engineering computations*, **30**(4), 521–547.

Gugercin, Serkan, & Antoulas, Athanasios C. 2004. A survey of model reduction by balanced truncation and some new results. *International Journal of Control*, **77**(8), 748–766.

Guo, Liwei, Latham, John-Paul, & Xiang, Jiansheng. 2015. Numerical simulation of breakages of concrete armour units using a three-dimensional fracture model in the context of the combined finite-discrete element method. *Computers & Structures*, **146**, 117–142.

Haasdonk, Bernard, & Ohlberger, Mario. 2008. Reduced basis method for finite volume approximations of parametrized linear evolution equations. *ESAIM: Mathematical Modelling and Numerical Analysis-Modélisation Mathématique et Analyse Numérique*, **42**(2), 277–302.

Hahn, Juergen, & Edgar, Thomas F. 2002. An improved method for nonlinear model reduction using balancing of empirical gramians. *Computers & chemical engineering*, **26**(10), 1379–1397.

Han, Chen. 2012. *Blackbox Stencil Interpolation Method for Model Reduction*. M.Phil. thesis, Massachusetts Institute of Technology.

He, J, & Durlofsky, LJ. 2015. Constraint reduction procedures for reduced-order subsurface flow models based on POD–TPWL. *International Journal for Numerical Methods in Engineering*.

He, Jincong. 2013. *Reduced-Order Modeling for Oil-Water and Compositional Systems, with Application to Data Assimilation and Production Optimization*. Ph.D. thesis, Stanford University.

Heijn, T, Markovinovic, R, Jansen, & J-D. 2004. Generation of low-order reservoir models using system-theoretical concepts. *SPE Journal*, **9**(02), 202–218.

Heiss, F., & Winschel, V. 2008. Likelihood approximation by numerical integration on sparse grids. *Journal of Econometrics*, **144**(1), 62–80.

Himpe, Christian, & Ohlberger, Mario. 2014. Cross-Gramian-Based Combined State and Parameter Reduction for Large-Scale Control Systems. *Mathematical Problems in Engineering*, **2014**.

Hinze, Michael, & Kunkel, Martin. 2012. Discrete empirical interpolation in POD model order reduction of drift-diffusion equations in electrical networks. *Pages 423–431 of: Scientific Computing in Electrical Engineering SCEE 2010*. Springer.

H.Klie. 2013. Unlocking Fast Reservoir Predictions via Non-Intrusive Reduced Order Models. *The SPE Reservoir Simulation Symposium held in The Woodland, Texas, USA*, 1–16.

Hoepffner, Jérôme, Akervik, Espen, Ehrenstein, Uwe, & Henningson, Dan S. 2006. Control of cavity-driven separated boundary layer. *In: Proceedings of the Conference on active flow control, Berlin.*

Hoteit, Ibrahim, & Köhl, Armin. 2006. Efficiency of reduced-order, time-dependent adjoint data assimilation approaches. *Journal of oceanography*, **62**(4), 539–550.

Hoteit, Ibrahim, & Pham, Dinh-Tuan. 2004. An adaptively reduced-order extended Kalman filter for data assimilation in the tropical Pacific. *Journal of marine systems*, **45**(3), 173–188.

Iman, Ronald L, & Helton, Jon C. 1988. An investigation of uncertainty and sensitivity analysis techniques for computer models. *Risk analysis*, **8**(1), 71–90.

Iollo, Angelo, Lanteri, Stephane, & Désidéri, J-A. 2000a. Stability properties of POD–Galerkin approximations for the compressible Navier–Stokes equations. *Theoretical and Computational Fluid Dynamics*, **13**(6), 377–396.

Iollo, Angelo, Dervieux, Alain, Désidéri, Jean-Antoine, & Lanteri, Stéphane. 2000b. Two stable POD-based approximations to the Navier–Stokes equations. *Computing and Visualization in Science*, **3**(1-2), 61–66.

Ito, K, & Ravindran, SS. 1998a. A reduced basis method for control problems governed by PDEs. *Pages 153–168 of: Control and estimation of distributed parameter systems*. Springer.

Ito, Kazufumi, & Ravindran, Sivaguru S. 2001. Reduced basis method for optimal control of unsteady viscous flows. *International Journal of Computational Fluid Dynamics*, **15**(2), 97–113.

Ito, Kazufumi, & Ravindran, SS. 1998b. A reduced-order method for simulation and control of fluid flows. *Journal of computational physics*, **143**(2), 403–425.

Ito, Kazufumi, & Schroeter, Jeffry D. 2001. Reduced order feedback synthesis for viscous incompressible flows. *Mathematical and computer modelling*, **33**(1), 173–192.

J.Burkardt. 2014. Sparse Grid Collocation for Uncertainty Quantification. *Presentation at Department of Scientific Computing Florida State University*, 1–64.

Jenny, P, Lee, SH, & Tchelepi, HA. 2005. Adaptive multiscale finite-volume method for multiphase flow and transport in porous media. *Multiscale Modeling & Simulation*, **3**(1), 50–64.

Jenny, Patrick, Lee, Seong H, & Tchelepi, Hamdi A. 2006. Adaptive fully implicit multi-scale finite-volume method for multi-phase flow and transport in heterogeneous porous media. *Journal of Computational Physics*, **217**(2), 627–641.

John Burkardt. 2012. The Sparse Grid Interpolant. *http://people.sc.fsu.edu/jburkardt/presentations/ sparse_interpolant.pdf*, 1–5.

Jolliffe, I.T. 2002. Principal Component Analysis. *Springer, second edition*, 559–572.

Judd, Kenneth L, Maliar, Lilia, Maliar, Serguei, & Valero, Rafael. 2014. Smolyak method for solving dynamic economic models: Lagrange interpolation, anisotropic grid and adaptive domain. *Journal of Economic Dynamics and Control*, **44**, 92–123.

Kalashnikova, I., & Barone, M. F. 2009. On the Stability and Convergence of a Galerkin Reduced Order Model (ROM) of Compressible Flow with Solid Wall and Far-Field Boundary Treatment. *International Journal For Numerical Methods In Engineering*, **00**, 1–28.

Kalashnikova, I, Barone, MF, & Brake, MR. 2013. A stable Galerkin reduced order model for coupled fluid–structure interaction problems. *International Journal for Numerical Methods in Engineering*, **95**(2), 121–144.

Kamakoti, Ramji, & Shyy, Wei. 2004. Fluid–structure interaction for aeroelastic applications. *Progress in Aerospace Sciences*, **40**(8), 535–558.

Khattak, Ahmad Jan, Tirmizi, SIA, *et al.* . 2009. Application of meshfree collocation method to a class of nonlinear partial differential equations. *Engineering analysis with boundary elements*, **33**(5), 661–667.

Klie, Hector, *et al.* . 2013. Unlocking Fast Reservoir Predictions via Nonintrusive Reduced-Order Models. *In: SPE Reservoir Simulation Symposium*. Society of Petroleum Engineers.

Kunisch, Karl, Volkwein, Stefan, & Xie, L. 2004. HJB-POD-based feedback design for the optimal control of evolution problems. *SIAM Journal on Applied Dynamical Systems*, **3**(4), 701–722.

Lall, Sanjay, Marsden, Jerrold E, & Glavaški, Sonja. 2002. A subspace approach to balanced truncation for model reduction of nonlinear control systems. *International journal of robust and nonlinear control*, **12**(6), 519–535.

Lass, Oliver, & Volkwein, Stefan. 2013. POD Galerkin schemes for nonlinear elliptic-parabolic systems. *SIAM Journal on Scientific Computing*, **35**(3), A1271–A1298.

Latham, John-Paul, Mindel, Julian, Xiang, Jiansheng, Guises, Romain, Garcia, Xavier, Pain, Chris, Gorman, Gerard, Piggott, Matthew, & Munjiza, Antonio. 2009. Coupled FEMDEM/Fluids for coastal engineers with special reference to armour stability and breakage. *Geomechanics and Geoengineering: An International Journal*, **4**(1), 39–53.

LeCun, Yann, Bengio, Yoshua, & Hinton, Geoffrey. 2015. Deep learning. *Nature*, **521**(7553), 436–444.

Lehmann, Oliver, Luchtenburg, Mark, Noack, Bernd R, King, Rudibert, Morzyński, Marek, & Tadmor, Gilead. 2005. Wake stabilization using POD Galerkin models with interpolated modes. *Pages 500–505 of: Decision and Control, 2005 and 2005 European Control Conference. CDC-ECC'05. 44th IEEE Conference on*. IEEE.

Lei, Qinghua, Latham, John-Paul, Xiang, Jiansheng, Tsang, Chin-Fu, Lang, Philipp, & Guo, Liwei. 2014. Effects of geomechanical changes on the validity of a discrete fracture network representation of a realistic two-dimensional fractured rock. *International Journal of Rock Mechanics and Mining Sciences*, **70**, 507–523.

Lei, Qinghua, Latham, John-Paul, Xiang, Jiansheng, & Tsang, Chin-Fu. 2015. Polyaxial stress-induced variable aperture model for persistent 3D fracture networks. *Geomechanics for Energy and the Environment*, **1**, 34–47.

Liberge, Erwan, Pomarede, Marie, & Hamdouni, Aziz. 2010. Reduced-order modelling by POD-multiphase approach for fluid-structure interaction. *European Journal of Computational Mechanics/Revue Européenne de Mécanique Numérique*, **19**(1-3), 41–52.

Lieu, T, Farhat, C, & Lesoinne, M. 2006. Reduced-order fluid/structure modeling of a complete aircraft configuration. *Computer methods in applied mechanics and engineering*, **195**(41), 5730–5742.

Lieu, Thuan, Farhat, Charbel, & Lesoinne, Michel. 2005. POD-based aeroelastic analysis of a complete F-16 configuration: ROM adaptation and demonstration. *AIAA Paper*, **2295**, 2005.

Lowe, D. 1988. Multi-variable functional interpolation and adaptive networks. *Complex Systems*, **2**, 321–355.

Lucia, David J, King, Paul I, Oxley, Mark E, & Beran, Philip S. 2001. Reduced order modeling for a one-dimensional nozzle flow with moving shocks. *AIAA paper*, 01–2602.

Lumley, J. L. 1967. The Structure of Inhomogeneous Turbulent Flows. *Pages 166–178 of: Atmospheric turbulence and radio propagation*. Moscow: Nauka.

Luo, Zhendong, Chen, Jing, Zhu, Jiang, Wang, Ruiwen, & Navon, IM. 2007a. An optimizing reduced order FDS for the tropical Pacific Ocean reduced gravity model. *International Journal for Numerical Methods in Fluids*, **55**(2), 143–161.

Luo, Zhendong, Zhu, Jiang, Wang, Ruiwen, & Navon, I Michael. 2007b. Proper orthogonal decomposition approach and error estimation of mixed finite element methods for the tropical Pacific Ocean reduced gravity model. *Computer Methods in Applied Mechanics and Engineering*, **196**(41), 4184–4195.

Ma, Zhanhua, Ahuja, Sunil, & Rowley, Clarence W. 2011. Reduced-order models for control of fluids using the eigensystem realization algorithm. *Theoretical and Computational Fluid Dynamics*, **25**(1-4), 233–247.

Madych, WR. 1992. Miscellaneous error bounds for multiquadric and related interpolators. *Computers & Mathematics with Applications*, **24**(12), 121–138.

Marley, Christopher D, Duraisamy, Karthikeyan, & Driscoll, James F. 2015. Reduced Order Modeling of Compressible Flows with Unsteady Normal Shock Motion. *Page 3988 of: 51st AIAA/SAE/ASEE Joint Propulsion Conference*.

Mehrmann, Volker, & Stykel, Tatjana. 2005. Balanced truncation model reduction for large-scale systems in descriptor form. *Pages 83–115 of: Dimension Reduction of Large-Scale Systems*. Springer.

Meyer, Marcus, & Matthies, Hermann G. 2003. Efficient model reduction in nonlinear dynamics using the Karhunen-Loeve expansion and dual-weighted-residual methods. *Computational Mechanics*, **31**(1-2), 179–191.

Milliken, WJ, Emanuel, AS, Chakravarty, A, *et al.* . 2001. Applications of 3D streamline simulation to assist history matching. *SPE Reservoir Evaluation & Engineering*, **4**(06), 502–508.

Mohaghegh, Kasra, Striebel, Michael, ter Maten, E Jan W, & Pulch, Roland. 2010. Nonlinear model order reduction based on trajectory piecewise linear approach: comparing different linear cores. *Pages 563–570 of: Scientific Computing in Electrical Engineering SCEE 2008*. Springer.

Mokhasi, Paritosh, & Rempfer, Dietmar. 2010. Nonlinear system identification using radial basis functions. *International Journal for Numerical Methods in Fluids*, **63**(2), 121–162.

Müller, Markus. 2008. *On the POD method: an abstract investigation with applications to reduced-order modeling and suboptimal control*. Ph.D. thesis, Georg-August-Universitt zu Gttingen.

Munjiza, A, Andrews, KRF, & White, JK. 1999. Combined single and smeared crack model in combined finite-discrete element analysis. *International Journal for Numerical Methods in Engineering*, **44**(1), 41–57.

Munjiza, Ante. 2004. *The combined finite-discrete element method*. John Wiley & Sons, Ltd.

My Ha, Dao, Tkalich, Pavel, & Chan, Eng Soon. 2008. Tsunami forecasting using proper orthogonal decomposition method. *Journal of Geophysical Research: Oceans (1978–2012)*, **113**(C6).

Myers, Donald E. 1999. Smoothing and interpolation with radial basis functions. *BOUNDARY ELEMENT TECHNOLOGY*, **13**, 365–376.

Nguyen, N.C., & Peraire, J. 2008. An efficient reduced-order modeling approach for non-linear parametrized partial differential equations. *Int. J. Numer. Meth. Engng.*, **76**, 27–55.

Nguyen, NC, Patera, AT, & Peraire, J. 2008. A best points interpolation method for efficient approximation of parametrized functions. *International journal for numerical methods in engineering*, **73**(4), 521–543.

Nguyen, NC, Rozza, G, & Patera, AT. 2009. Reduced Basis Approximation and A Posteriori Error Estimation for the Time-Dependent Viscous Burgers Equation. *Calcolo*, **46**(3), 157185.

Noack, B. R., Morzynski, M., & Tadmor, G. 2011. *Reduced-Order modelling for flow control*. Vol. 528. Springer.

Noack, Bernd R, Afanasiev, Konstantin, Morzynski, Marek, Tadmor, Gilead, & Thiele, Frank. 2003. A hierarchy of low-dimensional models for the transient and post-transient cylinder wake. *Journal of Fluid Mechanics*, **497**, 335–363.

Nobile, Fabio, Tempone, Raúl, & Webster, Clayton G. 2008. A sparse grid stochastic collocation method for partial differential equations with random input data. *SIAM Journal on Numerical Analysis*, **46**(5), 2309–2345.

Noori, R., Karbassi, A.R., Ashrafi, Kh., Ardestani, M., & Mehrdadi, N. 2013. Development and application of reduced-order neural network model based on proper orthogonal decomposition for BOD5 monitoring: Active and online prediction. *Environmental Progress and Sustainable Energy*, **32**(1), 120–127.

Osth, Jan, Noack, Bernd R., Krajnovi, Sinia, Barros, Diogo, & Bore, Jacques. 2014. On the need for a nonlinear subscale turbulence term in POD models as exemplified for a high-Reynolds-number flow over an Ahmed body. *Journal of Fluid Mechanics*, **747**(5), 518–544.

Pain, CC, Piggott, MD, Goddard, AJH, Fang, F, Gorman, GJ, Marshall, DP, Eaton, MD, Power, PW, & De Oliveira, CRE. 2005. Three-dimensional unstructured mesh ocean modelling. *Ocean Modelling*, **10**(1), 5–33.

Panzer, Heiko, Mohring, Jan, Eid, Rudy, & Lohmann, Boris. 2010. Parametric model order reduction by matrix interpolation. *at-Automatisierungstechnik Methoden und Anwendungen der Steuerungs-, Regelungs-und Informationstechnik*, **58**(8), 475–484.

Papadrakakis, M, Kojic, M, & Tuncer, I. 2014. REDUCED ORDER MODELLING OF HIGH-FIDELITY COMPUTATIONAL FLUID-STRUCTURE INTERACTION ANALYSIS FOR AEROELASTIC SYSTEMS.

Pearson, K. 1901. On lines and planes of closest fit to systems of points in space. *Philosophical Magazine*, **2**, 559–572.

Peherstorfer, Benjamin. 2013. *Model Order Reduction of Parametrized Systems with Sparse Grid Learning Techniques*. Dissertation, Technische Universitat Munchen, Munchen.

Peherstorfer, Benjamin, Butnaru, Daniel, Willcox, Karen, & Bungartz, Hans-Joachim. 2014. Localized discrete empirical interpolation method. *SIAM Journal on Scientific Computing*, **36**(1), A168–A192.

Peña, F Lopez, Casás, V Díaz, Gosset, A, & Duro, RJ. 2012. A surrogate method based on the enhancement of low fidelity computational fluid dynamics approximations by artificial neural networks. *Computers & Fluids*, **58**, 112–119.

Peterson, Janet S. 1989. The reduced basis method for incompressible viscous flow calculations. *SIAM Journal on Scientific and Statistical Computing*, **10**(4), 777–786.

Pflüger, Dirk, Peherstorfer, Benjamin, & Bungartz, Hans-Joachim. 2010. Spatially adaptive sparse grids for high-dimensional data-driven problems. *Journal of Complexity*, **26**(5), 508–522.

Powell, Michael JD. 1992. The theory of radial basis function approximation in 1990. *Advances in numerical analysis 2*, 105–210.

Qiu, C, & Chou, J. 2006. Four-dimensional data assimilation method based on SVD: Theoretical aspect. *Theoretical and applied climatology*, **83**(1-4), 51–57.

Qu, Liyan, & Chapman, Patrick L. 2004. A trajectory piecewise-linear approach to model order reduction for nonlinear stationary magnetic devices. *Pages 15–19 of: Computers in Power Electronics, 2004. Proceedings. 2004 IEEE Workshop on.* IEEE.

Raghavan, Balaji, Hamdaoui, Mohamed, Xiao, Manyu, Breitkopf, Piotr, & Villon, Pierre. 2013. A bi-level meta-modeling approach for structural optimization using modified POD bases and Diffuse Approximation. *Computers & Structures*, **127**, 19–28.

Raisee, M, Kumar, D, & Lacor, C. 2015. A non-intrusive model reduction approach for polynomial chaos expansion using proper orthogonal decomposition. *International Journal for Numerical Methods in Engineering*.

Ravindran, SS. 2000. A reduced-order approach for optimal control of fluids using proper orthogonal decomposition. *International journal for numerical methods in fluids*, **34**(5), 425–448.

Renard, Ph, & De Marsily, G. 1997. Calculating equivalent permeability: a review. *Advances in Water Resources*, **20**(5), 253–278.

Rewienski, M, & White, Jacob. 2002. Improving trajectory piecewise-linear approach to nonlinear model order reduction for micromachined devices using an aggregated projection basis. *Pages 128–131 of: Proceedings of the 5th International Conference on Modeling and Simulation of Microsystems*.

Rewieński, Michał, & White, Jacob. 2006. Model order reduction for nonlinear dynamical systems based on trajectory piecewise-linear approximations. *Linear algebra and its applications*, **415**(2), 426–454.

Rewienski, Michał Jerzy. 2003. *A trajectory piecewise-linear approach to model order reduction of nonlinear dynamical systems*. Ph.D. thesis, Citeseer.

Rozza, G, Huynh, DBP, & Patera, AT. 2008. Reduced Basis Approximation and A Posteriori Error Estimation for Affinely Parametrized Elliptic Coercive Partial Differential Equations- Application to Transport and Continuum Mechanics. *Arch Comput Methods Eng*, **15**(3), 229275.

R.Stefanescu, & Navon, I.M. 2013. POD/DEIM Nonlinear model order reduction of an ADI implicit shallow water equations model. *Journal of Computational Physics*, **237**, 95–114.

Sacks, Jerome, Welch, William J, Mitchell, Toby J, & Wynn, Henry P. 1989. Design and analysis of computer experiments. *Statistical science*, 409–423.

Sahyoun, Samir, & Djouadi, Seddik M. 2014. Nonlinear model reduction using Space Vectors Clustering POD with application to the Burgers' equation. *Pages 1661–1666 of: American Control Conference (ACC), 2014*. IEEE.

Salinas, P., Percival, J. R., Pavlidis, D., Xie, Z., Gomes, J., Pain, C. C., & Jackson, M. D. 2015. A discontinuous overlapping control volume finite element method for multi-phase porous media flow using dynamic unstructured mesh optimization. *In: SPE 173279*.

Saltelli, Andrea. 2002. Sensitivity analysis for importance assessment. *Risk Analysis*, **22**(3), 579–590.

Saltelli, Andrea, Ratto, Marco, Andres, Terry, Campolongo, Francesca, Cariboni, Jessica, Gatelli, Debora, Saisana, Michaela, & Tarantola, Stefano. 2008. *Global sensitivity analysis: the primer*. John Wiley & Sons.

San, O, & Borggaard, J. 2015. Principal interval decomposition framework for POD reduced-order modeling of convective Boussinesq flows. *International Journal for Numerical Methods in Fluids*, **78**(1), 37–62.

Schilders, Wilhelmus HA, Van der Vorst, Henk A, & Rommes, Joost. 2008. *Model order reduction: theory, research aspects and applications*. Vol. 13. Springer.

Schlegel, Michael, & Noack, Bernd R. 2015. On long-term boundedness of Galerkin models. *Journal of Fluid Mechanics*, **765**(2), 325–352.

Schmidt, S, KreuBer, L, & Zhang, S. 2012. POD-DEIM based model order reduction for a three-dimensional microscopic Liion battery model.

Seshagiri, Sridhar, & Khalil, Hassan K. 2000. Output feedback control of nonlinear systems using RBF neural networks. *Neural Networks, IEEE Transactions on*, **11**(1), 69–79.

Shankar, Varun, Wright, Grady B, Fogelson, Aaron L, & Kirby, Robert M. 2014. A radial basis function (RBF) finite difference method for the simulation of reaction–diffusion equations on stationary platelets within the augmented forcing method. *International Journal for Numerical Methods in Fluids*, **75**(1), 1–22.

Sharan, Maithili, Kansa, EJ, & Gupta, Suman. 1997. Application of the multi-quadric method for numerical solution of elliptic partial differential equations. *Applied Mathematics and Computation*, **84**(2), 275–302.

Siavashi, Majid, Blunt, Martin J, Raisee, Mehrdad, & Pourafshary, Peyman. 2014. Three-dimensional streamline-based simulation of non-isothermal two-phase flow in heterogeneous porous media. *Computers & Fluids*, **103**, 116–131.

Sirisup, S, & Karniadakis, GE. 2004. A spectral viscosity method for correcting the long-term behavior of POD models. *Journal of Computational Physics*, **194**(1), 92–116.

Sirisup, S, & Karniadakis, GE. 2005. Stability and accuracy of periodic flow solutions obtained by a POD-penalty method. *Physica D: Nonlinear Phenomena*, **202**(3), 218–237.

Sirovich, L. 1987. Turbulence and the Dynamics of Coherent Structures, Part III: Dynamics and Scaling. *Quarterly of Appl. Math.*, **XLV**, 583–590.

Smolyak, Sergey A. 1963. Quadrature and interpolation formulas for tensor products of certain classes of functions. **4**(240-243), 123.

Ştefănescu, R, & Navon, Ionel Michael. 2013a. POD/DEIM nonlinear model order reduction of an ADI implicit shallow water equations model. *Journal of Computational Physics*, **237**, 95–114.

Ştefănescu, R, & Navon, Ionel Michael. 2013b. POD/DEIM nonlinear model order reduction of an ADI implicit shallow water equations model. *Journal of Computational Physics*, **237**, 95–114.

Stefanescu, Razvan, Sandu, Adrian, & Navon, I.M. 2014a. Comparison of POD reduced order strategies for the nonlinear 2D shallow water equations. *International Journal for Numerical Methods in Fluids*, **76**(8), 497–521.

Stefanescu, Razvan, Sandu, Adrian, & Navon, Ionel Michael. 2014b. POD/DEIM Strategies for reduced data assimilation systems. *Journal of Computational Physics*.

Ştefănescu, Răzvan, Sandu, Adrian, & Navon, Ionel Michael. 2015. POD/DEIM reduced-order strategies for efficient four dimensional variational data assimilation. *Journal of Computational Physics*, **295**, 569–595.

Su, Kai, Latham, J-P, Pavlidis, Dimitrios, Xiang, Jiansheng, Fang, Fangxin, Mostaghimi, Peyman, Percival, James R, Pain, Christopher C, & Jackson, Matthew D. 2015. Multiphase flow simulation through porous media with explicitly resolved fractures. *Geofluids*.

Sumant, Prasad, Wu, Hong, Cangellaris, Andreas, & Aluru, Narayana. 2012. Reduced-order models of finite element approximations of electromagnetic devices exhibiting statistical variability. *IEEE Transactions on Antennas and Propagation*, **60**(1), 301–309.

Sumant, Prasad S, Wu, Hong, Cangellaris, Andreas C, & Aluru, NR. 2010. A sparse grid based collocation method for model order reduction of finite element approximations of passive electromagnetic devices under uncertainty. *Pages 1652–1655 of: Microwave Symposium Digest (MTT), 2010 IEEE MTT-S International*. IEEE.

Tchelepi, Hamdi A, Jenny, Patrick, Lee, Seong Hee, Wolfsteiner, Christian, *et al.* . 2007. Adaptive multiscale finite-volume framework for reservoir simulation. *SPE Journal*, **12**(02), 188–195.

Tchieu, Andrew Allen. 2011. *The development of low-order models for the study of fluid-structure interaction*. Ph.D. thesis, California Institute of Technology.

Tropea, Cameron, Yarin, Alexander L, & Foss, John F. 2007. *Springer handbook of experimental fluid mechanics*. Vol. 1. Springer Science & Business Media.

Ullmann, Sebastian, & Lang, Jens. 2014. POD-Galerkin Modeling and Sparse-Grid Collocation for a Natural Convection Problem with Stochastic Boundary Conditions. *Pages 295–315 of: Sparse Grids and Applications-Munich 2012*. Springer.

Vasile, Massimiliano, Minisci, Edmondo, Quagliarella, Domenico, Guénot, Marc, Lepot, Ingrid, Sainvitu, Caroline, Goblet, Jordan, & Filomeno Coelho, Rajan. 2013. Adaptive sampling strategies for non-intrusive POD-based surrogates. *Engineering computations*, **30**(4), 521–547.

Viré, A, Xiang, J, & Pain, CC. 2015. An immersed-shell method for modelling fluid–structure interactions. *Philosophical Transactions of the Royal Society of London A: Mathematical, Physical and Engineering Sciences*, **373**(2035), 20140085.

Voβ, T, Pulch, R, ter Maten, EJW, & El Guennouni, A. 2007. Trajectory piecewise linear approach for nonlinear differential-algebraic equations in circuit simulation. *Pages 167–173 of: Scientific Computing in Electrical Engineering*. Springer.

Voß, Thomas. 2007. Model reduction for nonlinear differential-algebraic equations. *In: Communications to SIMAI Congress*, vol. 2.

Walton, S, Hassan, O, & Morgan, K. 2013. Reduced order modelling for unsteady fluid flow using proper orthogonal decomposition and radial basis functions. *Applied Mathematical Modelling*, **37**(20), 8930–8945.

Wang, Hongwu, Chessa, Jack, Liu, Wing K, & Belytschko, Ted. 2008. The immersed/fictitious element method for fluid–structure interaction: volumetric consistency, compressibility and thin members. *International Journal for Numerical Methods in Engineering*, **74**(1), 32–55.

White, Tina R. 2015. A clustering algorithm for reduced order modeling of shock waves. *technical report, Department of Mechanical Engineering, Stanford University.*

Wilson, Kurt C, & Durlofsky, Louis J. 2013. Optimization of shale gas field development using direct search techniques and reduced-physics models. *Journal of Petroleum Science and Engineering*, **108**, 304–315.

Winter, M, & Breitsamter, C. 2014. *Reduced-Order Modeling of Unsteady Aerodynamic Loads Using Radial Basis Function Neural Networks.* Deutsche Gesellschaft für Luft-und Raumfahrt-Lilienthal-Oberth eV.

Wirtz, D, & Haasdonk, Bernard. 2012. Efficient a-posteriori error estimation for nonlinear kernel-based reduced systems. *Systems and Control Letters*, **61**(1), 203–211.

Wirtz, D., Karajan, N., & Haasdonk, B. 2013. *Model order reduction of multiscale models using kernel methods.* Tech. rept. SRC SimTech. University of Stuttgart.

Wirtz, D, Sorensen, DC, & Haasdonk, Bernard. 2014. A posteriori error estimation for DEIM reduced nonlinear dynamical systems. *SIAM Journal on Scientific Computing*, **36**(2), A311–A338.

Wörner, Martin. 2012. Numerical modeling of multiphase flows in microfluidics and micro process engineering: a review of methods and applications. *Microfluidics and nanofluidics*, **12**(6), 841–886.

Wright, Grady Barrett. 2003. *Radial basis function interpolation: numerical and analytical developments.* Ph.D. thesis, University of Colorado at Boulder.

Xiang, Jiansheng, Munjiza, Antonio, & Latham, John-Paul. 2009. Finite strain, finite rotation quadratic tetrahedral element for the combined finite–discrete element method. *International journal for numerical methods in engineering*, **79**(8), 946–978.

Xiao, D., Fang, F., Du, J., Pain, C.C., Navon, I.M., Buchan, A. G., ElSheikh, A.H., & Hu, G. 2013. Non-Linear Petrov-Galerkin Methods for Reduced Order Modelling of the Navier-Stokes Equations using a Mixed Finite Element Pair. *Computer Methods In Applied Mechanics and Engineering*, **255**, 147–157.

Xiao, D., Fang, F., Buchan, A. G., Pain, C.C., Navon*, I.M., Du, J., , & Hu, G. 2014. Non-linear model reduction for the Navier-Stokes equations using Residual DEIM method. *Journal of Computational Physics*, **263**, 1–18.

Xiao, D., Fang, F., Pain, C.C., & Navon, I.M. 2015a. Non-intrusive reduced order 3D free surface modelling. *submitted to Ocean Engineering*.

Xiao, D., Yang, P, Fang, F., Xiang, J, Pain, C.C., Navon, I.M., & Chen, M. 2015b. A non-intrusive reduced-order model for compressible fluid and fractured solid coupling and its application to blasting. *Submitted to jurnal of computational physics*.

Xiao, D., Fang, F., Pain, C.C., Navon, I.M., Salinas, P., & Muggeridge, A. 2015c. Non-intrusive reduced order modeling of multi-phase flow in porous media using the POD-RBF method. *submitted to Journal of Computational Physics*.

Xiao, D., Fang, F., Buchan, A.G., Pain, C.C., Navon, I.M., & Muggeridge, A. 2015d. Non-intrusive reduced order modelling of the Navier–Stokes equations. *Computer Methods in Applied Mechanics and Engineering*, **293**, 552–541.

Xiao, D., Fang, F., Pain, C., & Hu, G. 2015e. Non-intrusive reduced order modelling of the Navier-Stokes equations based on RBF interpolation. *International Journal for Numerical Methods in Fluids*, **79**(11), 580–595.

Xiao, D, Yang, P, Fang, F, Xiang, J, Pain, CC, & Navon, IM. 2016a. Non-intrusive reduced order modeling of fluid-structure interactions. *Computer Methods in Applied Mechanics and Engineering*, **303**, 35–54.

Xiao, D., Fang, F., Pain, C.C., Navon, I.M., & Muggeridge, A. 2016b. Variable-material non-intrusive reduced order modelling of multi-phase porous media flows. *In preparation*.

Xiao, D., Fang, F., Pain, C.C., & Navon, I.M. 2016c. Variable parameters non-intrusive reduced order modelling of Navier-Stoke equations. *Will submit to computer methods in applied mechanics and engineering*.

Xiao, Manyu, Breitkopf, Piotr, Coelho, Rajan Filomeno, Knopf-Lenoir, Catherine, Sidorkiewicz, Maryan, & Villon, Pierre. 2010. Model reduction by CPOD and Kriging. *Structural and multidisciplinary optimization*, **41**(4), 555–574.

Xiao, Manyu, Breitkopf, Piotr, Coelho, Rajan Filomeno, Knopf-Lenoir, Catherine, & Villon, Pierre. 2012. Enhanced POD projection basis with application to shape optimization of car engine intake port. *Structural and multidisciplinary optimization*, **46**(1), 129–136.

Yang, Chun, Tang, Dalin, & Liu, Shu Q. 2003. A multi-physics growth model with fluid–structure interactions for blood flow and re-stenosis in rat vein grafts: A growth model for blood flow and re-stenosis in grafts. *Computers & structures*, **81**(8), 1041–1058.

Yang, P., Xiang, J, Fang, F., Pavlidis, D, Latham, J., & Pain, C.C. 2015a. Modelling of fluid-structure interactions for multiphase viscous flows via an immersed-shell method. *to be submit to Journal of Computational Physics*.

Yang, Yanfang, Efendiev, Yalchin, Ghasemi, Mohammadreza, Gildin, Eduardo, Calo, Victor Manuel, *et al.* . 2015b. Fast Multiscale Reservoir Simulations using POD-DEIM Model Reduction. *In: SPE Reservoir Simulation Symposium*. Society of Petroleum Engineers.

Yoon, Seonkyoo, Alghareeb, Zeid, Williams, John, *et al.* . 2014. Development of Reduced-order Oil Reservoir Models using Localized DEIM. *Pages 1–26 of: SPE Annual Technical Conference and Exhibition*. Springer US.

Zhang, Zhen-yue, & Zha, Hong-yuan. 2004. Principal manifolds and nonlinear dimensionality reduction via tangent space alignment. *Journal of Shanghai University (English Edition)*, **8**(4), 406–424.

Zokagoa, Jean-Marie, & Soulaïmani, Azzeddine. 2012. A POD-based reduced-order model for free surface shallow water flows over real bathymetries for Monte-Carlo-type applications. *Computer Methods in Applied Mechanics and Engineering*, **221**, 1–23.